IDENTIFICATION OF DAMAGES IN STEEL STRUCTURES USING GUIDED WAVE METHOD

LU MINGYU

Ph.D

The Hong Kong Polytechnic University

2012

The Hong Kong Polytechnic University

Department of Mechanical Engineering

Identification of Damages in Steel Structures Using Guided Wave Method

LU Mingyu

A thesis submitted in partial fulfillment of the requirements for the degree of Doctor of Philosophy

February 2012

CERTIFICATE OF ORIGINALITY

I hereby declare that this thesis is my own work and that, to the best of my knowledge and belief, it reproduces no material previously published or written, nor material that has been accepted for the award of any other degree or diploma, except where due acknowledgement has been made in the text.

________________________________(Signature)

LU Mingyu (Name of student)

ABSTRACT

Ultrasonic guided wave (GW) has shown clear superiority and strong potential for identification and real-time monitoring of service-induced damage in structures which need on-demand interrogation, by virtue of its unique capability for forward or inverse analysis. The main challenges in GW-based structural health monitoring (SHM) and nondestructive evaluation (NDE) derive from two aspects of complex wave analysis: first, in applications in real structures, the signals collected are complex due to the large number of overlapping reflections obtained in time-traces because of the multiple boundaries of the structures; second, in application with real damage, the effects of closing and opening of a fatigue crack make the acquired wave signals more complex than in instances of artificial notch or crack. However, relatively little research has been devoted to investigation of the inspection of fatigue cracks, especially in complex structures.

In this thesis, a single piezoelectric lead zirconate titanate (PZT) actuator-sensor pair for locating a through-thickness crack within welded zone in thick steel plate is initially investigated through both finite element analysis and experiments to demonstrate GW-based techniques in plates with simple geometries which can be used to construct more complex structures for practical applications.

The feature extraction method is applied in a welded tubular steel structure (WTSS). A probability-based damage imaging approach is developed. As validation, the approach is employed to predict the presences and locations of multiple slot-like damages in the

welding zones of a WTSS. It can be concluded that the identification results using the extracted signal features are comparable, and accuracy when more damage-impaired sensing paths are involved.

An energy-based damage imaging approach is evaluated by identifying a fatigue crack in a thick steel plate. The propagation of GWs in the plate-like structure is complicated by thick geometry, wave dispersion, boundary reflection, and the existing boundary notch used to initiate the fatigue crack, resulting in diverse forms of interference with fatigue crack identification. Hence, signal features are extracted from the wave energy distribution. Simultaneously, the proposed method is demonstrated by FEM and good agreement is obtained between the numerical and experimental results using a new developed fatigue crack model.

The image-based approach is evaluated experimentally by detection and monitoring of a fatigue crack using time reversal method (TRM). Results indicate that several damage-sensitive features extracted in the normalized captured signals and different pattern recognition techniques are effective for monitoring of fatigue crack propagation in the steel plate, such as TRM, transmission coefficient and principal component analysis (PCA). Some of the experimental results are verified by FEM results.

PCA is validated by monitoring of the propagation of a surface fatigue crack in a welded steel angle structure (WSAS) using GWs generated by a PZT sensor network which is surface-mounted to classify and distinguish different structural conditions due to fatigue crack initiation and propagation. Instead of directly comparing the changes between a series of specific signal segments, signal statistical parameters extracted from the frequency domain are demonstrated to have the capability of monitoring fatigue crack in welded steel structures.

In summary, application of GW-based damage detection techniques using structurally integrated PZT transducers for SHM is still in its formative years, and one of the main challenges is use in complex real-world structures. Different approaches are validated systematically in this thesis via simulations and experiments. Results for typical cases indicate that the proposed methods are applicable and effective for detection and real-time monitoring of non-fatigue damage and fatigue cracks in engineering structures.

PUBLICATIONS ARISING FROM THIS THESIS

Refereed Journal Papers

1. Mingyu Lu, Xi Lu, Limin Zhou, Zhongqing Su, Lin Ye, Xiaoting Miao and Fucai Li, Fatigue crack detection in steel plates using guided waves and an energy-based imaging approach, submitted to **SMART MATER. STRUCT**, **2011.**

2. Xi Lu, Mingyu Lu, Limin Zhou, Zhongqing Su, Li Cheng, Lin Ye and Guang Meng, Evaluation of welding damage in welded tubular steel structures using guided waves and a probability-based imaging approach, **SMART MATER. STRUCT,** Volume: **20** Issue: **1** Article Number: **015018** Published: **JAN 2011.**

3. Mingyu Lu, Dong Wang, Limin Zhou, Zhongqing Su and Lin Ye, Monitoring of fatigue crack propagation using time reversal method and imaging approach, submitted to **SMART STRUCTURES AND SYSTEMS, 2012**.

4. Mingyu Lu, Limin Zhou, Zhongqing Su and Lin Ye, Monitoring of surface fatigue crack propagation in steel angle structures using guided waves, submitted to **JOURNAL OF INTELLIGENT MATERIAL SYSTEMS AND STRUCTURES, 2012**.

5. Ye Lu, Mingyu Lu, Lin Ye, Dong Wang, Limin Zhou and Zhongqing Su, Monitoring of fatigue crack growth using principal component analysis on Lamb wave signals, submitted to **SMART MATER. STRUCT, 2011.**

6. Xiaoting Miao, Fucai Li, Guang Meng, Lin Ye, Limin Zhou and Mingyu Lu, Guided wave-based damage detection for a cylindrical structure in plane-strain state, submitted to **SMART MATER. STRUCT, 2011.**

Refereed International Conference Papers

7. Mingyu Lu, Xi Lu, Limin Zhou, Zhongqing Su, Lin Ye and Fucai Li, Fatigue crack detection using guided waves and probability-based imaging approach, Proc. Structural Health Monitoring 2011, Vol. 1, pp. 282-289, The 8th International Workshop on Structural Health Monitoring, Stanford (IWSHM8), USA, September, 2011.

8. Mingyu Lu, Dong Wong, Limin Zhou, Zhongqing Su, Li Cheng and Lin Ye, Monitoring of fatigue crack propagation of engineering structures using time reversal method, Proc. ICCM 18, AF1629, 18th International Conference on Composite Materials, Jeju, Korea, August, 2011.

9. Mingyu Lu, Yongwei Qu, Ye Lu, Lin Ye, Limin Zhou and Zhongqing Su, Monitoring of surface-fatigue crack propagation in a welded steel angle structure using guided waves and principal component analysis, presented in 3d International Conference on Smart Materials and Nanotechnology in Engineering (SMN 2011), Shenzhen, China, December, 2011.

10. Mingyu Lu, Xi Lu, Limin Zhou and Fucai Li, Failure detection on train bogie frames using guided waves and an image-based approach, presented in The 1st International Workshop on High-speed and Intercity Railways (IWHIR 2011), Shenzhen and Hong Kong, China, July, 2011.

11. Mingyu Lu, Xi Lu, Limin Zhou, Zhongqing Su and Lin Ye, Guided-wave-based detections of weld and crack in steel plates, Proc. of International Conference on Smart Materials and Nanotechnology in Engineering (SMN 2009), July, 2009, Weihai, China, Proc. SPIE 7493, 74932S (2009); doi:10.1117/12.845656.

12. Xi Lu, Mingyu Lu, Limin Zhou, Zhongqing Su, Cheng Li, Lin Ye and Guang Meng, Guided wave and probability based diagnostic imaging for detection of multiple welding damages in welded tubular steel structures, Proc. Structural Health Monitoring 2011, Vol. 1, pp. 79-86, The 8th International Workshop on Structural Health Monitoring (IWSHM8), Stanford, USA, September, 2011.

13. Xi Lu, Mingyu Lu, Limin Zhou, Zhongqing Su, Li Cheng, Lin Ye and Guang Meng, Guided wave propagation based damage detection in welded rectangular tubular structures, Proc. of International Conference on Smart Materials and Nanotechnology in Engineering (SMN 2009), July, 2009, Weihai, China, Proc. SPIE 7493, 749313 (2009); doi:10.1117/12.838679.

ACKNOWLEDGEMENT

I would like to extend my appreciation to all those who helped me in the completion of this thesis.

My deepest gratitude goes first and foremost to Prof. Limin Zhou, my supervisor, who has offered me continuous, constant and irreplaceable guidance, encouragement and support. During all the stages in accomplishing this thesis, Prof. Zhou kept providing consistent and illuminating instruction, not only in my studies over past years, but also in inspiring my future academic life. His patient instruction, insightful criticism and expert guidance will no doubt have a profound effect on my life. I also appreciate the patience, encouragement and professional instruction from Prof. Lin Ye during my stay at the Laboratory of Smart Materials and Structures (LSMS) of the Centre for Advanced Materials Technology (CAMT) in the School of Aerospace, Mechanical and Mechatronic Engineering, the University of Sydney. I also cherish gratitude to Dr. Zhongqing Su, from whose valuable advice and enlightening supervision I benefited greatly.

During my studies in the Department of Mechanical Engineering (ME), the Hong Kong Polytechnic University (HK POLYU), I was fortunate to work with colleagues who helped me considerably. My sincere thanks are particularly given to Dr. Xi Lu, Dr. Jiangang Chen, Dr. Chao Zhou and Mr. Zheng Jiang. In addition, I forever feel grateful to those who gave me generous help when I was working in LSMS. I owe a special debt of gratitude to Dr. Shiqiang Deng, Dr. Ye Lu, Dr. Dong Wang, Dr. Xiaoting Miao and Mr. Samir Mustapha.

I am also deeply indebted to my friends Jianing Zhang, Xiaochun Zhang and Lei Xu, who gave considerable time and effort to my research experience. Their encouragement and support sustained me through frustration and depression.

Financial support from the Hong Kong Polytechnic University is much appreciated.

I should finally like to express my gratitude to my beloved parents for their loving consideration and great confidence in me all through these years; to my boyfriend, who has always helped me out of difficulty, giving me assistance and support. They all deserve far more credit than I can ever give them.

TABLE OF CONTENTS

LIST OF FIGURES

LIST OF TABLES

NOMENCLATURE

General symbols

S_0	Fundamental symmetric GW mode
A_0	Fundamental anti-symmetric GW mode
μ	Poisson's ratio
$\psi(t)$	Mother wavelet function
$\psi^*(\cdot)$	Complex conjugate of $\psi(\cdot)$
k	Wave number
C_p	Phase velocity
C_g	Group velocity
C_L	Velocities of longitudinal modes
C_T	Velocities of transverse modes
ω	Wave circular frequency
h	Plate thickness
C_1	The first IMF component
C_n	The *nth* IMF component
σ	Standard deviation
$t_{A\text{-}S}$	ToF of the incident wave propagating from actuator to sensor
$t_{A\text{-}D\text{-}S}$	ToF of the incident wave propagating from actuator to damage and then to sensor

$D_{A\text{-}D}$	The distance between actuator and the damage centre
$D_{D\text{-}S}$	The distance between the damage centre and sensor
$D_{A\text{-}S}$	The distance between actuator and sensor
$a(t)$	A wave signal
$P_{m,n}$	Arbitrary sensing path
$D_{m,j}$	Distance from a certain grid in sample to PZT element
V_d	Velocity of the dominant GW mode
P	Set of all involved sensing path pairs
N_P	Number of elements in set P
$V_e(t)$	Excitation waveform
$V_r(t)$	Reconstructed waveform
X	Signal matrix
T	Score matrix
L	Loading matrix
E	Other residuals
s	Skewness
β	Scaling parameter

Abbreviations

ANN	Artificial neural networks
CDF	Cumulative distribution function
CWT	Continuous wavelet transform
CF	Crest factor
DWT	Discrete wavelet transform
DPP	Damage presence probability
DI	Damage index
EMD	Empirical mode decomposition
enp	Shannon entropy
FEM	Finite element method
FBG	Fiber Bragg Grating
FIC	Fatigue-induced change
GW	Guided wave
HT	Hilbert transform
HHT	Hilbert-Huang transform
HIR	High-speed and intercity railways
IDT	Interdigital transducer
IMF	Intrinsic mode functions
k	Kurtosis
LBT	Laser-based technology
LDV	Laser Doppler vibrometer
MTR	Mass transit railway

NDE	Nondestructive evaluation
NDT/E	Nondestructive testing and evaluation
PZT	Piezoelectric lead zirconate titanate
PCA	Principal component analysis
ppk	Peak-to-peak
RTD/f	Relative time differences caused by fatigue crack
RMS	Root mean square
RMSD	Root mean square deviations
SHM	Structural health monitoring
SNR	Signal-to-noise ratio
SAM	Seam assigned model
SVM	Support vector machines
ToMD	Time of maximal difference
ToF	Time-of-flight
TRM	Time reversal method
TRM&L	Time reversal method combined with Lamb wave approach
var	Signal variance
WTSS	Welded tubular steel structure
WT	Wavelet transform
WSAS	Welded steel angle structure
2D	Two-dimensional
3D	Three-dimensional

CHAPTER 1 Introduction

1.1 Research Background

1.1.1 Elastic Waves and Guided Waves (GWs)

Applications of wave-propagation-based damage identification have attracted increasing attention over the past two decades. Elastic waves can be divided into several types, as shown in Table 1.1 [1]. Among all types of elastic wave which propagate in elastic media, GW, which propagates in media with boundaries, has assumed an important role for damage detection in the areas of mechanical and civil engineering. The main reasons why GW-based method are growing so quickly are:

a. GW possesses the capability of inspecting a large area of a structure using relatively few transducers in a specific configuration;

b. GW has high sensitivity for detecting damage, with high precision; and

c. GW can scan the entire cross-sectional area of a structure under inspection, allowing detection of internal damage.

A number of approaches now exist in applications of GW for damage identification, and applications using GW which propagates in thin plate or shell structures are widely accepted. Hence, good understanding of wave-propagation-based methods should be achieved, based on a fundamental grasp of the basic principles that lie at the foundation of wave generation and propagation in solid media.

Table 1.1 Waves in elastic solids [1]

Wave type	**Particle motion, main assumptions**
Pressure (a.k.a. longitudinal, compressional, dilatational; P-waves, axial waves)	Parallel to the direction of wave propagation
Shear (a.k.a. transverse waves; distortional waves; S-waves)	Perpendicular to the direction of wave propagation
Flexural (a.k.a. bending waves)	Elliptical, plane sections remain plane
Rayleigh (a.k.a. surface acoustic waves, SAW)	Elliptical, amplitude decays quickly with depth
Lamb (a.k.a. guided plate waves)	Elliptical, free-surface conditions satisfied at the upper and lower plate surface

1.1.2 Nondestructive Evaluation (NDE) and Structural Health Monitoring (SHM)

Traditional NDE techniques include a wide group of analysis technologies used in science and industry to evaluate the properties of materials, components and systems without causing damage. Common NDE methods include ultrasonic, magnetic-particle, liquid penetrant, radiographic, remote visual inspection, eddy-current testing and low coherence interferometry. Moreover, NDE is commonly used in forensic engineering, mechanical engineering, electrical engineering, civil engineering, systems engineering, aeronautical engineering, medicine and art [2]. With the development of theories and breakthroughs of techniques in sensor technology, manufacturing, electronic packaging, signal processing, diagnostics, applied mechanics and material sciences, conventional

NDE techniques are now being retrofitted, with the aim of continuous/real time and automated surveillance of the overall integrity of structures by providing working condition updates and reports on structural ageing. This technique, termed online damage identification or SHM, embraces four aspects: (1) operational and environmental loads; (2) damage caused by loads; (3) growth of damage; and (4) performance of the structure as damage accumulates, in aspects such as residual strength and life. Objectives (1) to (3) are connected with damage diagnosis (qualitative or quantitative identification and assessment of damage), and (4) falls into the category of damage prognosis (estimate of a system's remaining useful life) [3]. Understanding of damage identification using GWs can encompass GW generation and acquisition, wave propagation characteristics, feature extraction and evaluation, and determining damage parameters in terms of captured signals.

SHM can be considered as the integration of sensors and structures with the combination of automated advanced signal processing approaches for implementing a damage identification method [4]. The existence of damage, the location of damage, the type of damage, and the severity of damage are the main points of consideration entailed in the damage detection process [5, 26]. The relationship between the terms damage, defect and fault can be found in relevant literature. A defect is inherent in the actual materials, and leads to damage; damage is the structural state when the structure is no longer operating in its ideal condition but it can still function satisfactorily, but which can lead to fault; and fault is when the structure can no longer function satisfactorily [6]. Figure 1.1 shows a typical SHM process which is defined in terms of a four-step statistical pattern recognition paradigm: (a) operational evaluation; (b) data acquisition, normalization and cleansing; (c) feature selection and information condensation; and (d) statistical model development for feature discrimination.

GW-based SHM techniques use permanently attached transducers to inspect the integrity of a structure via captured GW signals containing information about damage. Thus it is essential to understand the physical mechanics of wave propagation in structures before undertaking GW-based SHM technologies.

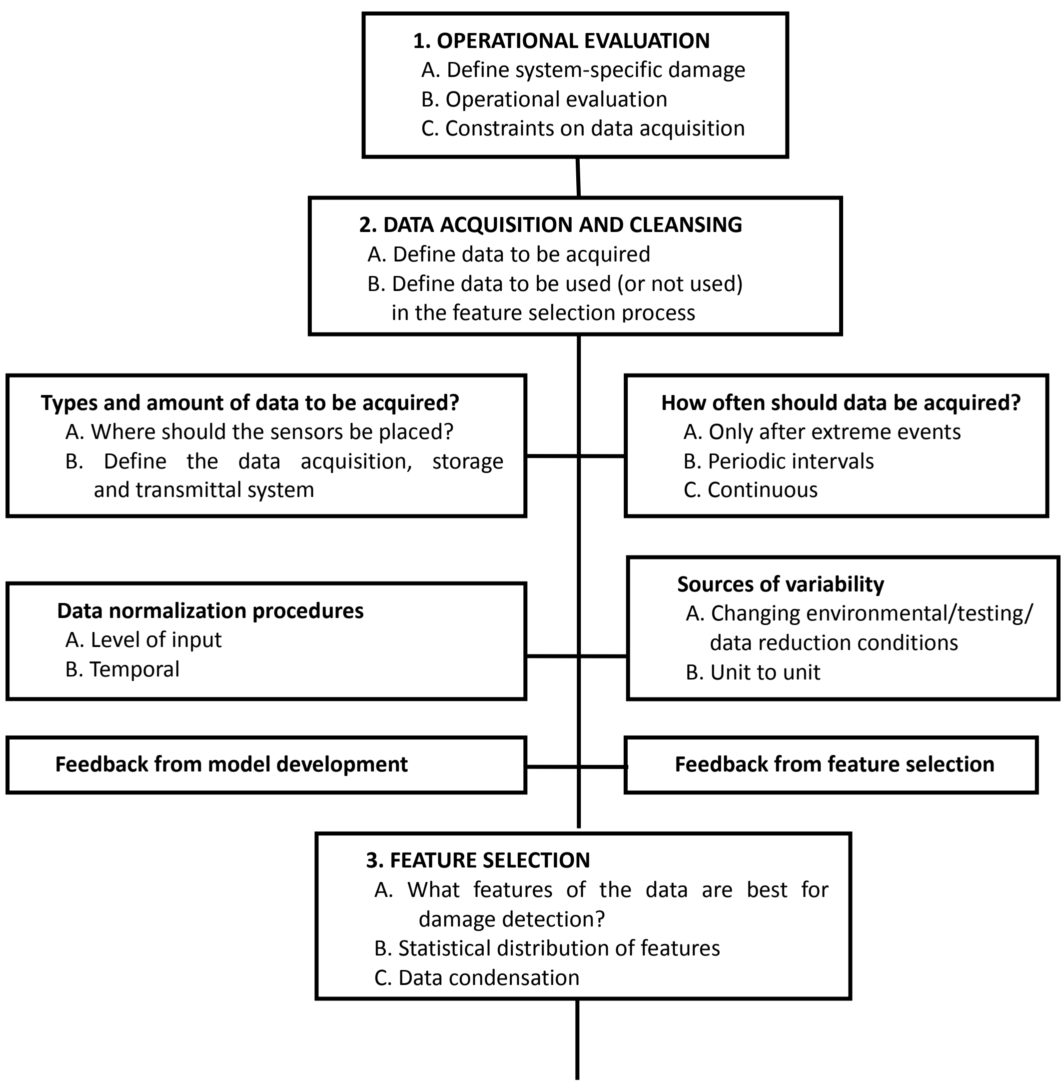

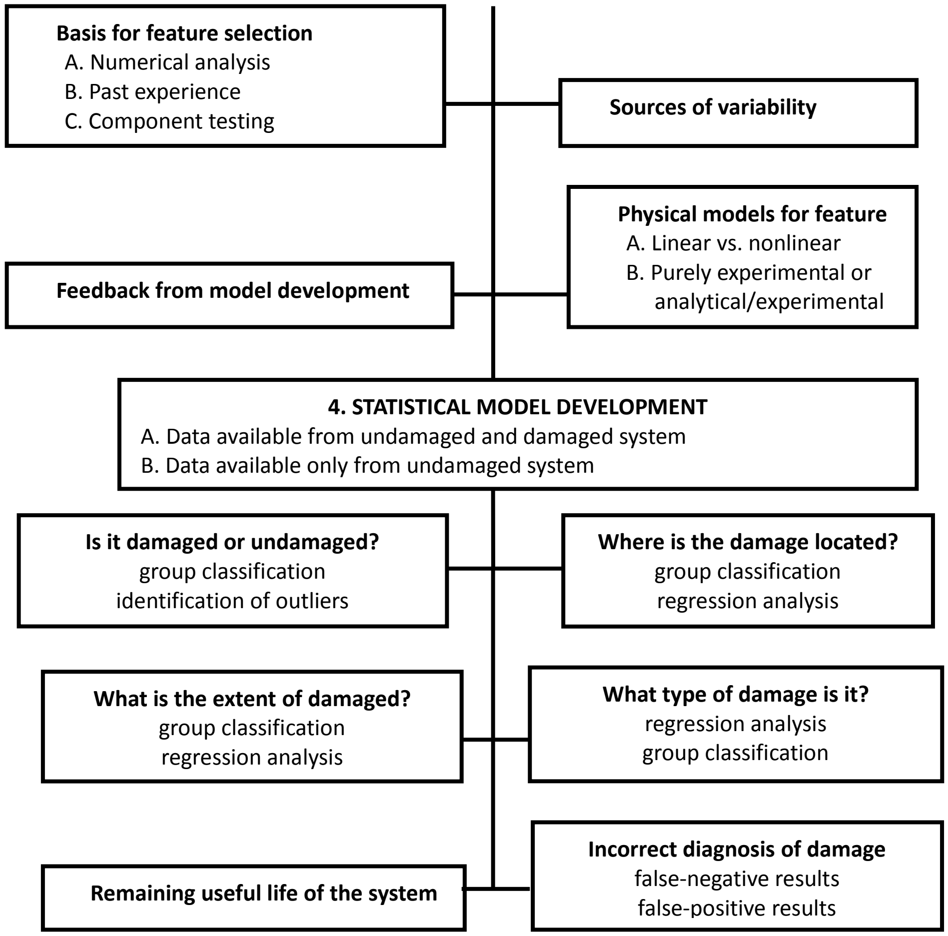

Figure 1.1 Flow chart of a typical SHM process [7]

Research into SHM techniques has mainly focused on the vibration-based method and wave-propagation-based method. The vibration-based method usually evaluates structural status using model frequency and modes, which are not sensitive to small failures in a structure. The wave propagation-based method has attracted increasing attention recently, as it can effectively detect small failures in a structure. From another perspective, SHM can be generally divided into two categories, as shown in Figure 1.2,

(a) passive approaches, involve no excitation [8, 9];

(b) active approaches, require well-calibrated and well-controlled excitation, as exemplified by applications of ultrasonic GW [10, 11].

GW-based SHM involves many disciplines, including structural dynamics, material science, signal processing, sensor technology and artificial intelligence [2], which can be applied to implement damage identification using either passive or active approaches.

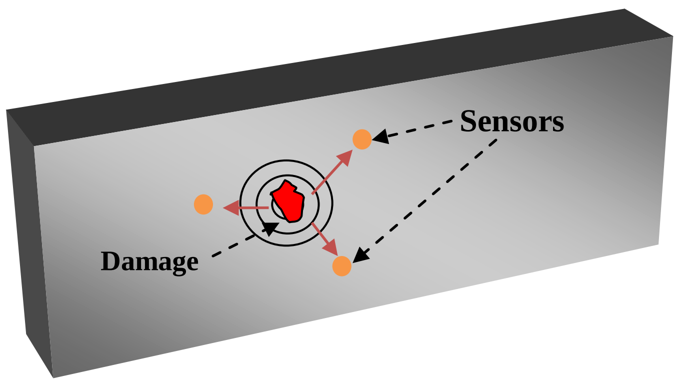

(a)

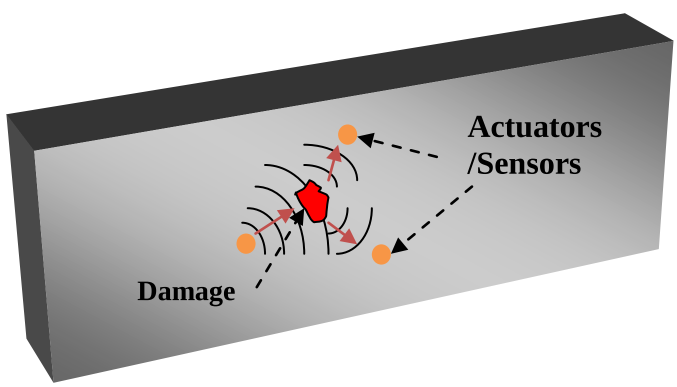

(b)

Figure 1.2 SHM techniques using (a) passive (b) active approaches [12]

1.2 Objectives and Scope of the Thesis

SHM is of great and increasing importance, covering a wide multidisciplinary range in today's technological environment. The GW method is applicable to most kinds of material, and requires less time and cost than other methods. In recognition of the problems of present-day SHM in engineering structures, the main objectives of this thesis are:

(a) to analytically understand the fundamental knowledge of GW propagation characteristics in plate-like structures and complex structures;

(b) to identify weld and locate damage in the welding zone of steel plates experimentally and numerically;

(c) to develop a damage diagnostic imaging algorithm for identification of multiple welding damages in a complex structure through both finite element method (FEM) and experiment;

(d) to develop a signal processing method and finite element modeling technique for demonstrating the detection of fatigue cracks in plate-like structures;

(e) to perform monitoring of fatigue crack propagation by a baseline-free method or a baseline-based method; and

(f) to apply the proposed method to a complex structure and monitor fatigue crack propagation in such a structure.

According to the above objectives, the scope of this thesis work can be described as follows:

(a) wave propagation in metallic plates and complex welded structures;

(b) FEM to simulate normal damages and fatigue cracks;

(c) GW excitation, scattering and collection;

(d) sensor network arrangement; and

(e) signal processing and data fusion.

1.3 About the Thesis

This thesis comprises eight chapters, organized as follows:

In Chapter 2, first the characteristics of fundamental knowledge about GW propagation in plate-like structures are introduced. Then, a comprehensive literature review is presented, covering different sensor types for use with GWs for damage identification, and the variety of data processing methods used for interpretation of GW signals in engineering structures.

Chapter 3 demonstrates the GW-based techniques in steel plates for identification of weld effects using pitch-catch configuration, detection of a 2 mm through-thickness crack in a welded zone using pulse-echo configuration, and study of the effects of different impurities in the crack on GW propagation, using the symmetric fundamental GW mode, S_0, based on a piezoelectric lead zirconate titanate (PZT) actuator-sensor pair.

Chapter 4 proposes an evaluation method called a "damage presence probability (DPP)-based imaging approach" for identification of through-thickness damage in a welded tubular steel structure (WTSS), based on time of maximal difference (ToMD). A PZT sensor network is designed and surface-bonded on the WTSS, to activate and collect GWs. Identification results demonstrate the performance of the proposed approach for identifying multiple damages in the WTSS and its high potential for real-time health monitoring of WTSSs.

Chapter 5 exploits the possibility and effectiveness of an energy-based imaging approach, based on GWs, for detecting fatigue crack through different sensing paths in a steel plate. The propagation of GWs in the 10mm-thick specimen is extremely complex, resulting in diverse forms of interference in the detection of fatigue crack. As a result, relative time differences caused by a fatigue crack (RTD/fs) are applied to investigate identification of the fatigue crack. Subsequently a fatigue crack model is established in FEM to simulate the propagation of GWs. The signals obtained from tensile tests and compressive tests are analyzed.

Chapter 6 focuses on monitoring fatigue crack propagation in steel plates. First, a 7 mm-long fatigue crack is detected, using the proposed method. Then, various approaches are applied to monitor fatigue crack propagation, including the time reversal method (TRM), transmission coefficient and principal component analysis (PCA). By applying a cyclic fatigue load, a fatigue crack propagates from 7 mm to 37 mm. The results show that the proposed methods are effective for classification and can distinguish different structural conditions attributable to fatigue crack growth.

Chapter 7 presents an experimental study for monitoring propagation of a surface fatigue crack from 15 mm to 38 mm in a welded steel angle structure (WSAS) using GWs and a PZT sensor network which is freely surface-mounted on the structure. Instead of directly comparing changes between a series of specific signal segments, signal statistics from a marginal spectrum are extracted and adopted to classify different structural conditions attributable to fatigue crack initiation and propagation. The results demonstrate the sensitivity of the proposed method for monitoring the growth of a fatigue crack.

Chapter 8 concludes the thesis and provides recommendations for future work.

CHAPTER 2 State-of-the-art Technologies for SHM

2.1 Introduction

The use of GW-based active damage detection techniques for SHM, especially applications based on GWs, is effective by virtue of the special features of these techniques, as stated in a variety of publications [13, 14]. This is particularly relevant to GWs, which can travel over a long distance even in a medium with a high attenuation ratio, and are often used for crack identification in metallic structures [15, 16] and composite structures [17, 18] with different transducers [19, 20]. Recently, GW-based techniques have been successfully applied by researchers not only in plate-like structures but also in pipe-like structures, where the use of cylindrical GWs propagating along the pipe wall is a potentially attractive solution because of their good performance in pipes and tubes [21, 22]. Detection becomes difficult in some complex structures with a welded zone or other attachments, as multiple wave modes exist synchronously and overlap each other. Some successful applications using GW-based methods in complex welded structures have been investigated in order to identify the changes in the time-of-flight (ToF) or wave amplitude of the GW associated with welds or defects. Wang et al [21] extended an comprehensive methodology based on ToF analysis of GW propagation and reflection from defects in a pipeline. Park et al [23] presented the results of experimental studies of PZT-based active damage detection techniques in steel bridge components employing several damage-sensitive features such as root mean square deviations (RMSD) in the impedances, wavelet coefficients and ToF of GWs. Juluri et al [24] investigated a compression wave guided by a weld, which is stronger than GW. In the finite element simulation of that study, a thickened region in the middle of the plate was taken as the welded zone. Croxford et al [25] described two damage identification strategies according to different sensor network relationships. One used a dense sensor network integrating numerous sensors into the structure, where the distance of sensor separation was similar to or smaller than the scale of the anticipated damage. The other strategy used a sparse sensor network, integrating fewer sensors into the structure, where the distance of sensor separation was much larger than the scale of the anticipated damage. Although these techniques were verified experimentally and numerically, most of the experimental specimens were not complex enough to apply to real-world applications.

Lamb-wave-based methods are suitable for SHM according to the strategy of a sparse sensor network. In a homogeneous medium, Lamb wave modes can be classified into symmetric or anti-symmetric modes according to the relationships between the direction of vibrating displacements and that of mid-plane, formulated by [3]:

$$\frac{\tan(qh)}{\tan(ph)} = -\frac{4k^2qp}{(q^2-k^2)^2} \qquad \text{for symmetric modes} \qquad (2.1)$$

$$\frac{\tan(qh)}{\tan(ph)} = -\frac{(q^2-k^2)^2}{4k^2qp} \qquad \text{for anti-symmetric modes} \qquad (2.2)$$

$$p^2 = \frac{\omega^2}{c_L^2} - k^2, \quad q^2 = \frac{\omega^2}{c_T^2} - k^2, \quad k = \frac{\omega}{c_p}$$

where h, k, c_L, c_T, c_p, ω are plate thickness, wave number, velocities of longitudinal and transverse modes, phase velocity and wave circular frequency, respectively. Symmetric and anti-symmetric Lamb wave modes are illustrated in Figures 2.1 (a) and 2.1 (b), respectively.

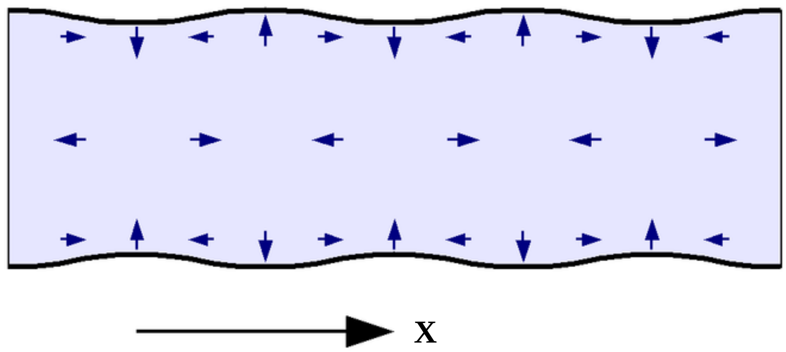

(a)

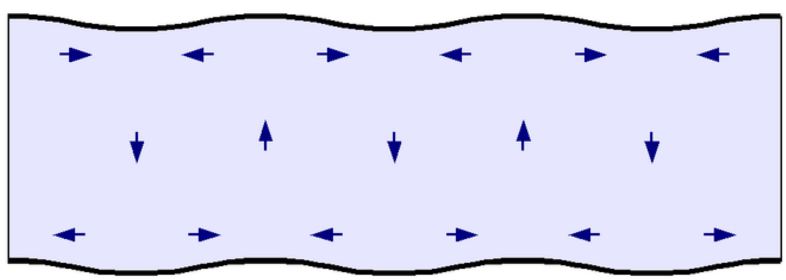

(b)

Figure 2.1 (a) Symmetric (b) anti-symmetric Lamb wave modes

Equations (2.1) and (2.2) indicate that GW possesses characteristics of disperse and multiple wave modes. Disperse implies that the propagating velocity (both group velocity and phase velocity) of GW changes with its frequency, plate thickness and material properties. This characteristic indicates that the interrogation of GW signals is complex. Much effort is required to ensure that only the required GW modes exist in non-dispersive regions [25].

To give prominence to damage in structures, pitch-catch and pulse-echo configurations are usually applied in GW-SHM techniques by an actuator-sensor pair, as shown in Figure 2.2.

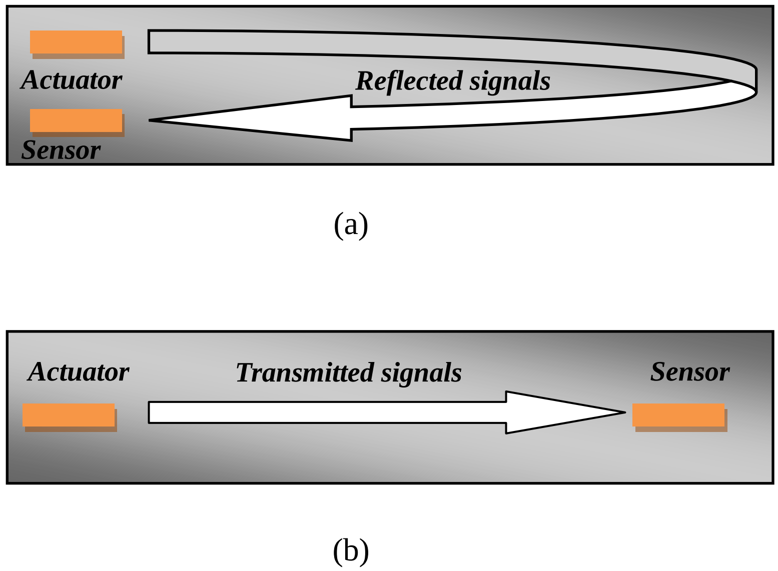

Figure 2.2 (a) The pulse-echo configuration (b) the pitch-catch configuration by a pair of PZT actuator and sensor [26]

Pulse-echo is the configuration that uses wave pulses to find the distance from actuator to damage or boundary and then back to sensor. The interval from the emission of a pulse to reception of its echo is recorded, and the distance can be calculated from the known speed of propagation of GW on its propagating path. In the pitch-catch configuration, the sensor records the wave signals directly transmitted through discontinuities.

2.2 Sensing Systems Used for Receiving GWs

Ultrasonic sensors work on a principle which is similar to radar or sonar for evaluation of a target by interpreting the echoes from wave signals. Ultrasonic actuators generate high frequency GWs and the echo is received back by the sensors. The time interval is recorded between sending the signal and receiving the echo and the distance is determined by wave velocity at a specific frequency. In comparison with some traditional ultrasonic probes [27], which can not be permanently installed into a structure under inspection, the following transducers are adequate for online SHM.

PZT is a ceramic perovskite material that shows a marked piezoelectric effect. PZT was developed by Uitaka Takagi and colleagues at the Tokyo Institute of Technology around 1952. There is no doubt that PZT elements are most popular for SHM applications, being small in size, light in weight, affordable in price and available in a variety of styles and capacities, allowing them to be embedded in or surface-bonded almost anywhere on a structure [2]. In particular, PZT can be used to make ultrasound actuators and sensors, as well as high-value ceramic capacitors. This property is extremely attractive for systems that require calibrated and controlled excitation signals [28]. Piezoelectricity is described mathematically within a material's constitutive equation, which defines how the piezoelectric material's stress, strain, charge-density displacement, and electric field interact. The piezoelectric constitutive law in strain-charge form is [26]:

$$\mathrm{S} = s_E \bullet T + d^t \bullet E \tag{2.3}$$

$$\mathrm{D} = d \bullet T + \varepsilon_E \bullet E \tag{2.4}$$

where S is the vector of mechanical strain components, T is the vector of mechanical stress components, E is the vector of electric field components, D is the vector of electric charge density displacement components, s is the matrix of compliance coefficients, d is the matrix of piezoelectric coupling coefficients for strain-charge form, and ε is the matrix of electric permittivity. Figure 2.3 shows a typical PZT actuator. When it is operated by a source of energy, usually in the form of electric current, the energy is converted into strain.

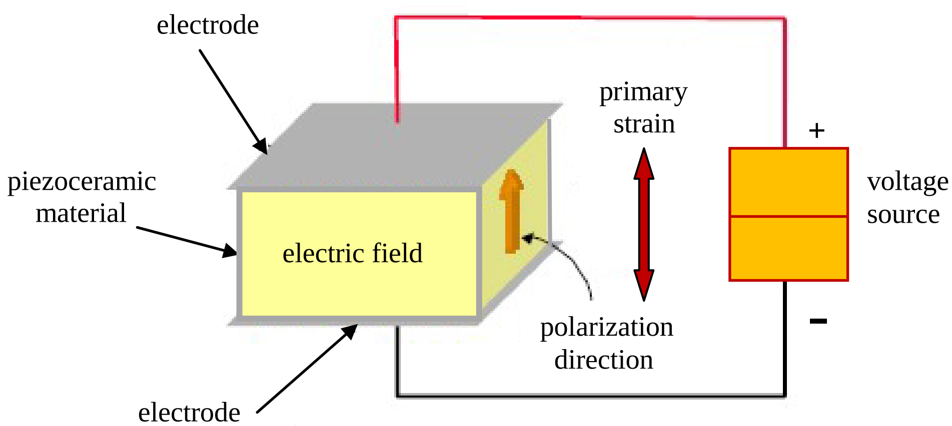

Figure 2.3 A typical piezoceramic actuator

Compared with integrating sensors individually with a structure, integrating a network of sensors with the structure would be a novel and cost-effective method [2]. Acellent's patented SMART Layer™ is a thin dielectric film with an embedded network of distributed piezoelectric actuators/sensors that can be surface-mounted on metallic structures or embedded inside composite structures. Acellent's system, shown in Figure 2.4, consists of SMART Layers™, SMART Suitcase™ and diagnostic software, which can be used for monitoring structural condition and for detecting damage while the structures are in service [29].

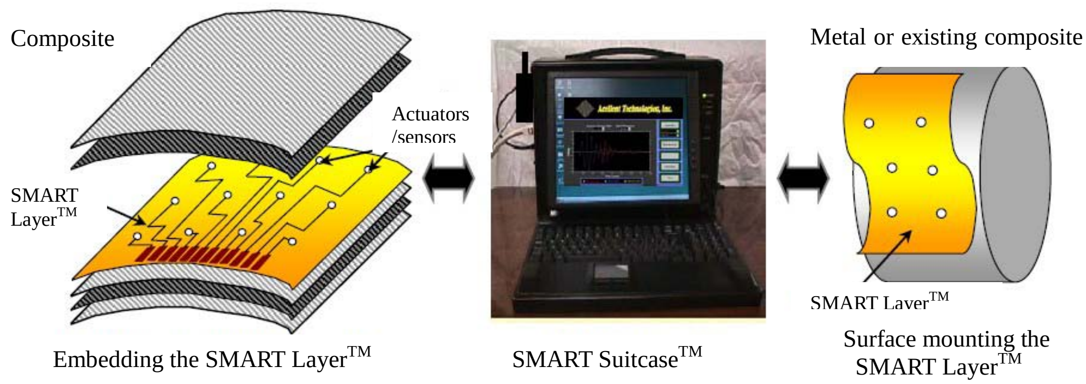

Figure 2.4 Acellent's SMART Layers™ and SMART Suitcase™ [30]

Studies have verified that GW wave sensing systems using a PZT network have many advantages for identifying damage in structures, mainly because of the dual functionality of PZT elements for GW excitation and acquisition.

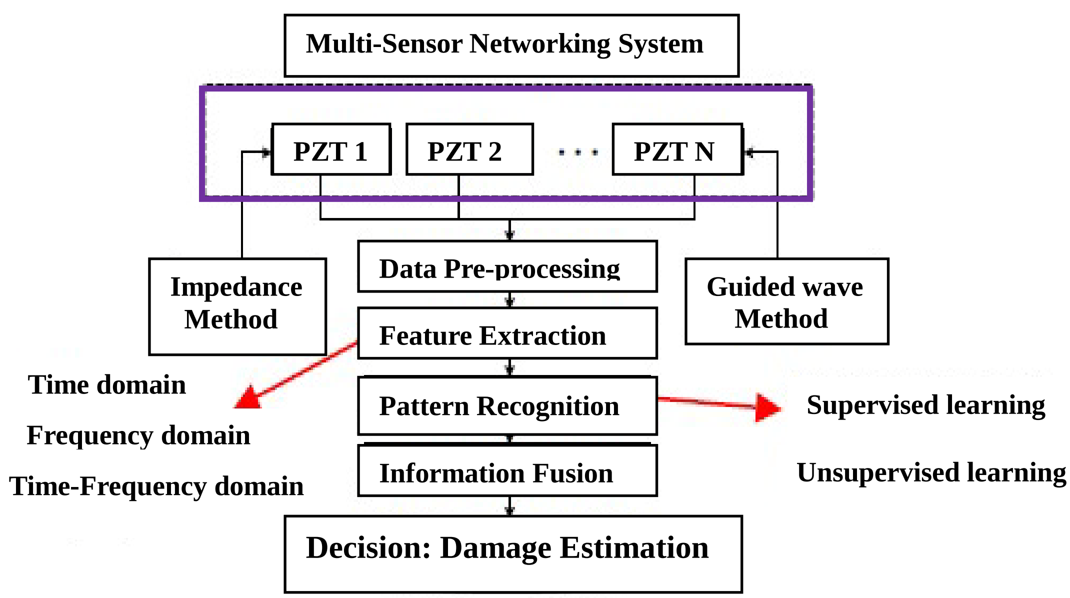

Figure 2.5 PZT-based active damage detection techniques [23]

Figure 2.5 shows a flowchart for PZT-based SHM techniques including a typical process for damage detection: signal generation, signal collection, data preprocessing, data processing and feature discrimination.

Compared with the aforementioned PZT sensors, Fiber Bragg Grating (FBG) Sensors are also considered among the most important sensors which have immunity to electromagnetic interference [30, 31]. Bragg wavelength is sensitive not only to strain but also to temperature, making FBG applicable as an optical fiber sensor. Moreover, a hybrid PZT-FBG damage identification system with dual transmission mechanisms has been developed, as shown in Figure 2.6, which displays premium actuator/sensor decoupling capability [29].

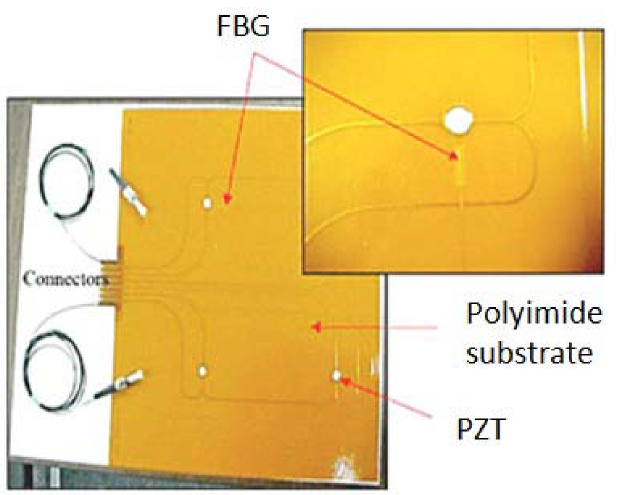

Figure 2.6 A kind of PZT-FBG sensor system [29]

Laser Doppler Vibrometers (LDVs) are scientific instruments used to carry out non-contact vibration measurement, which are different from the aforementioned GW and FBG-based sensing systems which are surface-mounted on or embedded into structures. Obviously LDV can reach targets that are difficult to access or where it is difficult to attach a transducer, and the LDV involves no mass attachment [131].

2.3 Applications of GW-based SHM

2.3.1 GW Used in Large and Complex Structures

Large-scale engineering structures and assets, built up by several welded segments, are becoming ubiquitous. Today, rail networks across the world are becoming busier than ever before. This is especially true for high-speed and intercity railways (HIR), which travel at higher speeds and carry more passengers. The combination of these factors places significant pressure on existing infrastructure, leading to increased demand for the inspection and maintenance of rail systems. Rail flaw detection has an important part to play in ensuring the safety of the world's railways. The propagation of cracks is in recent years considered a significant failure, affecting structural integrity and directly related to public safety. Clearly, failure during operation, as a consequence of structural damage in critical components such as the wheel or bogie system of a train carriage, can result in immense life and monetary loss. The German Eschede train crash in 1998, the world's most serious high-speed train disaster, which led to 200 casualties, was attributed to the cracks in the wheel rims under repetitive loads (500,000/day) [32]. In 2006, a number of cracks detected in the bogie systems of Hong Kong's Mass Transit Railway (MTR) trains, made of welded metallic tubular structures, aroused immense public attention. 'The excessive vibration experienced by the trains and material fatigue crack was the dominant reason', the MTR proclaimed [33]. In the rail industry, train carriages approaching their designated service life are not exceptional, entering the senior age of a train carriage. The older these trains become, the more critical defects they may have. These defects can progressively deteriorate as age of structures and undergo fatigue loads. There is no doubt that failure of these public transportation vehicles during operation can lead to irretrievable and catastrophic consequences.

With safety the paramount factor in any industry, especially public transport, dependability and durability criteria must be strictly met, prompting the rapid development of NDE techniques. Though playing a significant role in preventing the occurrence of failure, most of today's NDE in industry (visual inspection, radioscopy, ultrasonics, laser interferometry, thermography, eddy-current, electromagnetic inspection, etc. [34-38]) is conducted at periodic intervals, regardless of changes in the working condition or progressive structural deterioration (*i.e.*, non-condition-based). Such NDE costs a lot but delivers relatively poor efficiency. For example, ultrasonic inspection, the most widely adopted NDE approach in the railway industry, operates at a very low speed, consuming considerable time to scan whole train structures. To ensure the functionality of ultrasonic probes, downtime of the structure is often required. Even so, these techniques often ignore very small damage until it grows to a conspicuous level.

In recognition of this inefficiency, a condition-based philosophy in conjunction with embedded active sensor networks has been established since the 1990s to replace the traditional NDE [10, 39-42], to provide continuous and automated surveillance of structural health status by considering condition updates and structural ageing, termed SHM technology [43]. The industry is evaluating SHM techniques as a possible principle for improving safety and also for reducing operational costs relative to NDE techniques through self-sufficient systems for continuous monitoring [43]. There is no doubt that all in-service civil infrastructure would benefit significantly from the development of in-train structures. In particular, the development of damage identification techniques based on GWs, combined with a sensor network system that can be adapted to in-service structures, provides a huge advance to the paradigm of conventional passive sensing SHM tools, possessing superb capabilities including low attenuation, strong penetration, fast propagation, omnidirectional dissemination, convenience of activation and acquisition, low energy consumption and, most importantly, high sensitivity to structural damage even when it is small in size [10, 18, 49, 51]. GW-based damage identification and SHM techniques have been employed in numerous applications with demonstrated effectiveness [21, 23, 45-52]. Study of GW-based SHM in railways has been addressed by some research groups [53, 54], but train bogie frames are discussed only infrequently. Embedding active sensor networks in critical sections of train structures is a promising solution, in which multi-functional sensors are capable of sensing and providing continuous information about structural integrity status, facilitating awareness of defects at the early stage. It has been demonstrated that an effective SHM technique can reduce the total maintenance cost of an engineering system by over 30% [44], accompanying the substantial improvement in reliability and safety.

Recently, GW- based techniques have been successfully applied by some researchers not only in simple structures but also in complex structures [20, 21]. Also, research into damage identification and SHM in real train/rail structures has been undertaken by different research groups [53-55]. Although these techniques have been verified experimentally and numerically, limited activity has been directed to the development of

GW-based techniques for real-world applications. In comparison with plate-like structures such as those widely used in the engineering industry, welded steel structures are often seen in engineering structures, serving as the framework of the whole engineering system. They are very thick and large, necessitating a higher magnitude of wave excitation to cover a reasonable area. Multiple wave modes in complex structures and their interactions with damage and complex boundaries present substantial obstacles for effective signal interpretation. Moreover, demanding working conditions cause nonlinearity of various parameters and complex boundary conditions, contributing to additional difficulties in practical application.

However, some successful applications using GW-based method have been investigated in complex welded structures in order to identify the changes in the transmission velocity or energy of the elastic waves associated with weld. Juluri et al [24] described a multi-sensor networking system and discovered a compression wave guided by the weld which was stronger than GW. Their proposed system was used for detecting dual cracks in a specimen made as a part of a steel bridge, shown in Figure 2.7.

2.3.2 GW Applied in Tubular Structures

For GW-based SHM technology, Lamb waves and cylindrical Lamb waves are utilized in plate-like and tube-like structures, respectively. Quantitative assessment of the location and size of certain kinds of damage in pipe works using NDE techniques has been achieved [56-59]. As in complex structures with attachments [60], tubular structures are widely used in engineering fields, such as train bogie frames, port container crane components, etc. Some of these are vital parts of an assembly or of the entire machine construction, and aging/fatigue problems have been frequently reported. Efficient on-line monitoring and speedy damage assessment for such structures deserve in-depth investigation.

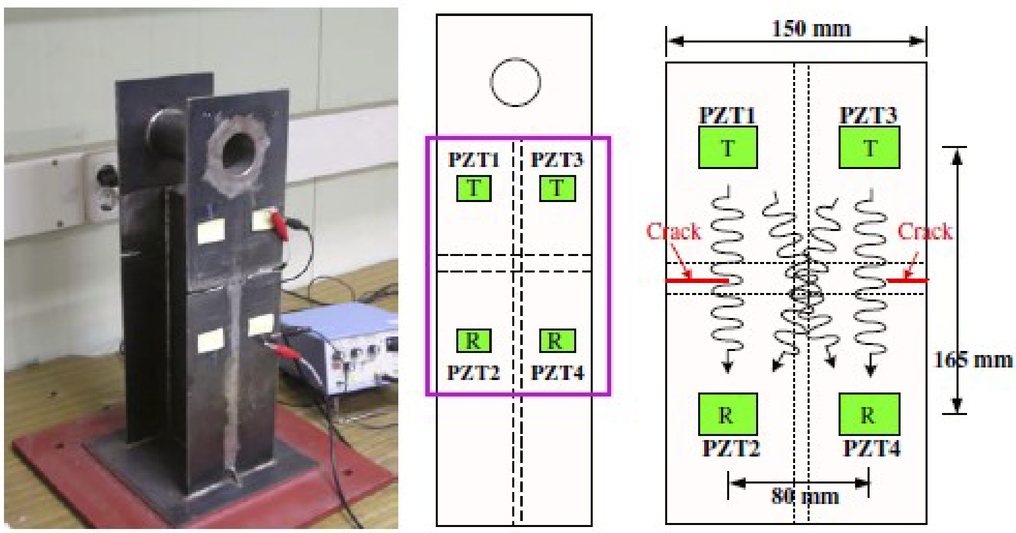

Figure 2.7 A built-in PZT sensor network for detecting dual cracks [24]

The characteristics of cylindrical GWs propagating in pipes are much more complex than those of GWs in plate-like structures. Hence, most endeavors have focused on the means to generate a single mode in order to avoid the difficulties entailed by multiple modes [61]. In research into damage detection and identification in structures of aluminum tubes with rectangular section, identification of the probability of the presence of damage, with good estimation of its location, has been achieved [23]. Overall, most research work using cylindrical waves in damage detection in pipes has used longitudinal modes [58, 61, 62, 135], which are symmetric modes travelling axially along the pipe, and torsional modes [57, 63], which have only the circumferential components of particulate vibration. However, most tubular structures are not manufactured in foundries but are formed by plates welded together according to the design requirements. Moreover, the section dimensions of these tubular structures are usually relatively large.

2.3.3 GW Used in Fatigue Crack Detection and Monitoring

2.3.3.1 Sensing techniques used in GW-based SHM

Degradation of engineering materials due to the initiation of fatigue cracks is known to be one of the main reasons for the widespread failure of older engineering structures [64]. Fatigue cracks usually occur at some initial flaws or sharp corners of structures which are subjected to cyclic loading and unloading due to elevated local stresses, when the loads are above a certain threshold. Fatigue cracks that appear under cyclic loads are the most common cause of failure in metallic structures. If the fatigue cracks grow uncontrolled, they will eventually reach a critical size and the structure will suddenly fracture. There is no doubt that fatigue cracks that appear during the operation of public transportation vehicles can lead to irreversible and catastrophic consequences. It is especially important, therefore, to detect and monitor fatigue cracks initiated by pitting in order to predict the remaining fatigue life of aging public transportation vehicles and to ensure that they are maintained in a timely manner.

SHM is one of the major maintenance activities undertaken in a broad range of industries that can be adopted to instantly detect fatigue crack and its propagation and then take measures to prevent structural deterioration [65]. Heterogeneous detecting technologies have been developed for identification of fatigue cracks, including contact and non-contact sensing methods which have been employed with a view to locate or monitor fatigue cracks in variable material [66, 67]. Laser-based technology (LBT) has received much attention and is a topic of considerable interest [3, 68] in metallic [69] and composite structures [70, 71] as a baseline-free technique, because GW methods based on PZT transducers have a major drawback using traditional signal processing and interpretation techniques that require baseline measurements. The measured parameters can change due to applied cyclic loading or bad coupling between the PZT transducers and structure. In contrast, non-contact approaches such as LBT have been employed effectively for fatigue crack detection [71, 80]. Although such methods can avoid baseline measurements and save some complex data interpretation processes, the setup of delicate equipment for data acquisition makes them difficult to apply in real-time defect monitoring in large and complex structures.

The LBT mentioned above was initially established for out-of-plane measurement of GW mode, A_0. However, the three-dimensional (3D) laser vibrometer has attracted increased attention for simultaneous measurement of both anti-symmetric A_0 and symmetric GW modes S_0. A 3D laser-based GW sensing system was evaluated by monitoring fatigue crack growth in an aluminum plate, indicating that the laser vibrometer is sufficiently sensitive to capture both GW modes A_0 and S_0, which are dominated by out-of-plane movement and in-plane movement, respectively [72]. In that study, the largest local increase in magnitude of displacement occurred around the damage location, where the incident wave component interacted with the damage-induced components. This baseline-free system successfully eliminated the need for damage identification in detailed analysis of complex GW propagation characteristics.

From another perspective, GW method using a PZT sensing network has some unique advantages over the LBT-based sensing system. First, monitoring strategies that employ the GW method rely solely on a series of PZT actuator/sensor transducers for the generation and collection of GWs. Laser vibrometry systems involved in data acquisition also require a PZT actuator to generate GWs in order to obtain adequate results. Second, although LBT has been adopted and shown to be effective in a large number of applications [3, 68-71, 73], it seems more suitable for metallic or composite plate-like structures than for complex structures, due to the conditions in which it is applied. However, welded structures with complex boundaries are ubiquitous across a wide range of industries. Moreover, the PZT-based GW method has been shown to be effective in detecting welds [74] and detecting damage in welded tubular steel structures [75]. The comparative practicability of the GW method over LBT is abundantly clear in terms of its use in the framework of a bogie system for a train carriage, located on the underside of a train. Third, the PZT-based GW method is capable of detecting damage remote from sensors which can be mounted permanently both easily and economically. In comparison with LBT, in which laser vibrometers must be used to scan the material surface directly for signs of damage, the GW method involving active sensor networks in critical sections of structures is a promising method for the online sensing and provision of data to reveal structural integrity status.

There is no doubt that the development of ultrasonic techniques using PZT transducers has taken the contact sensing method of crack detection to an advanced stage, and in view of this technique GW-based methods have been extensively investigated for failure identification in infrastructure, given the attractive features of GWs [11, 16, 76].

Synthetically, any developments that can meet the challenge of fatigue crack detection are thus very attractive for real engineering applications. The GW response has been carefully analyzed for its ability to detect the presence of perturbation in riveted aluminum joints of plate under cyclical loading [82]. It was shown that the perturbation was directly dependent on crack initiation and growth in the vicinity of the joint. In that study, the capability of the GW technique was demonstrated for monitoring damage initiation and growth in riveted plates despite the structural complexity. A built-in diagnostic technique for monitoring hidden fatigue crack growth in aircraft structures has also been developed [83]. Later, that technique was applied to monitor fatigue crack growth in riveted fuselage joints and in a cracked metallic plate repaired with a bonded composite patch combined with a sensor network, hardware and the diagnostic software [84]. Predictions correlated quite well with measurements from the ultrasonic scan methods as well as visual inspection.

Recent research in rail detection has shown that early detection of rail flaws, especially of fatigue cracks, is of paramount importance for the safe and reliable operation of rail networks around the world. It is thus of practical interest to investigate the use of GW-based SHM technology in terms of fatigue cracks in metallic structures [80, 87]. Many methods for fatigue crack detection have been developed in recent times. A surface acoustic wave method for in situ monitoring of fatigue crack initiation and evolution from a pit-type surface flaw was described, involving the use of a specially designed polystyrene wedge transducer [86]. A study of Rayleigh wave energy generated by miniature interdigital transducer (IDT) propagation through fatigue crack surfaces using a laser machining technique was described experimentally [88]. Research has also been conducted on welded steel components for fatigue crack damage monitoring using a sensor and data storage system based on an autonomous microcontroller [78].

Besides linear GWs, nonlinear GWs can also be used for characterizing fatigue damage, although an accurate experimental realization of nonlinear GWs is generally difficult due to their dispersive and multi-mode nature [3]. An experimental procedure for characterizing fatigue damage in metallic plates using nonlinear GWs was developed [64]. The work first considered the propagation of nonlinear waves in a dispersive medium and determined the theoretical and practical considerations for the generation of higher order harmonics in GWs. The results showed that the normalized acoustic nonlinearity measured with GWs was directly related to fatigue damage in a fashion similar to the behavior of longitudinal and Rayleigh waves. The normalized acoustic nonlinearity was then compared with the measured cumulative plastic strain, confirming that these two parameters are related and reinforcing the notion that GWs can be used to quantitatively assess plasticity driven fatigue damage using established higher harmonic generation techniques.

2.3.3.2 Advanced signal processing approaches used for GW-based SHM

To avoid redundant cost caused by maintenance of engineering frameworks, it is necessary to employ continuous assessment of the circumstance of such structures and take effective tools for data processing. Clearly, the ultrasonic testing technique is most acceptable in industrial applications. This technology relies on the scattering of high frequency ultrasonic bulk wave propagation through the thickness of structures.

However, most conventional nondestructive testing and evaluations (NDT/E) for crack identification, exemplified by acoustic emission, X-ray, ultrasonic scan and eddy current, are limited to on-ground or offline application, which means that the structural components under inspection must be overhauled or out of service [93]. Such inspections are therefore generally labor-intensive, time-consuming and costly, and can only be conducted at specific time points during the life-cycle of service. In particular, many NDT/E techniques are sensitive to environmental conditions. For example, poor signal-to-noise (SNR) ratio always complicates the effective signal interpretation of acoustic emission although it is very sensitive to an initial crack [94].

To overcome the disadvantages of conventional NDT/E methodologies, the development of damage identification techniques based on structural vibration has been a research focus in the engineering and academic communities [37, 95]. The basic principle of vibration-based methods is that changes in structural physical parameters, such as natural frequency, mode shapes and modal damping, can be used to indicate the existence of damage. It is well appreciated, however, that vibration-based methods have low sensitivity to minute or local damage, which in general leads to less detectable or undetectable changes in global structural dynamic parameters. More importantly, the linear assumption of vibration-based approaches is invalid for fatigue cracks that display nonlinear vibrations due to crack opening and closing [51]. Besides, structural dynamic parameters are affected not only by damage but also by other effects such as measurement location, applied force, boundary conditions, and even environmental humidity and temperature [51, 96].

Whereas conventional ultrasonic inspection generally uses ultrasonic waves propagating through the thickness of a structure in the megahertz range, GWs at relatively lower frequencies can propagate over a relatively long distance, and thus cover and interrogate a broad structural area for cost-effective damage identification with only a few transducers. The influences of environmental temperature on GW signals that are activated and captured by piezoelectric elements have also been investigated, proving the potential for applications under demanding conditions [97, 98]. Surface-mounted piezoelectric wafers can therefore be incorporated with host structures for the generation and acquisition of GWs to achieve online integrity surveillance, for instance, continuously monitoring the growth of fatigue crack.

The SHM process observes structural configurations using a series of transducers by monitoring periodically sampled dynamic responses. The process obtains damage-sensitive characteristics from these responses, and analyzes these features to determine the current state of structural health. For long-term consideration, SHM techniques can periodically update reliable information which indicates the integrity of the structure in near real time, evaluating its overall quality regarding inevitable aging and degradation [89]. Compared with other techniques in SHM, methods based on GWs, especially on Lamb waves which can propagate over a relatively long distance in solid plates at limited frequencies, have been developed as a common and effective approach. In general, GW-based SHM problems can be addressed in the context of a pattern recognition paradigm [7]. This paradigm can be broken down into four steps. First, operational evaluation attempts to answer questions relating to the implementation of a damage identification capability. Second, data acquisition and cleansing involve selecting the excitation, the sensor types, number and locations, and the data acquisition methods, and selectively choosing data to pass on to or reject using the feature selection process in data cleansing. In this process, economic considerations play a major role in decision making. Third, feature extraction and data compression aim to distinguish data features between the undamaged and damaged structure. Fourth, feature discrimination attempts to apply this paradigm to data from real world structures. Clearly, the ability to cleanse, compress, normalize and fuse data to account for operational and environmental variability is a key implementation issue when addressing steps 1-3 of this paradigm. These processes can be implemented by combinations of several approaches [2, 37]. For GW-based technology, various types of transducer can be used to excite and access GW signals, also including different types of laser and optically based methods [71]. Among all the transducers that can be employed, PZT elements deliver excellent performance in GW excitation and acquisition, by virtue of their negligible mass/volume, easy integration, excellent mechanical strength, wide frequency responses, low power consumption and acoustic impedance, as well as low cost, and they are particularly available for integration into a host structure as in-situ transducers [65]. As a result, applications of PZT transducers to GW generation and reception for damage identification purposes are numerous [46, 77]. Some restrictions are obligatory with the use of PZT transducers. For example, the maximum voltage that can be applied on a PZT without depolarizing it is 250–300 V/mm [79]. Thus the voltage used in our experiments is usually less than 80V according to the specific experimental setup.

Lamb waves consist of symmetrical (S) and anti-symmetrical (A) modes, generally co-existing and propagating together in plate-like structures with different group velocities. A relatively lower frequency is usually preferable for damage identification, where only two fundamental modes, namely the A_0 and S_0 modes, are available with minimal dispersive properties, so as to prevent the occurrence of higher order wave modes with complex mode shapes [16]. Generally speaking, the A_0 mode is more sensitive to marginal defects because of its shorter wavelength than that of the S_0 mode at the same frequency, whereas the S_0 mode propagates more quickly than the A_0 mode at lower frequencies, facilitating signal differentiation and minimizing wave reflections from structural boundaries. In comparison with the conventional acoustic emission method, Grondel et al proved the feasibility of GWs for monitoring crack initiation and growth in riveted aluminum strap joints during cyclical loading [84]. The research group at the University of Sheffield, UK, detected a fatigue crack and its propagation in metallic plates using the A_0 and S_0 modes respectively, which were generated by a surface-mounted piezoelectric wafer and collected by a 3D laser vibrometer [78, 87]. Kim and Sohn employed pairs of piezoceramic transducers attached on both sides of an aluminum plate to generate and measure GWs, and the existence of a fatigue crack was identified by mode conversion between the A_0 and S_0 modes as a baseline-free approach [99]. Rokhlin et al developed an in situ GW technique to measure the initiation time and growth history of primary and multiple secondary cracks of Ti-6242 alloy samples during fatigue testing, which demonstrated good agreement with X-ray results [100]. Various PZT-based technologies have proven success in identifying fatigue crack in metallic plate using a probability-based imaging approach [90] and monitoring fatigue crack growth by a damage index [51], TRM [91], and PCA [92] in a selected individual mode such as S_0 and A_0. Overall, most research work in fatigue crack monitoring based on PZT generated GWs has been restricted to a regular sensor network which is usually mounted along the direction of fatigue crack growth. These data fusion techniques are mainly focused on signals from fixed wave mode. It is difficult, however, to clearly differentiate an isolated wave mode for subsequent analysis in some cases, due to complex structural geometries and boundaries, frequency dispersion, mode conversion and confusion, and even environmental humidity and temperature.

Less investigation has been undertaken of the effects of closing and opening of a fatigue crack on the acquired wave signals. It is understood that when a hairline fatigue crack is under compressional stress or when no tensile stress is applied, as in the unloading condition, part of the crack may be tightly closed or semi-contacted [101]. If a pitch-catch configuration is applied, the wave received by the sensor is actually the combination of a directly transmitted wave crossing the crack line and the scattered wave from the crack tip, and that is obviously more complex than the scenario of an opening crack as a notch, where the received wave is just the wave scattering from the crack tip [51]. The result is that a the crack may be undetectable due to the marginal difference in comparison with the baseline signals, or the characteristics of the received signal, e.g. the damage index, may exhibit non-linear properties.

In consideration of the nonlinear correlation between signal characteristics and crack parameters, data fusion and pattern recognition based on the extracted signal features from multiple sensing paths have been developed to conduct a comprehensive inverse diagnosis, circumventing the straightforward but notoriously intricate differentiation of damage-generated wave components from GW signals because of dispersion and the coexistence of multiple modes [102]. However, many pattern recognition techniques, such as artificial neural networks (ANN) or support vector machines (SVM), require careful offline training of a database containing massive wave data, with iterative adjustment of model parameters to find the best fit of the training data [103]. In contrast, PCA is capable of reducing the dimensions of a data set while still retaining its characteristic information, and then classifying the engaged data into different groups that can be used to describe the evolution of structural integrity conditions.

PCA is a multivariate statistics technique which projects a complex set of original data or variables into a lower dimension using linear transformation [68]. The newly generated set of variables is termed the principal components, each of which is a linear combination of the original variables. As a whole the principal components form an orthogonal basis for the space of the data [104]. In detail, the covariance matrix is first calculated for the matrix of mean deviations of the original data set. The eigenvalues and eigenvectors of the covariance matrix are then calculated, the eigenvalues are arranged in order of decreasing magnitude, and the columns of the eigenvector matrix are reordered corresponding to the rearranged descending eigenvalues. The matrix of mean deviations is then multiplied by the matrix of eigenvectors to generate the matrix of principal components, whose vectors are sorted in order of decreasing variance and therefore of decreasing significance in terms of the amount of information representing the original data set [103].

The full set of principal components is as large as the original set of variables. It is appreciated, however, that the sum of the variances of the first few principal components generally exceeds 80% of the total variance of the original data [41], indicating that the first few principal components are capable of characterizing the information in the original data set and the remaining components are redundant, with negligible contribution. PCA is therefore an effective approach not only for data compression but also for feature extraction and fusion, so as to distinguish the difference and accordingly classify the data set.

Many parameters denoted as damage indices can be used to describe the severity of fatigue crack damage, such as transmission and reflection coefficients based on crack-scattered energy [51, 102], modulation intensity and cross-correlation coefficient [105], escort distribution [94], and other statistical parameters in the time, frequency or joint time-frequency domains [104]. Applications of the TRM based on a Lamb-wave approach for SHM are not new, and include research work on damage detection in metallic and composite structures [50, 81]. The effectiveness and robustness especially characteristic of baseline-free TRM make it feasible for fatigue crack monitoring.

2.3.4 Concluding Remarks

Among the most common sensing systems applied for GW-SHM, such as PZT transducers, FBG sensors and laser-based vibrometer, PZT-based sensing systems in terms of GWs deliver excellent performance in detection and location of cracks. This chapter reviewed the state of the art of Lamb-wave-based NDE and SHM technologies applied in plate-like structures, complex and tubular structures, for the identification of damage and fatigue crack in science and industry.

CHAPTER 3 Detection of Weld and Crack in Welded Zone of Welded Steel Plate

3.1 Introduction

As welded steel plates are the commonest structures in applications, it is of practical interest to investigate wave propagation characteristics within them, and whether GW-SHM techniques can address defects in such structures. In this chapter, the ability of the GW-SHM to detect a weld effect is investigated. Then a 2 mm-gap through-crack is generated by appropriately welding two steel plates, and is then filled with different materials to simulate the impurities in the crack. PZT transducers are used to detect the presence and location of the crack and also the effect induced by different impurities in the crack. Wavelet coefficients obtained from the continuous wavelet transform (CWT) of GWs, Hilbert coefficients from Hilbert transform (HT), and ToF extracted from captured signals are used as damage-sensitive features. As well, 3D finite element models under the same conditions are established to simulate GW propagation and stress responses for validation of experimental results.

3.2 Inspection of Weld in Steel Plate Using GWs

The first experimental study was carried out to assess the feasibility of detection of the existence of a weld using a PZT actuator and sensor pair as shown in Figure 3.1. Two 600 mm×200 mm×10 mm rectangular steel plates were used, one of which was fabricated by welding two 300 mm length steel plates at the middle and the other as a benchmark contained no welding. Two identical PZT transducers were surface-mounted in the pitch-catch configuration respectively, a 455 mm apart. The dispersion curves obtained theoretically for GW propagation in a steel plate indicate that many wave components exist with different group velocities in the higher frequency range. Hence, limiting the bandwidth of excitation to a low frequency range within which only two fundamental modes existed was necessary for the whole experimental process. Figure 3.2 shows the group velocity dispersion curves below 160 kHz in frequency for the steel plates from theoretical analysis and experimental study. The group velocity curves describe the speed at which a GW packet travels. Accordingly, the plates were excited in the in-plane direction using a 5 cycle tone burst multiplied by a Hanning window at a central frequency of 150 kHz. When the actuator initiated a wave pulse by an arbitrary waveform generator (HIOKI® 7075), the output analog signals were amplified by an amplifier (Piezo System® EPA-104) to make them capable of inducing a sufficiently strong electric field in the PZT actuator. The peak to peak voltage of the output signal from amplifier was about 80 V. The PZT sensor was individually connected to an oscilloscope (HP® Infinium 54810 A) and the corresponding response signals were sampled one by one at a rate of 10 M samples per second. The wave propagating within the plate was received by the sensor. Assuming a constant wave velocity, with a known distance between the sensor and the actuator, the arrival time of the incident wave at the sensor could be computed. All the experiments were undertaken in the same environment and conditions to ensure accuracy of results. Table 3.1 shows the properties of the PZT used in the experiments.

Table 3.1 Mechanical and electrical properties of the PZT transducer used in experiments

Geometry	20×5×1 mm^3
Density	7.80 g/cm^3
Poisson's ratio	0.31
Charge constant, d31	-170×10^{-12} m/V
Charge constant, d33	450×10^{-12} m/V
Relative dielectric constant, K3	1280
Dielectric permittivity, P0	8.85×10^{-12} F/m
Elastic constant, E	72.5 GPa

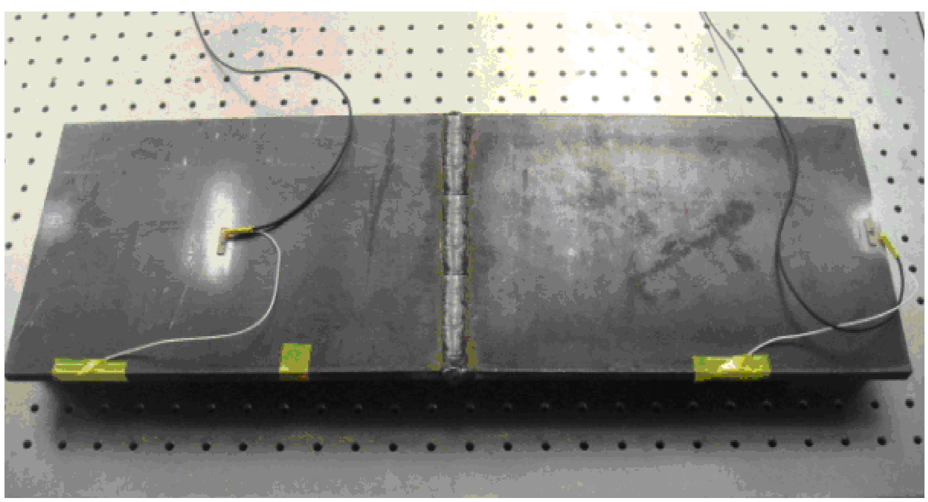

(a)

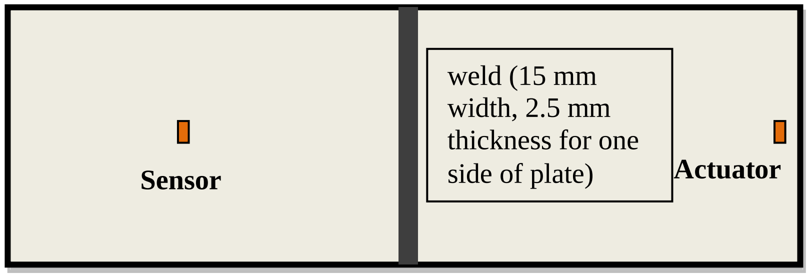

(b)

Figure 3.1 (a) Specimen (b) schematic diagram of the steel plate with weld for investigating the existence of weld

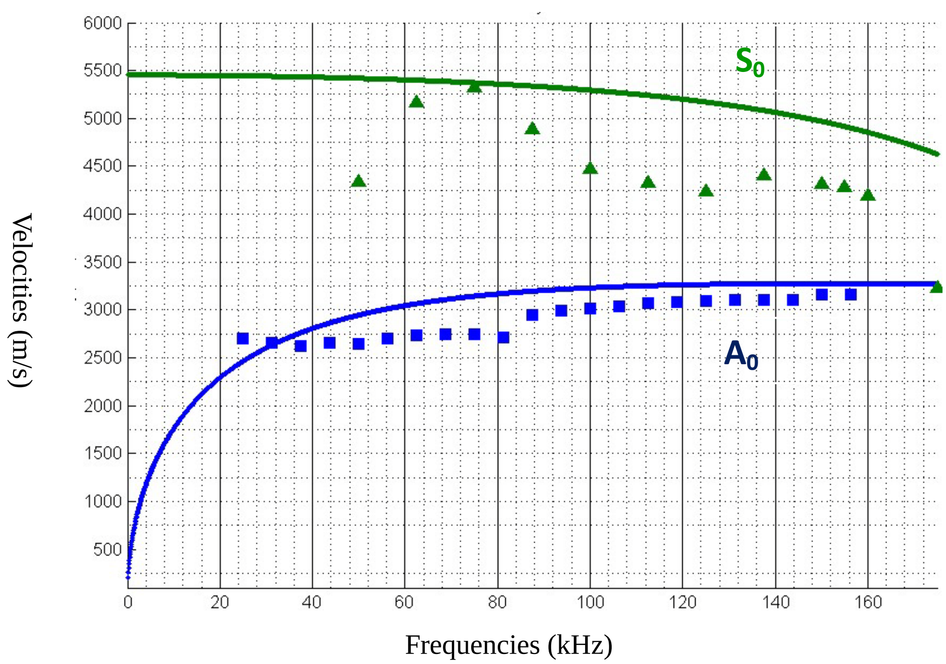

Figure 3.2 Theoretical and experimental velocities versus frequencies

In the process of GW-SHM, a taxonomy for categorizing GW-SHM approaches is in terms of the domain where the processing is conducted, such as time domain, frequency domain and joint time-frequency domain analyses. In this study, it was necessary to implement time-frequency analysis for the diagnostics of transient signals. To overcome the limitations of harmonic analysis, alternative families of orthogonal basis functions known as wavelets were used. A general overview of wavelet analysis can be found in [23]. By using a suitable mother wavelet function, $\psi(t)$, the CWT decomposes a signal $x(t)$ into the time and frequency domain as

$$(wf)(b,a) = \int_{-\infty}^{+\infty} x(t) \frac{1}{\sqrt{a}} \psi^* \left(\frac{t-b}{a} \right) dt \tag{3.1}$$

where continuous variables *a* and *b* are the scale and translation parameters, respectively. In the present study, a 'Gauss' wavelet was employed as a mother wavelet function.

The HT is a useful approach for processing the response signal in the time domain and extracting specific information in terms of its energy distribution, defined as Equation (3.2) [107]

$$H[x(t)] = \int_{-\infty}^{+\infty} \frac{x(\tau)}{t-\tau} d\tau \tag{3.2}$$

Figure 3.3 displays the experimental results in which the curve in the dashed line shows the HT coefficients of transmitted signal through the weld and the curve in the solid line shows the HT coefficients of transmitted signal obtained from a plain plate. HT coefficients were obtained by HT module. It indicates that with the presence of a weld, some wave energies are reflected by the weld and therefore the amplitude of the S_0 wave package is lower than that of the intact plate, due to the change of geometry [24].

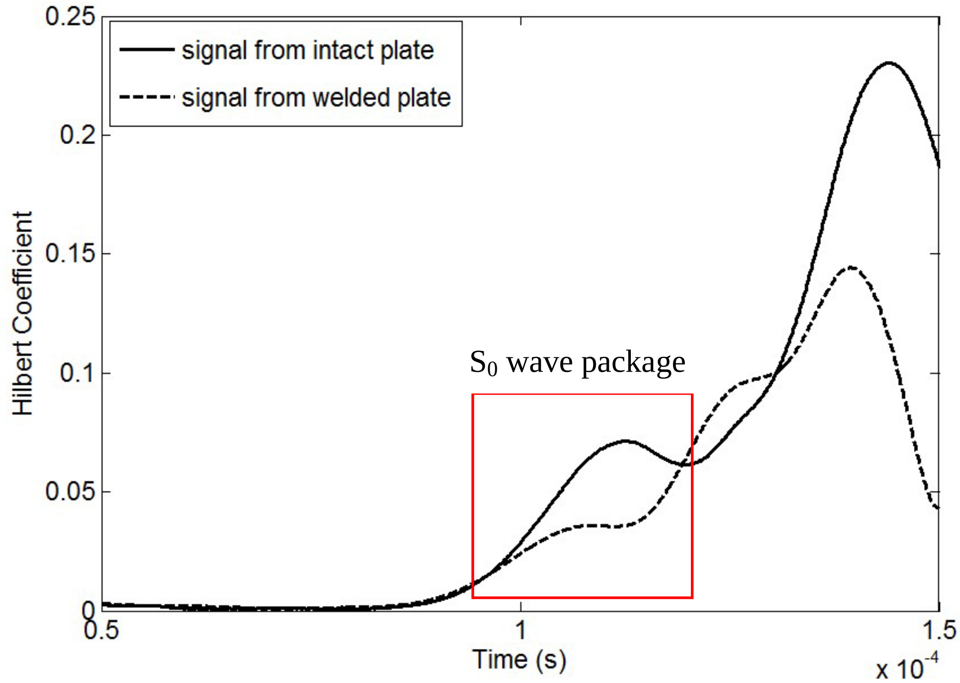

Figure 3.3 Experimental results for plates with (dashed line) and without (solid line) welding

To verify the experimental results, a finite element model with the same dimensions as the real specimen and with the material properties given in Table 3.2 was employed as shown in Figure 3.4. The idealized welding zone is modeled using two curved surfaces with a maximum thickness of 15 mm. An 8-node brick element was used to mesh the model in 3D with more than 10 elements per wavelength. An explicit central difference scheme was used to perform the time marching solution, the time step being chosen as time differential of active load. The plate was excited by the PZT actuator using a five-cycle Hanning-window-modulated sinusoid tone bursts with a central frequency of 150 kHz (shown in Figure 3.4). The software ABAQUS®/CAE was used to process the finite element calculations. Table 3.3 compares the velocities and amplitudes obtained from FEM in which different layers are established in the meshed part. The results indicate that the difference in velocity between the results from displacement and stress was smallest when the established mesh layer was controlled at 10 layers and the element size was 1 mm. Thus, 1 mm element size was used in the simulations.

Table 3.2 Material properties of simulation model

Young's modulus	210 GPa
Poisson's ratio	0.3
Mass density	7850 kg.m^3

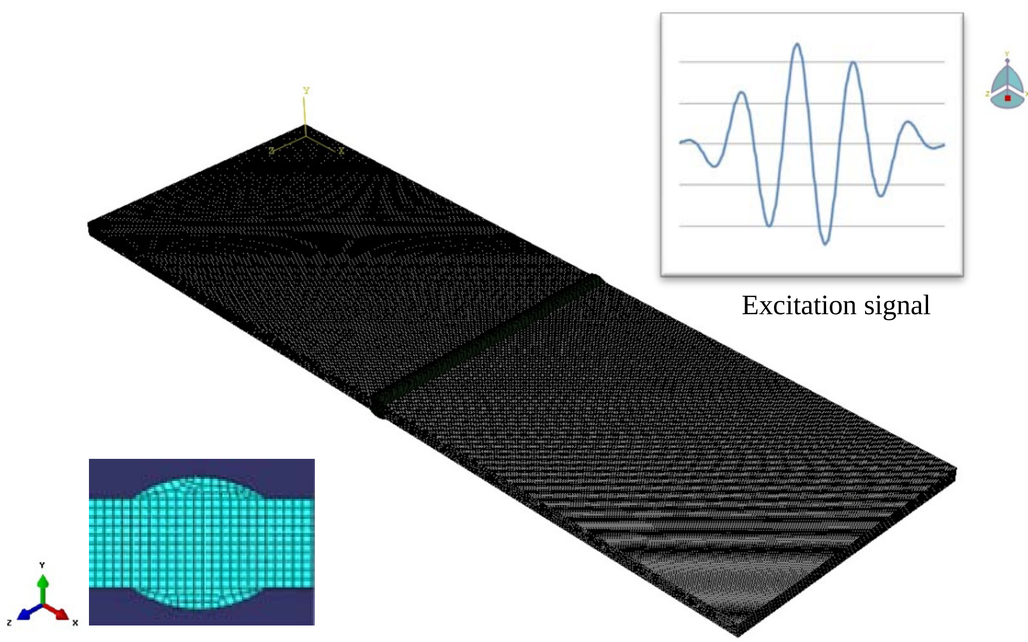

Figure 3.4 Model and actuation pulse used in simulation

Table 3.3 Differences between different layers established in FEM

Layers	Time(s)		Speed (m/s)	Amplitude	Difference
2 (1mm element)	U (Displacement)	0.0001029	4324.587	2.74E-15	1.156%
	S (Stress)	0.0001029	4274.637	1.86E-02	
4 (1mm element)	U	0.0000987	4508.612	3.37E-15	1.886%
	S	0.0001006	4423.459	2.75E-02	
5 (1mm element)	U	0.000096	4635.417	3.40E-15	1.446%
	S	0.0000974	4568.789	2.22E-02	
8 (1mm element)	U	0.0000977	4657.114	2.81E-15	3.500%
	S	0.000099	4494.949	1.46E-02	
10 (1mm element)	U	0.0000953	4669.465	3.54E-15	0.728%
	S	0.000096	4635.417	1.15E-02	
2mm element	U	0.0000987	4508.612	4.73E-15	2.573%
	S	0.0001013	4392.892	3.33E-02	

As it is not possible to excite motion at a single point in all in-plane directions, the excitation could be applied to a range of nodes without creating a rectangular sheet in order to model a localized source. An element at a distance of 455 mm from the excitation point was chosen as the sensor to monitor the stress. Responses at the monitored element are plotted in Figure 3.5. At a low frequency, the S_0 Lamb mode has very little dispersion, which is ideal for long-range detection [106]. In this case, S_0 is easily identified as the first wave package. From the figure, the amplitude of the S_0 wave transmitted through the welding zone was smaller than that from the intact plate, which is consistent with the experimental results.

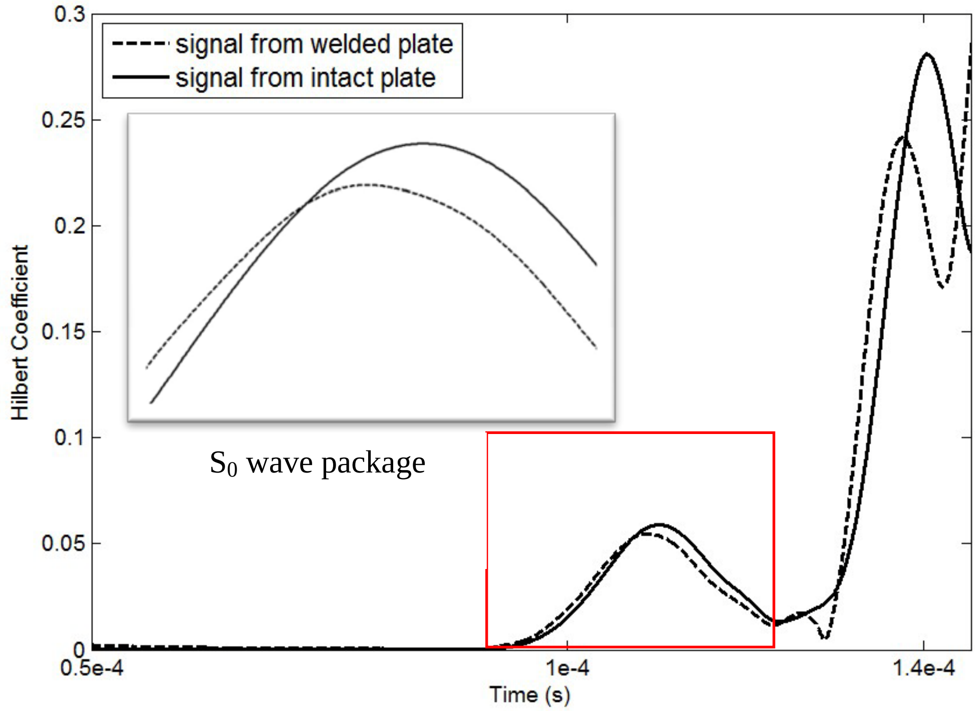

Figure 3.5 Simulation results for plates with and without welding

3.3 Detection of Crack in Welding Zone Using GWs

The second experimental study of this chapter was carried out to check the feasibility of crack detection in a welding zone using a PZT pair surface-bonded on the specimen. The specimen was prepared by welding two steel plates which had wide flange sections of different flange thickness. A 2 mm-gap through-crack was developed at the welding zone. PZT transducers were used in conjunction with the GW methods to detect the presence and location of the crack as shown in Figure 3.6. The PZT pair was aligned parallel to the induced crack. The response signal received at the sensor was collected and processed using CWT and HT.

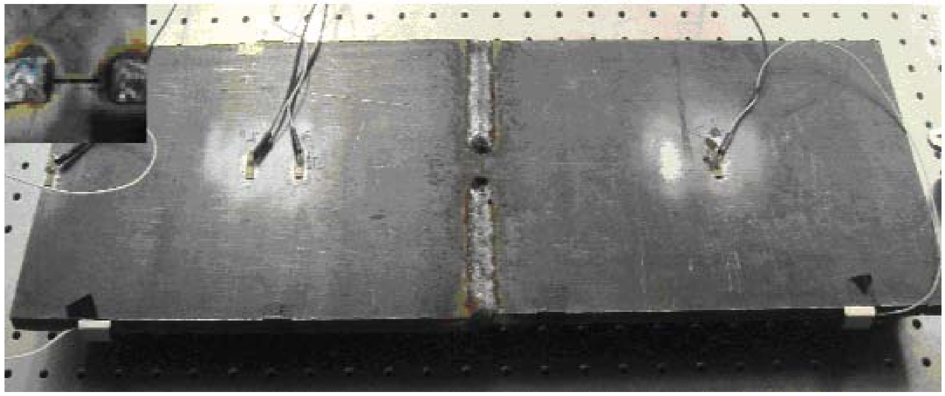

(a)

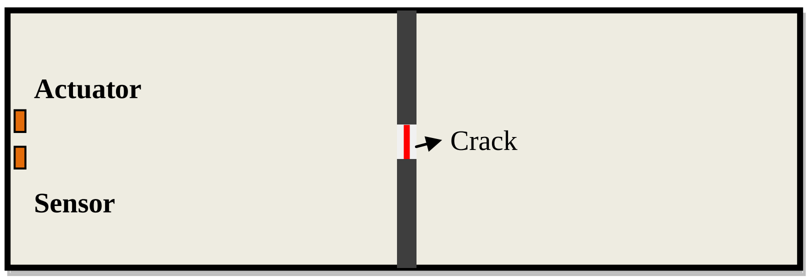

(b)

Figure 3.6 (a) Specimen (b) schematic diagram of crack detection in the steel plate with a weld and a crack for investigating the existence of a crack

Figure 3.7 (a) shows the original GW signals captured at the sensor for the cases of a welded steel plate with crack and without crack. To obtain the energy concentrations of various GW modes and to extract damage-sensitive features, the CWT was applied and wavelet coefficients were selected based on maximum peak values corresponding to the center frequency of 150 kHz (scale: 47), as illustrated in Figure 3.7 (b).

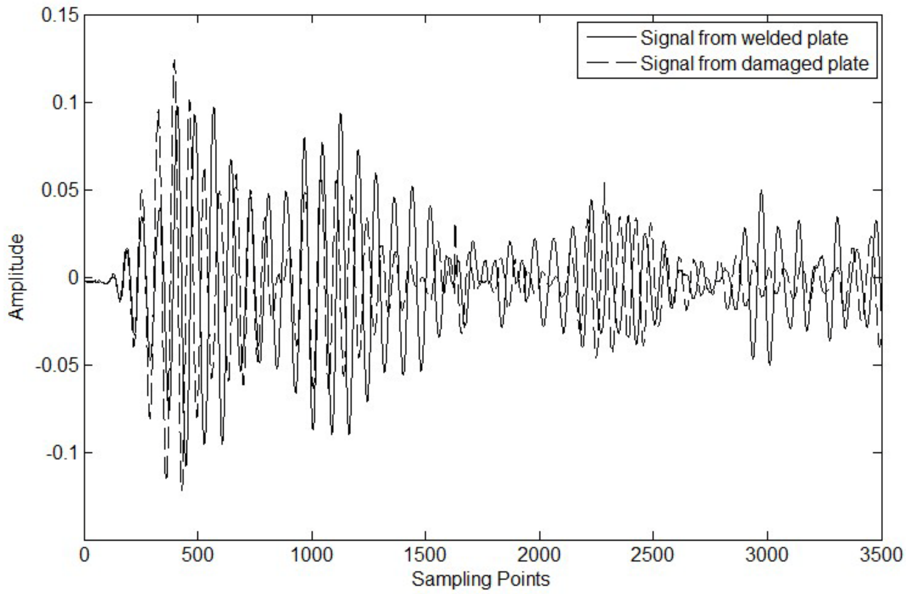

(a)

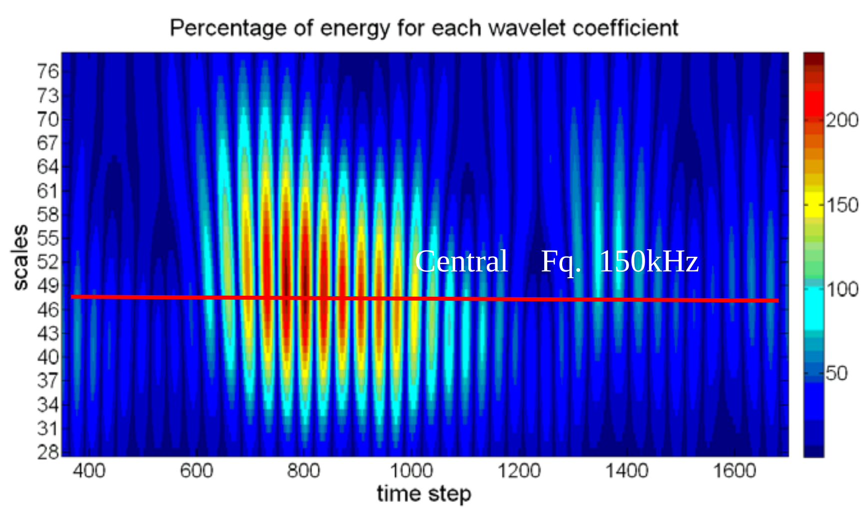

(b)

Figure 3.7 (a) Original signal for the cases of a welded steel plate without crack and with crack (b) CWT coefficients within a selected scale range

To identify the crack in the welded zone, the welded plate without a crack was taken as the benchmark. Figure 3.8 shows the corresponding energy spectra in the 3D form obtained from the baseline signal in terms of Equation (3.1). As shown in this figure, the energy concentration of various GW modes are calibrated by the CWT coefficients.

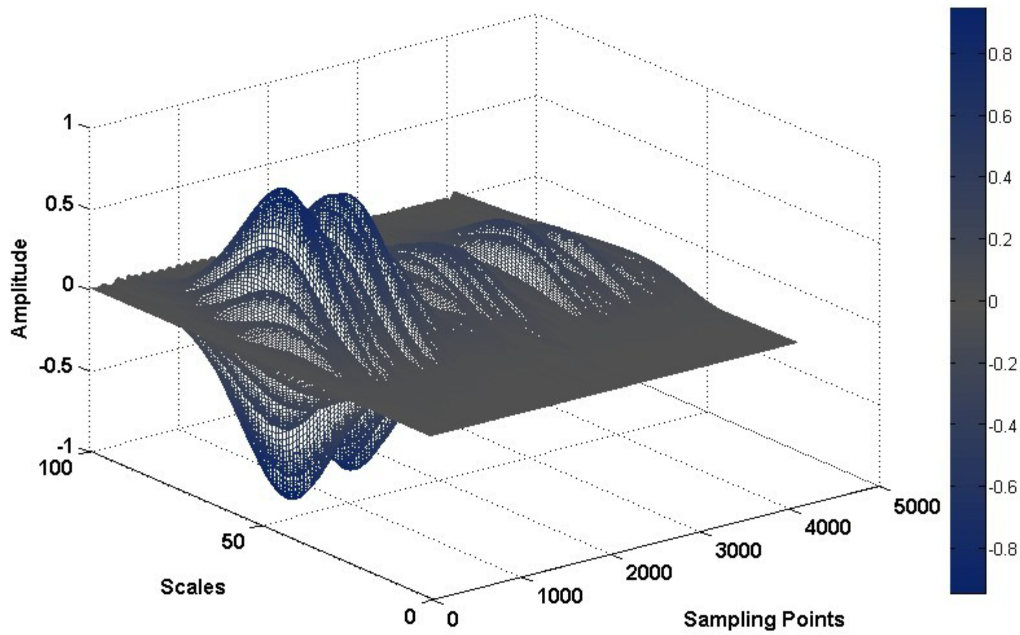

Figure 3.8 3D contour of CWT coefficients from baseline data

.

If the maximum peak values at scale 47 are chosen and extracted from Figure 3.8, we can obtain the CWT coefficients of the welded case and the damaged case as shown in Figure 3.9. From this figure the incident wave package and its reflection from boundaries and the wave mode induced by the weld and the crack within the weld can be clearly observed in the energy spectra. After applying HT to the CWT coefficients from CWT, Figure 3.10 shows the transform mechanism and HT coefficient for the welded plate without and with crack in the welding zone.

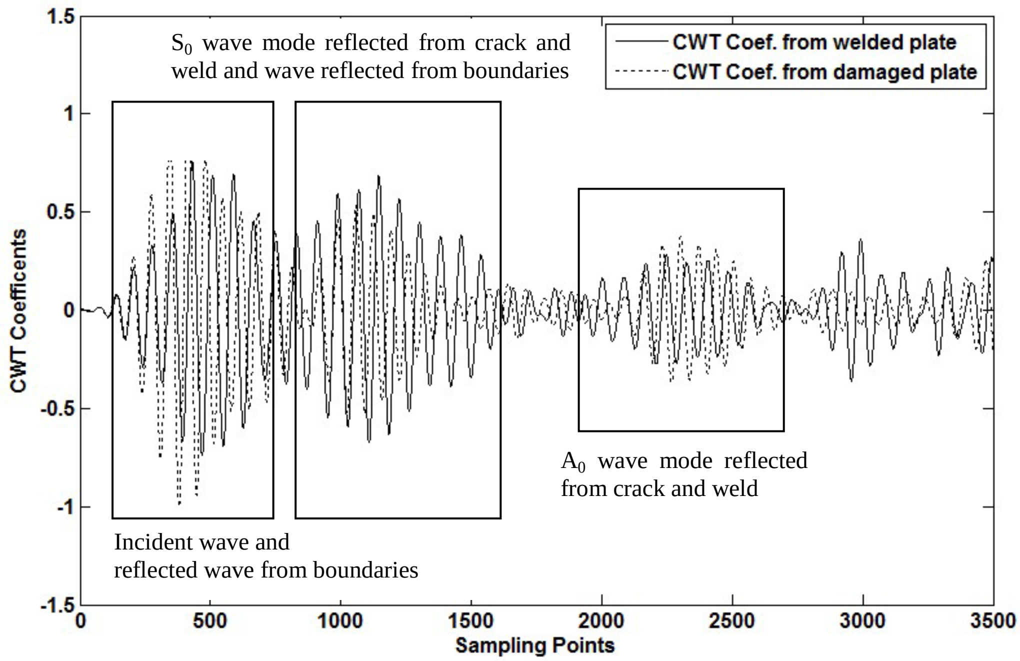

Figure 3.9 CWT results at central frequency of 150 kHz

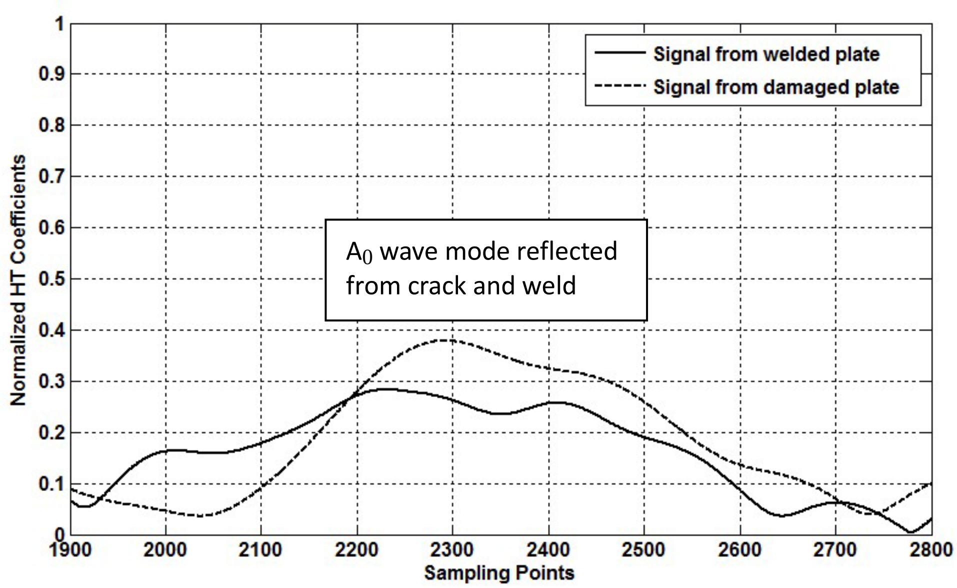

Figure 3.10 HT coefficient for welded plate with crack

From the HT coefficient in the time domain as shown in Figure 3.10, it is easy to identify the A_0 wave package received from the sensor directly reflected from the actuator by the ToF, whereas the S_0 mode is difficult to identify due to the short distance. The experimental wave velocity of the A_0 mode at 150 kHz can be calculated according to the distance of 0.1 m between the long-side boundary and the sensor, which is about 2800 m/s. The arrival of the incident and damage-reflected A_0 mode can be read, from which the flight distance can be computed using the experimental velocity from the time of the incident energy peak. The result thus calculated of the distance between the sensor and crack is 0.29 m, comparing well with the exact value of 0.30 m.

To verify the experimental result, the finite element model for a welded plate with a crack in welding zone was employed to simulate the GW propagation. Figure 3.11 (a) shows the model established in FEM and (b) shows the change in wave propagation before and after the crack, in which obvious reflection from the crack can be seen. HT coefficients obtained from sensor by simulation result are shown in Figure 3.12 for the 2 mm×16 mm crack. The major features which can be observed are very similar to the experimental results. Additional wave scattering and attenuation effects can be observed due to interactions with the crack and weld. The incident and crack-reflected wave packages can be seen in this figure. The arrival of the incident and crack-reflected A_0 mode can be read, from which the flight distance can be computed using the theoretical velocity from the time of the incident energy peak. The result for the distance between crack and sensor is 0.324 m, comparing well with the exact value of 0.30 m.

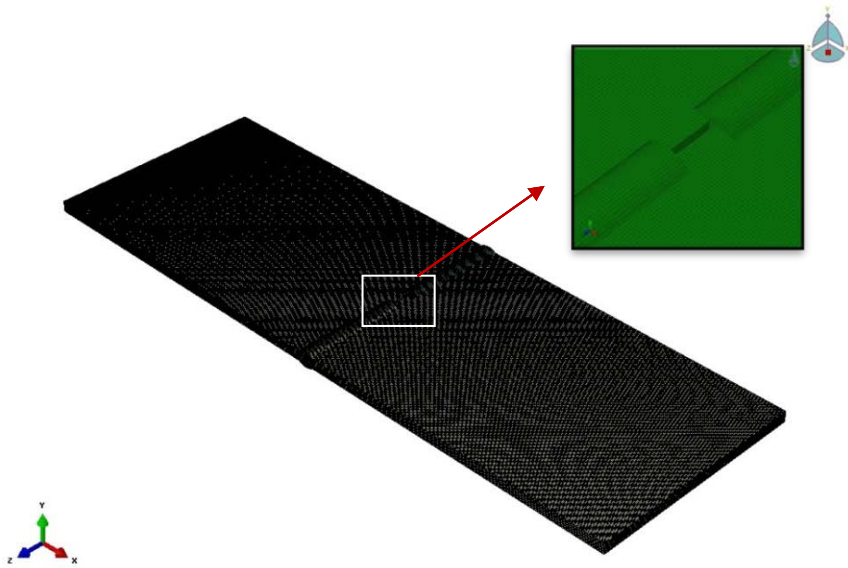

(a)

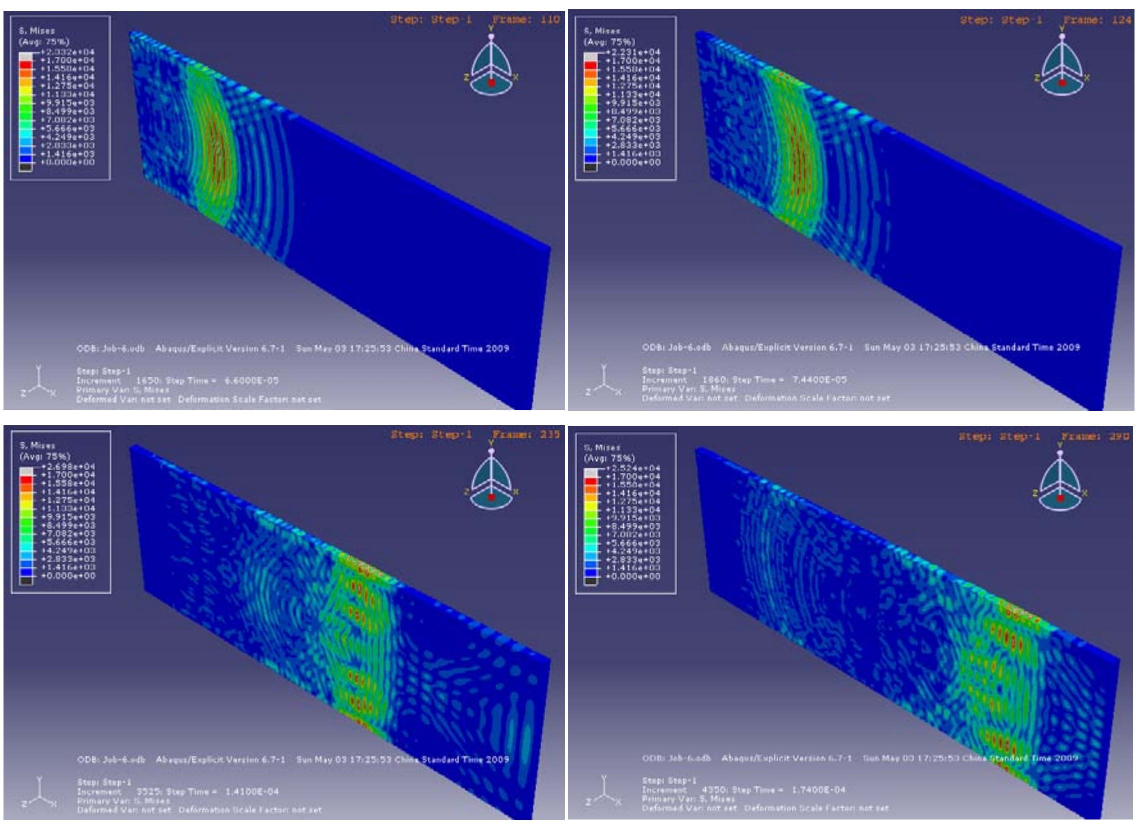

(b)

Figure 3.11 (a) Model established in FEM (b) wave propagation in steel plate with crack

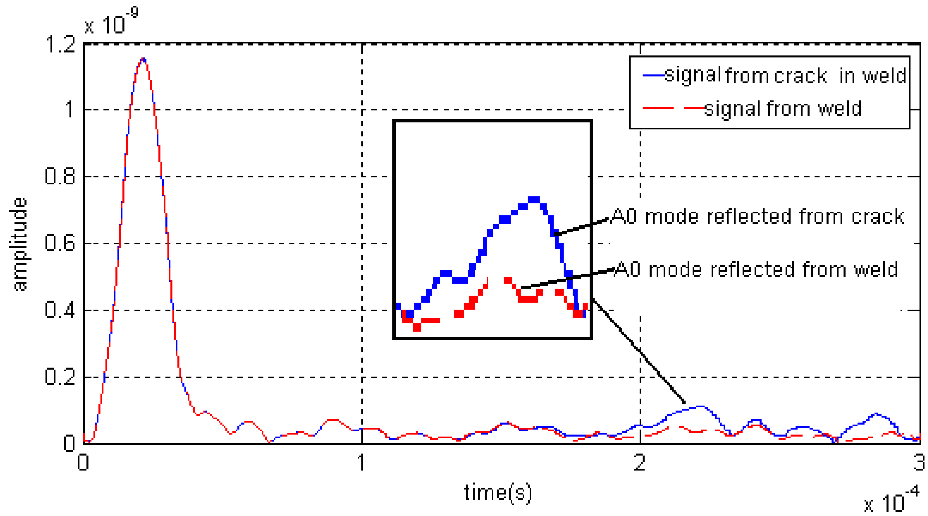

Figure 3.12 Amplitudes of cases with weld and crack in simulation

3.4 Effect of Different Impurities in Crack

In real applications, steel plates or structures are usually used in the natural environment and it is inevitable that some impurities are included within damage. To identify the effects of different impurities and to verify the accuracy of this technology in different circumstances, the 2 mm×16 mm crack was filled separately with different materials, namely water, alcohol, epoxy, and mud, to simulate the presence of impurities within the crack. The wave velocities were then estimated using the same procedure as described in the previous analysis, with the setup of the actuator and sensor as given in Figure 3.1. The signals collected by the sensor were analyzed and the results are depicted in Figure 3.13. The experimental results summarized in Table 3.4 show the calculated wave velocities under the different conditions.

It can be seen from the table that with the presence of each impurity, the wave velocity across the filled crack was slower than that for the welded plate with the same crack but without impurity. This difference can be attributed to the effect of the interface between different materials. Obviously, the amplitudes obtained from the various cases differ slightly according to the different kinds of impurity, as can be seen from Figure 3.13, indicating that the different medium couplings can affect the energy concentration in the damaged region.

Table 3.4 Results for experiment with different impurities inside crack

Different cases	***Theoretical S_0 velocity at 150 kHz (m/s)***	***Experimental S_0 velocity at 150 kHz***
Plate with crack	4961 m/s	4744 m/s
crack with epoxy		4700 m/s
crack with water		4715 m/s
crack with alcohol		4730 m/s
crack with mud		4735 m/s
Different cases		***Numerical S_0 velocity at 150 kHz***
Plate with crack		4676 m/s
crack with epoxy		4537 m/s

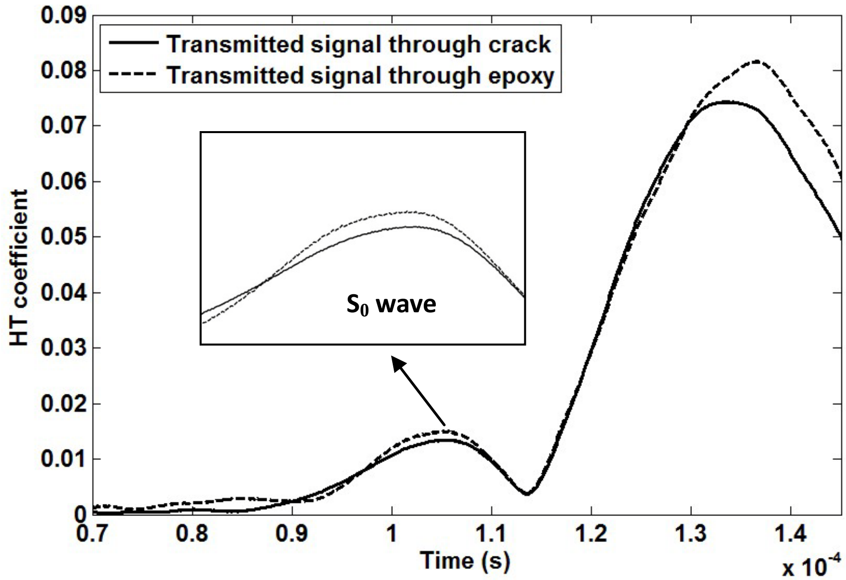

Transmitted signal through crack
Transmitted signal through epoxy
HT coefficient
Time (s)
x 10^-4
S0 wave
0.09
0.08
0.07
0.06
0.05
0.04
0.03
0.02
0.01
0
0.7
0.8
0.9
1
1.1
1.2
1.3
1.4

(a)

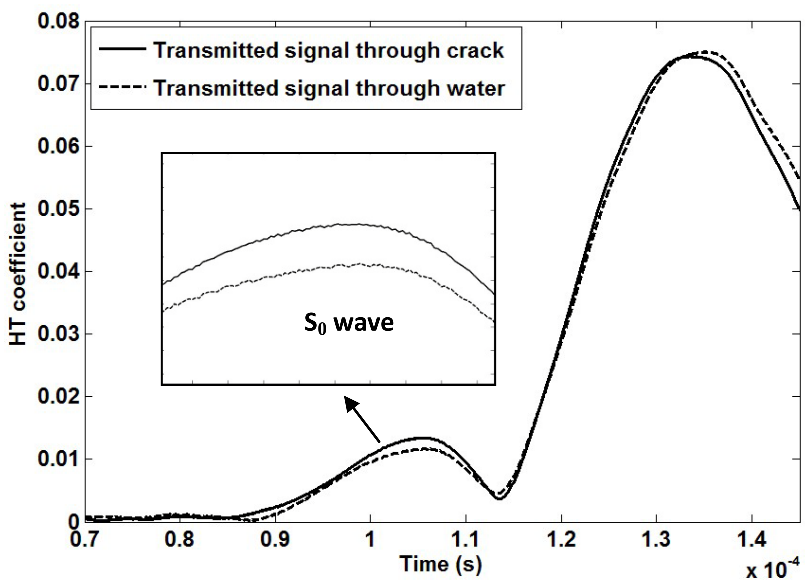

Transmitted signal through crack
Transmitted signal through water
HT coefficient
Time (s)
x 10^-4
S0 wave
0.08
0.07
0.06
0.05
0.04
0.03
0.02
0.01
0
0.7
0.8
0.9
1
1.1
1.2
1.3
1.4

(b)

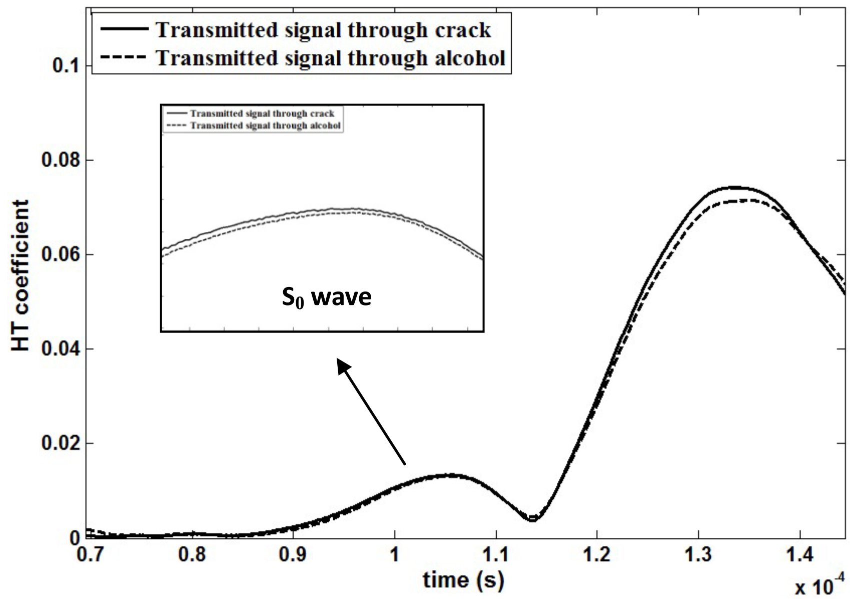

(c)

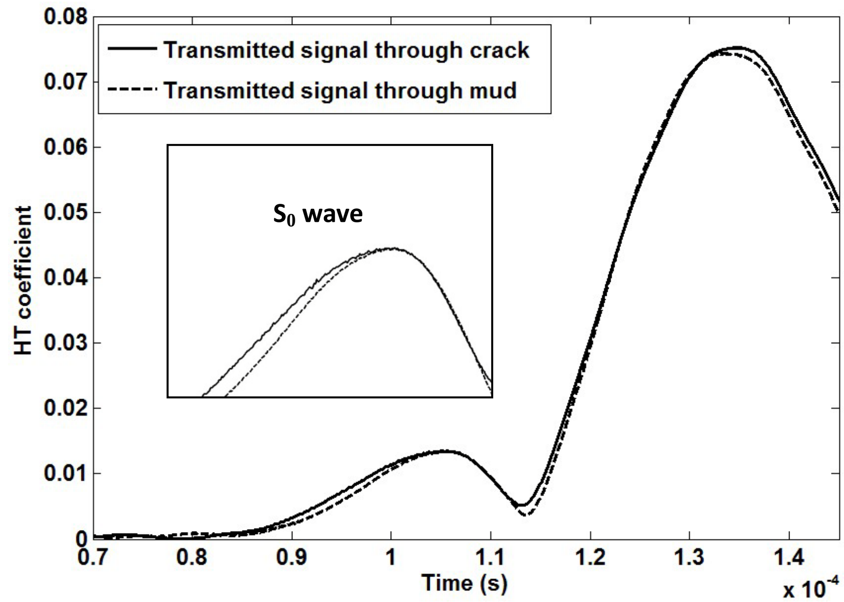

(d)

Figure 3.13 Experimental results of different cases (a) HT amplitudes of signal from crack and crack with epoxy (b) HT amplitudes of signal from crack and crack with water (c) HT amplitudes of signal from crack and crack with alcohol (d) HT amplitudes of signal from crack and crack with mud

Finally, the situation of filling epoxy in the crack was simulated using FEM by changing the material properties in the cracked region. The simulation results are plotted in Figure 3.14. Comparing the result with that of the experiment, it can be clearly observed that there is a time delay for the wave propagating across the crack with epoxy, which is consistent with the experimental results.

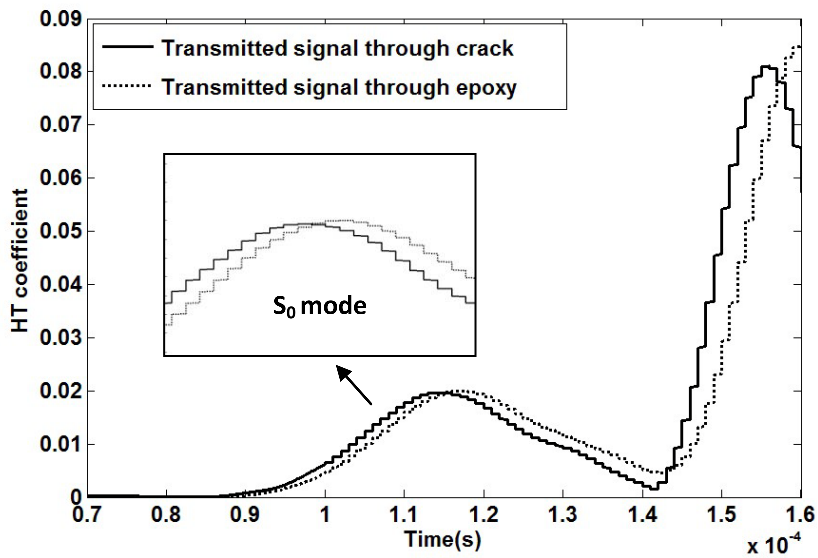

Figure 3.14 HT amplitudes for crack with and without epoxy in simulation

3.5 Concluding Remarks

The study presented in this chapter can enhance understanding of propagation behavior of GWs in steel plate with weld and crack. Experiments based on GWs obtained via PZT actuator and sensor were presented, confirming that the GW-based methodology is capable of detecting and locating a weld, crack, and cracks with different impurities in steel plates. The peak-to-peak amplitude of the transmitted S_0 wave package and reflected damage-induced wave components was investigated for crack detection.

Further, 3D finite element models were employed to verify the experimental results. An amplitude and arrival time analysis, useful in crack detection studies, was performed. It was found that the amplitude reflected from a crack is larger than that from a weld. In a welded plate with a crack, different kinds of impurity can affect both wave velocity and wave amplitude.

CHAPTER 4 Damage Identification in Tubular Steel Structures Using GWs and Probability-based Imaging Approach

4.1 Introduction

In this chapter, a GW-based damage identification approach was specialized for the WTSS used in bogie system of a train carriage. Both FEM and experimental analysis were employed to investigate the propagation of GWs in a WTSS of rectangular cross-section with welding damage, a true-scale model of a train bogie frame segment. With the assistance of an active piezoelectric sensor network, GW signals were activated and captured, from which a signal feature, ToMD, was extracted to establish damage presence probability (DPP). CWT and HT are subsequently employed to implement signal purification and feature highlighting. A probability-based damage imaging approach was developed based on ToMD. As validation, the approach was used to predict presences and locations of slot-like damages in the welding zones of the WTSS. Furthermore, a two-level image fusion scheme using different strategies was developed to enhance the tolerance of the approach to signal noise.

4.2 Propagation Characteristics of GWs in WTSS with Welding Damage

4.2.1 Description of the Problem

A bogie frame dismantled from a real train carriage is shown in Figure 4.1 (a), which is comprised of a number of WTSSs of rectangular cross-sections. WTSS in a train carriage is a grillage-like structure designed to carry various operational loads. The complexity in geometry of a WTSS and numerous attachments make the access to critical areas which structural damage is likely to exist highly prohibitive, posting great challenge in implementing damage identification and SHM techniques based on GW. With the occurrence of damage, propagation characteristics of GWs in a WTSS become more difficult to interpret. To investigate the propagation of GWs in WTSS, a WTSS, a true-scale section model of the bogie frame from HK MTR train carriage, was fabricated, as shown schematically in Figure 4.1 (b). The WTSS consists of four facets which were pre-welded to shape a tube of rectangular cross-section. The detailed geometrical dimensions are shown in the same figure and the material properties of the WTSS are detailed in Table 4.1. Considering most damage in WTSS initiates and propagates from welding zones between adjacent facets, slot-like damage in welding zone between Facets A and B was focused on.

Table 4.1 Material properties of the WTSS

Density	7.85 g/cm^3
Poisson's ratio	0.28
Elastic constant, E	210 GPa

An active senor network consisting of twelve circular PZT wafers, 6.9 mm in diameter and 0.5 mm in thickness each, was symmetrically surface-mounted to Facets A and C. Each PZT wafer can function as either the actuator to generate waves or sensor to receive damage-scattered waves in accordance with the dual piezoelectric effects. Detailed layout and nomenclature of PZT wafers on Facet A are shown in Figure 4.2. A simulated damage scenario, through-thickness slot-like welding defect, 12 mm long, 1 mm wide and 10 mm deep, was assumed in the welding zone between Facets A and B (x-axis), with its centre being 275 mm away from the origin of the coordinate system in Figure 4.2. In the active sensor network, to minimize the influence of complex boundary reflections from opposite facet upon wave signal interpretation, each sensor was limited to capture GW signals activated by actuators located on the same facet. Therefore, the displayed sensor network segment on Facet A (half of the entire sensor network) is able to render thirty sensing paths, consisting of one actuator and one sensor each. For convenience of discussion, each sensing path is denoted by A_mA_n for those on Facet A or C_mC_n for those on Facet C (m, n=1,2,⋯,6, but m≠n) in what follows.

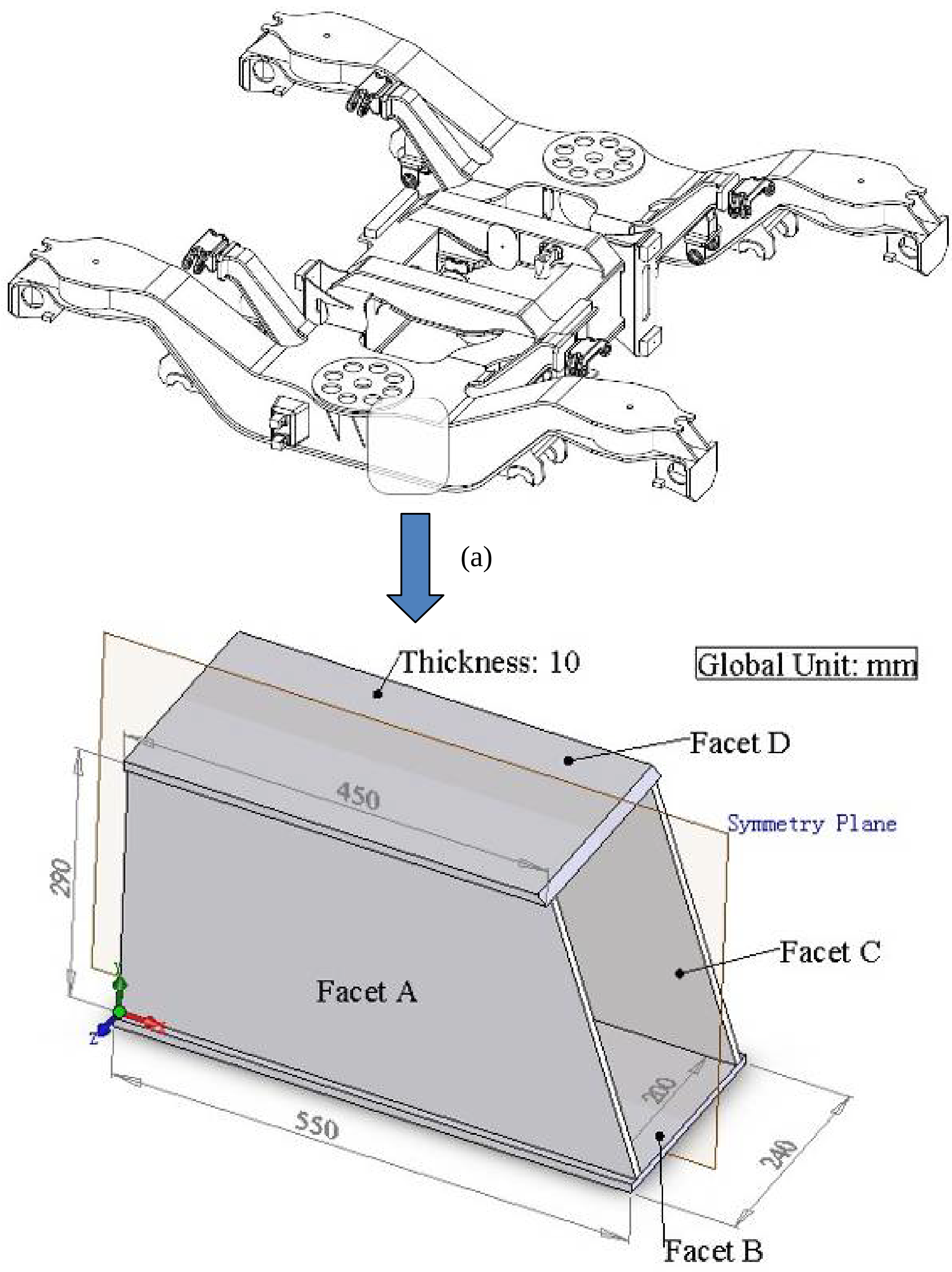

(b)

Figure 4.1 (a) A typical bogie frame of a train carriage consisting of a number of WTSSs and attachments (b) geometrical details of the WTSS under investigation

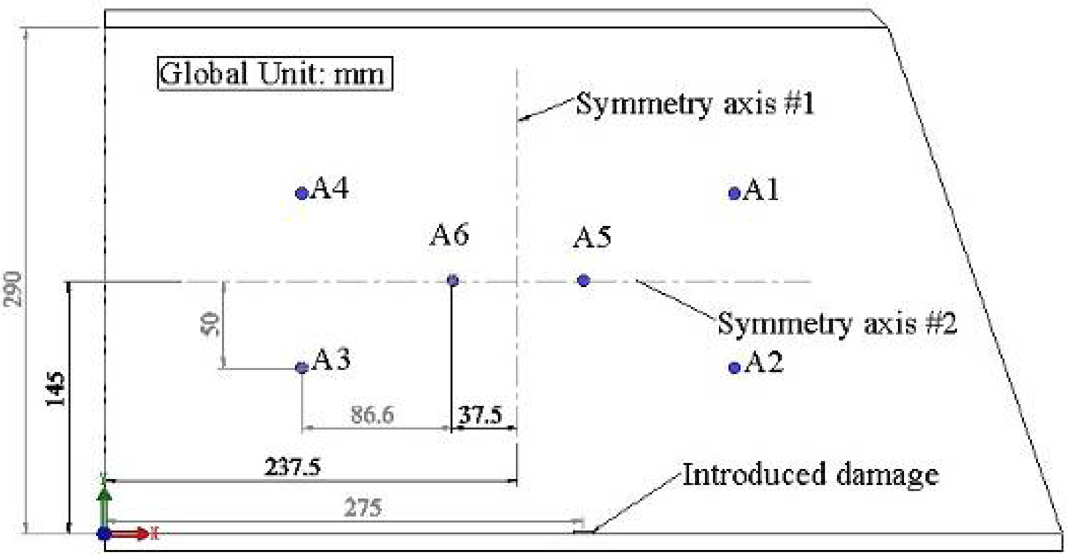

Figure 4.2 Layout of the active PZT sensor network surface-bonded to the WTSS (diagram showing half of the sensor network on Facet A, and Facet C sharing the same network configuration)

An infinite number of GW modes co-exist once being activated, which can be deemed as the superposition of a series of longitudinal and transverse modes. Generally speaking, both the longitudinal and transverse modes are sensitive to structural damage and both can be used for identifying damage but the former is used more frequently. Recently, there has been increasing awareness of using the transverse mode for damage identification. Its merits, in comparison with the longitudinal mode, include: (i) shorter wavelength at a given excitation frequency (in recognition of the fact that the half wavelength of a selected wave mode better be shorter than or equal to the damage size to allow the wave to interact with the damage); (ii) larger signal magnitude (the transverse mode in a wave signal is usually much stronger than the longitudinal mode if two modes are activated simultaneously, giving a signal with high SNR, though it attenuates more quickly); and (iii) easier means of activation (the out-of-plane motion of particles in a plate can more easily be activated). In this study, attentions focused on the transverse mode which dominated the sensed wave signals.

4.2.2 FEM Analysis

A 3D finite element model for the WTSS shown in Figure 4.1 (b) was developed using the commercial finite element software ABAQUS®/CAE, in Figure 4.3 (a). The WTSS was modeled with 3D eight-node solid brick elements (C3D8R in ABAQUS®). All the elements were set as 2 mm in 3Ds, guaranteeing that at least seven elements were allocated per wavelength of the transverse mode at any excitation frequency that would be used in this chapter. The welding damage was formed by removing associated finite elements from the meshed model (elements in damaged zone was resized to match the geometry of the damage), shown in Figure 4.3 (b).

The PZT wafer was simulated using a piezoelectric actuator/sensor model pre-developed. Uniform in-plane (x-y axis) displacement constraints were applied on finite element nodes of the upper surfaces of the PZT actuator model, as shown in Figure 4.4, in recognition of the mechanism of a PZT wafer. GW signals were activated using three-cycle Hanning-window-modulated sinusoid tone bursts at a central frequency of 150 kHz as incident wave signal. Dynamic simulation was carried out using commercial finite element software ABAQUS®/EXPLICIT. The crack-reflected wave signals were captured by calculating the deformation at places where sensors were located. With the aim of ensuring calculation accuracy, time interval of the calculation step was fixed on 4 $\times 10^{-8}$ s which is much less than the time needed for GW propagating across the minimum distance of any two adjacent nodes at the largest possible velocity.

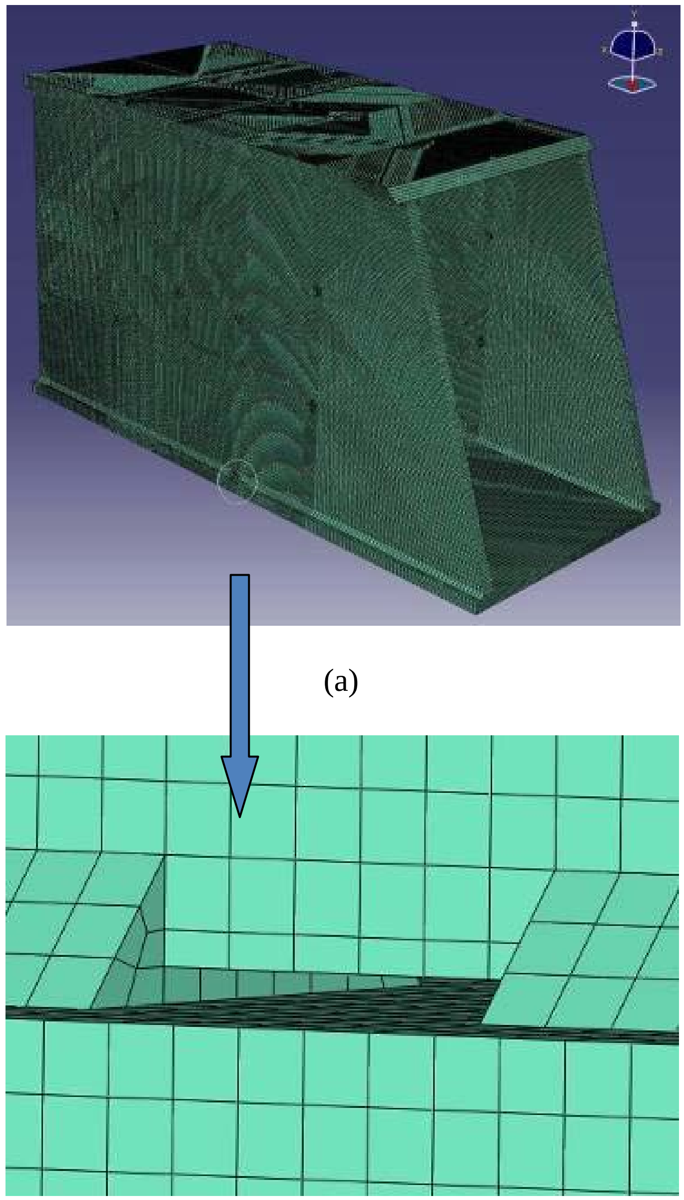

(a)

(b)

Figure 4.3 FEM model of the WTSS (a) global view (b) zoomed-in part containing the simulated welding damage

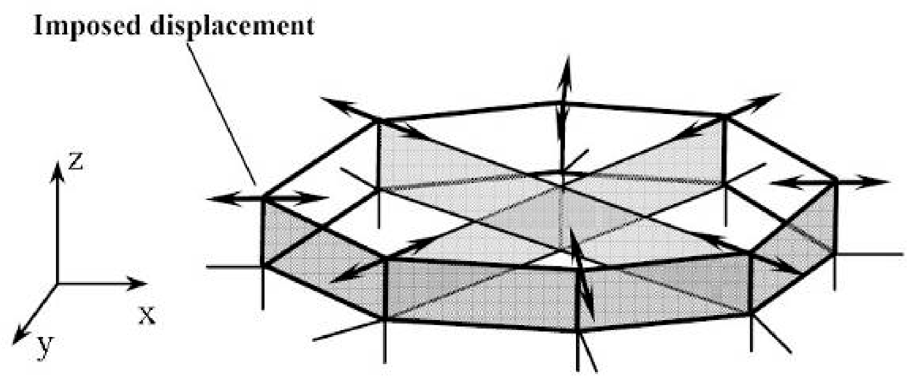

Figure 4.4 FEM model of the pre-developed GW actuator with uniform radial displacement constraints applied on circumferential FEM nodes

4.2.3 Propagation Characteristics of GW in WTSS

As some typical results from simulation, snapshots for propagation of GWs generated by A_5 at several representative moments are exhibited in Figure 4.5. From the simulation results, it can be concluded that GWs generated by surface-bonded PZT actuator on any facet of the WTSS propagate are confined within the same facet at first, as shown in Figure 4.5 (a) and (b); when incident GWs reach boundaries (welding zones and original edges of different facets of WTSS), they are scattered including wave reflection, transmission and diffraction, as seen obviously in Figure 4.5 (c); all the scattered wave components continue their propagation in adjacent facets. The simulation results have revealed that propagation characteristics of GWs in a WTSS, though it is in a shape of tube, are similar to those propagating in a flat sheet (GWs) in individual facets and different from those in cylinder (cylindrical GWs) [109] which are described by longitudinal, torsional and flexural modes.

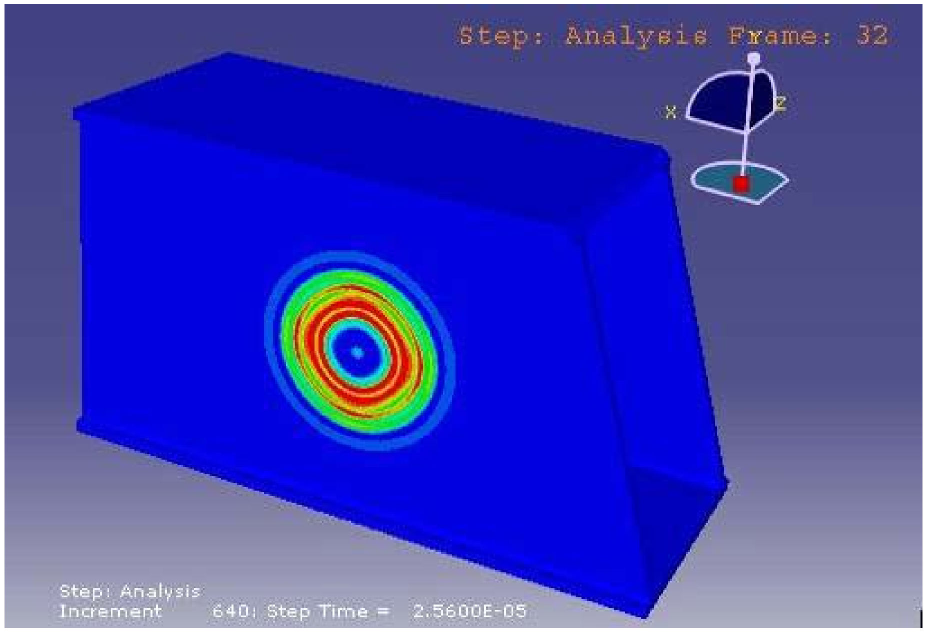
Step: Analysis Frame: 32
Step: Analysis
Increment 640: Step Time = 2.5600E-05

(a)

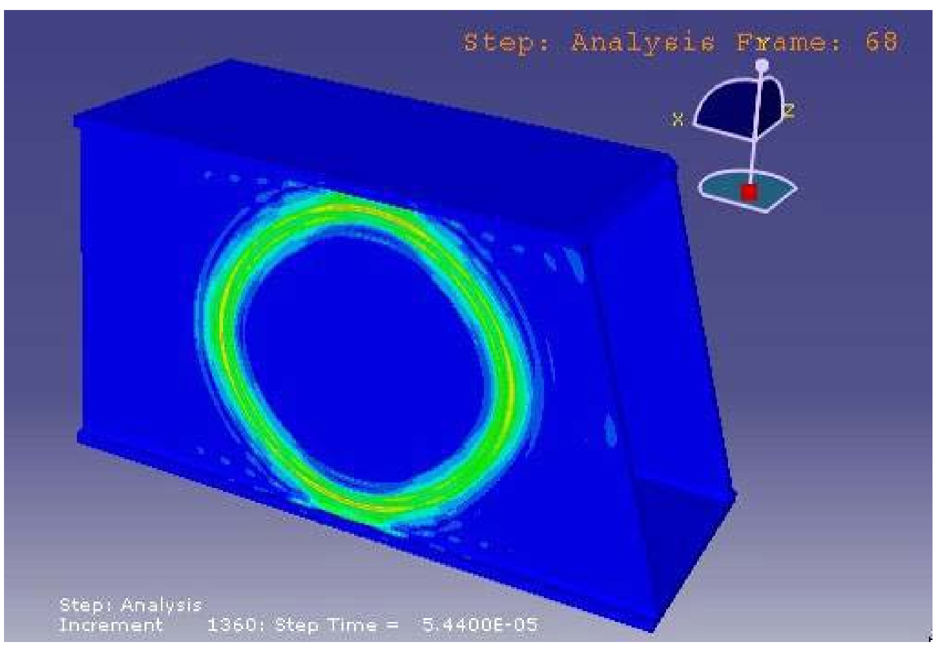
Step: Analysis Frame: 68
Step: Analysis
Increment 1360: Step Time = 5.4400E-05

(b)

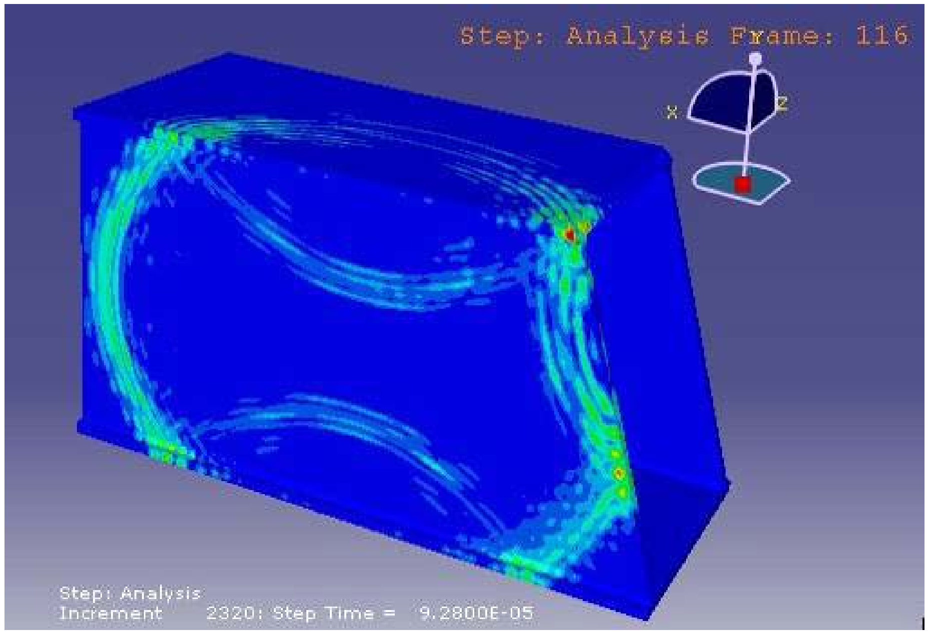

(c)

Figure 4.5 Snapshots for GW propagation in the WTSS at selected moments from FEM simulation (a) 25.6 μs (b) 54.4 μs (c) 92.8 μs

Considering the above observation and location of the simulated welding damage, Facet *C* was deemed as the benchmark relative to Facet *A*, where benchmark is referred to as the structure of the same dimension and properties but without any damage that is intentionally introduced. The introduced damage, deemed as extra boundary conditions of the WTSS to GWs in comparison with benchmark, modulates the propagation of GWs, leading to wave scattering. Comparing with baseline signals captured from benchmark, pronounced changes in both waveform and amplitude can be observed, as shown in Figure 4.6. For illustration, wave signals captured via two representative sensing paths, and their corresponding benchmark counterpart, C_5C_2 and C_5C_6 (serving as baseline signals), are presented in Figure 4.7. Although the amplitudes of signals from

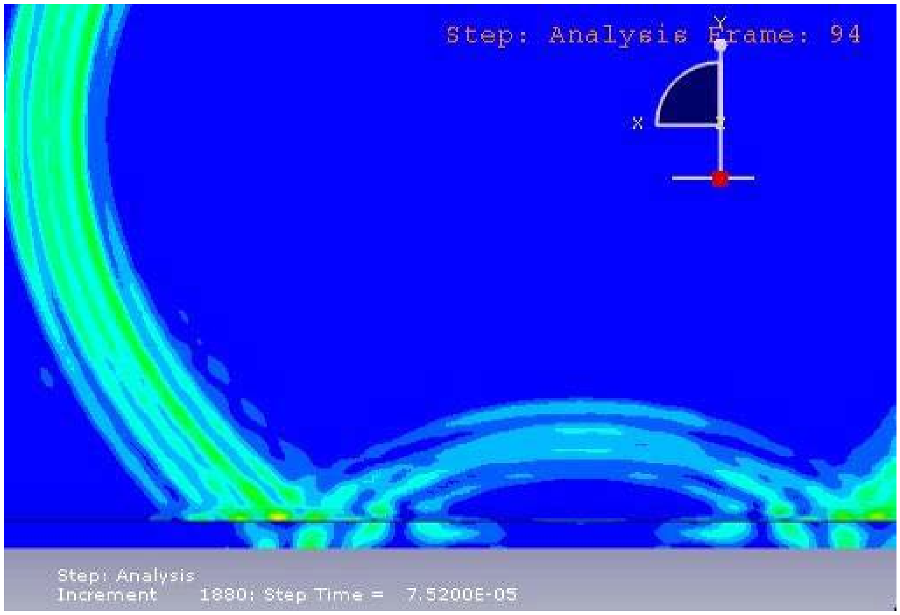

(a)

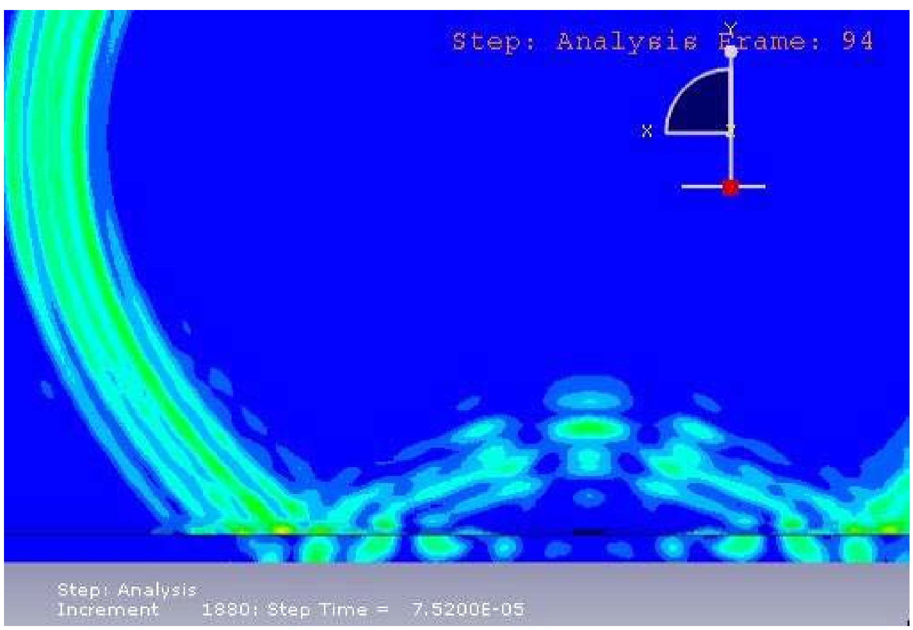

(b)

Figure 4.6 Wave scattering at the welding zone of the WTSS (a) without damage (benchmark) (b) with the introduced slot-like damage

A_5A_2 and A_5A_6 changed in different ways in comparison with their baseline signals, becoming smaller in Figure 4.7 (a) and bigger in Figure 4.7 (b), there is no doubt that the changes implied the occurrence of damage. Such changes, carrying damage information, were then used for evaluating the damage in the study.

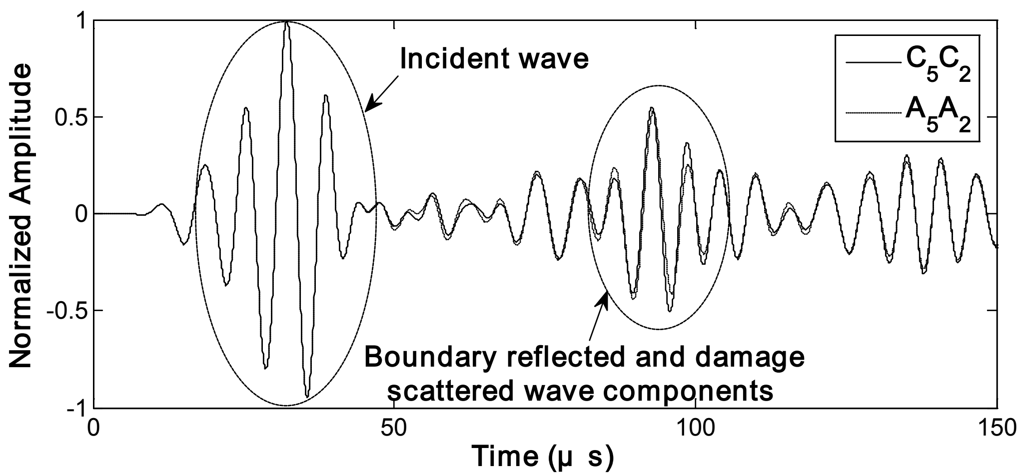

(a)

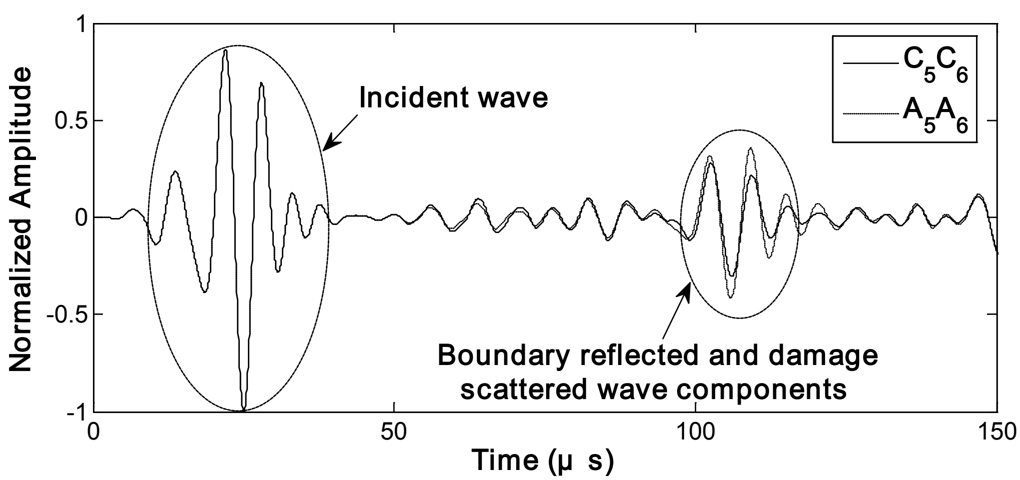

(b)

Figure 4.7 Comparison of raw signals captured in simulation via different sensing paths (a) C_5C_2 (benchmark) and A_5A_2 (damaged) (b) C_5C_6 (benchmark) and A_5A_6 (damaged)

4.3 Experiments

With the understanding of propagation characteristics of GWs in WTSS with welding damage, experiment was carried out with the purpose of identifying the welding damage.

4.3.1 Sample and Equipment

Figure 4.8 (a) shows a sample of the WTSS in Figure 4.1 (b). All the material properties and geometric dimensions, layout and nomenclature of PZT wafers in the active sensor network, as well as location and dimension of the welding damage were remained unchanged as those in the above simulation. To introduce the welding damage, the welding defect, measuring about 12 mm × 1 mm × 10 mm, was introduced by keeping corresponding location intact during the welding procedure, as shown in Figure 4.8 (b). Twelve PZT wafers, with their detailed properties listed in Table 4.2, configured the active sensor network. The sample was supported along two free edges of Facet *B* on a TMC® testing table. Shielded wires and standard BNC connectors were used with the aim of reducing mutual interference. The excitation signal, three-cycle Hanning-window-modulated sinusoid tonebursts at selected central frequencies, were generated in MATLAB® and downloaded to an arbitrary waveform generator (HIOKI® 7075) in which D/A conversion was performed. Subsequently, the analog signal was amplified by an amplifier (PiezoSys® EPA-104) to 80 $V_{p\text{-}p}$ which was then applied on each PZT wafer in turn to activate the GWs. When a PZT wafer was activated, the rest served as sensors to monitor the propagation of GWs in WTSS using an oscilloscope (HP® Infinium 54810A) at a sampling rate of 10 MHz.

(a)

(b)

Figure 4.8 (a) Global view of the WTSS sample with emphasis on active PZT sensor network on facet A (b) zoomed-in part containing simulated welding damage

Table 4.2 Mechanical and electrical properties of the PZT wafer used in experiment

Geometry	φ: 6.9 mm, thickness: 0.5 mm
Density	7.80 g/cm^3
Poisson's ratio	0.31
Charge constant, d_{31}	-170×10^{-12} m/V
Charge constant, d_{33}	450×10^{-12} m/V
Relative dielectric	1280
Dielectric permittivity, P_0	8.85×10^{-12} F/m
Elastic constant, E	72.5 GPa

4.3.2 Excitation Frequency and Wave Velocity

In terms of the dispersive properties of GWs in steel [109], the excitation frequency of GW must be small enough in order to avoid emergence of higher-order GW modes which complicate the signal appearance and make it hard to extract signal features. In the contrast, excitation of excessively low frequencies brings on very large wavelength and accordingly low time resolution of signal, and as a result the sensitivity of the wave to damage was reduced. Towards this concern, a sweep frequency test was conducted to investigate the performance of excitations at a frequency range from 80 to 250 kHz with a step of 5 kHz. It was found that the amplitude of wave signals was too small to be distinguished from background noise when excitation frequencies were lower than 120 kHz. Balancing the observability and handleability of the collected signals, three-cycle

Hanning-window-modulated sinusoid tonebursts at 150 kHz, 175 kHz and 200 kHz were utilized as excitations in both experiment and simulations.

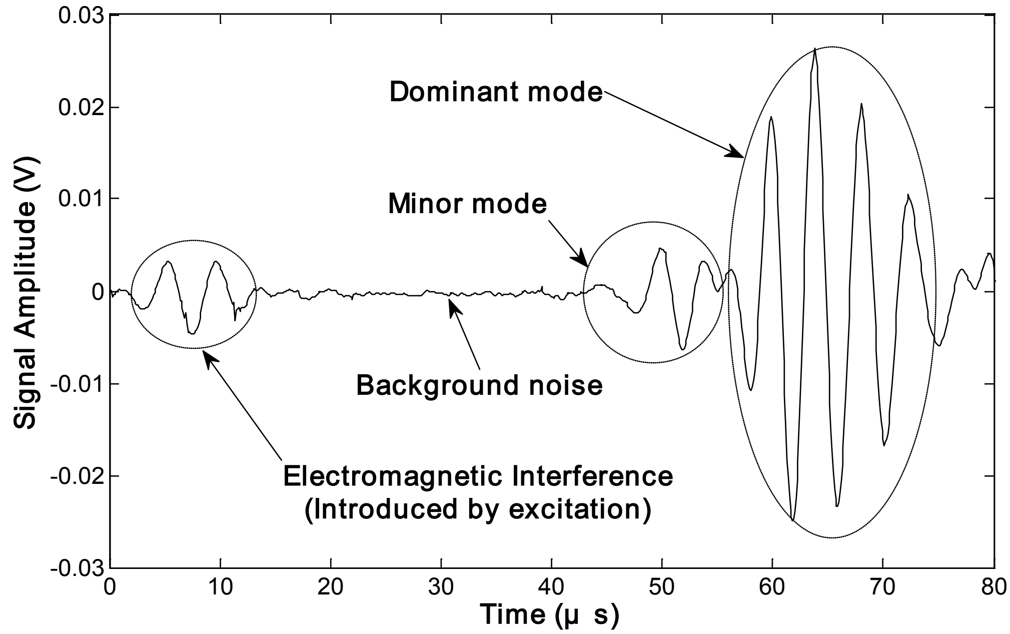

Figure 4.9 A typical raw signal from sensing path C_4C_5 in preparatory test

In preparatory test the wave components scattered by damage were often observed to overlap those reflected from boundaries of the WTSS, because the damage locates near physical edges of WTSS. At the same time, different wave modes existed in all captured signals. Though stimulated using excitations at carefully selected frequencies of 150 kHz, 175 kHz and 200 kHz so as to avoid interference from multiple modes in a GW signal, interaction of multiple wave modes was unavoidable. Therefore, it’s difficult to distinguish clearly different wave components in captured GW signals. Thanks to the relatively great magnitude, the dominant modes, amentioned transverse modes, in signals could be isolated from other signal components, like one example shown in Figure 4.9. Through the preparatory test results, velocity of the dominant GW mode in the sample, V_d, was calculated as about 2950 m/s.

4.3.3 Experiment and Signal Processing

Experiments were conducted according to the configuration introduced above. The same procedure was repeated with excitations of different central frequencies. As observed in both finite element simulation and experiment, captured GW signals in WTSS are often complex in appearance, posing difficulty in damage identification. A series of signal processing was applied, including signal pre-processing (averaging), CWT and HT, with the aim of de-noising and feature highlighting. Furthermore, in order to avoid extra influence of opposite-boundary reflections and circumferential transmission on signal interpretation, only the first few packages of each GW signal were taken into account. Such truncation was applied to each collected signal, ensuring the absence of those unwanted wave components.

4.4 Identification of Welding Damage in WTSS

4.4.1 Traditional ToF-based Methods

Damage-scattered GW components carry damage information, which, upon a series of signal processing, can be used for identifying damage. In many studies [23, 42, 68], a signal feature, ToF, is often used to triangulate damage. The difference in ToFs, defined as the time lag between the incident wave that the sensor first captures and the wave scattered by damage that the same sensor subsequently captures, substantially suggests the relative positions among the actuator, sensor and damage. From such difference in the ToFs extracted from a certain number of signals, damage can accordingly be triangulated. To brief its principle, consider a two-dimensional (2D) plate with a sensing path, as shown in Figure 4.10 (a), one can obtain the following equation

$$\Delta t = t_{A-D-S} - t_{A-S} = \left(\frac{D_{A-D} + D_{D-S}}{V}\right) - \frac{D_{A-S}}{V}, \tag{4.1}$$

where

$$D_{A-D} = \sqrt{(x_D - x_A)^2 + (y_D - y_A)^2},\ D_{D-S} = \sqrt{(x_S - x_D)^2 + (y_S - y_D)^2},$$

$$D_{A-S} = \sqrt{(x_S - x_A)^2 + (y_S - y_A)^2},$$

In the above equation, t_{A-D-S} is the ToF of the incident wave propagating from the actuator to the damage and then to the sensor, and t_{A-S} is the ToF of the incident wave propagating directly from the actuator to the sensor. Δt is the difference between the above two ToFs, which can be extracted from the captured GW signal. D_{A-D} is the distance between the actuator located at (x_A, y_A), and the damage centre, presumed at (x_D, y_D) and to be determined; D_{D-S} is the distance between the damage centre and the sensor located at (x_S, y_S); D_{A-S} is the distance between the actuator and sensor. V is the group velocity of the incident GW activated by the actuator and the GW scattered by the damage. Theoretically, the solutions to Equation (4.1) configure a locus, a dotted line in Figure 4.10 (a), indicating possible locations of the centre of the damage. With ToF extracted from another sensing path, an equation similar to Equation (4.1) can be obtained, and a nonlinear equation group, containing two equations contributed by two

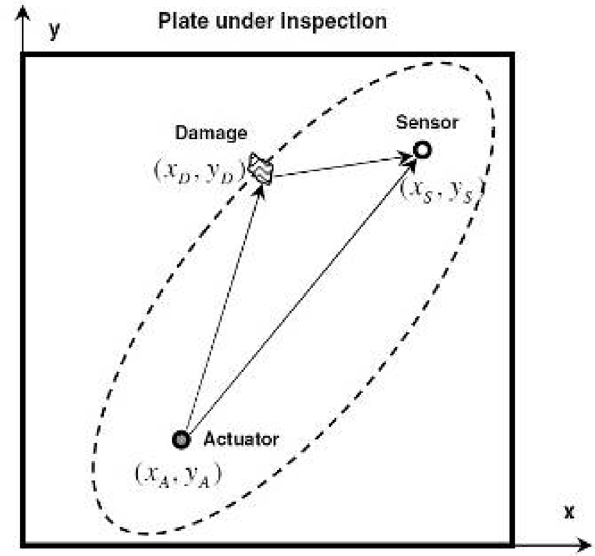

(a)

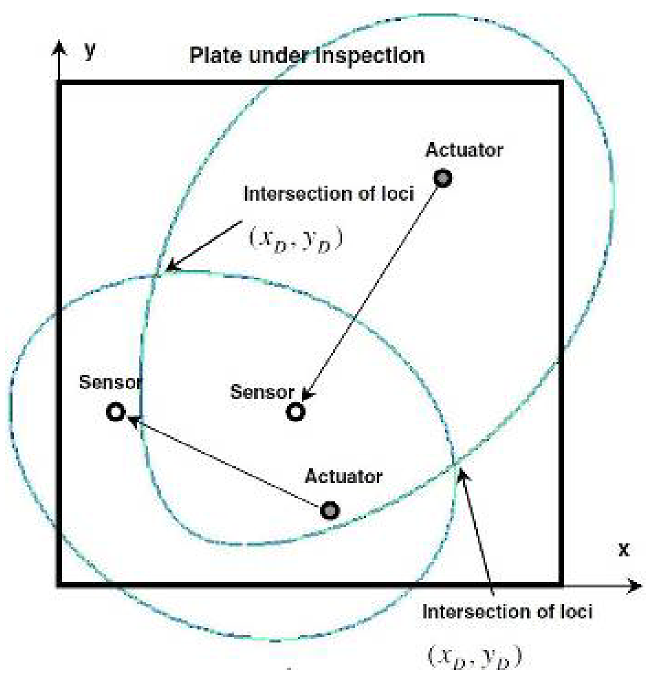

(b)

Figure 4.10 ToF-based triangulation of damage in a 2D plate with two sensing paths (a) locus established by one sensing path (b) two loci established by two paths sensing paths and involving the position of the damage centre (x_D, y_D) (two unknown variables), is available. Two loci established by the two equations lead to intersection(s), *i.e.*, the solution(s) to the equation group, sketched in Figure 4.10 (b), which is (are) the location of the damage centre (x_D, y_D).

However it is envisaged that, because of the complex superposition of various wave components in the WTSS amentioned and allowing for measurement noise/uncertainties under demanding operational conditions, it is highly impossible to exactly locate damage based on the above-addressed procedure.

4.4.2 ToMD and DPP-based damage imaging

In recognition of the fact that that Facets *A* and *C* of the sample are entirely symmetrical regarding the symmetry plane not only in geometry but also in active sensor network configuration, as shown in Figure 4.1 (b), differences, if any, between captured GW signals from corresponding sensing paths of two facets can be fully attributed to the damage. For convenience of discussion, $P_{m,n}$ ($m, n = 1, 2, ...6, m \neq n$) hereinafter stands for arbitrary sensing path pair consisting of sensing path A_mA_n and its corresponding benchmark counterpart C_mC_n. For a given $P_{m,n}$, two raw GW signals were captured (one via C_mC_n and the other via A_mA_n). After applying averaging and CWT to raw signals, as described before, HT was subsequently employed to obtain envelop of the difference signal to highlight features of such signal in the time domain, *i.e.*, amplitude peaks and their corresponding arrival times. In the envelop of the difference signal, the arrival time of local amplitude maximum was termed ToMD in regard to $P_{m,n}$, denoted by $ToMD_{m,n}$

in what follows. Representatively, $ToMD_{m,n}$ extracted from raw signals experimentally captured via $P_{2,3}$ (*i.e.*, $ToMD_{2,3}$) is shown in Figure 4.11.

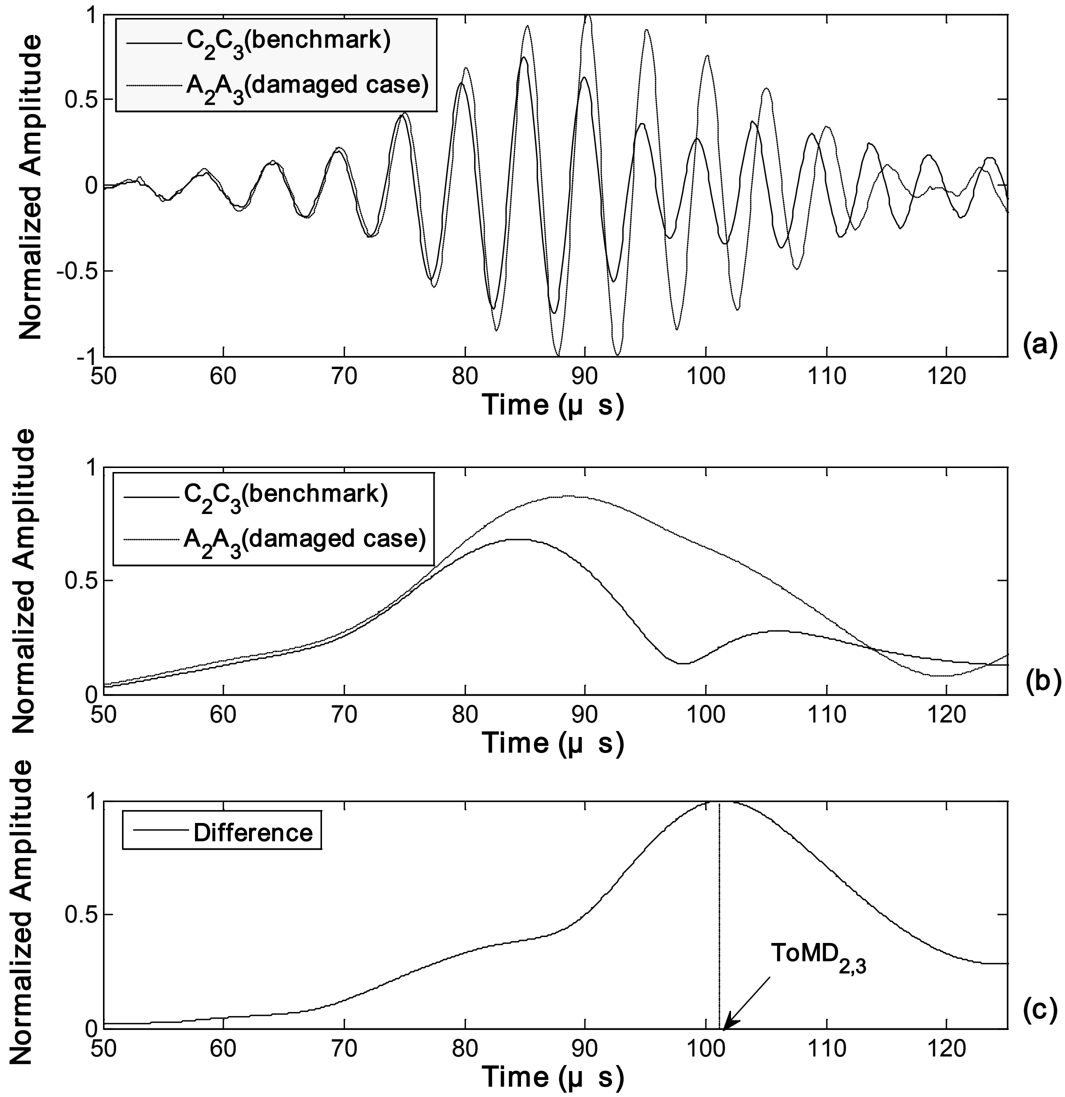

Figure 4.11 Normalized signals for sensing path $P_{2,3}$ at excitation of 150 kHz (a) raw signals (b) envelope of corresponding CWT coefficients (c) envelope of the difference of signals

Instead of exactly locating the damage, this study focused on DPPs at all locations of the WTSS. The following imaging algorithm was developed to calculate DPP value(s) for arbitrary location(s) of the WTSS and firstly applied to Facet *A*. Without loss of generality, supposing that Facet *A* was meshed virtually using *K* grids (*e.g.*, 1x1 mm^2 each in following), the distance from a certain grid L_j ($j=1,2,...K$) to PZT wafer A_m can be expressed as $D_{m,j}=\left|\overline{r_m}-\overline{r_j}\right|$ where $\overline{r_m}$ and $\vec{r_j}$ are location vectors of A_m and L_j in the global coordinate system, as shown in Figure 4.12. The time needed for GWs to travel along the route $A_m \rightarrow L_j \rightarrow A_n$ can then be defined as $T_{m,j,n}=(D_{m,j}+D_{n,j})/V_d$. Similar to Equation (1) in the above section, for equation

$$ToMD_{m,n}-T_{m,j,n}=0 \quad , \tag{4.2}$$

coordinates of the damage centre are two unknown variables. The solution of Equation (4.2) presented an ellipse locus with the two PZT wafers being two foci, as portrayed with a dashed-dotted line in Figure 4.12. In principle, the grids that rightly locate on this locus, i.e., their coordinates can satisfy Equation (4.2), have the highest probability of bearing damage from the prospect of the sensing path pair $P_{m,n}$ that produces such a locus. Therefore, DPP values of these grids were determined as 100%.

For grids at other locations, their coordinates can never satisfy Equation (4.2). The further these grids away from the ellipse locus, the less the probability that they bear damages. In this sense, to quantify the DPP values at such grids in relation to their locations L_j ($j=1,2,...K$) and sensing path pair $P_{m,n}$ ($m,n=1,2,...6, m\neq n$), a cumulative distribution function (CDF) [110] defined as

$$F_{m,n}(t) = \int_{-\infty}^{t} f(T'_{m,j,n}) \cdot dT'_{m,j,n} \tag{4.3}$$

was then introduced where $f(T'_{m,j,n}) = \frac{1}{\sigma_{m,n}\sqrt{2\pi}} \exp[-\frac{(T'_{m,j,n})^2}{2\sigma^2_{m,n}}]$ is the Gaussian distribution function, representing the density function of DPP. In the above equation, $T'_{m,j,n} = \left|ToMD_{m,n} - T_{m,j,n}\right|$ is a function of L_j when $ToMD_{m,n}$ is given, denoting the 'distance' between grid L_j and the ellipse locus in time domain. $\sigma_{m,n}$ is the standard variance and integral upper limit t is the value of $T'_{m,j,n}$ when m, j, n are specified. Given a $T'_{m,j,n}$, the DPP value of grid L_j regarding $P_{m,n}$ becomes

$$\mathrm{DPP}(L_j, P_{m,n}) = 1 - \left|F_{m,n}(T'_{m,j,n}) - F_{m,n}(-T'_{m,j,n})\right| \tag{4.4}$$

as exhibited in Figure 4.13.

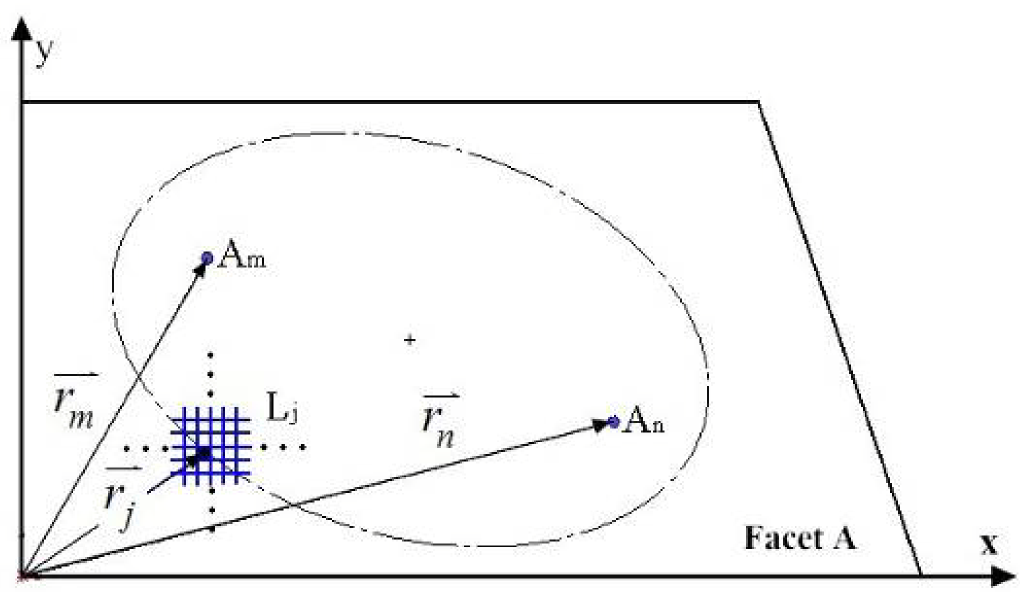

Figure 4.12 ToMD-based determination of DPP on Facet A of the WTSS

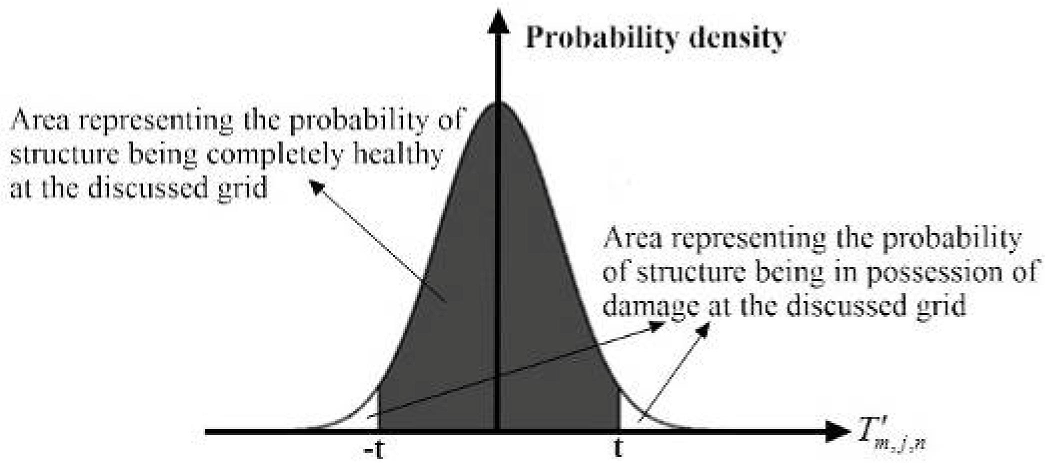

Figure 4.13 Gaussian distribution of the probability density in regard to the occurrence of damage at a specific grid of the WTSS

Applying the above algorithm to all grids on Facet A, an image for estimated values of $P_{m,n}$ involved DPP can be obtained. After extending such a process to all other facets of the WTSS, a 3D DPP image was constructed where damage was intuitionally visualized. As a typical experimental result, the DPP image contributed by $P_{2,4}$ is illustrated in Figure 4.14. In this image, DPP values vary within the range of [0, 1] (indicated by grey-scale colors shown in the color bar) with the two extremes standing for the lowest and highest DPP, i.e., 0% and 100%, respectively. Similar to some other recently developed imaging techniques for describing a damage event in engineered structures [53, 111-114], the darker the grey-scaled image appears, the greater the DPP of this grid is. However, it’s insufficient to determine the damage location from the image because all grids on central line of the darkest region are of the same DPP value. Therefore, images contributed by all the available $P_{m,n}$ in the active sensor network were fused to configure out the common estimate of the damage location.

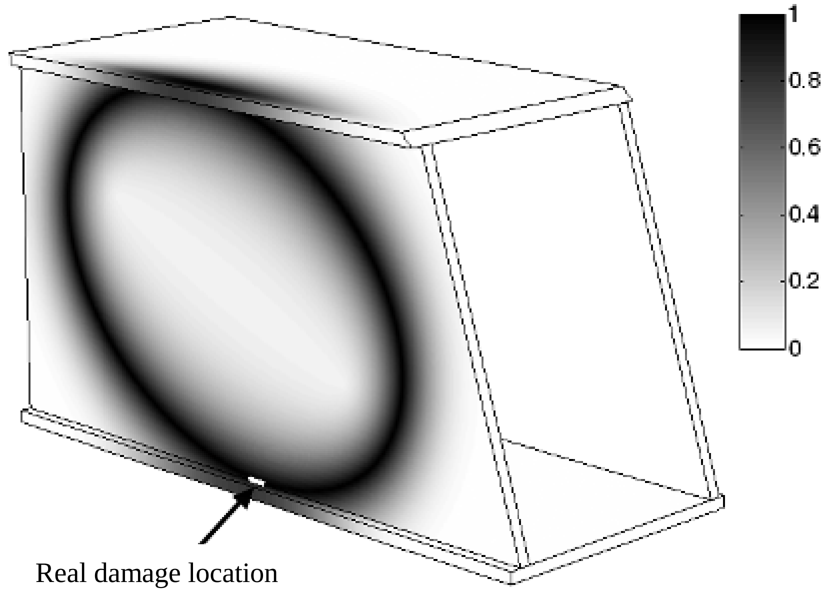

Figure 4.14 DPP image contributed by $P_{2,4}$ (from experiment)

4.4.3 Two-level Hybrid Image Fusion Scheme

To strengthen damage-associated information in final estimation result, a two-level hybrid image fusion scheme was proposed based on conjunctive and compromised image fusion techniques. For simplicity, DPP images established by all the available $P_{m,n}$ were sorted according to the wave excitation frequency (150 kHz, 175 kHz and 200 kHz), denoted by Set-150 k, Set-175 k and Set-200 k, respectively. Image fusion procedures within each image set and across sets, namely, the first and second level image fusions, were taken successively.

Table 4.3 Set P: sensing path pairs involved in the first level image fusion

(A_1A_2, C_1C_2)	(A_3A_1, C_3C_1)	(A_5A_1, C_5C_1)
(A_1A_3, C_1C_3)	(A_3A_2, C_3C_2)	(A_5A_2, C_5C_2)
(A_1A_4, C_1C_4)	(A_3A_4, C_3C_4)	(A_5A_3, C_5C_3)
(A_1A_5, C_1C_5)	(A_3A_5, C_3C_5)	(A_5A_4, C_5C_4)
(A_1A_6, C_1C_6)	(A_3A_6, C_3C_6)	(A_5A_6, C_5C_6)
(A_2A_1, C_2C_1)	(A_4A_1, C_4C_1)	(A_6A_1, C_6C_1)
(A_2A_3, C_2C_3)	(A_4A_2, C_4C_2)	(A_6A_2, C_6C_2)
(A_2A_4, C_2C_4)	(A_4A_3, C_4C_3)	(A_6A_3, C_6C_3)
(A_2A_5, C_2C_5)	(A_4A_5, C_4C_5)	(A_6A_4, C_6C_4)
(A_2A_6, C_2C_6)	(A_4A_6, C_4C_6)	(A_6A_5, C_6C_5)

Table 4.4 Estimated damage locations from two-level fusion procedure

	Case	Estimated results from simulation			Estimated results from experiment		
		Coordinates (mm)	Distance to real location (mm)	Relative error (%)	Coordinates (mm)	Distance to real location (mm)	Relative error (%)
Real damage location		(275, 0, 0)	--	--	(275, 0, 0)	--	--
First-level fusion	Conj_DPP_150 k	(276, 0, -8)	8.1	2.95%	(282, 8, 0)	10.6	3.85%
	Conj_DPP_175 k	(291, 0, -1)	16.0	5.82%	(270, 6, 0)	7.8	2.84%
	Conj_DPP_200 k	(281, 4, 0)	7.2	2.62%	(253, 10, 0)	24.2	8.80%
	Comp_DPP_150 k	(275, 0, -7)	7.0	2.55%	(282, 8, 0)	10.6	3.85%
	Comp_DPP_175 k	(291, 0, -1)	16.0	5.82%	(281, 8, 0)	10.0	3.64%
	Comp_DPP_200 k	(281, 4, 0)	7.2	2.62%	(260, 14, 0)	20.5	7.45%
Second-level fusion	Comb_DPP_S1	(280, 0, -2)	5.4	1.96%	(269, 6, 0)	8.5	3.09%
	Comb_DPP_S2	(280, 0, -2)	5.4	1.96%	(269, 6, 0)	8.5	3.09%
	Comb_DPP_S3	(278, 0, -3)	4.2	1.53%	(276, 7, 0)	7.1	2.58%
	Comb_DPP_S4	(278, 0, -3)	4.2	1.53%	(276, 7, 0)	7.1	2.58%

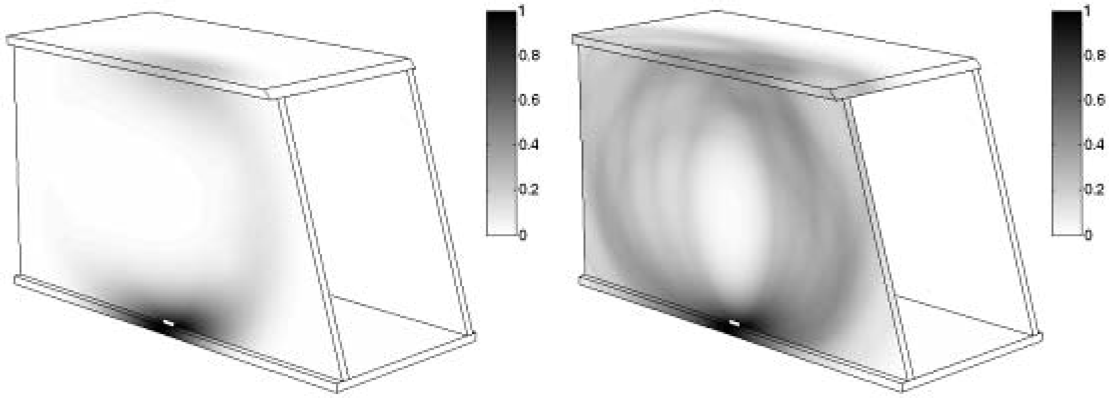

(a)

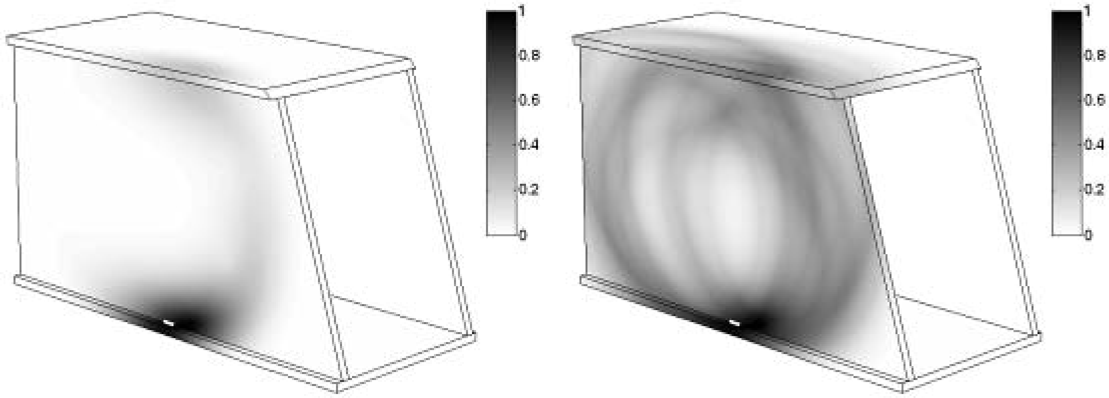

(b)

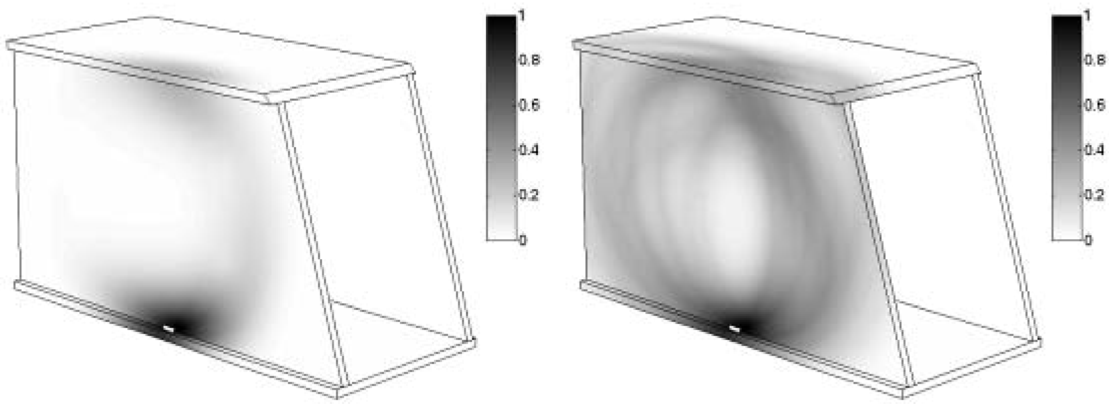

(c)

Figure 4.15 Fused DPP images based on the first level image fusion (from simulation) for (a) Set-150 k (b) Set-175 k (c) Set-200 k using conjunctive (left) and compromised (right) schemes

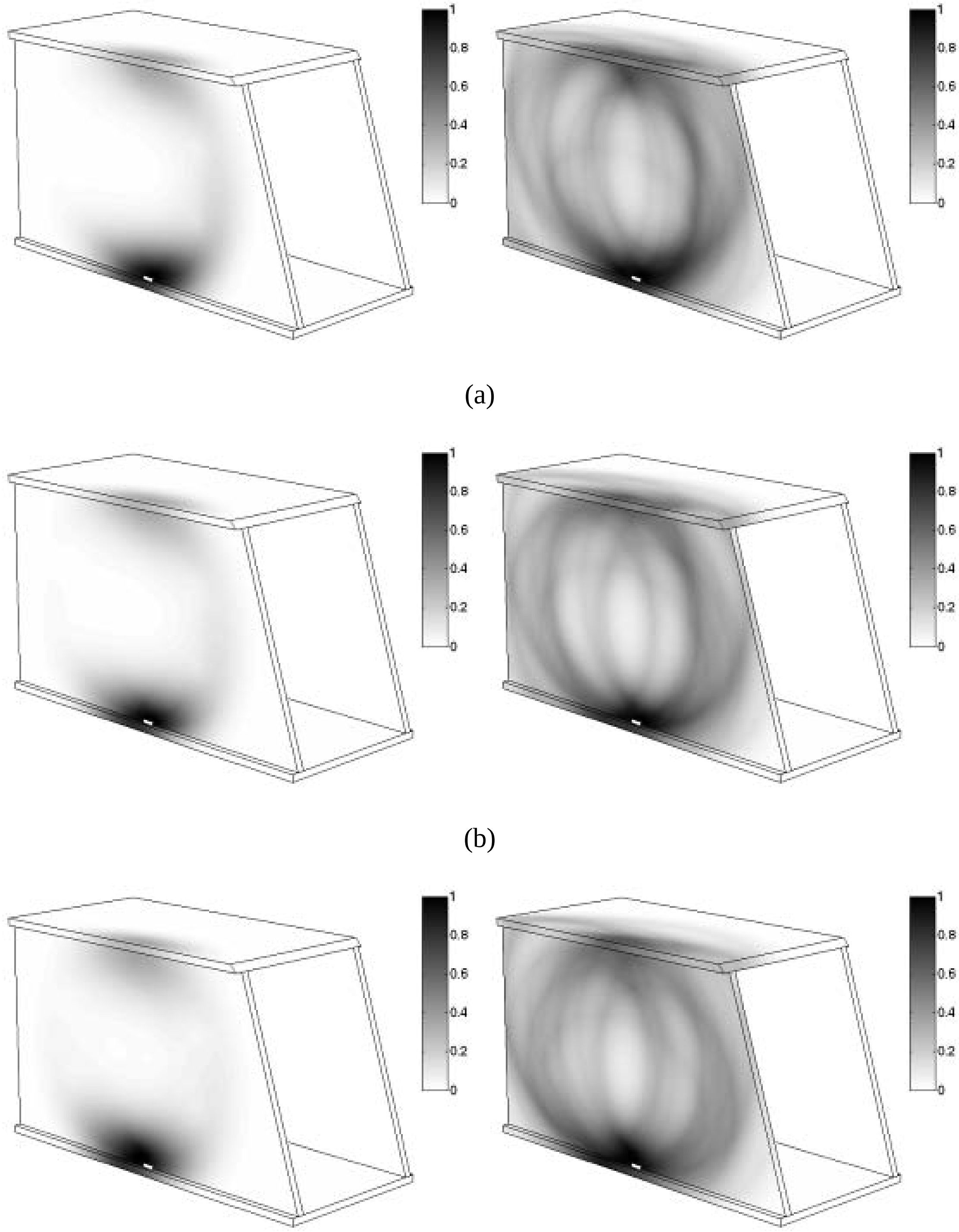

(a) (b) (c)

Figure 4.16 Fused DPP images based on the first level image fusion (from experiment) for (a) Set-150 k (b) Set-175 k (c) Set-200 k using conjunctive (left) and compromised (right) schemes

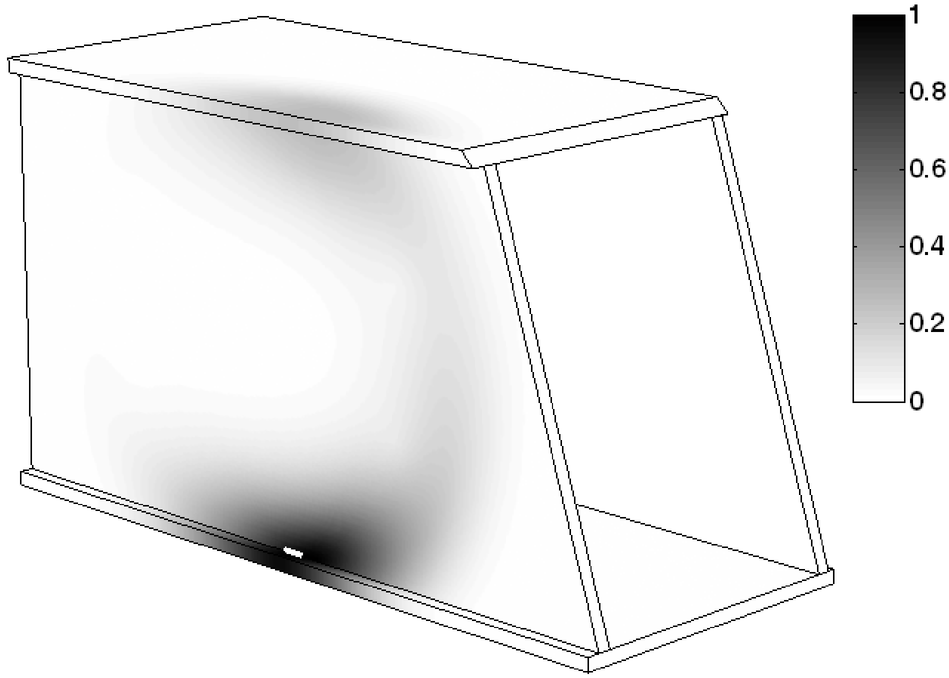

(a)

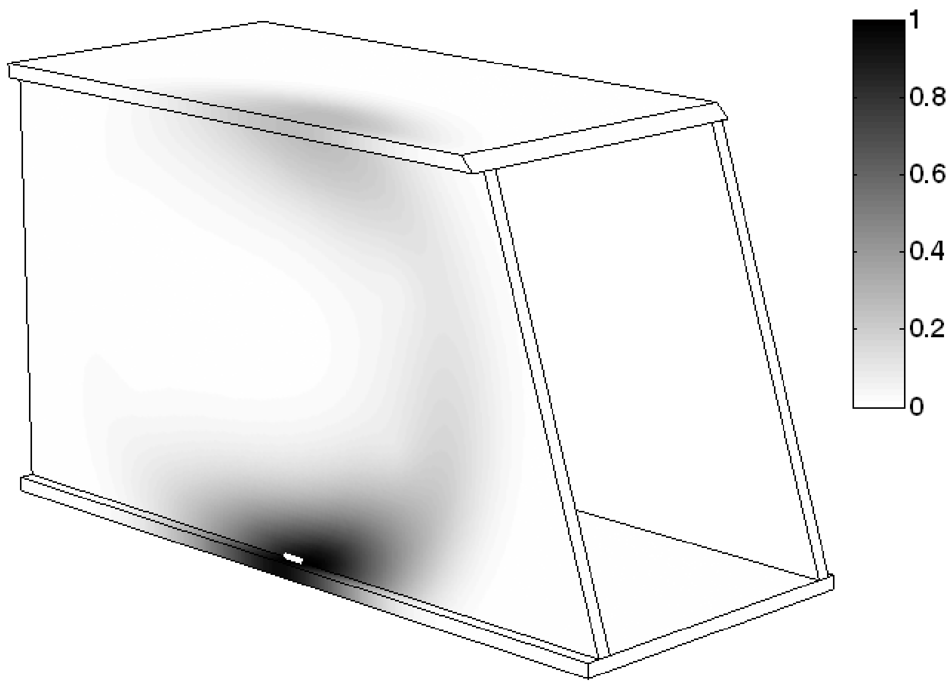

(b)

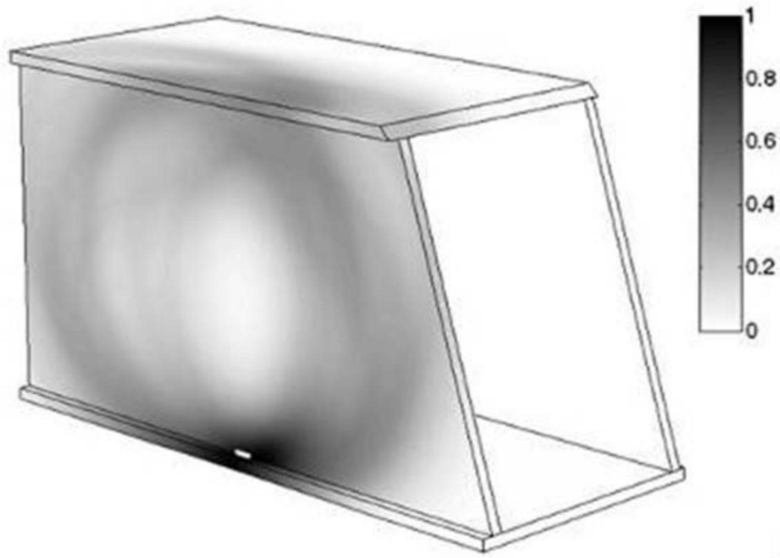

(c)

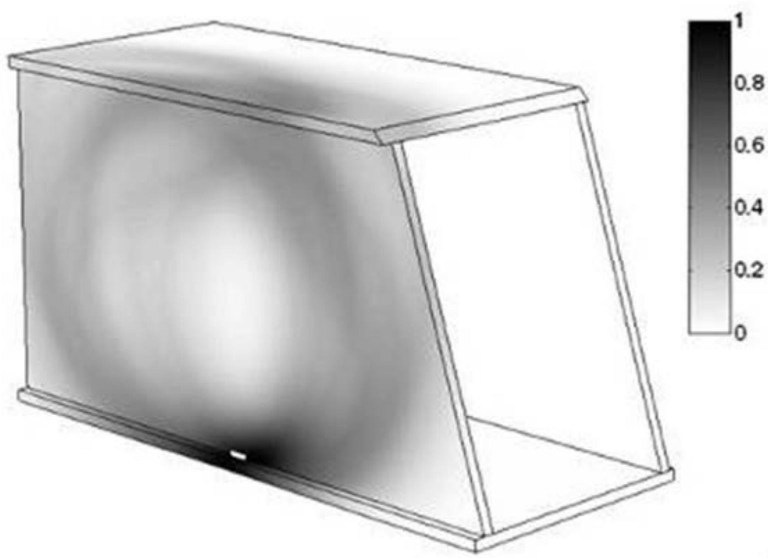

(d)

Figure 4.17 Fused DPP images based on the second level image fusion (from simulation) using (a) purely conjunctive (b) conjunctive-compromised (c) compromised-conjunctive (d) purely compromised schemes

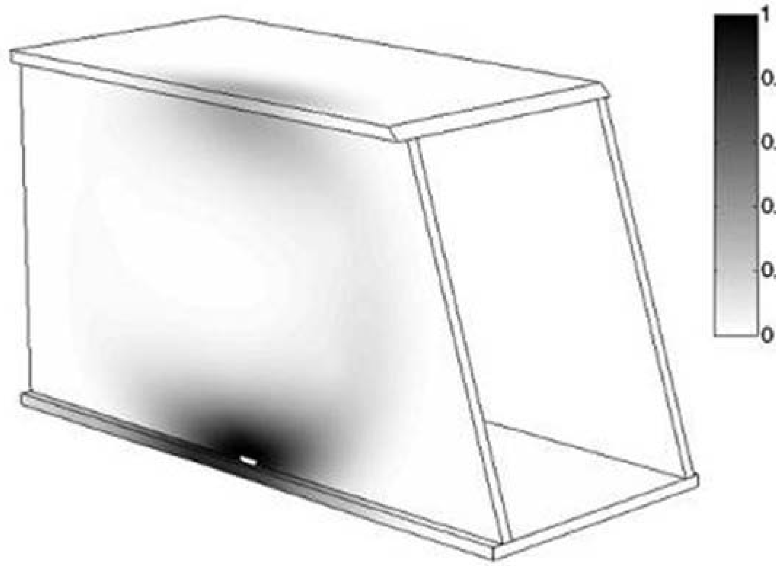

(a)

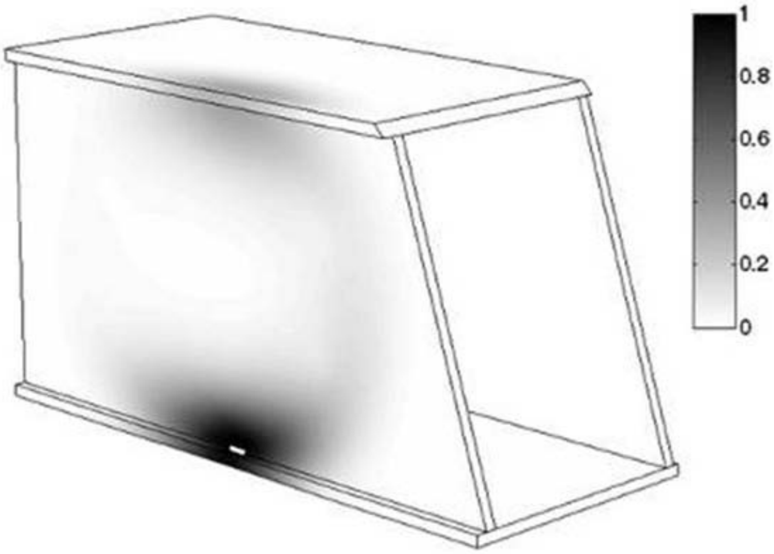

(b)

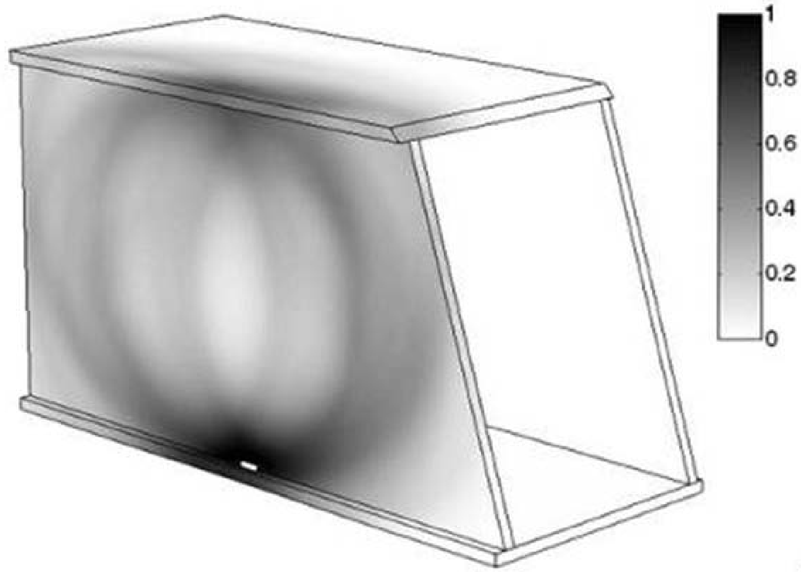

(c)

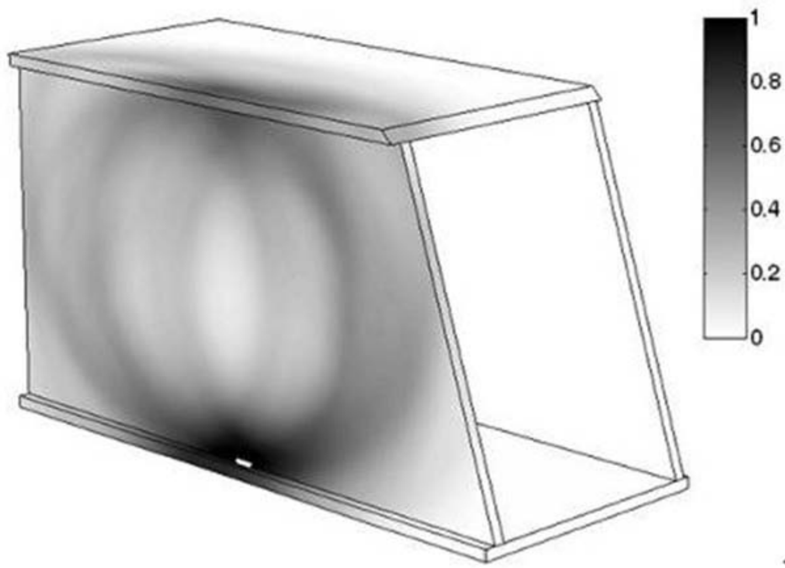

(d)

Figure 4.18 Fused DPP images based on the second level image fusion (from experiment) using (a) purely conjunctive (b) conjunctive-compromised (c) compromised-conjunctive (d) purely compromised schemes

4.4.3.1 First level fusion

Taking Set-150 k as an example, algebraic operations were applied to DPP values of all images in Set-150 k using conjunctive and compromised fusion techniques which are respectively defined as

$$Conj\_DPP\_150k(L_j, P) = \sqrt[N_P]{\prod_{m,n\in\{1,2,\ldots 6\}}^{m\neq n} DPP(L_j, P_{m,n})} \;\;,\;\; j = 1, 2, \ldots K \qquad (4.5a)$$

$$Comp\_DPP\_150k(L_j, P) = \frac{1}{N_P}\sum_{m,n\in\{1,2,\ldots 6\}}^{m\neq n} DPP(L_j, P_{m,n}) \;\;,\;\; j = 1, 2, \ldots K \qquad (4.5b)$$

where P is the set of all involved sensing path pairs, as listed in Table 4.3; N_p is the number of elements in set P and equal to 30 in this study. '*Conj_DPP_150 k*' and '*Comp_DPP_150 k*' are so-called first level fusion results for Set-150 k. Similarly, the same operation was applied to Set-175 k and Set-200 k. Figures 4.15 and 4.16 show the first level image fusion results from simulation and experiment data, respectively. In the images, the welding damage at the welding zone between Facets A and B is clearly observed. In addition, DPP values in these fused images, as well as in the following ones, were normalized in regard to the maximal DPP value of the current image, ensuring the DPP values are always in the range [0, 1].

4.4.3.2 Second level fusion

In order to enhance accuracy of the estimate result by properly employing as much useful information as possible, the second level image fusion, *i.e.*, fusion across DPP image sets for different excitation, was undertaken. Both conjunctive and compromised schemes were utilized again to combine the first level image fusion results. By applying different strategies, four joint schemes were established and expressed below:

$$Comb\_DPP\_S1 = \sqrt[3]{\prod_{Freq\in\{150k,175k,200k\}} Conj\_DPP\_Freq} \quad (4.6\text{ a})$$

$$Comb\_DPP\_S2 = \frac{1}{3}\sum_{Freq\in\{150k,175k,200k\}} Conj\_DPP\_Freq \quad (4.6\text{ b})$$

$$Comb\_DPP\_S3 = \sqrt[3]{\prod_{Freq\in\{150k,175k,200k\}} Comp\_DPP\_Freq} \quad (4.6\text{ c})$$

$$Comb\_DPP\_S4 = \frac{1}{3}\sum_{Freq\in\{150k,175k,200k\}} Comp\_DPP\_Freq \quad (4.6\text{ d})$$

where S1-S4 stand for purely conjunctive, conjunctive-compromised, compromised-conjunctive, and purely compromised schemes in turn. Figures 4.17 and 4.18 show the results of the second level image fusion from simulation and experiment data, respectively. In the images, approach of the estimated damage location to the real one, though not very obvious due to the large dimensions of the WTSS, can be found, as detailed in the next section. Meanwhile, DPP images for '*Comb_DPP_S1*' and '*Comb_DPP_S3*', as well as those for '*Comb_DPP_S2*' and '*Comb_DPP_S4*', can be found highly accordant, implying the robustness of the second level fusion.

4.4.3.3 Analysis of fusion results

Locations with highest probability of damage occurrence in Figures 4.15-4.18 were picked out and detailed in Table 4.4. The coordinate system is the same as that indicated in Figure 4.1 (b). The distances between estimated locations and the real damage position, as well as relative errors which are ratios of these distances to that between the real damage location and the origin, are also included in this table. It is found that (1) comparing with the sample dimensions, the distances between estimated locations and the real one are relatively small, implying the acceptability of the proposed approach; (2) whichever fusion schemes were adopted in the two-level fusion procedure, obvious improvement on identification accuracy can be observed when the second-level fusion is applied, validating its necessity; and (3) although not every result of the second level fusion is more accurate than those based on sole first level fusion, more convinced decision can be drawn from the two-level data fusion procedure.

4.4.4 Analysis of Error

The arithmetic of DPP stated in section 4.4.2 is sensitive to ToMD. Any factor that can affect the ToMD value may lead to error in single sensing path involved DPP image. Such error could be amplified during subsequent data fusion procedure, especially under schemes containing conjunctive operation(s) [115]. In this chapter, many factors would affect the final fusion results of experiments. Firstly, uncertainties, such as the diversity for the facets of benchmark and with damage in geometry (despite the introduced damage), variation of welding quality, etc, are almost unavoidable. Secondly, weld ends beside the induced damage enlarges the expected damage zone so that the consequent fusion results would be affected. Thirdly, the time duration of interested wave package in received signal is always longer than its original form due to intrinsic dispersion characteristic of utilized GWs. However, in virtual of the advantages of two-level data fusion, errors from different first-level fusion results are somewhat diminished. Taking all these matters into consideration, the fused results for damage location, as well as their relative errors listed in Table 4.4, are acceptable.

4.5 Identification of Dual Damages in WTSS

4.5.1 Simulation Analysis

3D finite element model of the WTSS in combination with assumed two welding damages was created using the commercial software ABAQUS®/CAE. Elements in damage zones were removed to simulate the welding damages. Similar procedure applied in analysis mentioned before was taken in this section. The crack-reflected wave signals were captured by calculating deformation at places where the sensors located.

4.5.2 Experimental Analysis

Meanwhile, with the same sample of the WTSS shown in Figure 4.1 (b) was prepared for collecting experimental signals. Except for the slot-like defect, which was introduced by keeping corresponding location intact during the welding procedure, eight through holes, measuring about ø 1.5 mm each and very close to each other, were fabricated using a drill press in workshop, as shown in Figure 4.19. The sample was supported along two free edges of Facet B on a TMC® testing table. Arbitrary waveform generator (HIOKI® 7075) and oscilloscope (HP® Infinium 54810A) functioned as excitation generation unit and signal acquisition unit, respectively.

Figure 4.19 Zoom-in view of through holes

4.5.3 Result and Discussion

Three-cycle Hanning-window-modulated sinusoid tonebursts at 150 kHz, 175 kHz and 200 kHz were utilized as excitations in both experiment and simulations according to the identical procedures as amentioned in this chapter. Simulations and experiments were conducted by taking each PZT wafer as actuator in turn, while others functioning as sensors. The same procedure was repeated with excitations of different central frequencies. Values of $ToMD_{m,n}$ $(m,n=1,2,...8, m \neq n)$ of all signals were figured out one by one and then employed in calculation of $\mathrm{DPP}(L_j, P_{m,n})|_{m,n=1,2,...8,m\neq n}^{j=1,2,...K}$. In this manner, fifty-six DPP images can be drawn from either simulations or experiments under excitation at a specific frequency. The two-level image fusion scheme was then adopted as stated above.

Results of the second level image fusion from simulation and experiment data are shown in Figure 4.20. In this image, dark areas rendering highest DPP values imply the spots that most likely contain damages. The two welding damages at the welding zones indicated by contrast colour are properly covered by corresponding dark areas simultaneously. Detailed results for damage location estimation are listed in Table 4.5. It can be found that the relative error of the estimated location in regard to the real one is very small, indicating the effectiveness of the proposed diagnostic imaging approach.

Table 4.5 Estimated damage locations from two-level fusion procedure

Case		Results from simulation				Results from experiment		
		Coordinates (mm)	Distance to real location (mm)	Relative error (%)		Coordinate s (mm)	Distance to real location (mm)	Relative error (%)
Slot-like Damage	Real location	(275, 0, 0)	--	--		(275, 0, 0)	--	--
	Estimated location	(278, 0,-1)	3.2	1.16%		(276, 0, 7)	7.1	3.09%
Through holes	Real location	(150,290,0)	--	--		(150,290,0)	--	--
	Estimated location	(152,291,0)	2.2	1.45%		(146,289,0)	4.1	2.73%

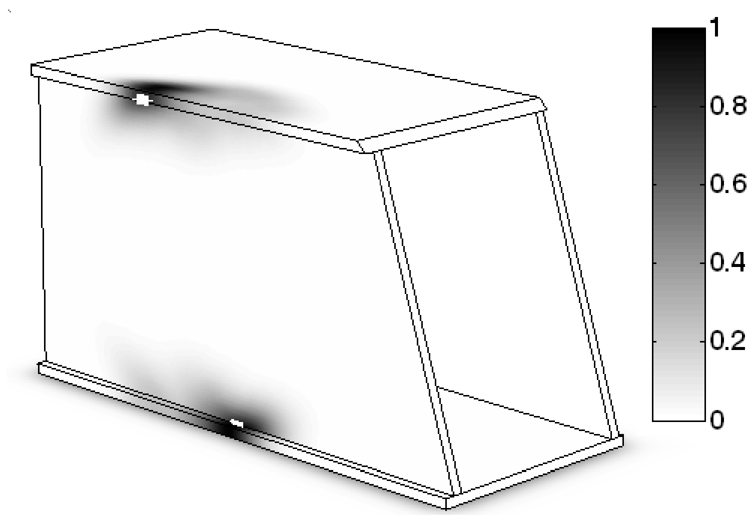

(a)

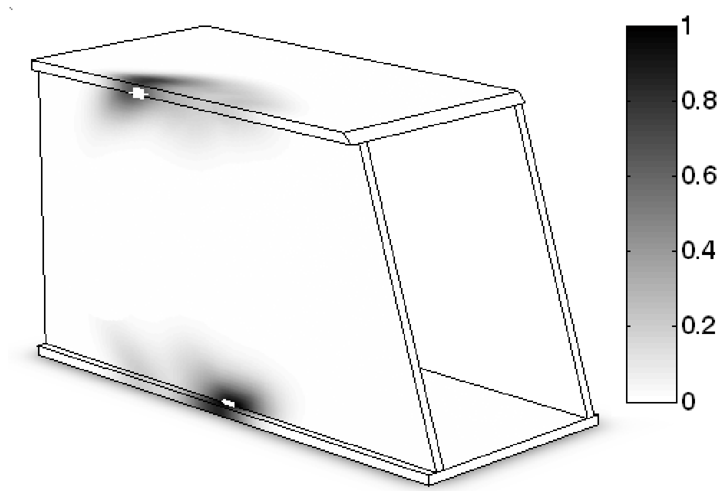

(b)

Figure 4.20 Fused DPP images based on the two-level image fusion for (a) simulation (b) experiment

4.6 Concluding Remarks

Propagation behavior of GWs in a WTSS, a true-scale model of a train bogie frame segment containing two welding damages, were investigated in this chapter. The damage-scattered wave components carrying damage information were mainly concerned. An active sensor network consisting of twelve PZT wafers was established to activate or collect GWs in the WTSS. Excitations at different frequencies were used to obtain rich signals for investigation. An imaging approach based on GW propagation and concepts, ToMD and DPP, was developed in estimation of damage presence and location. A two-level image fusion scheme was further proposed with the aim of enhancing robustness of the approach to measurement with noise and uncertainties. From results for estimation of damage location, it can be concluded that, although the damages located within the welding zones and near the original edges of the WTSS, making damage evaluation much more difficult, acceptable estimation results of damage location can still be gained by applying the proposed imaging approach and the first level image fusion. Additional improvements in consistency and accuracy of the damage evaluation results were achieved when the second level fusion was performed. In one word, acceptable visualized evaluation of two slot-like damages in the welding zones of a WTSS was accomplished using an approach combining GW propagation based imaging and two-level image fusion procedure, indicating the effectiveness of the recommended approach in evaluating presence and location of such welding damages in WTSSs and its large potential for real-time SHM of WTSSs.

CHAPTER 5 Fatigue Crack Detection in Steel Plates Using GWs and an Energy-Based Imaging Approach

5.1 Introduction

In the previous chapters the possibility of GWs applied for damage detection in plate-like structures and complicated structures was investigated. However, the GW-SHM methodology for real damage detection in engineering structures is a task to be achieved. The aim of this chapter was to demonstrate the application of a probability-based imaging approach based on GWs for detecting fatigue cracks and load effects, while eliminating the effect of adjacent notch. This chapter is organized as follows. The first section describes how a fatigue crack was introduced into a thick steel plate with multiple boundaries due to two supporting holes and a notch. GWs generated by an active PZT transducer network were then combined with an imaging approach with the aid of the RTD/fs concepts to estimate the presence and location of the fatigue crack. The following section of the chapter then describes a series of tensile tests and compressive tests employed to assess the different load effects of the fatigue crack. The experimental results were validated by FEM analysis. At last the chapter concludes with a brief summary of the findings made and a discussion of their implications.

5.2 GW Generation Using a PZT Sensor Network

5.2.1 Thick Steel Specimen

As shown in Figure 5.1, the steel plate investigated was 555 mm × 200 mm in size and 10 mm in thickness, and was designed according to previous chapters. The detailed material properties of the specimen are reported in Table 5.1. Considering that most fatigue cracks in this kind of structure are initiated and propagated from edges between adjacent facets, an artificial notch of 20 mm long and 5 mm wide was induced on one longer edge of the specimen to initiate a fatigue crack. Two 26-mm-diameter holes were drilled in the top and bottom close to the notched side of the plate to facilitate clamping in the fatigue machine.

Table 5.1 Material properties of the steel plate

Density	7.85 g/cm^3
Poisson's ratio	0.28
Elastic constant, E	210 GPa

Figure 5.1 Specimen used in experiments

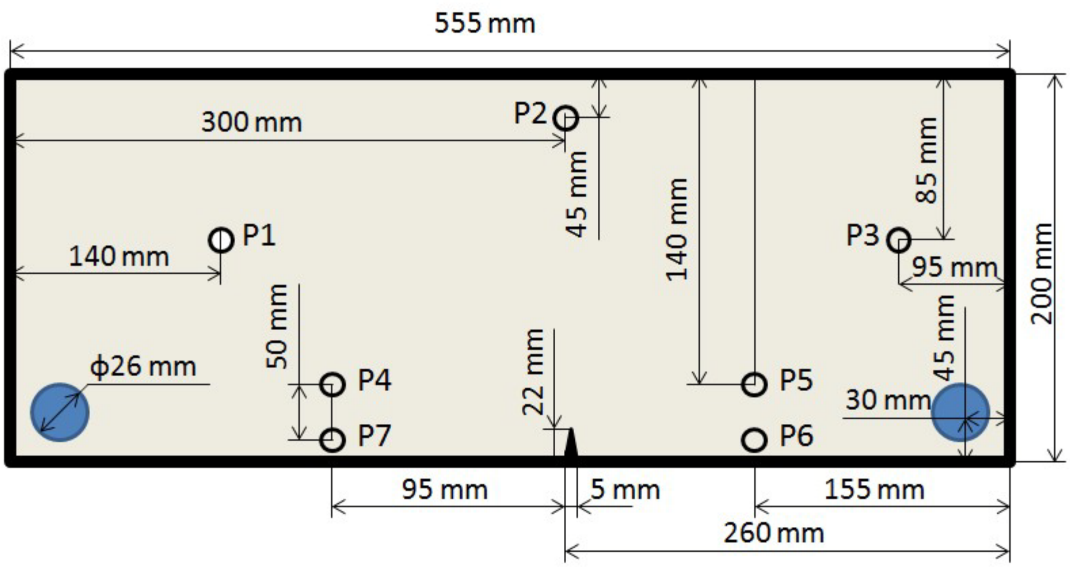

Figure 5.2 Layout of PZT sensor network

5.2.2 PZT Sensor Network

Seven circular PZT transducers with the identical dimensions of 6.9 mm in diameter and 0.5 mm in thickness were surface-mounted onto the plate to function as an active sensor network. Each PZT transducer which was the same as used in chapter 4 with the properties shown in Table 4.2 could function as either an actuator or a sensor according to the layout illustrated in detail in Figure 5.2. The reason for installing this kind of sensor network is to generate an available and isolated wave component and negate the effect of intricate boundaries.

5.2.3 Generation of GWs

The excitation frequency of GWs should be restricted to within a low range according to the dispersive properties of GWs in steel and to avoid the emergence of higher order GW modes which complicate the signal representation and make it hard to extract signal features. However, low frequencies result in comparatively long wavelengths and accordingly low time resolutions for signals. The PZT actuators were excited at a central frequency of 150 kHz by a series of burst signals comprising five cycles of sine waves with the Hanning window envelope in the course of our experiments. The excitation signals were generated in MATLAB® and downloaded to an arbitrary waveform generator (HIOKI® 7075) in which D/A conversion was performed. An amplifier (PiezoSys® EPA-104) was then used to amplify the analog signal to 80 $V_{p\text{-}p}$, which was then applied to each PZT wafer in turn to activate the GWs. When one of the PZT transducers was activated, the rest of them served as sensors to monitor the propagation of GWs in the steel plate using an oscilloscope (HP® Infinium 54810A) at a sampling rate of 10 MHz.

It is clear that multiple wave modes cannot be avoided in captured signals although the excitation frequency was strictly restricted to 150 kHz due to the multiple boundaries of the plate. Moreover, the wave packages scattered by the fatigue crack were likely to overlap with those reflected from boundaries because the crack was located particularly close to the physical edges of the plate and to the notch. Based on these conditions, the key points in defining the location of the fatigue crack were a suitable sensor network, an outstanding dominant wave component and a useful set of signal post-processing methods.

5.3 Fatigue Experiment and Fatigue Crack Identification

5.3.1 Fatigue Test

The steel plate described above was clamped in a 100 kN MTS fatigue-testing machine in the force-controlled mode via an MTS load unit controller (as shown in Figure 5.1). The shorter edges of the plate were symmetrically clamped by inserting two wedges through the two holes. The fatigue test was undertaken through a series of tension-tension tests designed to initiate and grow a crack along the notch. A dynamic cyclic loading of 5-50 kN was employed in the fatigue test. A fatigue crack formed by creating an initial notch before cyclically loading the plate was then introduced to the specimen. The length of the fatigue crack after the fatigue test was 15 mm. The crack was located along the sharp angle of the notch and was parallel to the shorter edges of the plate. A zoom view of the fatigue crack resulting from this fatigue test is shown in Figure 5.3.

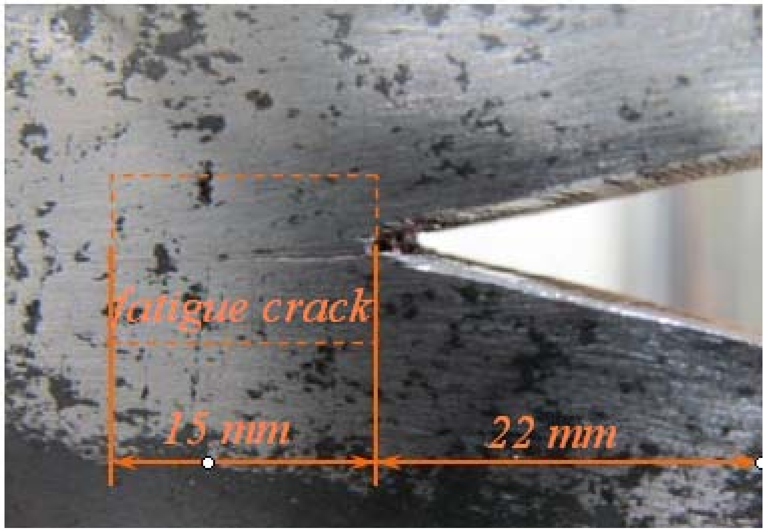

Figure 5.3 Zoom view of fatigue crack introduced

5.3.2 Fatigue Crack Identification

5.3.2.1 Wavelet transform-based signal processing

In comparison with other GW transducers, PZT transducers can serve as both actuators and sensors, and their portability enables them to be permanently mounted onto the structure to facilitate automated online SHM through an appropriate sensor network. However, PZTs generally excite multi-mode GWs simultaneously, after which the waves reflected, transmitted or converted at the boundaries cause damage, thus producing complicated wave signals. In addition to the diverse forms of interference caused by materials and natural vibration, fatigue cracks make it more difficult to detect damage due to the characteristics of fatigue failure. In light of the above complications, appropriate high-grade signal processing methods must be applied to discriminate between wave signals and extract wave characteristics. Using advanced signal processing algorithms that have now become prevalent, wavelet transform (WT) technology including a discontinuous wavelet transform (DWT) and a CWT was applied to process the signals obtained in this chapter. Wavelet analysis can be used to transfer GW signals from the time domain to the time-frequency domain. In numerical analysis and functional analysis, a DWT is any wavelet transform for which the wavelets are discretely sampled. As with other wavelet transforms, one of its key advantages over Fourier transforms lies in temporal resolution: it captures both frequency and location information (location in time). In this study, the DWT defined by Equations (5.1) and (5.2) was adopted for signal coding to represent a discrete signal in a more redundant form as a precondition for data compression [116]:

$$x_q(t) = \sum_{-\infty}^{+\infty} a_k \psi_{q,w}(t) \tag{5.1}$$

$$\psi_{q,w}(t) = 2^{q/2} \psi(2^q t - w), \tag{5.2}$$

where *q*, *w* and a_k are the dyadic time-scale integers and wavelet amplitudes. The aims of the DWT procedure were to decompose and rebuild the signals using the Mallat algorithm at different levels of frequency for multi-resolution analysis and to reduce the number of redundant coefficients of equal magnitude.

A CWT has the ability to construct a time-frequency representation of a signal that offers very good time and frequency localization, which is then used to divide a continuous-time function into wavelets. In mathematical terms, the CWT of a continuous, square-integrable function *x(t)* of scale $a > 0$ is expressed by the following integral.

$$WT_x(a,b) = \frac{1}{\sqrt{a}} \int_{-\infty}^{+\infty} x(t) \psi^* \left(\frac{t-b}{a} \right) dt = < x(t), \psi_{ab}(t) >, \tag{5.3}$$

where a, b, $\psi(t)$ and $\psi^*(\bullet)$ are the scale parameter, translation parameter, mother wavelet function and complex conjugate of $\psi(\bullet)$, respectively. To obtain the energy distribution of a sample signal, we integrate Equation (5.3) as shown by Equation (5.4) [76]:

$$E = C \int_{-\infty}^{+\infty} \int_{-\infty}^{+\infty} \left| WT_x(a,b) \right|^2 \frac{da \cdot db}{a^2}, \tag{5.4}$$

where the wavelet coefficients stand for the energy density of the relevant signal in the time-frequency domain [41, 116].

According to the principles of WT, the scale representative in the WT is proportional to its reciprocal as a substitute for frequency. Thus, after transformation, each previous scale in terms of the time domain bears an equivalence to homologous frequencies in the time-frequency domain. As a result, signal differences due to reflections from a fatigue crack pertaining to an induced notch can be isolated in a specific sub-domain. The fatigue crack can be separated from the signal rebuilt in the sub-domain corresponding to the excitation frequency via the DWT with a combination of wave energy distributions based on the CWT by extracting the *RTD/fs*.

5.3.2.2 Extraction of RTD/f

A typical signal obtained in the course of the experiment by the actuator-sensing path $P_{1,2}$ (no. 1 as the actuator and no. 2 as the sensor) in the time domain before and after initiating the fatigue crack is illustrated in Figure 5.4. Identifying the fatigue crack in the plate purely on the basis of these original signals would have been extremely difficult. Thus, to obtain information that would be useful for detecting the fatigue crack, the raw signals were decomposed into multiple frequency segments using the DWT procedure, and the corresponding level including the excited frequency of 150 kHz was selected, with outside noises from other frequency bands being filtered out. The purified signals were then transformed into CWT coefficients in the time domain using the CWT procedure. To obtain and extract signal characteristics for fatigue crack detection, it is better to enhance the signals of waves scattering from the fatigue crack and concentrate the information they convey into a narrow band of the excited frequency. Thus, the energy distribution based on the wavelet coefficients was integrated along the scale axis. In comparison with the raw signals shown in Figure 5.4, Figure 5.5 shows that the different levels of wave energy induced by the fatigue crack could be observed clearly in the wavelet-reconstructed signals. A similar phenomenon can also be seen from the wavelet coefficient distribution in the time domain constructed through the CWT analysis as shown in Figure 5.6. The changes in wave energy represent the early waves scattered by the fatigue crack rather than those scattered by the initial notch. As shown in Figure 5.7, the energy profile in the time domain was obtained after integrating the CWT coefficients along the scale axis according to Equation (5.4). These energy distribution coefficients were then purified with low pass filters to obtain the slick wave

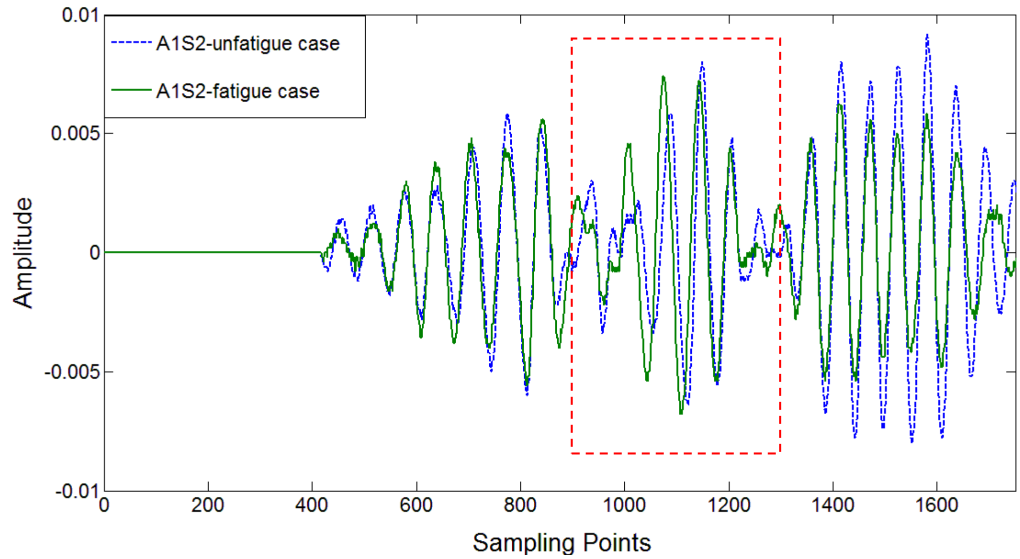

(a)

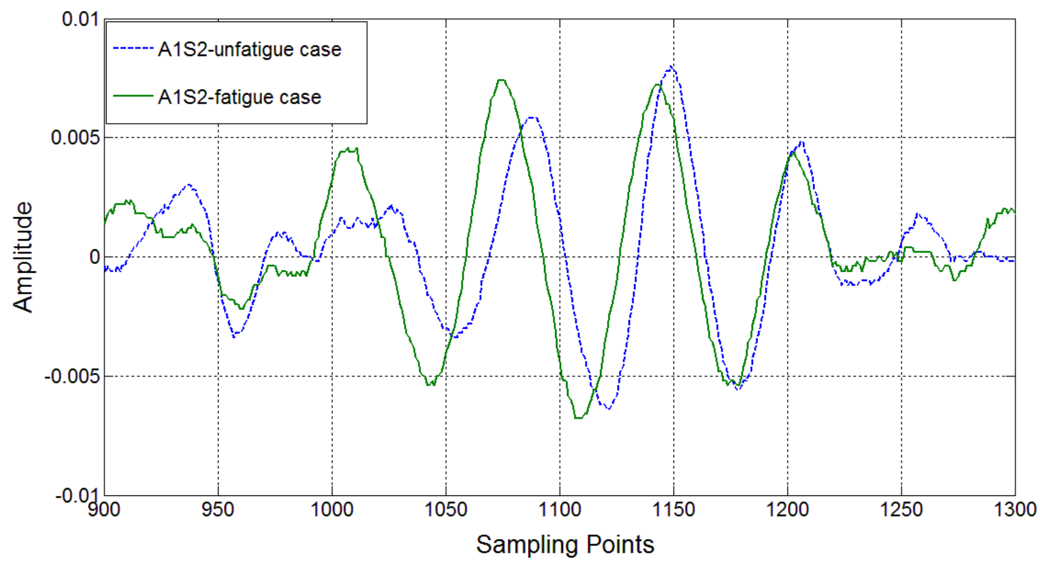

(b)

Figure 5.4 Original signal derived from $P_{1,2}$ (a) Boundary reflected and damage(notch/notch+fatigue crack) scattered wave components (b) zoom view of wave components including fatigue information signal shown in Figure 5.8. The difference between the signals emitted by the non-fatigue plate and those scattered by the fatigued plate then became perceptible and was clearly discerned.

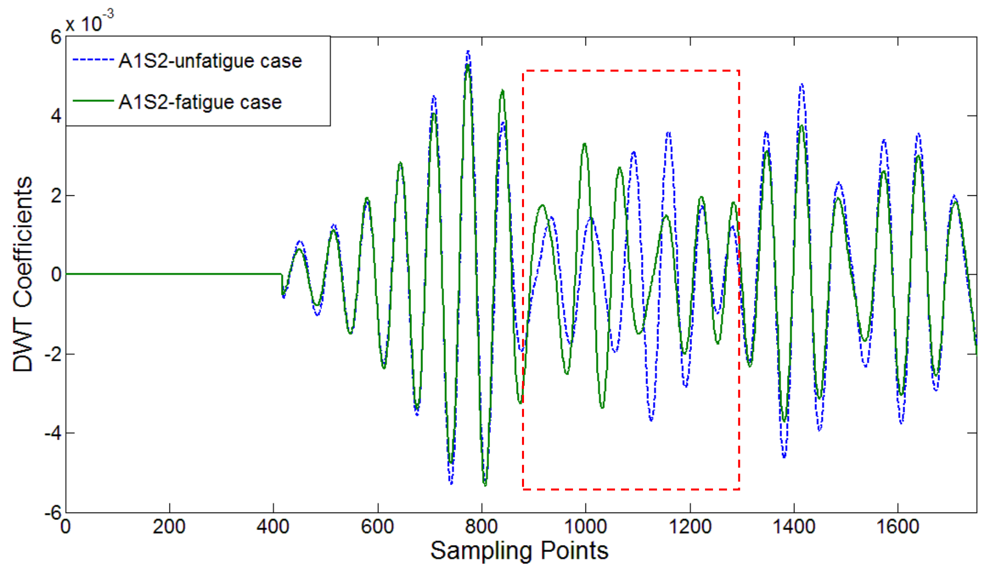

(a)

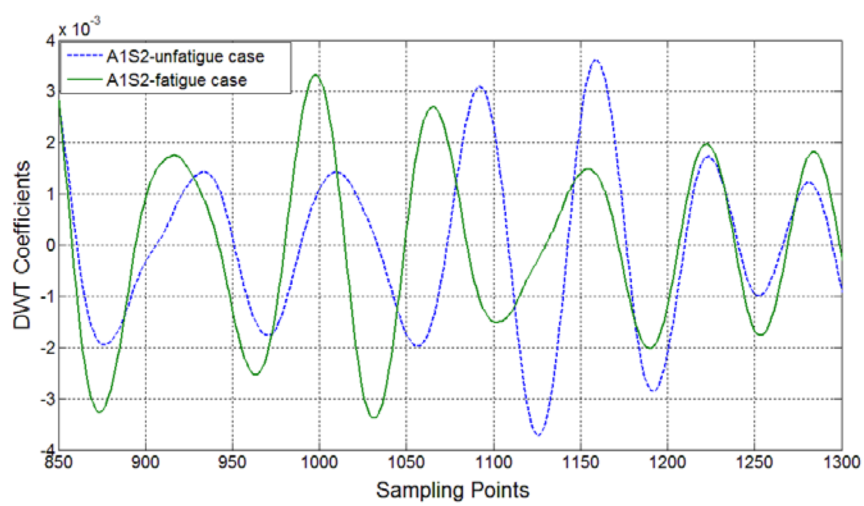

(b)

Figure 5.5 Signal compression result of signal from $P_{1,2}$ (a) Boundary reflected and damage(notch/notch+fatigue crack) scattered wave components (b) zoom view of wave components including fatigue information

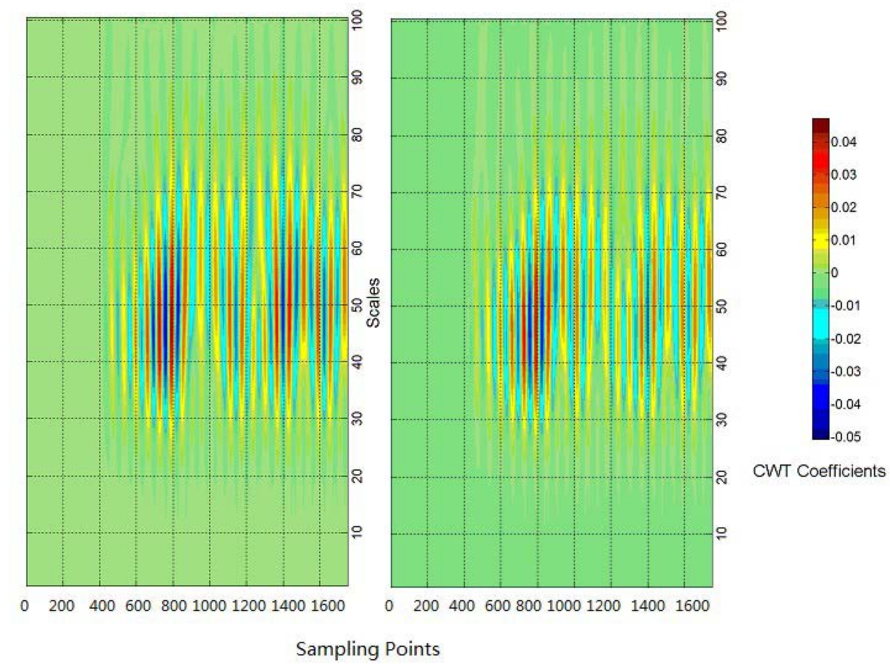

(a) (b)

Figure 5.6 CWT spectrum in scale obtained from (a) non-fatigue case through sensing path $P_{1,2}$ (b) post-fatigue case through sensing path $P_{1,2}$

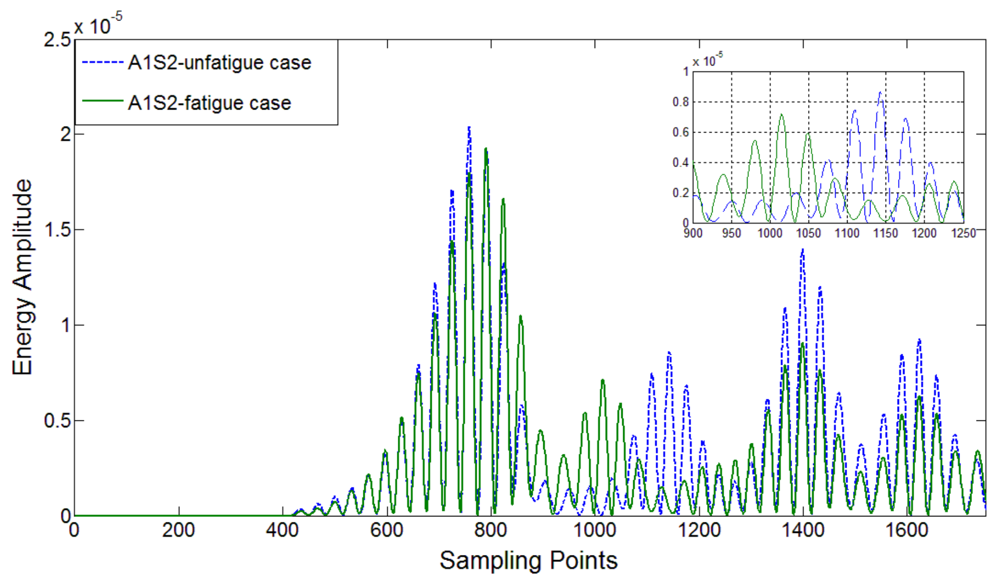

Figure 5.7 CWT-based energy distribution of signal from sensing path $P_{1,2}$

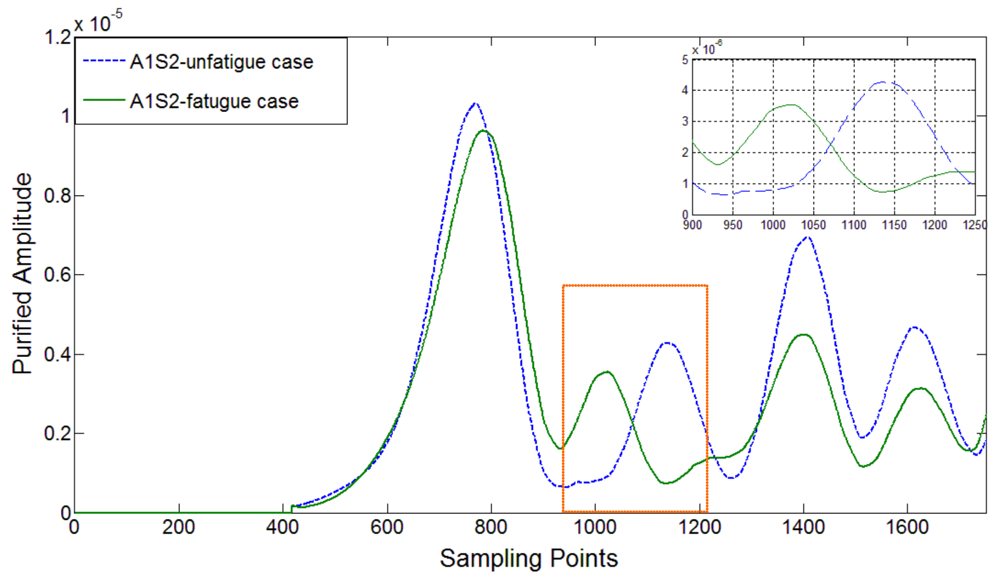

Figure 5.8 Purified energy distribution of signal from sensing path $P_{1,2}$

In this chapter, the key point in detecting the fatigue crack was to identify the difference caused by GW interactions with the fatigue crack when incidental GWs propagated through it. According to the wave scattering rule, the signal collected from the sensor network must include a wave component that differs from the baseline and represents the signal scattering from the fatigue crack. The arrival time of the wave component can also be used to locate the fatigue crack. The direct transmission, reflection and possible mode conversion of the dominant mode are monitored to identify the fatigue crack due to its high level of wave energy. In this chapter, with the dominant wave velocity of about 3249 m/s (V_d) obtained in the experiment, we employed a correlation function to extract the RTD/fs between the signal packets [117]:

$$R_{xy}(m) = \begin{cases} \sum_{n=0}^{N-M-1} x_n + my_n^*(m \geq 0) \\ R_{yx}^*(-m)(m \leq 0) \end{cases}, \tag{5.5}$$

where x_n and y_n are correlated time series. There will be a peak in the correlation coefficient curve, and the corresponding time lag represents the difference in the arrival time of these two peak values when the peak values in the two signals are correlated with each other [117]. In this study, x_n and y_n served as the time responses of the purified energy envelope obtained from the wavelet analysis in the autocorrelation function. They were used to establish the correlation coefficient curves of the intact plate and the fatigued plate shown in Figure 5.9. As described in the definitions, the time lag corresponding to each peak in the correlation coefficient curve measures the time difference between the highest amplitude of the incipient wave components and that of the following wave components [16]. The difference represented by the local wave package can be enhanced when the correlation coefficient curve for the damaged plate is divided by the baseline curve. The first discrepancies between the fatigued and non-fatigued plates derived from the peaks represent signals directly transmit from one actuator to one sensor. If the peak value due to amplitude change is taken as threshold, the discrepancies derived from the first peaks excess the threshold represent differences induced by the fatigue crack. The fatigue-induced peak highlighted in Figure 5.10 allowed for the RTD/f to be identified.

5.3.2.3 Determination of DPPs

In this part of the chapter, effort was focused on determining the fatigue crack presence probabilities of all positions on the steel plate. An imaging algorithm as proposed before was adopted to represent DPP values for every position on the steel plate, the results being expressed in an intuitional manner [75]. To be consistent with previous chapters and without loss of generality, most of the definitions used in amentioned

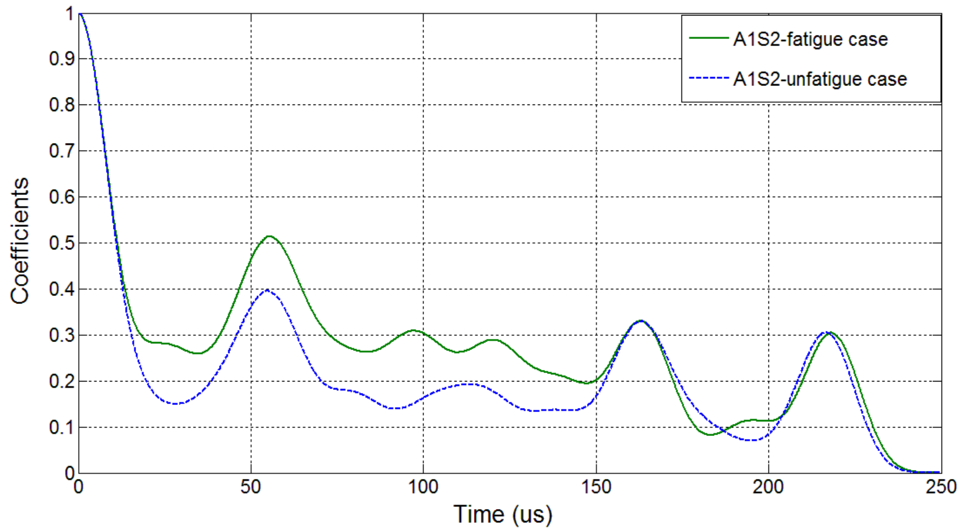

Figure 5.9 Correlation coefficient curves from sensing path $P_{1,2}$

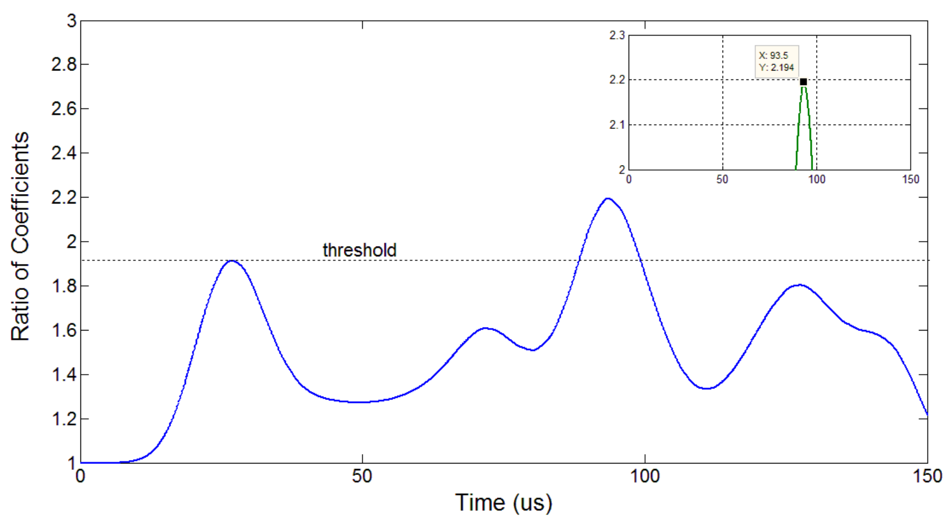

Figure 5.10 Ratio of correlation coefficient curves from sensing path $P_{1,2}$

investigations were adopted, the exception being the geometries and parameters for determination of DPPs. Supposing the plate is represented as a virtual mesh with *K* grids (*e.g.*, of 1x1 mm^2 each in what follows), the distance from a certain grid L_j ($j \in \{1,2,...K\}$) to PZT wafer A_m can be expressed as $D_{m,j} = \left| \overline{r_m} - \overline{r_j} \right|$, where $\vec{r_m}$ and $\vec{r_j}$ are the location vectors of A_m and L_j in the global coordinate system, as shown in Figure 5.11. The time needed for GWs to travel along the route $A_m \rightarrow L_j \rightarrow A_n$ can then be defined as $T_{m,j,n} = (D_{m,j} + D_{n,j}) / V_d$. Supposing the time difference made by a fatigue crack is RTD/f, in the following equation,

$$RTD / f_{m,n} - T_{m,j,n} = 0\,, \tag{5.6}$$

the coordinates of the damage center are two unknown variables. The solution of Equation (5.6) presented an ellipse locus with the two PZT wafers being two foci, as portrayed by the dashed-dotted line in Figure 5.11. In principle, the grids correctly located on this locus, i.e., those with coordinates that satisfy Equation (5.6), have the highest probability of sustaining damage from the sensing path pair $P_{m,n}$ that produces such a locus. Therefore, the DPP values of these grids were determined to be 100%. The coordinates will not satisfy Equation (5.6) for grids at other locations. Moreover, the further these grids are from the ellipse locus, the lower the probability they will sustain damage. Accordingly, to quantify the DPP values at such grids in relation to their locations L_j and the sensing path pair $P_{m,n}$ (m, n $\in \{1,2,...7\}$, m$\neq$n)), a CDF [110] defined as

$$F_{m,n}(t) = \int_{-\infty}^{t} f(T'_{m,j,n}) \cdot dT'_{m,j,n} \tag{5.7}$$

is then introduced, where $f(T'_{m,j,n}) = \dfrac{1}{\sigma_{m,n}\sqrt{2\pi}} \exp[-\dfrac{(T'_{m,j,n})^2}{2\sigma^2_{m,n}}]$ is the Gaussian distribution function representing the density function of the DPP. In the above equation, $T^{'}_{m,j,n} = \left| RTD / f_{m,n} - T_{m,j,n} \right|$ is a function of L_j when $RTD/f_{m,n}$ is given, denoting the 'distance' between grid L_j and the ellipse locus in the time domain, $\sigma_{m,n}$ is the standard variance and the integral upper limit t is the value of $T'_{m,j,n}$ when m, j, n are specified. Given $T'_{m,j,n}$, the DPP value of grid L_j regarding $P_{m,n}$ becomes

$$\mathrm{DPP}(L_j, P_{m,n}) = 1 - \left| F_{m,n}(T'_{m,j,n}) - F_{m,n}(-T'_{m,j,n}) \right| \tag{5.8}$$

The DPP can be obtained by applying the above algorithm to all K grids for estimated values of $P_{m,n}$. To illustrate, suppose the plate is virtually meshed into K grids as in the DPP (L_j, $P_{m,n}$) image shown in Figure 5.12. In this image, the DPP values vary within the range of [0, 1] with the two extremes standing for the lowest and highest DPP, i.e., 0% and 100%, respectively. The lighter the image, the greater the DPP of the grid. However, determining the damage location from such an image is insufficient because all grids on the locus derived from Equation (5.6) will have the same high DPP value. Therefore, in the experiment conducted in this chapter, images contributed by all available $P_{m,n}$ in the active sensor network were fused to arrive at a common estimate of the fatigue crack location. An image fusion scheme was adopted to strengthen damage-associated information in final estimation result, based on conjunctive image fusion techniques [118]. Supposing DPP images established from all effective $P_{m,n}$ are available for use in conjunctive fusion schemes, as stated in following expressions

$$DPP_{L,P} = \frac{1}{N_p} \sum_{m,n \in \{1,2,\ldots 7\}} DPP(L_j, P_{m,n}),\ j = 1,2,\ldots K \tag{5.9}$$

where P are all involved sensing path pairs; Np is the number of elements in P. $DPP_{L,P}$ is so-called fusion result for all DPP. Thus, for the fatigue crack with up and down tips at (300 mm, 37 mm) and (300 mm, 22 mm), after employing all of the PZT path pairs, the location of the fatigue crack could be clearly seen in both the 2D DPP image (shown in Figure 5.13) and the 3D DPP image (shown in Figure 5.14). The estimated location was around (299 mm, 30 mm).

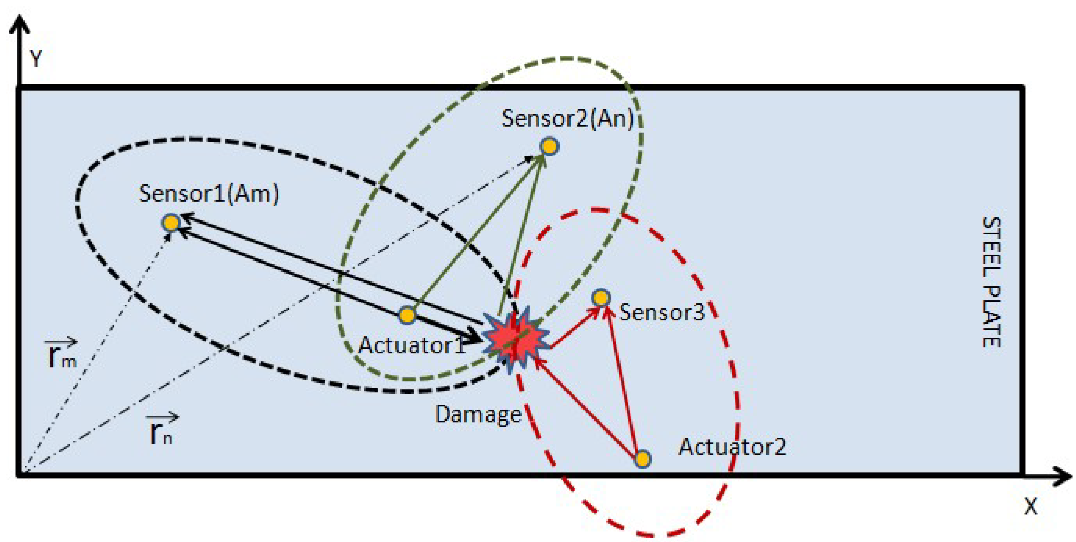

Figure 5.11 RTD/f-based triangulation of damage in a 2D plate with three sensing paths

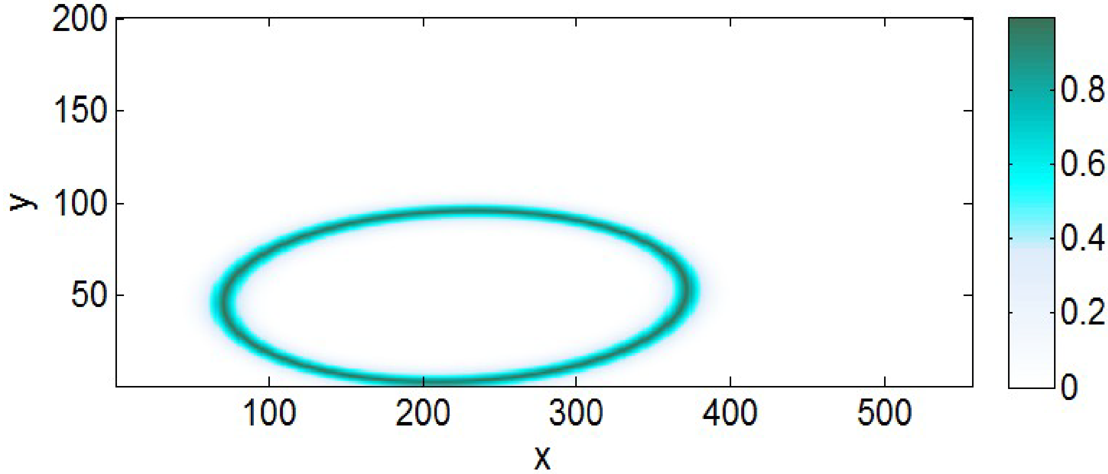

Figure 5.12 DPP image obtained from a single sensing path

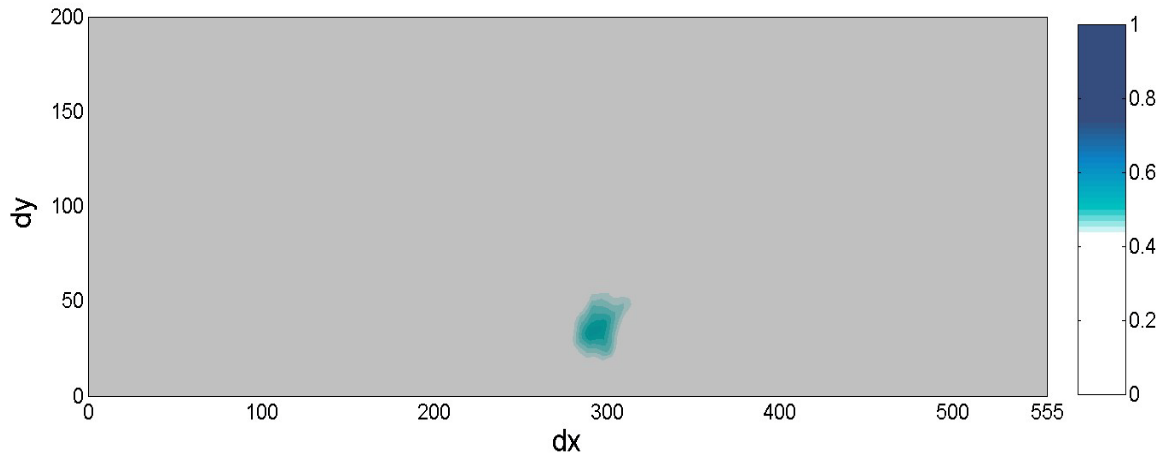

Figure 5.13 2D DPP image of damage location derived from all sensing paths

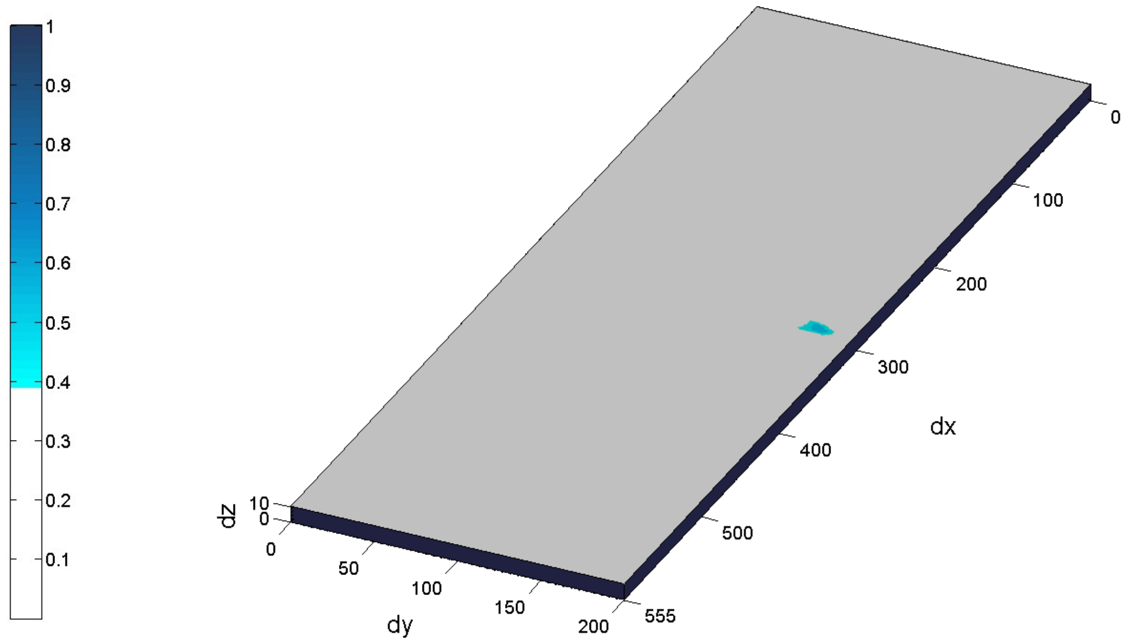

Figure 5.14 3D DPP image of damage location derived from all sensing paths

5.3.3 Load Effect Detection

After generating the fatigue crack, both a tensile load and a compressive load were applied to the steel plate to identify the effect of these loads on the fatigue crack. Figure 5.15 shows the original signals derived from path $P_{6,7}$ via the experiments. The envelopes of the amplitudes of this family of periodic curves can be seen in zoom view figure of Figure 5.15. The results show that the S_0 waves transmitted were marginally smaller if the fatigue crack was under tension, as represented by a smaller wave amplitude. In contrast, the S_0 waves transmitted were somewhat larger if the fatigue crack was under compression, as represented by a much larger wave amplitude. Apart from amplitude, ToF when the transmitted wave reaches the corresponding sensor after being generated appeared a little in advance in the case of the S_0 wave transmitted when the fatigue crack was under compression. The reason for this is that for a partially open fatigue crack under compression, some of the open area will be closed due to the load being applied and the wave can be transmitted through the closed area instead of scattering from the open area. In cases of GWs transmitted when the fatigue crack was under a fatigue load and a tensile load, there was very little difference in either amplitude or ToF, thus indicating that wave signals transmitting through a fatigue crack under fatigued condition is most like the wave signals transmitting through an open crack under damaged condition, and there were enough PZT transducers and sensing paths that although some signals derived from the paths just passed through the closed fatigue crack, the signals derived from the rest of the paths were adequate for detecting the fatigue crack.

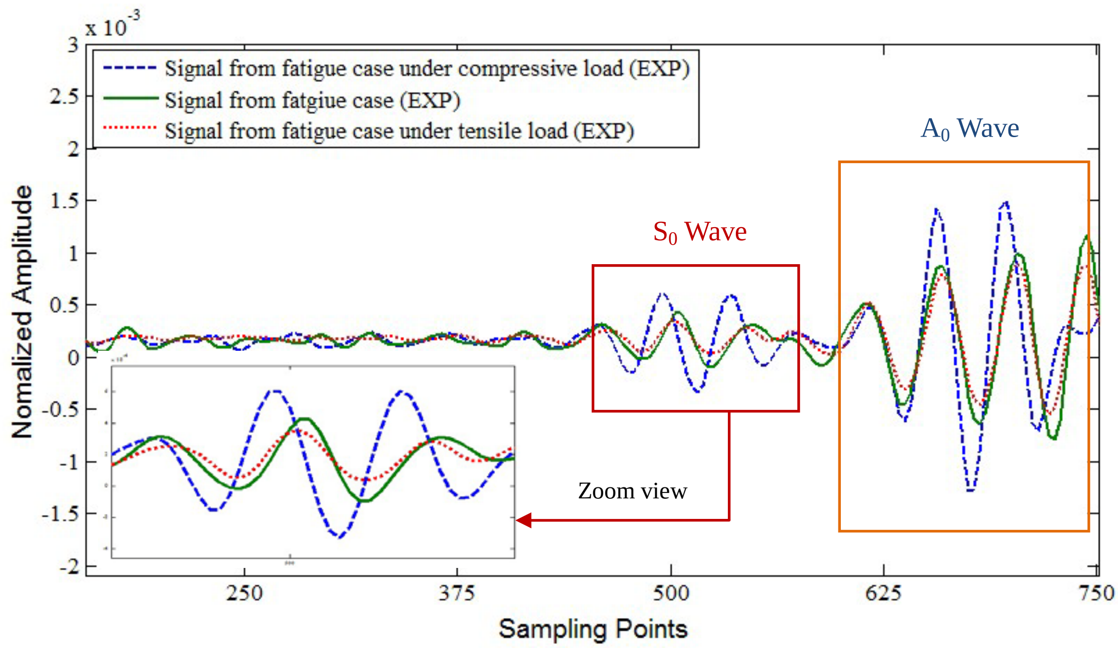

Figure 5.15 Loading effect on wave signals through fatigue crack

5.4 Simulation Analysis

The fatigue crack was simulated by the Seam Assigned Model (SAM) in FEM software ABAQUS®/CAE combined with contact effect to ensure part of the pressure pass through the intersurfaces of the fatigue crack. All the simulation procedures and parameters adopted were same with previous simulation work in this thesis except the model part and mesh part, which were suitable for SAM analysis. Simulation model is shown in Figure 5.16 (a) and the regions around the notch, fatigue crack and PZT elements were meshed with finer meshes as shown in Figure 5.16 (b). In order to establish the fatigue crack model, the model of steel plate was firstly partitioned with a specific length, *i.e.* the fatigue crack length, 15 mm in this case, which originated from the notch tip and then the seam and contact effect were assigned on the partitioned surfaces. At the same time, a model of a intact steel plate with the same dimensions and properties was established for obtain a baseline data.

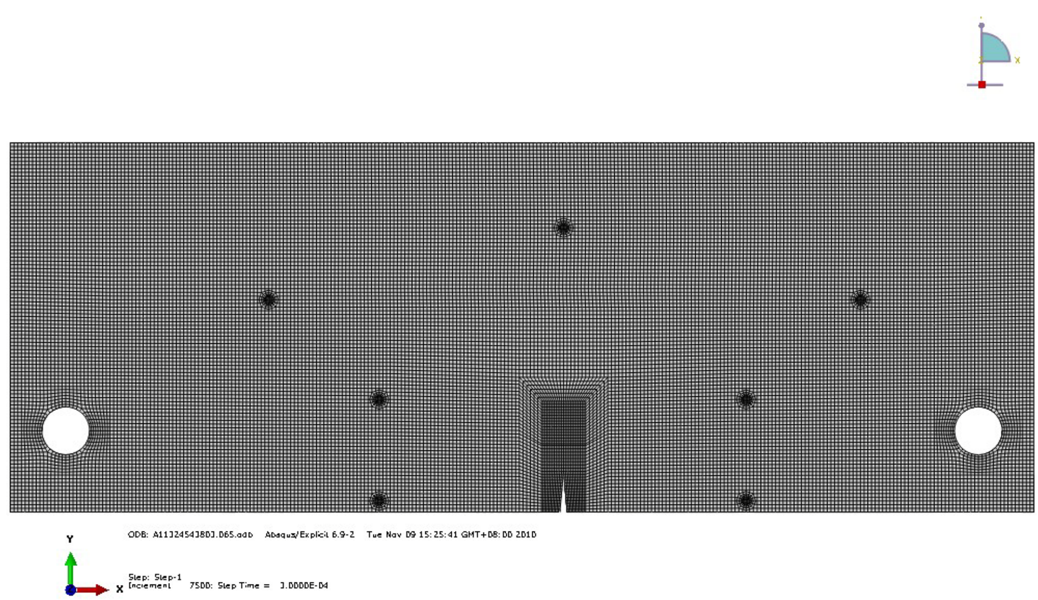

(a)

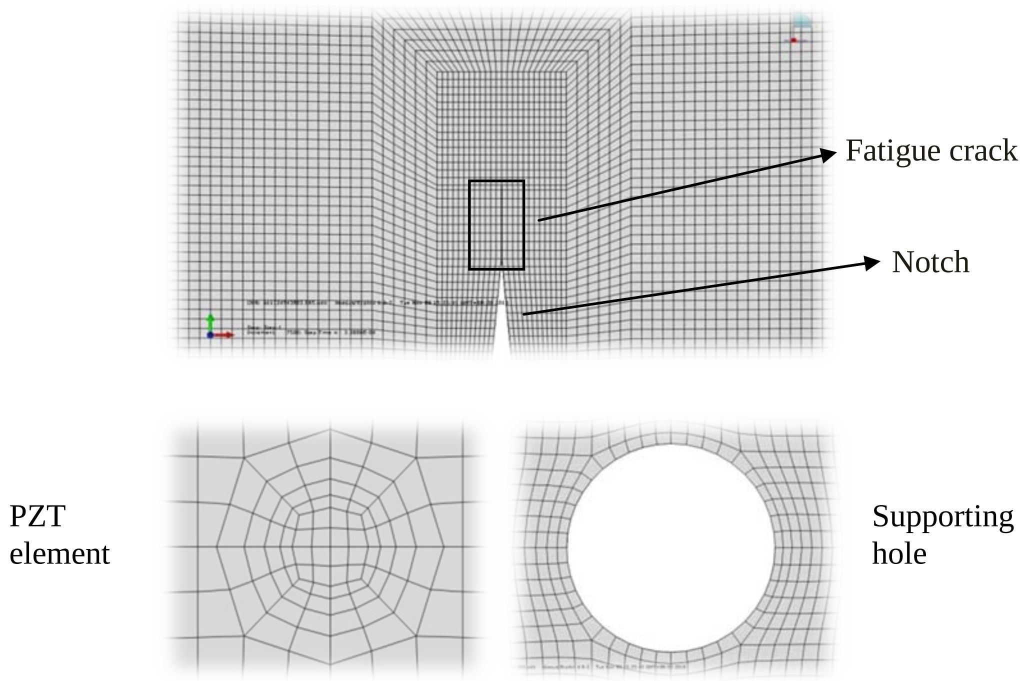

(b)

Figure 5.16 (a) Simulation model (b) zoom view of notch, fatigue crack, supporting hole and PZT element in mesh part

Figure 5.17 shows time history output of the simulation results which represent the process of wave propagation before and after passing through the fatigue crack. It is clear to observe that the wave can be reflected by the fatigue crack and additional wave scattering and attenuation effects due to interactions with the notch and boundaries exist. From simulation results, the arrival of the incident and fatigue crack-reflected dominant wave packages can be obtained, from which the flight distance can be computed using the wave velocity.

Using the same analytical method and procedure as amentioned in experiments, simulation results obtained from $P_{1,2}$ and processed by data compression and interpretation are shown in Figure 5.18 and Figure 5.19. We can see that simulation results and experimental results agree well with each other no matter from the difference of ToFs or amplitudes between the baseline data and signals from fatigued sample. By all the RTD/fs extracted from FEM analysis, locations with highest probability of fatigue crack occurrence was picked out and detailed in Figure 5.20. The coordinate system is the same as that indicated in experimental results. It can be found that comparing with the dimensions of specimen, the distance between estimated location and the true location is relatively small, implying the acceptability of the proposed approach.

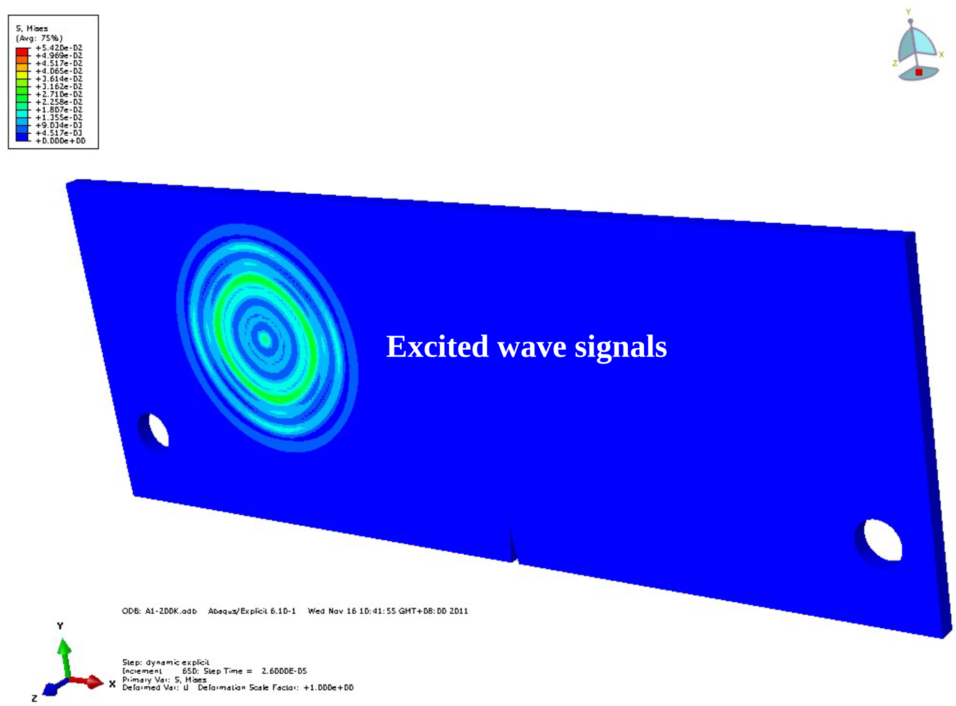

(a)

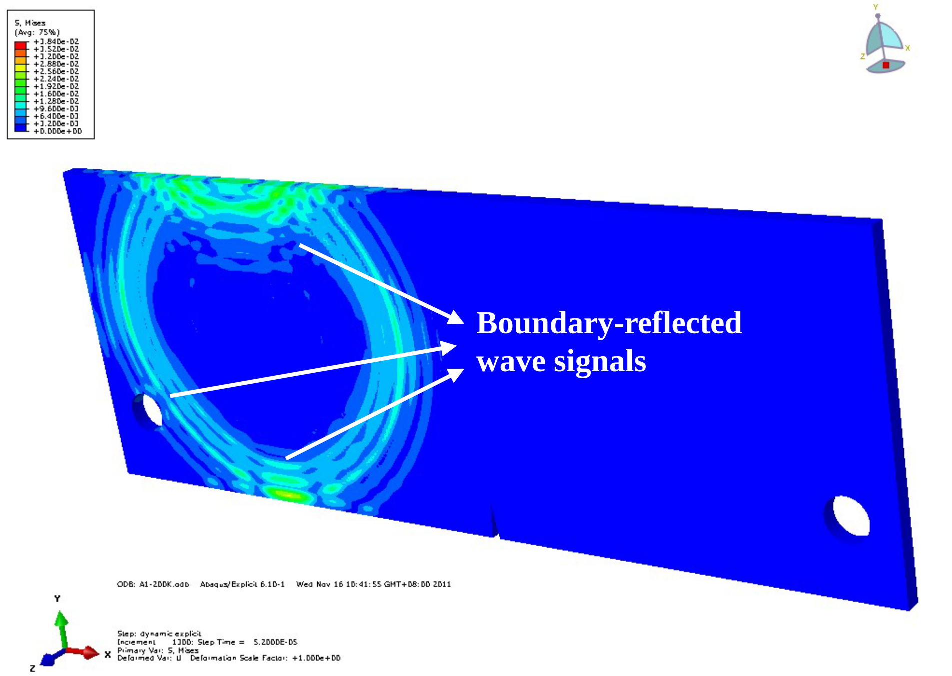
Boundary-reflected
wave signals

(b)

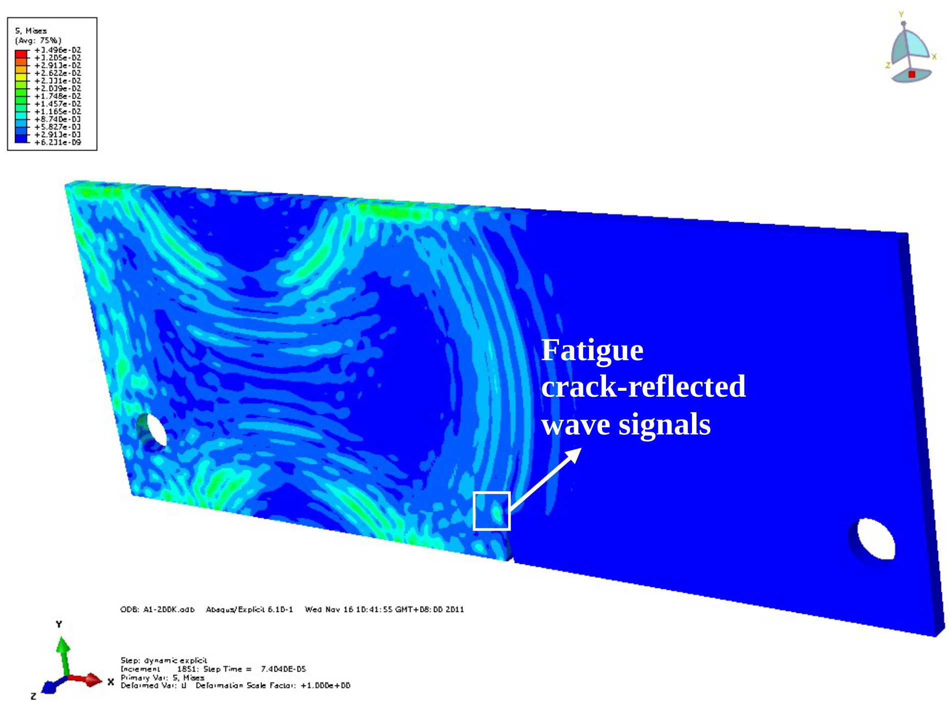
Fatigue
crack-reflected
wave signals

(c)

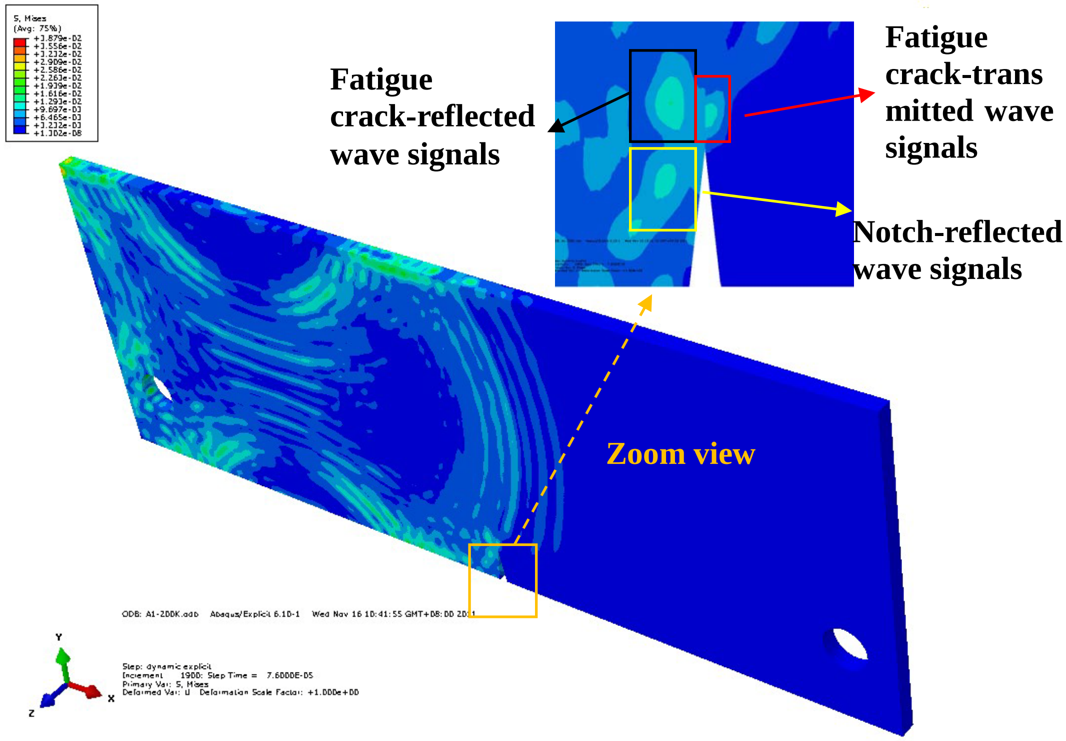

(d)

Figure 5.17 Snapshots for GW propagation through a fatigue crack at selected moments from FEM analysis (a) 26 μs (b) 52 μs (c) 74.04 μs (d) 76 μs

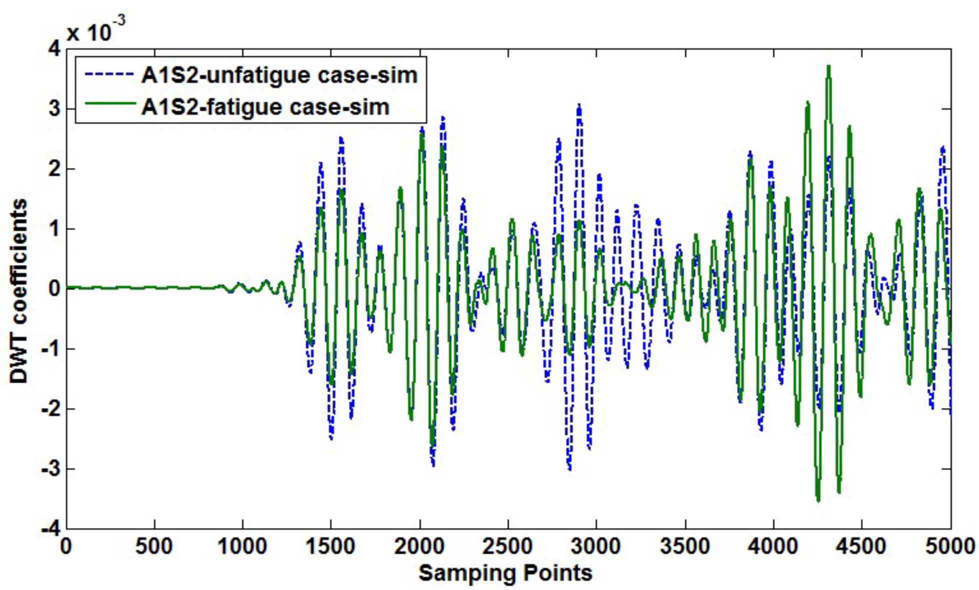

Figure 5.18 Signal compression result from $P_{1,2}$ including boundary reflected and damage(notch/notch+fatigue crack) scattered wave components (FEM)

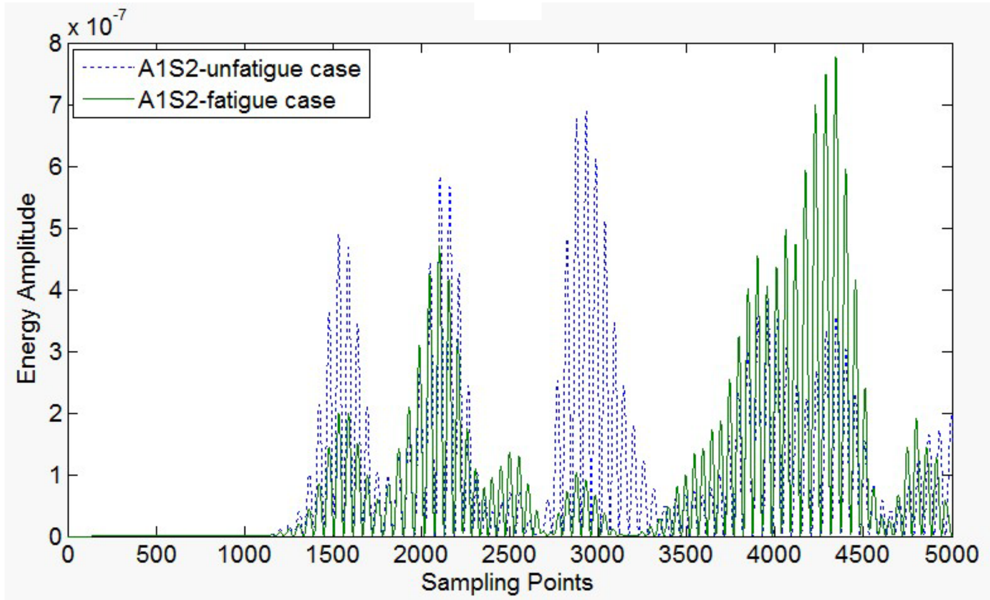

Figure 5.19 CWT-based energy distribution of signal from sensing path $P_{1,2}$ (FEM)

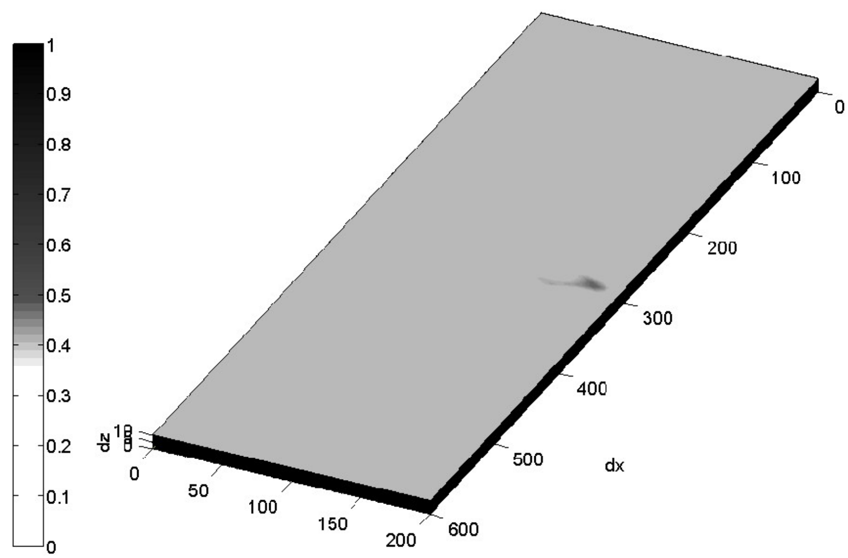

Figure 5.20 3D DPP image of damage location derived from all sensing paths (FEM)

In order to differentiate the developed fatigue crack modal with traditional crack modal, which was established by deleting element, three different models for one was an intact plate without crack, one was a plate with a fatigue crack model and one was a plate with deleted elements in the fatigue zone. Except the establishment of crack, the other properties and parameters about the models were the same. Figure 5.21 shows the original signals derived from path $P_{6,7}$ via the simulations. The envelopes of the amplitude and ToFs of this family of periodic curves can be seen by zoom view from S_0 wave mode which was transmitted through the crack zone. Results indicate that the S_0 wave modes transmitted were marginally smaller for model with fatigue crack and model with deleted elements compared with that of model for intact plate as the crack reflected most of the wave energy. And for the amplitude obtained from fatigue crack model, wave amplitude is a little larger than that obtained from model with deleting elements because this developed fatigue crack model can transmit part of wave energy through the fatigue crack. Apart from amplitude, ToF when the transmitted wave reaches the corresponding sensor after being generated appeared in advance in the case of the S_0 wave transmitted for the intact plate model. And ToF for wave package transmitted from fatigue crack model shows a little in advance than that from model with deleting elements. The reason for this is that transmitted time from actuator to sensor is shortest when the wave directly transmitted between each other which is just like the case of intact plate and time becomes longer when the wave has to be reflected, scatted and transmitted by the fatigue crack and even longer when it has to be scatted and reflected by crack. However, there was very little difference in either amplitude or ToF for fatigue crack case and deleting element case, thus indicating that wave signals transmitted through a fatigue crack is most like the wave signals transmitted through an open crack.

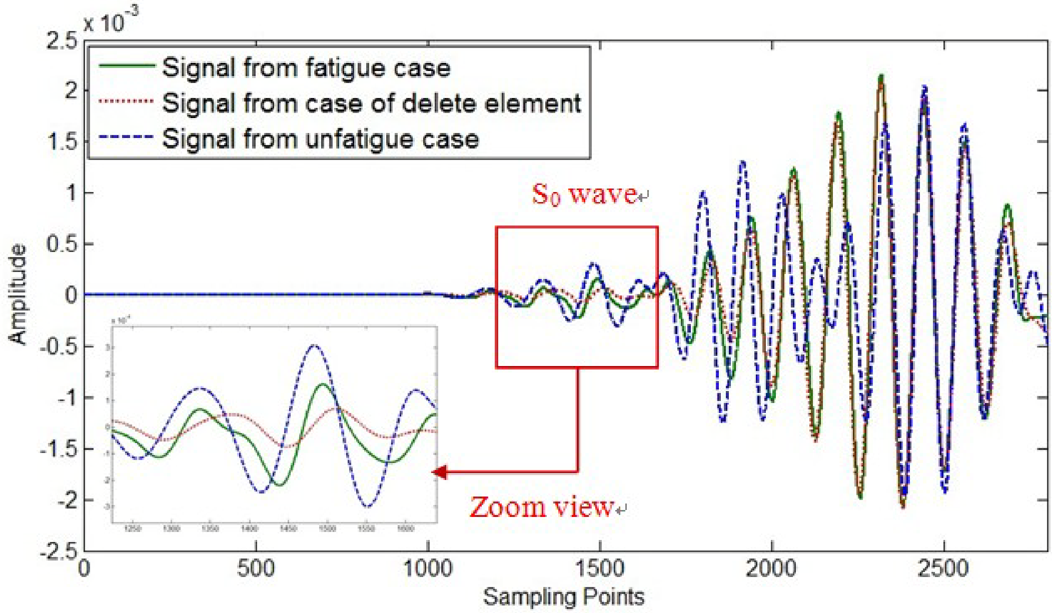

Figure 5.21 Comparison of wave signals from different cases of sensing path $P_{6,7}$ (FEM)

5.5 Concluding Remarks

This chapter reports on a study in which an active PZT sensor network was successfully used to identify the location of a 15 mm fatigue crack in a thick steel plate by experiments and FEM analysis with a satisfactory degree of precision. WT technology and the correlation function on the energy distribution envelope were employed to determine the RTD/fs, after which the DPP based on the RTD/fs was applied to define the crack location using an imaging approach and energy-based spectrum.

The results show that although the location of the fatigue crack adjacent to the notch and near the original edges of the plate made fatigue crack evaluation much more difficult, the proposed approach still produced an acceptable estimate of the fatigue crack location. The outcome of the chapter indicates that this method combining a GW propagation-based imaging approach with estimation of the load effect on waves passing through the fatigue crack delivers an acceptable visual estimate of the location of fatigue cracks in steel plates. The proposed approach thus represents an effective method of evaluating the presence and location of real damage in engineering structures and has great potential for their real-time SHM.

CHAPTER 6 Monitoring of Fatigue Crack Propagation in Steel Plates Using GWs

6.1 Introduction

In this chapter, GWs are applied to detect and monitor the propagation of a fatigue crack. In the detect part, imaging approach was applied for locating a 7 mm-length fatigue crack based on ToF extracted from experimental signals. In the monitoring part, three approaches were applied to identify propagation of the fatigue crack from 0 mm to 38 mm including traditional transmission coefficient-based approach, which was then verified by FEM, TRM with the combination of imaging approach and PCA method. For PCA method, statistical characteristics as damage indices were extracted from the wave signals which were acquired at several stages when the crack reached different lengths at certain numbers of cycles. The robustness of principal components for damage identification was then compared with single damage index in adverse conditions, where the arrival times of the desired wave signals were artificially tailored in accordance with the effect of temperature change on GW modes.

6.2 Monitoring of Fatigue Crack Propagation of Engineering Structures Using TRM

6.2.1 Fatigue Crack Detection

6.2.1.1 Fatigue test and GW generation by PZT transducers

Figure 6.1 shows a steel plate of 600 mm×200 mm×5 mm in size which was clamped in the 250 kN MTS fatigue-testing machine in the force-controlled mode via a MTS Load Unit Controller. The material properties of the specimen are same as detailed in previous chapters. In order to initiate a fatigue crack, an artificial notch of 5 mm×5 mm was induced in the middle of one longer edge of the specimen. The tension-tension fatigue test was implemented to initiate and grow a fatigue crack along the notch. The dynamic cyclic loading of 5 kN-50 kN was adopted in the fatigue test. The length of the fatigue crack was firstly generated to 7 mm. The crack was located along the sharp angle of the notch as shown in Figure 6.2.

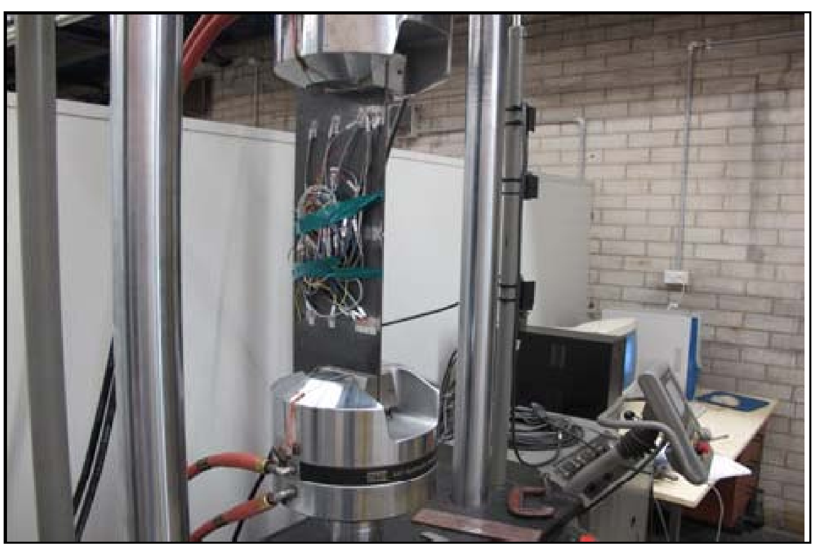

Figure 6.1 Specimen used in experiment

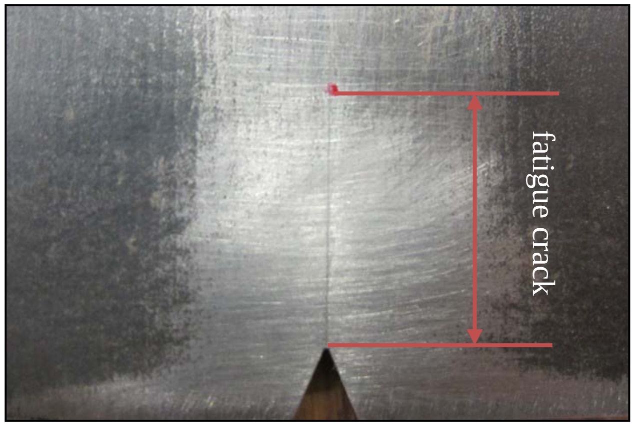

Figure 6.2 Zoom view of fatigue crack introduced into the plate

As shown in Figure 6.3, six circular PZT transducers of sensor network 1 and six identical transducers with the dimensions of 6.9 mm in diameter and 0.5 mm in thickness were surface-mounted on the plate to serve as either actuators or sensors. MATLAB® software was used to generate the excitation signals and the signals were fulfilled using a system developed on the VXI platform, consisting mainly of an arbitrary signal generator (Agilent_ E1441), signal amplifier (PiezoSys_ EPA-104), signal conditioner (Agilent_ E3242A), and signal digitizer (Agilent_E1437A). A 5-cycle sinusoidal toneburst (60V peak-to-peak) enclosed in a Hanning window at a central frequency of 200 kHz was generated and acquired at a sampling rate of 20.48 MHz. When a PZT transducer was activated, the rest were regarded as sensors to monitor propagations of GWs in the steel plate. Locations of all the PZT transducers in the two sensor networks are shown in Table 6.1. When a PZT transducer was regarded as actuator, the others served as sensors to monitor the circumstance of wave propagation in this specimen.

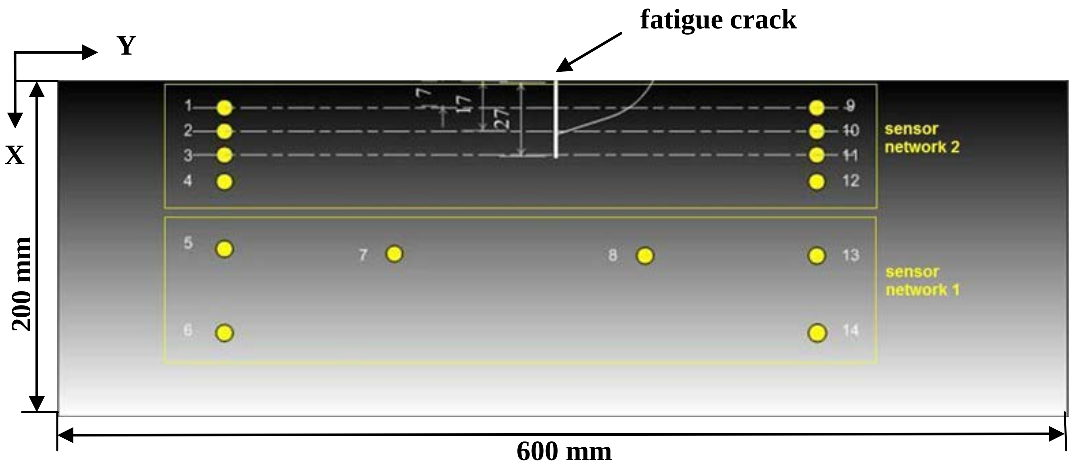

Figure 6.3 Two PZT sensor networks

Table 6.1 Locations of PZT transducers

PZT No.	**P1**	**P2**	**P3**	**P4**	**P5**	**P6**	**P7**
Location	(15,100)	(25,100)	(35,100)	(45,100)	(105,100)	(155,100)	(105,200)
PZT No.	**P8**	**P9**	**P10**	**P11**	**P12**	**P13**	**P14**
Location	(105,350)	(15,450)	(25,450)	(35,450)	(45,450)	(105,450)	(155,450)

6.2.1.2 Identification of fatigue crack by probability-based imaging approach

The GW signals obtained from sensing paths were captured when the structure was in the pristine condition and after the introduction of fatigue crack. Wavelet analysis can be used to transfer the GW signals from the time domain into the time-frequency domain. In the part of locating fatigue crack, CWT and HT were applied for processing of the acquired signals. For one typical sensing path $P_{4,7}$, the HT coefficients of processed wave signals at reference and damage states are illustrated in Figure 6.4. The first difference of ToF and amplitude between baseline data and fatigued case for reflected signals can be observed and used for locating fatigue crack for this sensing path, which was defined as fatigue-induced change (FIC) meaning that the reflecting sensing path was seriously impaired by the fatigue crack.

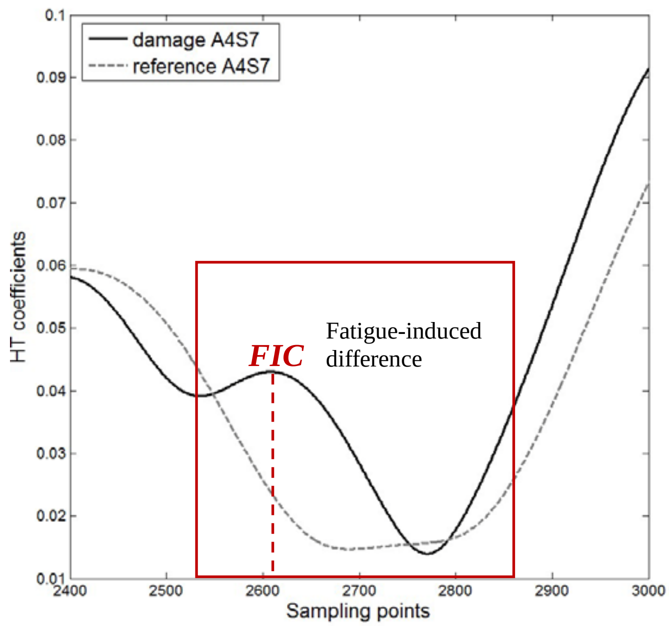

Figure 6.4 HT coefficients from a typical sensing path $P_{4,7}$

With the FIC obtained from experiment, effort was focused on determining DPPs of all positions of the steel plate rather than defining exact location of fatigue crack. The imaging algorithm amentioned was adopted to represent DPP values which vary within the range of [0, 1] with the two extremes standing for the lowest and highest DPP, i.e., 0% and 100%, respectively, for the steel plate, expressing the result in an intuitional manner. The analytical procedure keeps consistent with chapters 4 and 5, and without loss of generality, in which most of the definitions were inherited except the geometries and parameters. On account of the same principle and based on the data fusion method, images contributed by all the available paths in the active sensor network were fused to figure out the common estimate of the location of the fatigue crack, which can be clearly seen from the 2D DPP image result. The evaluated location is shown in Figure 6.5 at the darkest area and the real location of the fatigue crack tip is illustrated as the red square.

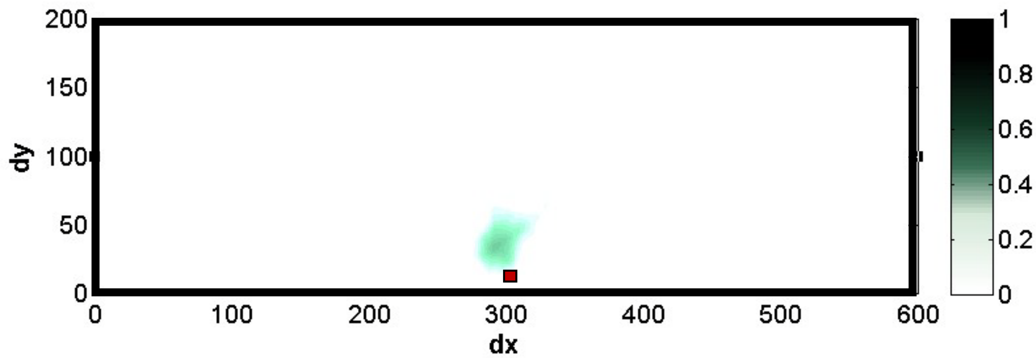

Figure 6.5 Estimation of fatigue crack location by FIC-based DPP

6.2.2 Fatigue Crack Monitoring

After location of the fatigue crack was identified in the first estimation, the steel plate with 7 mm fatigue crack was considered to be monitored by PZT sensor network 2 (shown in Figure 6.2). It can be clearly seen that after millions of cycles, the captured signals change a lot according to previous state. In order to obtain more accurate results, baseline-free methodology can be adopted for subsequent analysis.

6.2.2.1 TRM-based signal interpretation

TRM combined with GW approach (TRM&L) has been established [50, 81], and the TRM has been formulated in the frequency domain incorporating the PZT transducers used for excitation and measurement of GWs [118]. However, the study of the TRM&L for fatigue crack monitoring has never been mentioned.

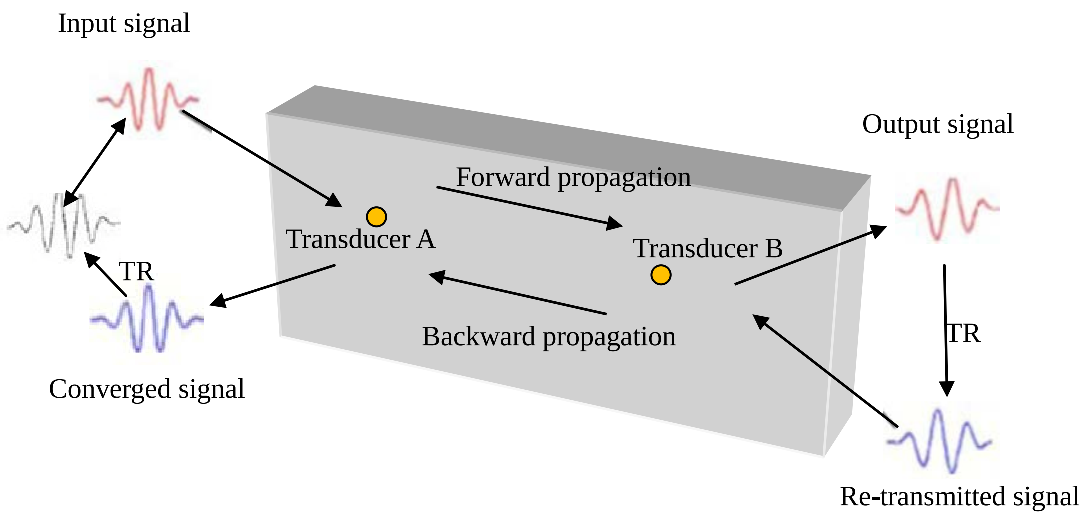

Figure 6.6 TRM principle

The principle of TRM can be explained as follows. An input signal can be firstly rebuilt at a PZT transducer while an output signal recorded at another PZT transducer is retransmitted to the original PZT transducer after being reversed in the time domain as illustrated in Figure 6.6 [45]. The specific goal of the research described in this section is to reconstruct the known excitation signal at the original input location through the TRM based on GWs in order to monitoring the fatigue crack ahead of 7 mm length.

6.2.2.2 TR-based diagnostic imaging approach with the combination of damage index for fatigue crack monitoring

The damage index ($DI_{m,n}$) from each sensing path $P_{m,n}$ is obtained to stand for the similarity between the excitation waveform ($V_e(t)$) and reconstructed waveform ($V_r(t)$) after the TRM process, given as

$$\mathrm{DI}_{m,n} = 1 - \sqrt{\left\{\int_{t1}^{t2} V_e(t)V_r(t)dt\right\}^2 \Big/ \left\{\int_{t1}^{t2} V_e(t)^2dt \int_{t1}^{t2} V_r(t)^2dt\right\}} \tag{6.1}$$

Value of $DI_{m,n}$ varies from 0 to 1, and increases with more disparity between the two waveforms. Finally a series of coefficients can be obtained according to the differences of original required signals and retransmitted signals. For estimating the probability of the propagation of the fatigue crack in the monitoring area, the correlation of two signals offers a clue as to how well the value of one signal can be approximated from the value of the other [119]. In this study, the propagation of the fatigue crack is assumed to be the exclusive explanation for the changes in coefficient by TRM based on GW signals between the initial state and the states when the crack extended to a certain length. On the basis of this principle, the complexity of structural geometry or boundary condition, especially the adverse effect caused by applied cyclic load would not affect the capability of this probabilistic damage diagnostic algorithm, as these influences are implicitly included in both the reference and present signals. The degree of changes in signals from a certain sensing path before and after crack propagation is introduced will be clearly increased if the sensing path is much closer to the tip of the fatigue crack. It is evident that the Damage indexes for seriously damage-impaired sensing paths are larger than those for slightly damage-impaired sensing paths.

The damage diagnostic imaging algorithm corresponds to the DI from one individual sensing path to all sensing paths can be involved to the analysis. If there are P sensing paths in this case, the specimen for identification is meshed into uniform grids. For damage located at (x_d, y_d), the damage presence probability DPP is defined as [127]:

$$\mathrm{DPP} = \sum_{i=1}^{P} \mathrm{DPP_i}\,(x_d, y_d) = \sum_{i=1}^{P} \mathrm{DI_{m,n}} \cdot \mathrm{W_{m,n}}\left[\mathrm{R_{m,n}}(x_d, y_d)\right] \tag{6.2}$$

$\mathrm{W_{m,n}}\left[\mathrm{R_{m,n}}(x_d, y_d)\right]$ is the weight given to the $DI_{m,n}$ at (x_d, y_d) at the damaged zone of either sensing path, while $R_{m,n}$ is defined as the relative distance from (x_d, y_d) to the

P_{th} sensing path. Assuming distances from actuator to sensor, from damage to actuator and from damage to sensor are $D_{A\text{-}S}$, $D_{A\text{-}D}$ and $D_{D\text{-}S}$, respectively as defied in previous sections,

$$\mathrm{R_{m,n}}(\mathrm{x_d}, \mathrm{y_d}) = \frac{\mathrm{D_{A-D}} + D_{D-S}}{D_{A-S}} - 1 \ , \tag{6.3}$$

while

$$\mathrm{W_{m,n}}[\mathrm{R_{m,n}}(\mathrm{x_d}, \mathrm{y_d})] = \begin{cases} 1 - \frac{\mathrm{R_{m,n}}(\mathrm{x_d}, \mathrm{y_d})}{\beta}, & \mathrm{R_{m,n}}(\mathrm{x_d}, \mathrm{y_d}) < \beta \\ 0, & \mathrm{R_{m,n}}(\mathrm{x_d}, \mathrm{y_d}) \geq \beta \end{cases} , \tag{6.4}$$

in which the scaling parameter β determines the size of the affected zone [26]. In this study, β was set as 0.0005 for 4 paths and part of 16 paths, 0.05 for part of 16 paths and 35 paths. As a result, the damage signatures for individual sensing paths can be calculated by subtracting the corresponding DPP, which can be presented in the uniformly distributed grids of the monitoring area [120]. The actuators and sensors of individual sensing paths were summarized in Table 6.2.

Table 6.2 Selected sensing paths for fatigue crack monitoring

Sensing Path No. (16 paths)	P1-P9	P1-P10	P1-P11	P1-P12	P2-P9	P2-P10	P2-P11	P2-P12
	P3-P9	P3-P10	P3-P11	P3-P12	P4-P9	P4-P10	P4-P11	P4-P12
Sensing Path No. (35 paths)	P1-P9	P1-P10	P1-P11	P1-P12	P1-P13	P2-P9	P2-P10	P2-P11
	P2-P12	P2-P13	P3-P9	P3-P10	P3-P11	P3-P12	P3-P13	P3-P14
	P4-P9	P4-P10	P4-P11	P4-P12	P4-P13	P5-P9	P5-P10	P5-P11
	P5-P12	P5-P13	P6-P9	P6-P10	P6-P11	P6-P12	P7-P9	P7-P10
	P7-P11	P7-P12	P7-P13					

The result of normalized DPP-based image according to TRM with scaling parameter of 0.0005 was illustrated in Figure 6.7 with values from 0 to 1, which represents the state when the fatigue crack is 7 mm in length when 16 paths were applied. It can been seen that the location of fatigue crack obtained from DPP based on TRM is less accurate than that from ToF which means that it is better to use ToF-based instead of correlation information-based probability imaging approach for locating a fatigue crack. The normalized DPP constructed using transmitted S_0 wave mode were illustrated in Figures 6.8 (a), (b), (c) and (d) which were obtained from 4 direct sensing paths as shown in Table 6.2 indicate the states when the fatigue crack was growing from 0 mm to 7 mm, 17 mm and 27 mm, respectively. Red marks highlighted in the figures show the real locations of notch (fatigue 0 mm) and fatigue tip (fatigue 7, 17, 27 mm). The fatigue crack tip was identified through searching the maximum probability value in the darkest area which can be clearly seen that the maximum of probability propagate with fatigue crack grows, demonstrating the possibility of the developed approach based on time reversal baseline-free method. However, it is noteworthy that the estimation results will be confused due to the small distance between two adjacent PZT sensing paths.

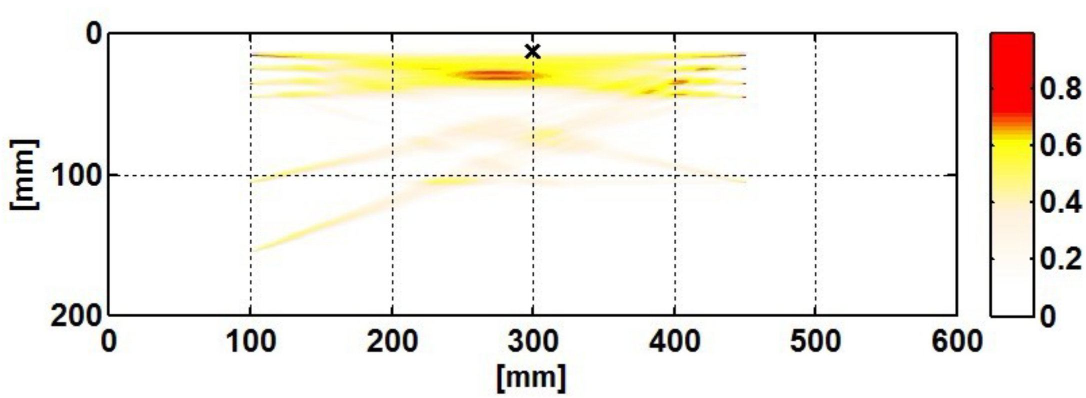

Figure 6.7 Normalized DPP result when fatigue crack is 7 mm in length

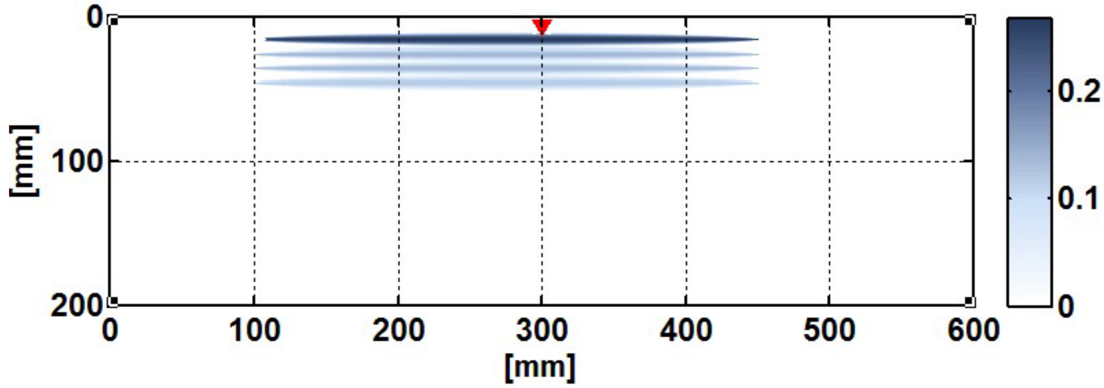

0
100
200
[mm]
0
100
200
300
400
500
600
[mm]
0.2
0.1
0

(a)

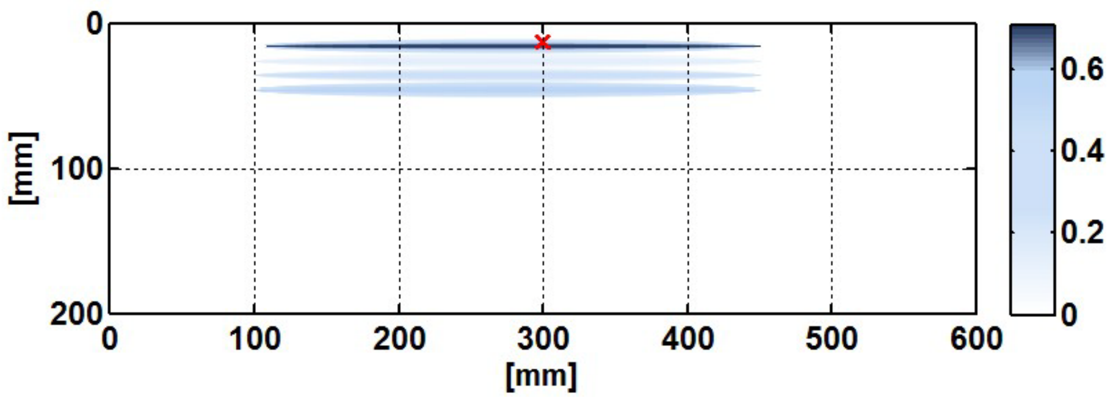

0
100
200
[mm]
0
100
200
300
400
500
600
[mm]
0.6
0.4
0.2
0

(b)

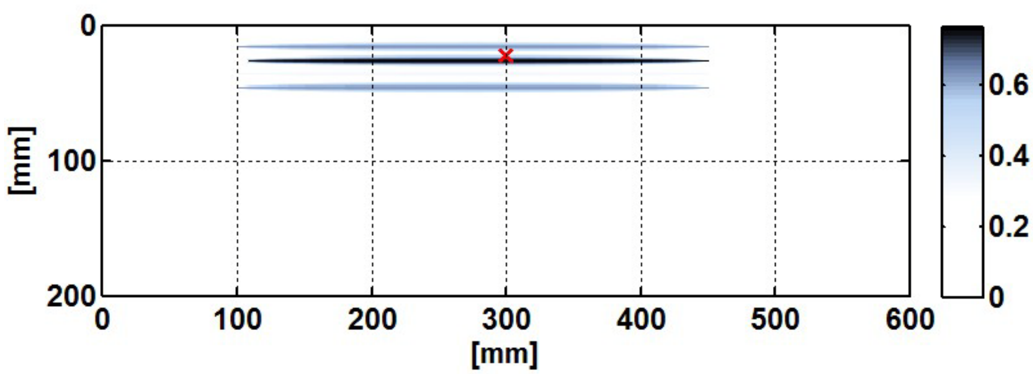

0
100
200
[mm]
0
100
200
300
400
500
600
[mm]
0.6
0.4
0.2
0

(c)

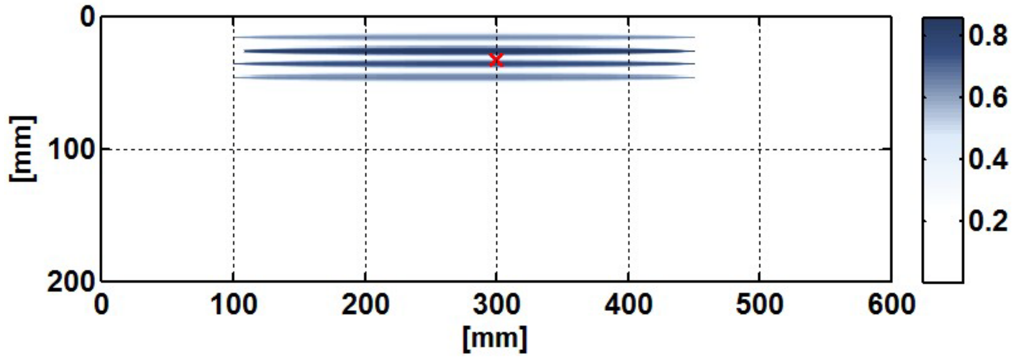

(d)

Figure 6.8 Fatigue crack monitoring results based on DPP extracted from TRM (a) 0 mm length fatigue crack (b) 7 mm length fatigue crack (c) 17 mm length fatigue crack (d) 27 mm length fatigue crack (4 sensing paths)

Figure 6.9 show the details of microscope photos of the fatigue crack when it is growing to 27 mm. It can be seen that the fatigue crack was divided into three different parts due to thousands of cyclic loading, which are open part, open-close part and close part. And its possible for us to detect the fatigue crack of open part and open-close part by proposed GW-SHM method but difficult to detect the totally close part by the same approach.

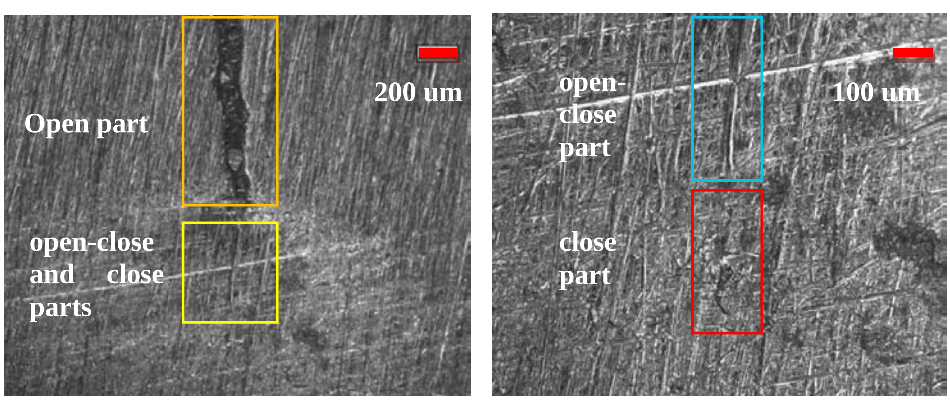

(a) (b)

Figure 6.9 Microscope photos of fatigue crack (a) open part, open-close and close parts (b) open-close part and close part

By employing 16 sensing paths and 35 sensing paths detailed in Table 6.2, the DPP image results according to different fatigue crack lengths were illustrated in Figures 6.10 and 6.11. We can see that it's difficult to identify the fatigue crack tip when it propagated along the sensors P1 to P4. However, the sum of pre-normalized DPP values shown in Figure 6.12 increases with the propagation of fatigue crack from 7 mm to 27 mm, which demonstrates that the sensing paths involved in the affected area are significantly affected and affected worse due to the fatigue crack initiation and propagation.

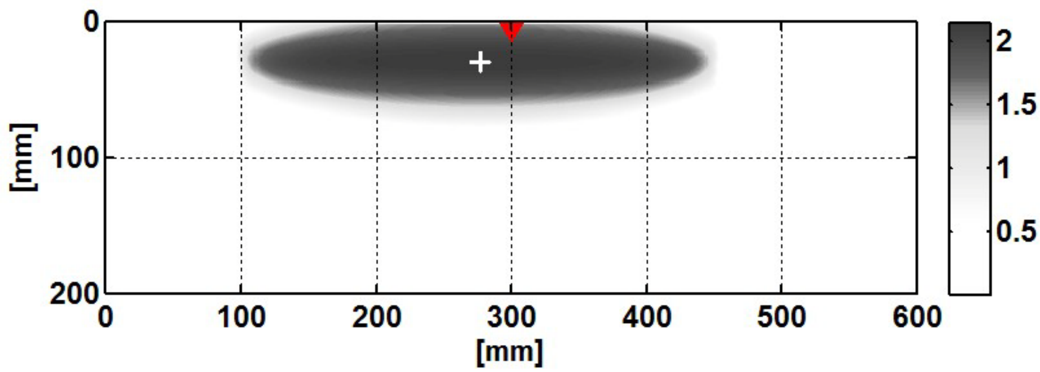

(a)

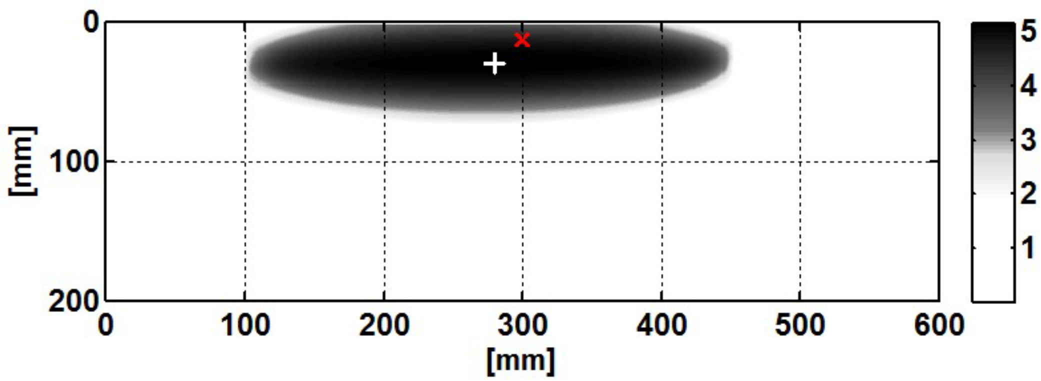

(b)

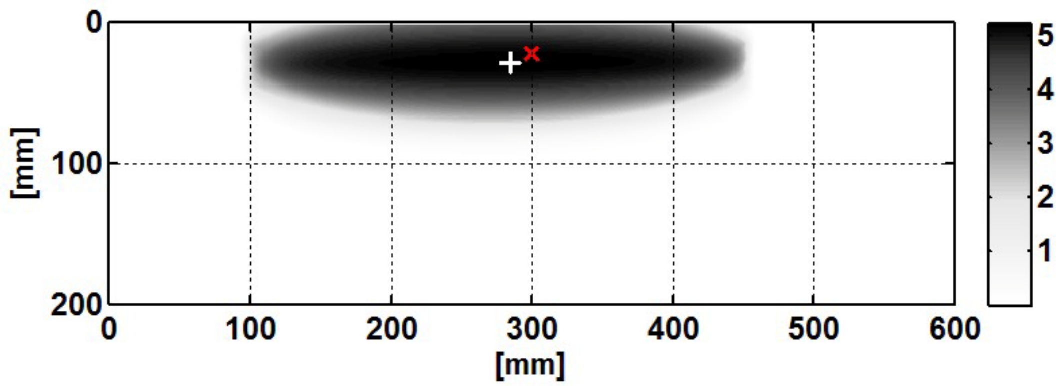

(c)

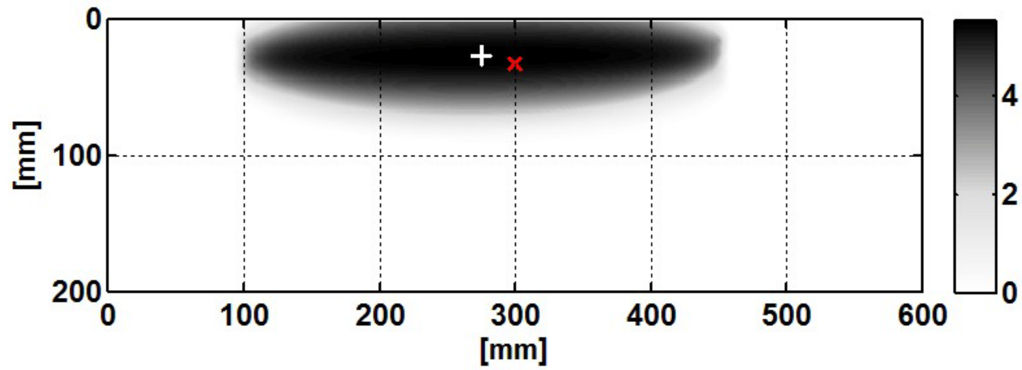

(d)

Figure 6.10 Fatigue crack monitoring results based on coefficients extracted from TRM (a) 0 mm length fatigue crack (b) 7 mm length fatigue crack (c) 17 mm length fatigue crack (d) 27 mm length fatigue crack (16 paths)

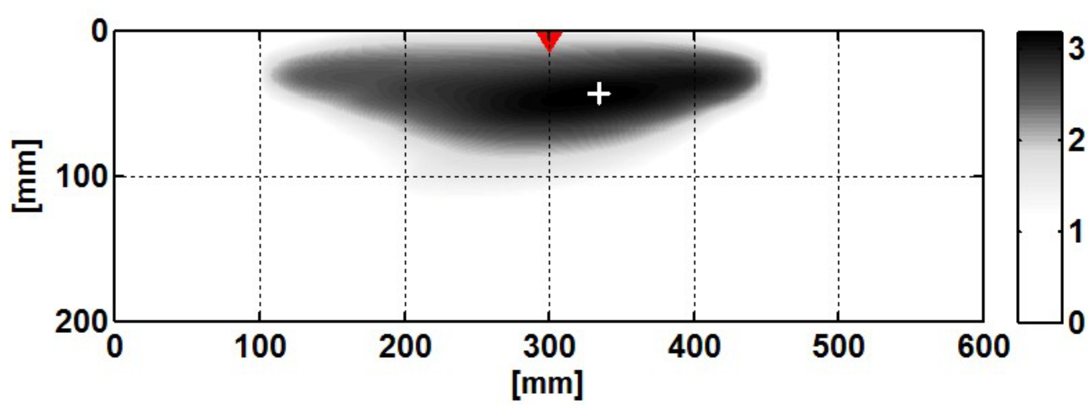

(a)

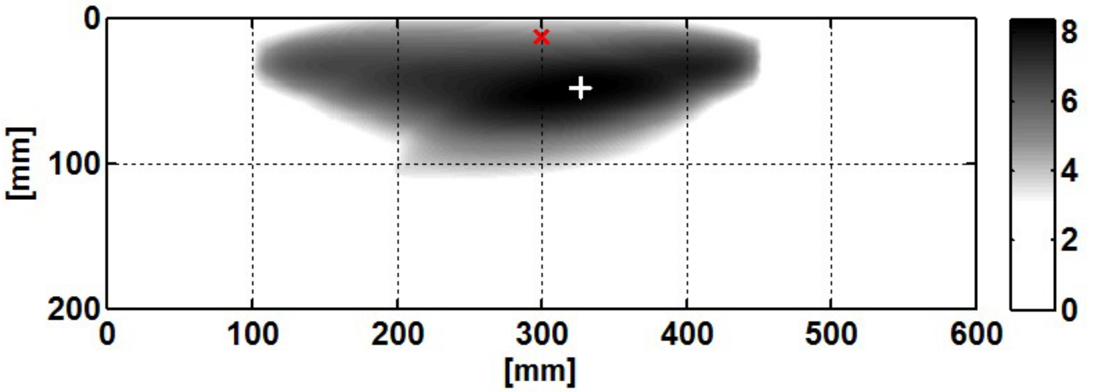

(b)

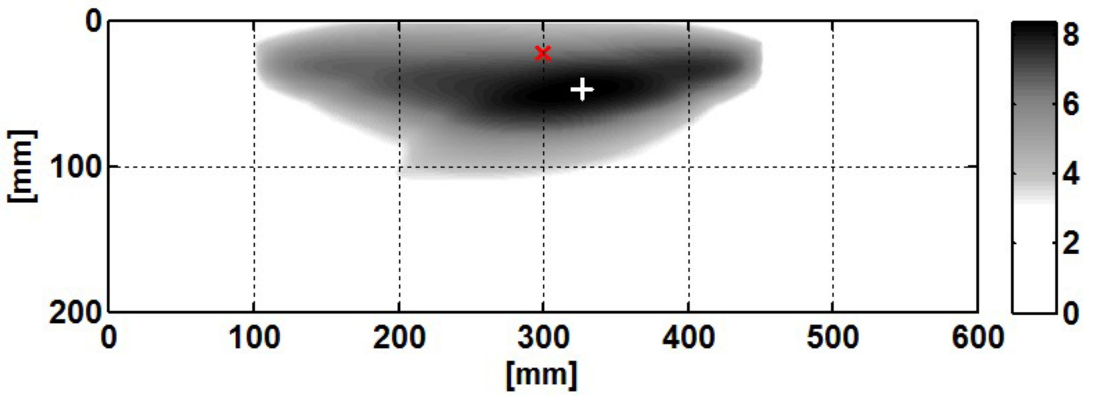

(c)

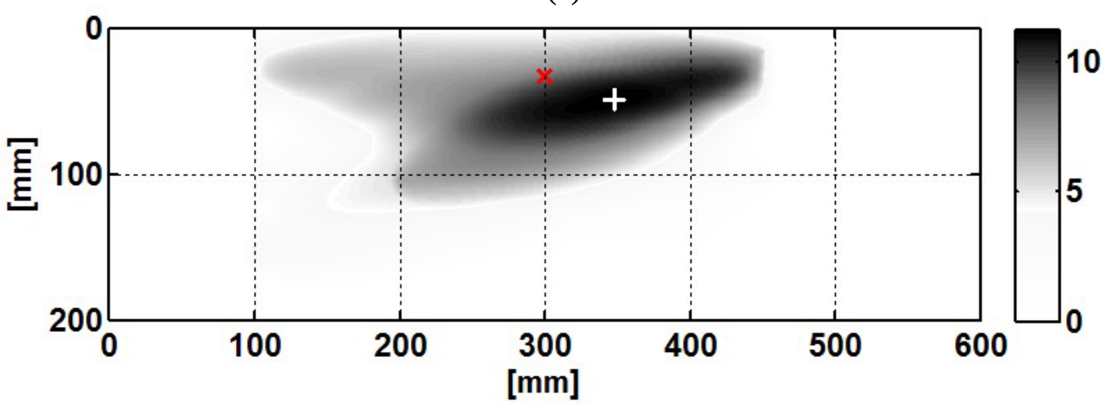

(d)

Figure 6.11 Fatigue crack monitoring results based on coefficients extracted from TRM (a) 0 mm length fatigue crack (b) 7 mm length fatigue crack (c) 17 mm length fatigue crack (d) 27 mm length fatigue crack (35 paths)

The maximum in sum of DPP value obtained from Figures 6.10 and 6.11 were detailed in Table 6.3 which were normalized by non-fatigue value, meaning the damage degree and a kind of damage index. And corresponding tendency with fatigue crack propagation can be seen from Figure 6.12. Results show that the damage index is increased with the growth of fatigue crack for all chosen sensing paths, which demonstrates the reliability of the DPP imaging approach based on TRM.

Table 6.3 Maximum in sum of DPP values

Damage Index / Path No.	Notch (0 mm length fatigue crack)	Notch+ 7 mm length fatigue crack	Notch+ 17 mm length fatigue crack	Notch+ 27 mm length fatigue crack
4	1	2. 6379	2. 8454	3. 1017
16	1	2. 4103	2. 4471	2. 5841
35	1	2. 6253	2. 6171	3. 5127

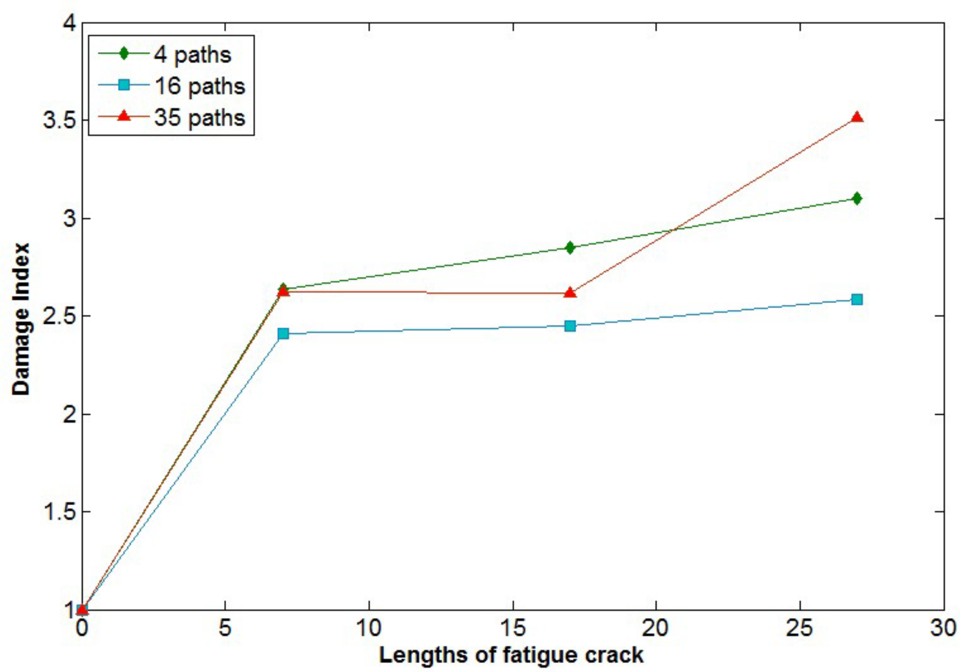

Figure 6.12 Fatigue crack monitoring results based on different sensing paths

6.2.2.3 Transmission coefficient-based signal interpretation

Method based on transmission coefficients is effective for the assessment of fatigue crack propagation, which can be obtained by normalizing amplitude values of wave package corresponding to baseline data in the time domain. Figure 6.13 illustrates zoom view of S_0 wave package transmitted from P1 to P9 from original signal data. It can be seen that differences between S_0 parts of transmitted wave components according to different fatigue crack lengths are easily figured out and the corresponding transmission coefficients were extracted and listed in Table 6.4.

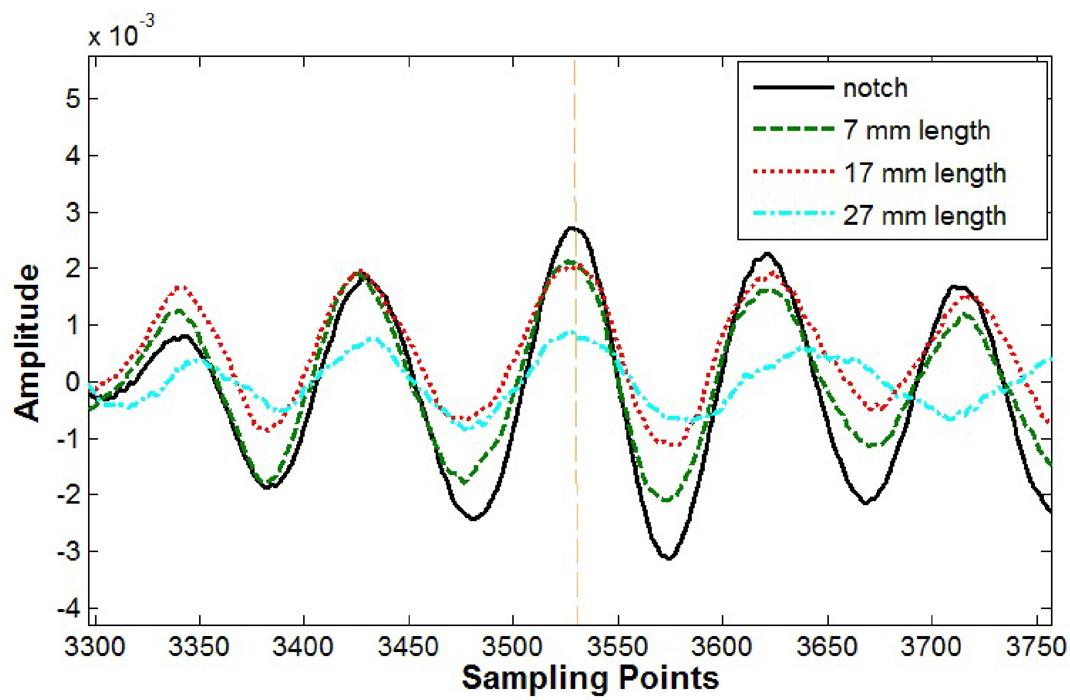

Figure 6.13 Original signal from experiments of sensing path $P_{1,9}$

Curves of transmission coefficients with regard to crack lengths were established and shown in Figure 6.14. It is noticed that the transmission coefficients decrease with the crack length, implying that less wave signals penetrate through the fatigue crack with the growth of the crack. FEM results obtained by the same procedure of previous studies are also show the same tendency which verify the experimental results.

Table 6.4 Transmission coefficients obtained from experiments and FEM

Cases / Trans-mission Coefficients	Notch	Notch+ 7 mm length fatigue crack	Notch+ 17 mm length fatigue crack	Notch+ 27 mm length fatigue crack
Experiments	1	0.780103	0.754405	0.320778
FEM	1	0.86468	0.72446	0.52847

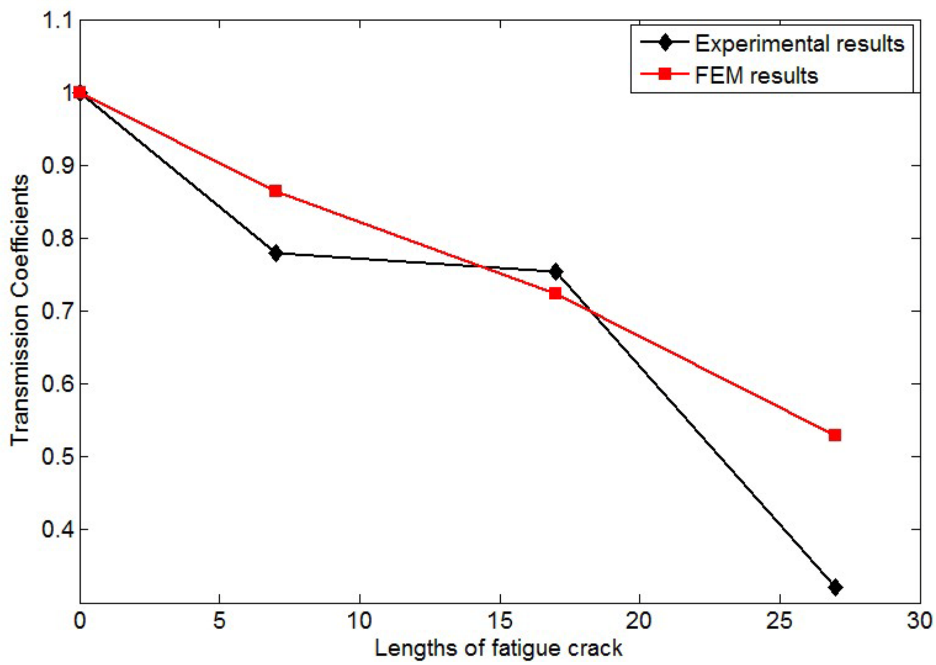

Figure 6.14 Transmission coefficients from $P_{1,9}$ by experiments and simulations

6.2.3 Discussion

Probabilistic damage diagnostic algorithms based on ToF and TRM coefficients were validated experimentally for a steel plate with an introduced fatigue crack. The algorithm is independent of the analysis of detailed information of GW signals from individual sensing paths. The location of the fatigue crack was firstly detected using extracted FICs with image algorithm and then the degree of changes in signals corresponding to the propagation of the fatigue crack was calibrated by values of DPPs extracted from TRM**,** using the captured signals and the reconstructed signals, respectively. Estimations of four fatigue crack lengths were performed using both the wave signals captured at states of the 0 mm, 7 mm, 17 mm and 27 mm lengths fatigue cracks by 4, 16 and 35 sensing paths. The identified location of fatigue crack and monitoring of fatigue crack propagation from ToF-based, TRM-based and transmission coefficients-based methods agreed well with the actual situations, demonstrating the algorithm with the applications of proposed method was capable of locating and monitoring fatigue crack in plate-like structures.

6.3 Monitoring of Fatigue Crack Growth Using PCA on GW Signal

6.3.1 Experimental Study

6.3.1.1 Testing setup and waveform analysis

In the next section, the same steel plate was employed for monitoring of the fatigue crack which propagates to 37 mm and a PZT network was employed including 10 circular PZT wafers with the same size of previous studies in dimension were surface-mounted on the plate, in which wafers P1-P5 play as actuators respectively and wafers P6-P10 are sensors correspondingly as a pitch-catch configuration, detailed in Figure 6.15.

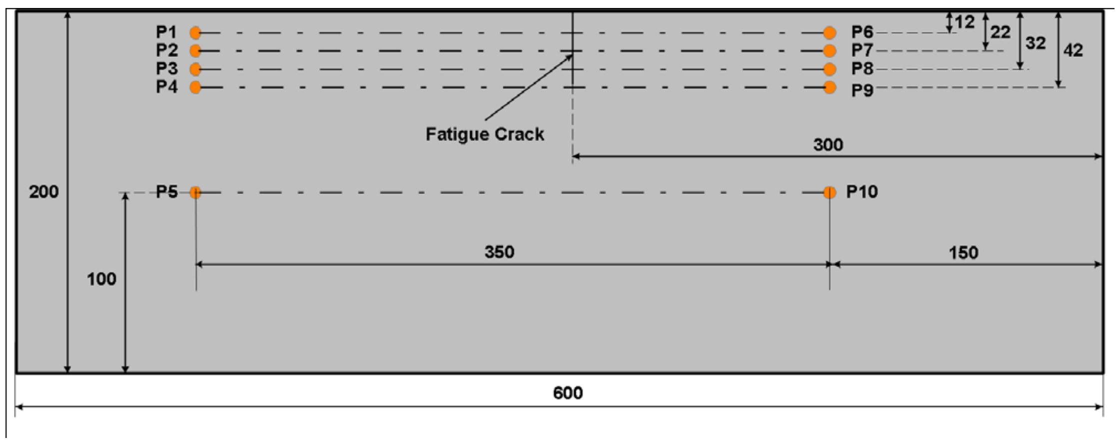

Figure 6.15 Schematic diagram of specimen and PZT positions (unit: mm)

For GW actuation and acquisition, a 5-cycle Hanning-windowed toneburst at a central frequency of 0.2 MHz was programmed and actuated by an Agilent® E1441 arbitrary waveform generator. After being converted by a built-in D/A converter and amplified by a Piezo system amplifier (EPA-104), an electric field was imposed on the PZT actuator with a peak-to-peak voltage of 60 V. Dual-channel synchronous signal acquisition was performed on individual PZT sensors by a digitizer (Agilent® E1437A) through the IEEE-488 bus at a sampling rate of 20.48 MHz. A signal conditioner (Agilent® E3242A) was used to condition the signal and complete the functions of amplification, de-noising, electrical isolation and multiplexing, before the signal was acquired by the digitizer. With the thickness and mechanical properties of the steel plate (Young's modulus = 210 GPa, Density = 7850 kg/m3, Poisson's ratio = 0.28), the theoretical phase and group velocities of the GW modes calculated by DISPERSE® [121] in terms of excitation frequency up to 1.6 MHz were plotted in Figure 6.16, where the S_0 and A_0 modes show less dispersive phenomena at the frequency of 0.2 MHz with group velocities of 5280 m/s and 3242 m/s, respectively.

During the fatigue testing, GW actuation and acquisition were accomplished in the unloading condition when the length of a fatigue crack was 7 mm, 17 mm, 27 mm and 37 mm generated at different number of cycles, denoted as C1, C2, C3 and C4, respectively. All signal data were first processed by a linear-phase bandpass signal filter [122] to filter out the noise from different frequency bands. Figure 6.17 (a) compared the purified signals for the sensing path P3-P8 for the cases of benchmark condition (with an artificial notch only) and C2. It is shown that the A_0 mode with a group velocity of 3116.5 m/s is more dominant than the S_0 mode with a group velocity of 5251.3 m/s at the frequency of 0.2 MHz although the latter arrives first in the time sequence, achieving a good agreement with the theoretical results of group velocities. The dominance of the A_0 mode is mainly attributed to the factor of the diameter of PZT wafers (6.9 mm) selected for actuators and sensors, which is close to the half of wavelength of the A_0 mode at 0.2 MHz (around 12 mm) for this specimen. Such a configuration proved effective for achieving maximal magnitude of desired GW mode excited and captured by PZT elements in a previous study [123]. The A_0 mode was therefore selected for monitoring crack growth in this section. Amplitude difference is also observed in Figure 6.17 (a) between these two conditions due to wave scattering and possible mode conversion from the crack tip. However, no significant difference can be observed directly in the signals between benchmark and C3, shown in Figure 6.17 (b).

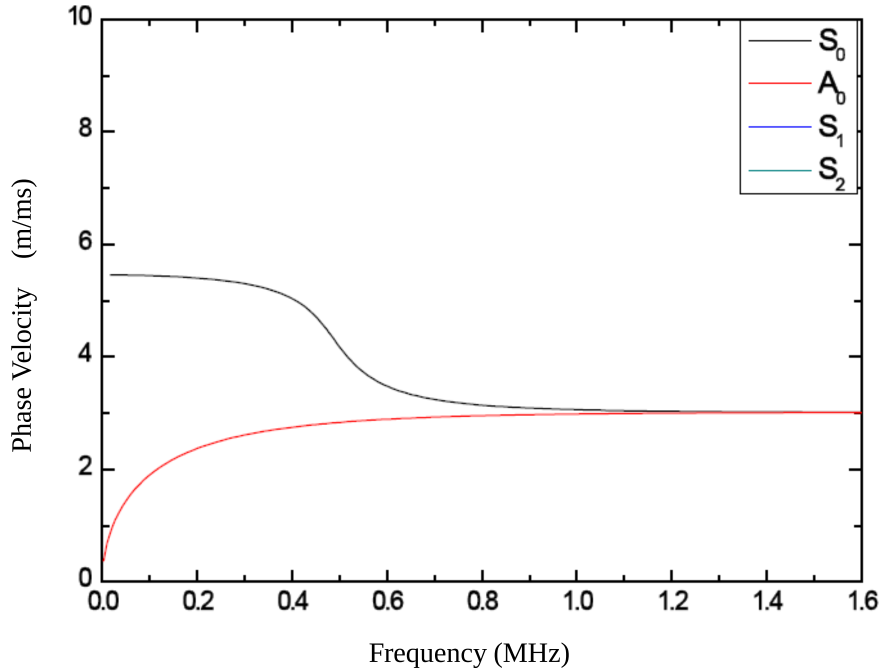

(a)

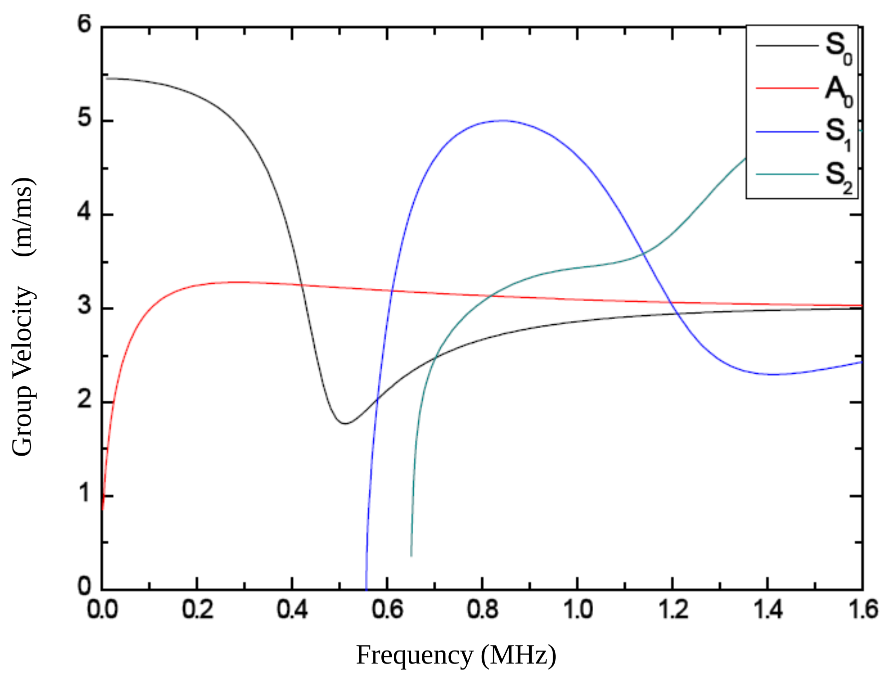

(b)

Figure 6.16 Dispersion curves for a steel plate of 5 mm in thickness (a) phase velocity (b) group velocity

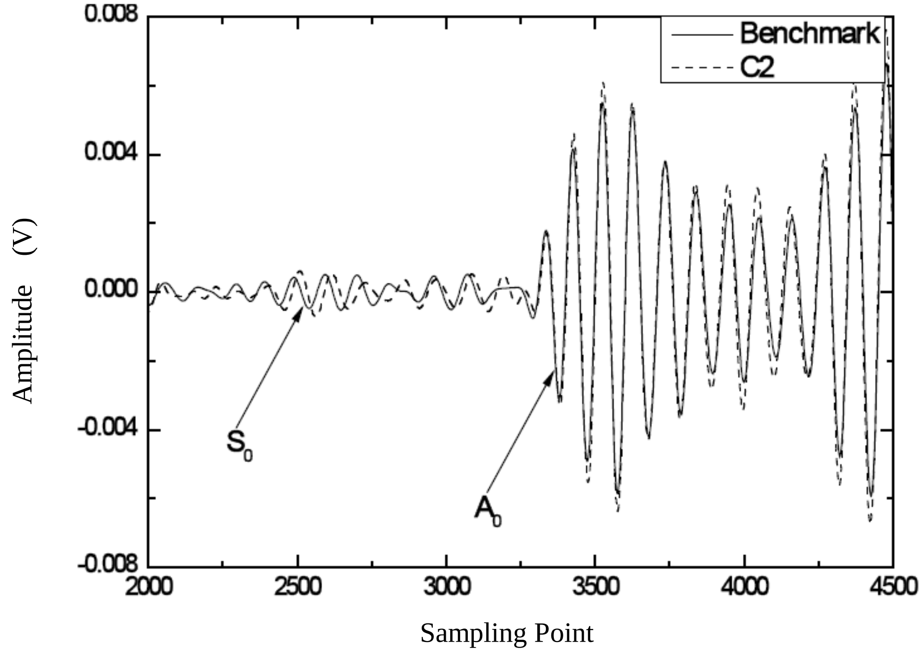

(a)

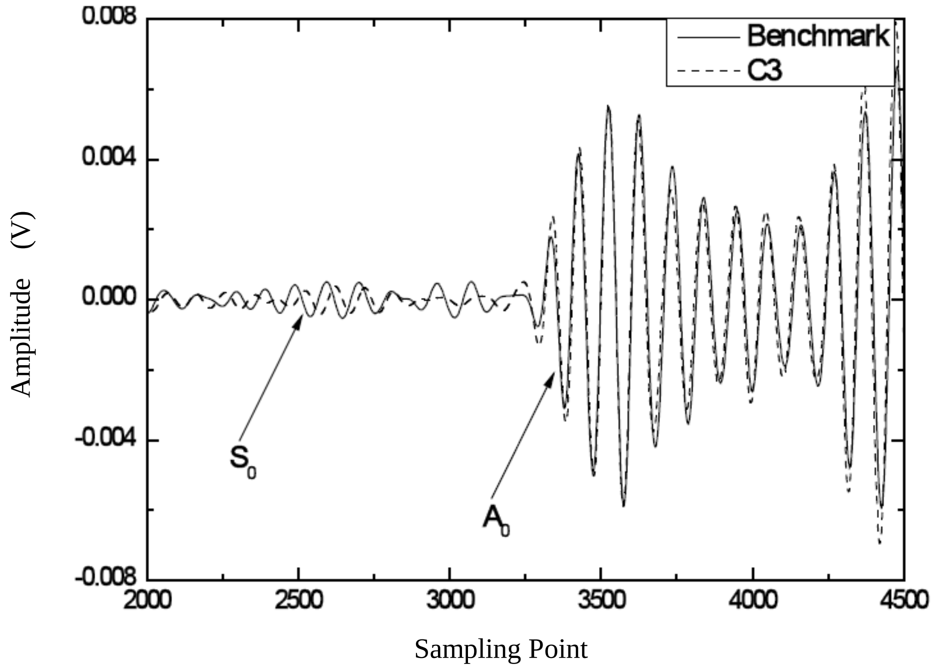

(b)

Figure 6.17 Comparison of waveforms for sensing path P3-P8 at the excitation frequency of 0.2 MHz (a) benchmark vs. C2 (b) benchmark vs. C3

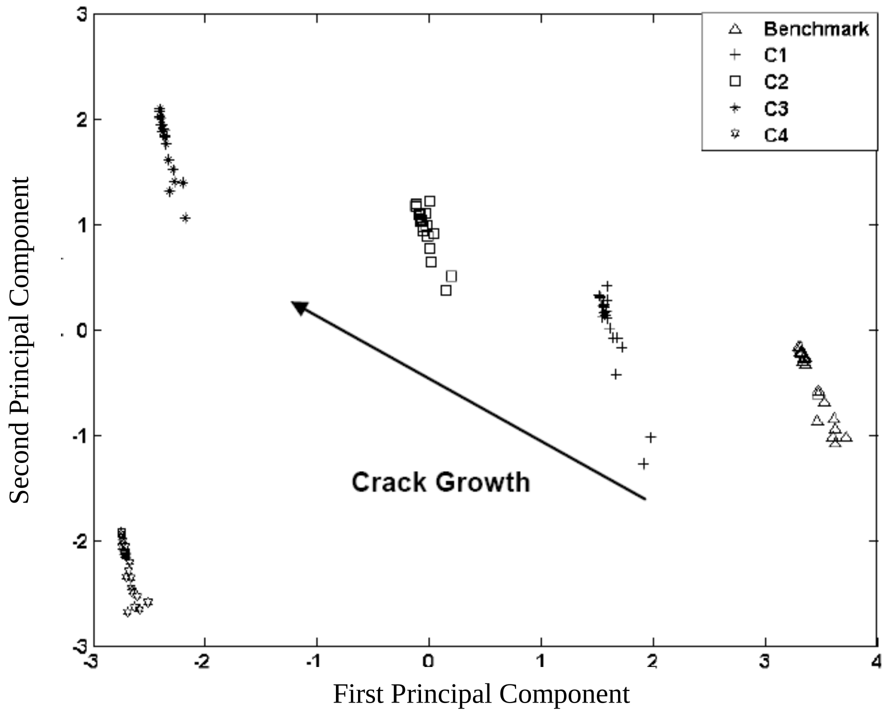
Benchmark
C1
C2
C3
C4
Crack Growth
Second Principal Component
First Principal Component
3
2
1
0
-1
-2
-3
-3
-2
-1
0
1
2
3
4

(a)

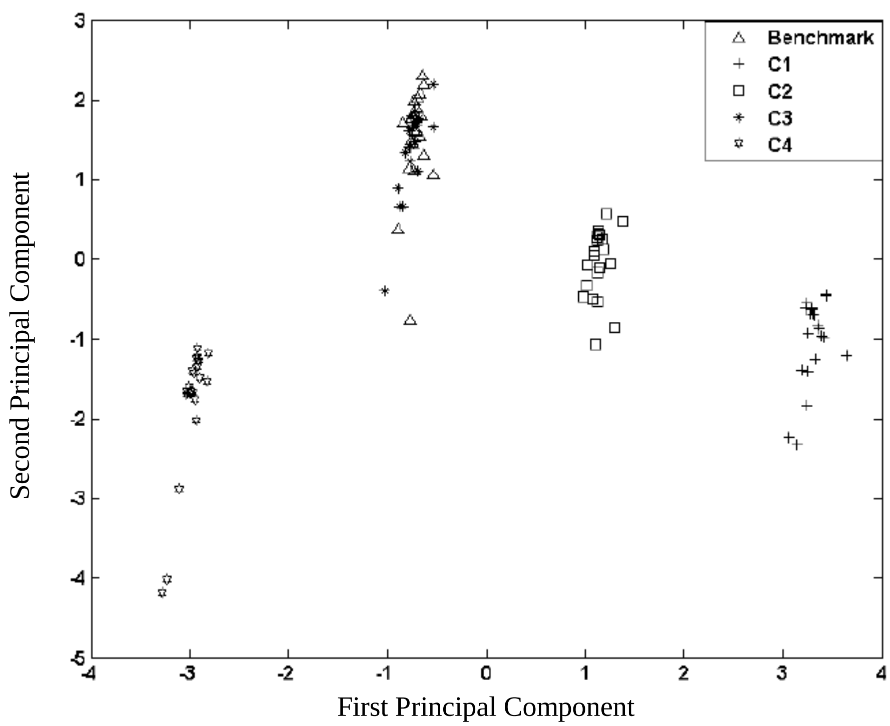
Benchmark
C1
C2
C3
C4
Second Principal Component
First Principal Component
3
2
1
0
-1
-2
-3
-4
-5
-4
-3
-2
-1
0
1
2
3
4

(b)

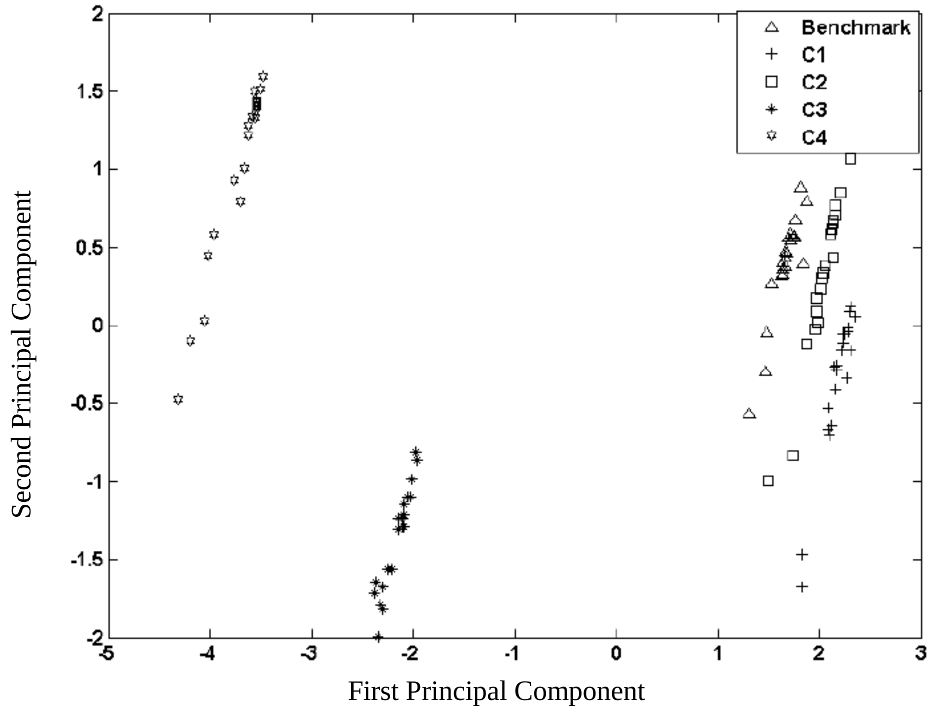

(c)

Figure 6.18 Distribution of the first two principal components of different crack lengths for sensing paths (a) P1-P6 (b) P3-P8 (c) P5-P10

6.3.1.2 Observation of crack growth based on PCA

Instead of direct comparison of complex waveforms to differentiate the effect of crack length, eight statistical parameters in the time domain as variables were selected in total for individual sensing paths, namely signal variance (var), Kfactor, crest factor (CF), peak-to-peak (ppk), skewness (s), kurtosis (k), Shannon entropy (enp) and correlation coefficient (ρ), defined as [104 , 122 , 124]

$$\mathrm{var} = \frac{1}{N}\sum_{i=1}^{n} x_i - \bar{x}; \quad \mathrm{Kfactor} = \max(x_i) \times \mathrm{RMS}$$

$$\mathrm{CF} = \frac{\max(x_i)}{\mathrm{RMS}};\ \mathrm{ppk} = \max(x_i) - \min(x_i)$$

$$s = \frac{\frac{1}{N}\sum_{i=1}^{n}(x_i - \bar{x})^3}{\left[\sqrt{\frac{1}{N}\sum_{i=1}^{n}(x_i - \bar{x})^2}\right]^3};\ \ k = \frac{\frac{1}{N}\sum_{i=1}^{n}(x_i - \bar{x})^4}{\left[\frac{1}{N}\sum_{i=1}^{n}(x_i - \bar{x})^2\right]^2} \tag{6.5}$$

$$\mathrm{enp} = \sum_{i=1}^{n} x_i \ln(x_i);\ \ \rho = \frac{\mathrm{cov}(x_i, S_e)}{\sigma_{x_i}\sigma_{S_e}}$$

where x_i is the dominant A_0 mode and RMS is the corresponding root mean square. S_e is the standard excitation signal generated by the actuator and cov and σ are the corresponding covariance and standard deviation [125]. In particular, high-order statistical parameters of a signal, e.g. kurtosis as an indication of the “peakedness” of amplitude distribution, and Shannon entropy as a demonstration of energy concentration, have been employed for processing and analysis of dispersive wave signals with respective advantages and disadvantages [122 , 124].

In order to increase the size of the data set for PCA calculation, each wave signal captured at different stages of testing was added with white Gaussian noise with a SNR from 40 dB, which is equivalent to 100 times in signal amplitude and therefore the signal can be regarded as same as the original one, to 20 dB (10 times in signal amplitude) with an incremental step of -1 dB [130]. Eight statistical parameters were then calculated for the 21 contaminated signals for 5 different specimen conditions (benchmark and 4 crack lengths). As a result, 5 matrixes for 5 sensing paths with an identical dimension of 105×8 each were established, where 105 represented the total number of wave signals and 8 denoted the number of statistical parameters as damage indices from each signal.

Following the procedure detailed mentioned before, PCA as a linear transformation were then applied to separately project these five matrixes of 105×8 into five new matrixes with a lower dimension where only the first few principal components were retained as the most important vectors. The original eight statistical parameters containing crack information were therefore substituted by the first few principal components as new damage indices, achieving efficient data compression and fusion. For example, Figures 6.18 (a)-(b) plotted the first two principal components against each another for sensing paths P1-P6 and P3-P8, respectively. It is evident that the principal components in the new coordinate system were classified into five distinct clusters with acceptable deviation in each because of the added noise, indicating different structural conditions with the growth of a fatigue crack. In detail, the principal component clusters for sensing path P1-P6 generally leave increasingly further away from the benchmark condition, demonstrating a quasi-linear trend with an increase in crack length. In contrast, non-linearity is observed for the sensing path P3-P8 and the clusters for benchmark and C3 are almost overlapped, similar to the situation shown in Figure 6.17 (b). However, the difference between this two scenarios can be highlighted by PCA when the third principal component was introduced, shown in Figure 6.19 where the principal components were plotted against one another. Figure 6.18 (c) also plotted the distribution of the first two principal components for sensing path P5-P10. It is observed that the clusters for C3 and C4 as longer crack lengths are quite isolated to the consistent clusters for benchmark, C1 and C2 as smaller crack lengths, implying only a longer crack starts to influence the sensing path P5-P10 due to the mode conversion at the tip. The singularity of C4 as the longest crack length in Figures 6.18 and 6.19 should also be attributable to the bonding degradation of surface-mounted PZT wafers with the progress of the fatigue testing.

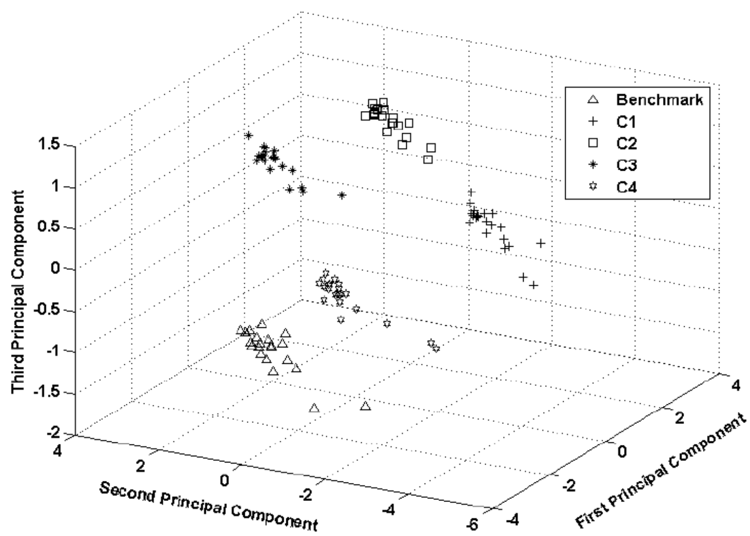

Figure 6.19 Distribution of the first three principal components of different crack lengths for sensing path P3-P8

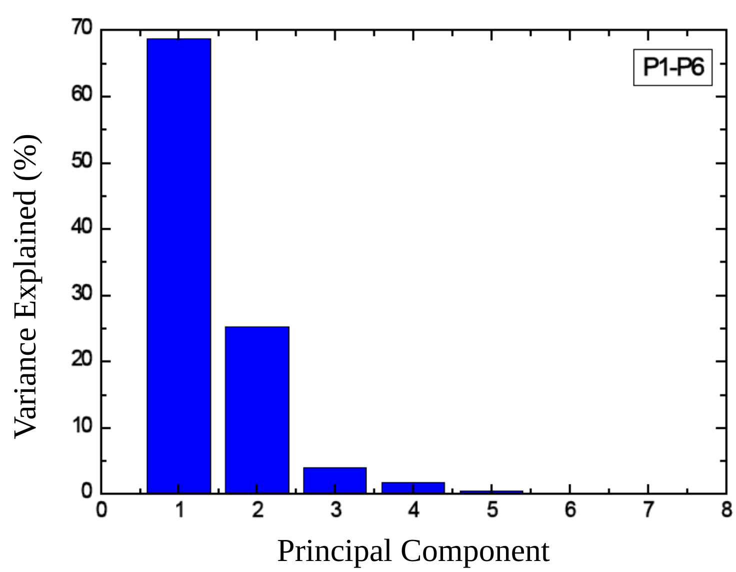

(a)

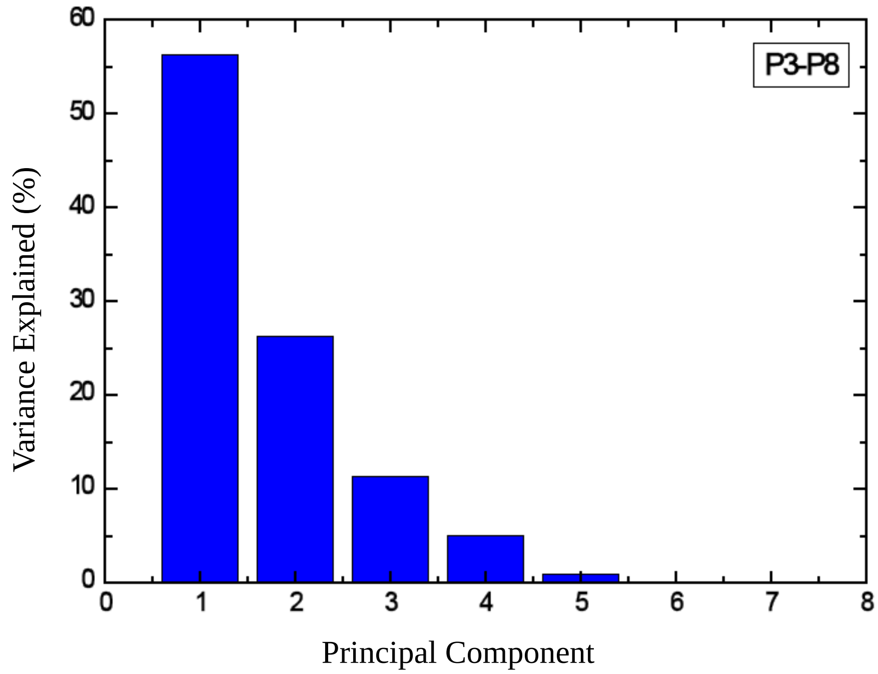

(b)

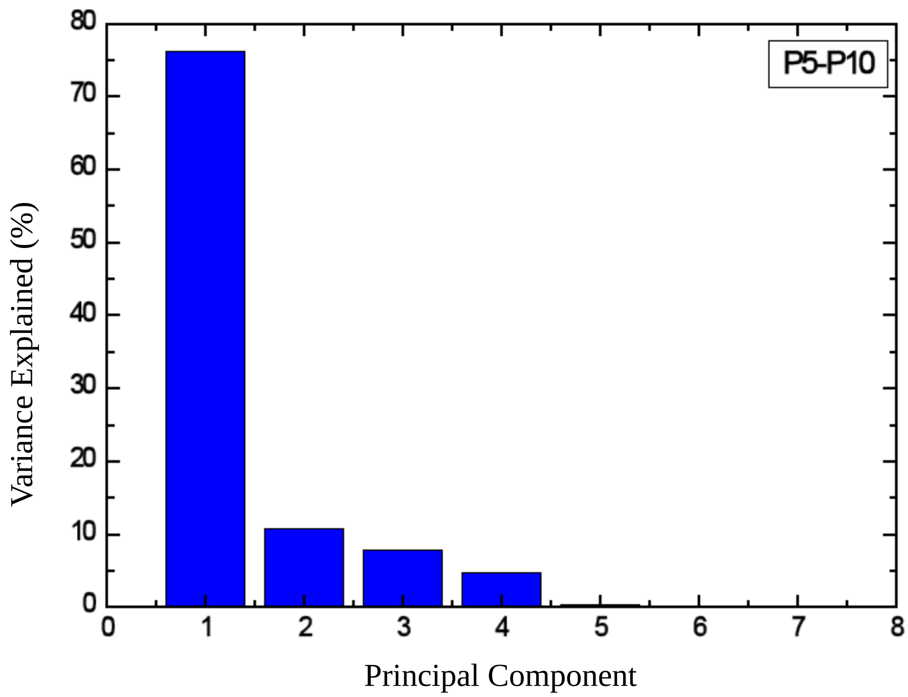

(c)

Figure 6.20 Signal variances explained by the principal components for sensing paths (a) P1-P6 (b) P3-P8 (c) P5-P10

The main reason for the different properties of principal components for sensing paths P1-P6 and P3-P8 was due to the fact that the generation and acquisition of GW signals were completed in the unloading condition. For sensing path P1-P6, which was the first path affected by crack propagation, the hairline fatigue crack always evolved from closing or semi-contact to full opening monotonously even under the unloading condition. In Contrast, the captured wave signals for sensing path P3-P8 when crack length was 27 mm was actually the combination of directly transmitted wave crossing certain contacted crack surfaces because of unloading condition and the scattered wave from the crack tip, which was quite different to the situation of smaller crack lengths of 7 mm and 17 mm where only the wave scattering from the crack tip was received. Nevertheless, PCA is still sensitive to distinguish these scenarios as demonstrated in Figure 6.19.

The performance of principal components that represent the original data set can be illustrated by the amount of the variances of original data covered by the first few principal components [41]. The percentage distributions of data variances for involved principal components were shown in Figures 6.20 (a)-(c) for abovementioned sensing paths, respectively. It is noticed that the first two principal components for these three paths all account for over 80% of the total variability of the original data set and there was generally a clear difference in the amount of variance between them and the remaining principal components. It is therefore reasonable to characterize and visualize the original high-dimensional data set using the first few principal components only. In particular, it is also reasonable to introduce the third principal component for sensing path P3-P8 as it account for a considerable variance of the original data set as well.

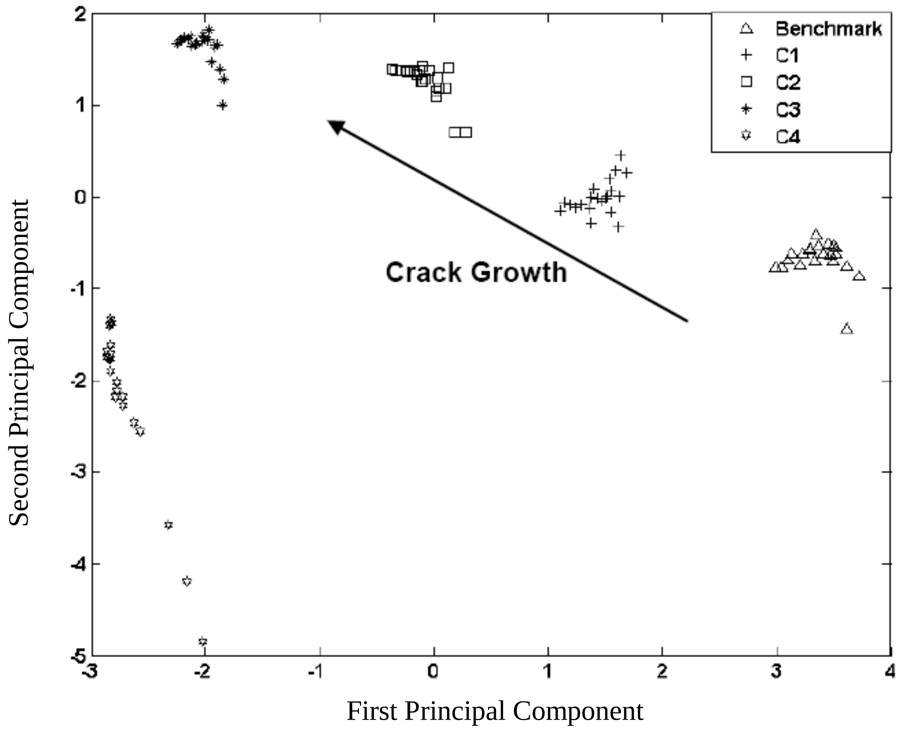
Benchmark
C1
C2
C3
C4
Crack Growth
Second Principal Component
First Principal Component

(a)

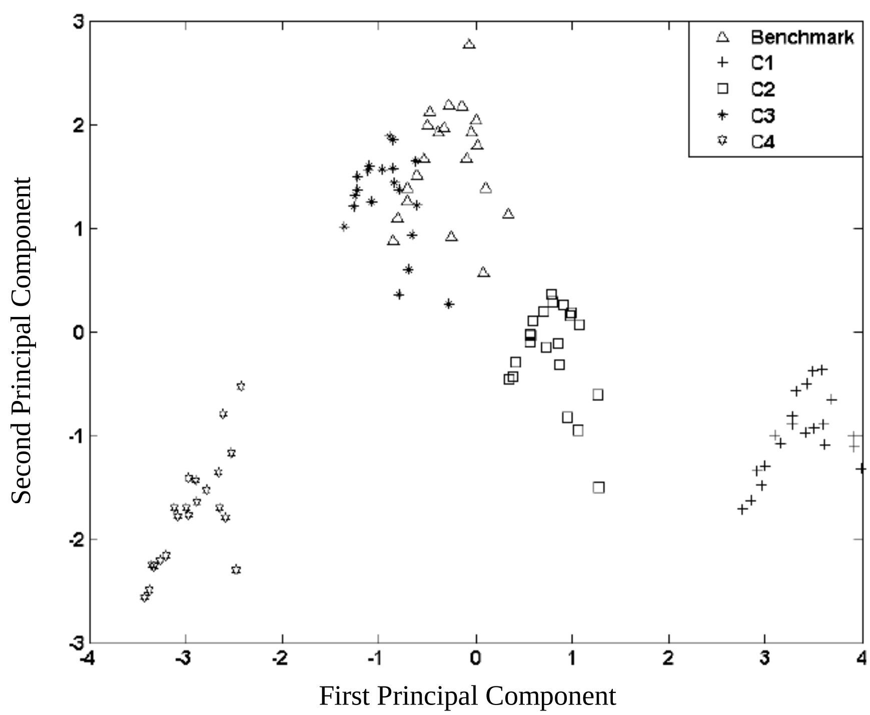
Benchmark
C1
C2
C3
C4
Second Principal Component
First Principal Component

(b)

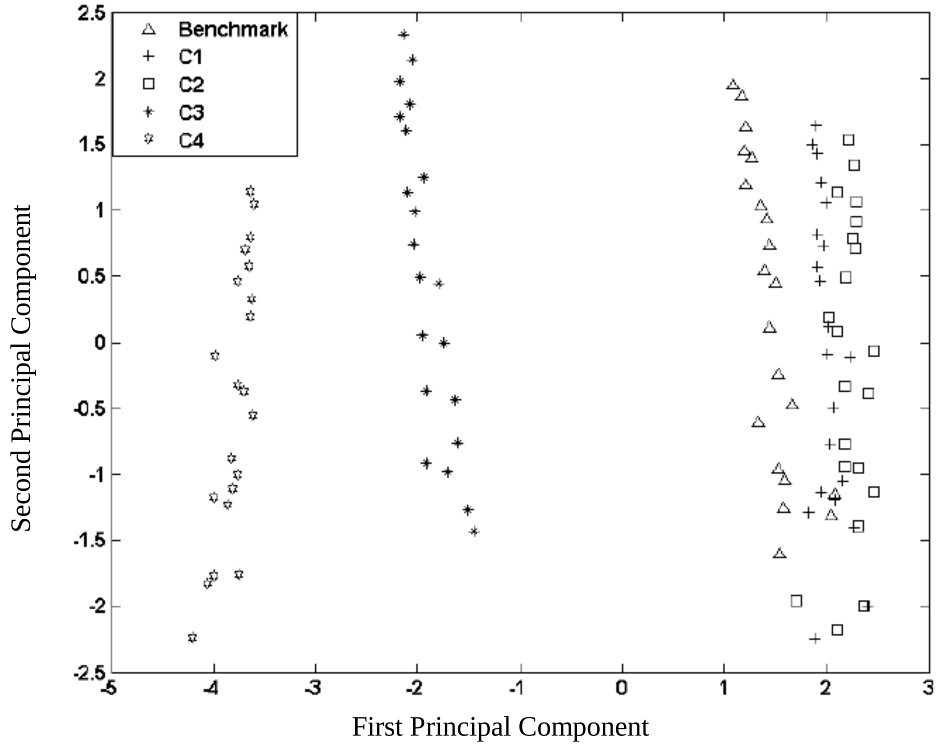

(c)

Figure 6.21 Distribution of the first two principal components of different crack lengths with temperature change for sensing paths (a) P1-P6 (b) P3-P8 (c) P5-P10

6.3.2 Discussion

For long term stability and efficiency of damage identification, a DI should be sensitive to the damage while maintaining the robustness to the environmental noise and varying conditions [126]. For instance, it is appreciated that the decrease in environmental temperature would increase the group velocities of GW modes whereas the increase in temperature would result in opposite trends [98, 127]. It is therefore of significance to investigate the robustness of principal components with respect to temperature changes, in comparison with other statistical parameters as damage indices. For this purpose, the 21 noise-contaminated wave signals were further artificially shifted forward from 0 to

20 sampling points respectively in the time domain for each sensing paths to simulate the earlier arrival of the wave mode because of temperature decrease, where the signal with a SNR of 20 dB was shifted with 20 sampling points as the worst scenario, influenced by the severest combined effect of noise and temperature.

Following the similar procedure, PCA was accomplished again on the new established matrix of 105×8 for individual sensing paths, and the distributions of principal components for the same sensing paths are plotted in Figures 6.21 (a)-(c), respectively. It is evident that principal components still depicted the crack growth well, although the clusters for benchmark and C3 are still overlapped for sensing path P3-P8, and the deviation in each clusters somewhat increases for sensing path P5-P10 due to the additional adverse effect of temperature change. In particular, Figure 6.22 compared the first principal component as the most important vector in PCA and other damage indices for sensing path P1-P6, where the first principal component was successful to differentiate all crack cases, demonstrating superior robustness against interferences of noise and temperature. For single statistical parameter, the variance, Kfactor, peak-to-peak and Shannon entropy show less sensitivity to the difference between C4 and C5 but they are still capable of classifying the general conditions of different crack lengths. In contrast, the crest factor, skewness, kurtosis and correlation coefficient totally lost their niches when the environmental temperature changes. Nevertheless, PCA as an efficient approach for data fusion still displayed good compatibility to the parameters engaged in the data set even some of them perform poorly under demanding circumstances.

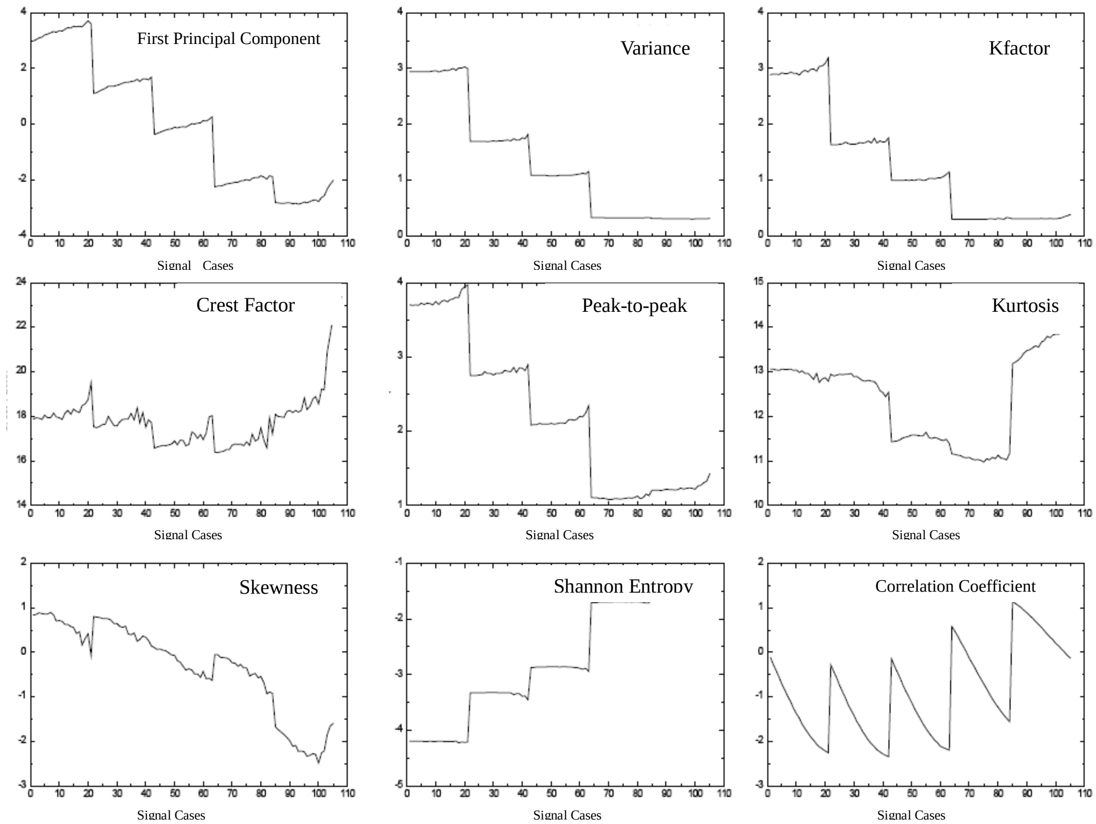

Figure 6.22 Robustness of the first principal component and typical statistical parameters in terms of temperature change, where signal cases 1-21 for benchmark; 22-42 for C1; 43-63 for C2; 64-84 for C3; 85-105 for C4

On the basis of these observations, a sub-matrix of 105×4 comprising the variance, Kfactor, peak-to-peak and Shannon entropy as robust damage indices was extracted from the original matrix, aiming to improve the classification accuracy of the proposed method. It is observed in Figure 6.23 (a) that the overlapped clusters for benchmark and C3 shown in Figure 6.21 (b) for sensing path P3-P8 now can be discriminated by the optimized sub-matrix. Furthermore, the amount of the total variability of the extracted

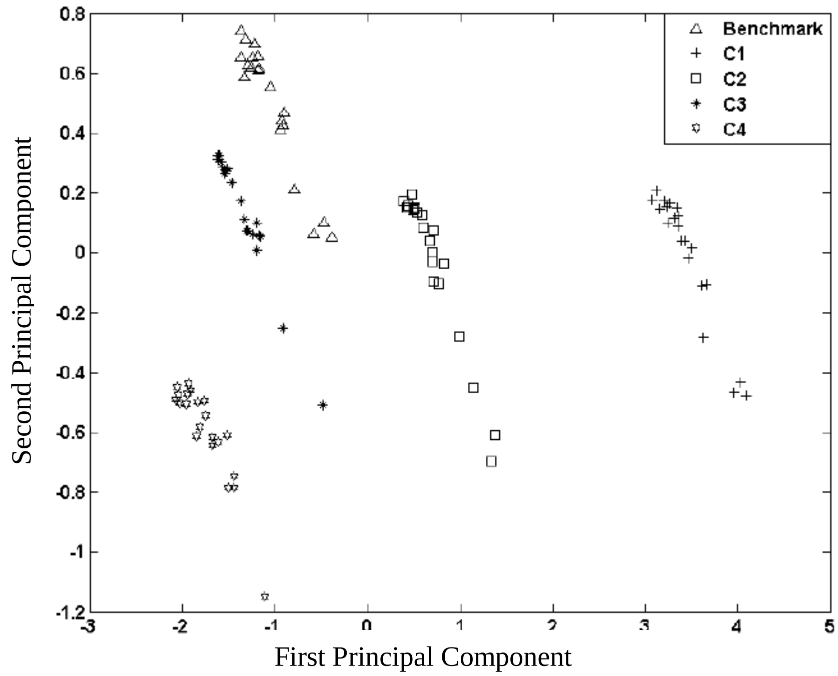

(a)

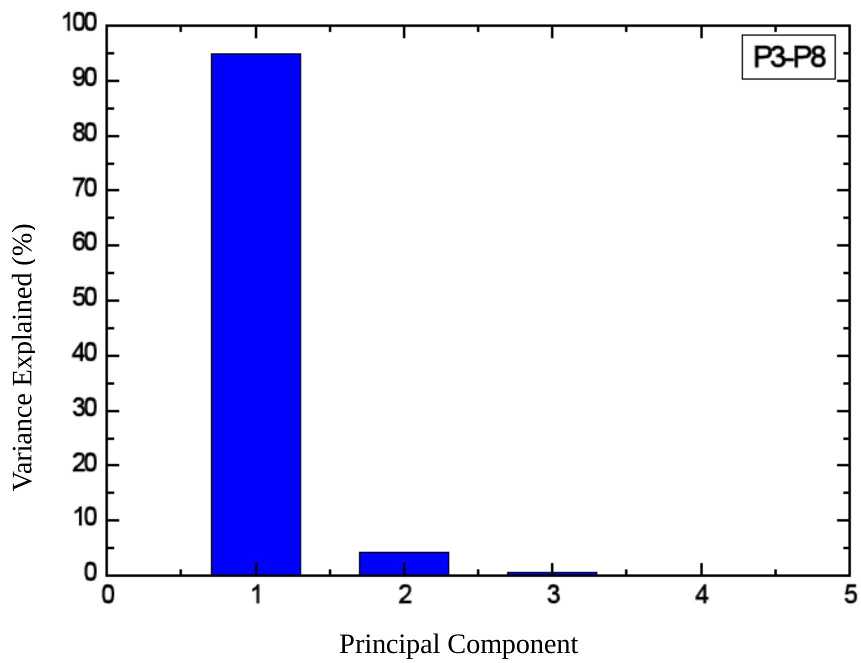

(b)

Figure 6.23 Performance of PCA in terms of temperature change using an optimized data set for sensing path P3-P8 (a) distribution of the first two principal components of different crack lengths (b) signal variances explained by the principal components data set covered by the first two principal components was also significantly increased, shown in Figure 6.23 (b), indicating that these two components are sufficient to describe the information in the data set. It is noteworthy that the variables in each column of the data set in PCA were standardized by dividing the standard deviation from all involved conditions, rather than being normalized by the benchmark values from a previous condition. In this context, the prerequisite for intact structural condition as a baseline on most current straightforward methods will no longer be necessary, provided the conditions sampled during observation are plenty enough for classification in PCA. This feature is essential for online surveillance of structural integrity development, especially for those ageing structures where the baseline condition is generally absent. However, it should also be noted that no information with respect to the location and severity of damage can be obtained directly by PCA, although the first few principal components can be regarded as new damage indices to quantify the severity.

6.4 Concluding Remarks

In this chapter, DPP-based imaging approach according to ToF, coefficients obtained from TRM and transmission coefficients were validated experimentally and numerically for a steel plate with an introduced fatigue crack. The fatigue crack propagated from 0 mm to 27 mm was firstly detected when it was growing to 7 mm using extracted FICs with image algorithm and then the fatigue crack growing from 0 mm to 27 mm was monitored by values of DPP extracted from TRM**,** using the captured signals and the reconstructed signals by 4, 16 and 35 sensing paths, respectively. Then the results were compared with experimental and FEM results from transmission coefficients.

For the PCA method, due to complex waveforms caused by possible crack opening and closing during fatigue testing, typical statistical parameters in the time domain representing wave characteristics were first extracted from the dominant A_0 mode signals as damage indices at different stages of crack propagation. PCA was then applied to the data set comprising original statistical parameters and noise-contaminated counterparts, so as to classify the structural conditions when a fatigue crack propagates in it. The robustness of principal components generated by PCA was then evaluated in terms of temperature change, whose effect on the performance of individual statistical parameters was also justified.

It is concluded that TRM and PCA are capable for structural condition classification, where some statistical parameters as damage indices are incapable of differentiating conditions with the existence of damage. The performances of TRM and PCA were sensitive to the damage involved and subsequent optimization can be conducted to improve the classification accuracy. Without any complex scrutiny in wave signals, TRM and PCA on the basis of statistic parameters which are easy to obtain are therefore a promising solutions for online monitoring of structural condition and information classification.

CHAPTER 7 Monitoring of Surface-Fatigue Crack Propagation in a Welded Steel Angle Structure Using GWs and Principal Component Analysis

7.1 Introduction

In this chapter, GW was employed to monitor the growth of a surface-fatigue crack on a WSAS with a freely arranged PZT sensor network which was surface-mounted on the structure throughout. The PZT sensor network was arranged not relying on the propagating direction of fatigue crack. After each substep of a three-point bending fatigue test, statistical characteristics from the major energy in the frequency domain were extracted as damage indices by marginal spectrum in Hilbert-Huang transform (HHT). Depending on different actuators, several different data matrices consisting of original characteristic parameters were obtained. As a substitute for massive damage indices for differentiating structural integrity status, principal components were accordingly calculated by PCA.

7.2 Marginal Spectrum in HHT

The HHT was first proposed by Huang et al in 1998 [128], as a way to decompose a signal into intrinsic mode functions (IMF) by the empirical mode decomposition (EMD) method, to obtain instantaneous frequency data. Compared with the time domain, the frequency domain always presents the essence of signals. HHT is designed based on frequency, and works well for data which are non-stationary and nonlinear. The procedure of the EMD method is described in the following [129].

For a signal *a(t)*, identify all the local extrema in *a(t)* and connect all the local maxima by a cubic spline line as the upper envelope and repeat the procedure for the local minima to produce the lower envelope. Thus, the upper and lower envelopes should cover all the data between them. Their mean is m and the difference between the signal and *m* is given by

$$\mathrm{a(t) - m = h.} \tag{7.1}$$

After the first round of sifting, the crest may become a local maximum. New extrema generated in this way actually reveal proper modes lost in the initial examination. In the subsequent shifting process, *h* can be treated as the first IMF component, c_1, when it meets the requirement of stoppage criteria. Then, separate c_1 from the rest of the signal by

$$\mathrm{a(t) - c_1 = r,} \tag{7.2}$$

where *r* is treated as the new signal and subjected to the same shifting process as described above. This procedure can be repeated for all subsequent IMF components, c_n (n=1,2,……) and stopped finally when the residue r_n becomes a monotonic function from which no more IMF can be extracted,

$$\mathrm{r_{n-1} - c_n = r_n.} \tag{7.3}$$

From above formula, it can be induced that

$$\mathrm{a(t) = \textstyle\sum_{k=1}^{n} c_k + r_n.} \tag{7.4}$$

Ignoring r_n in Equation (7.4), and applying the HT to every IMF component yields

$$\mathrm{a(t)} = \mathrm{Re}\sum_{k=1}^{n} \mathrm{a_k}\,(\mathrm{t})\mathrm{e}^{\mathrm{j}\emptyset_{\mathrm{k}}(\mathrm{t})} = \mathrm{Re}\sum_{k=1}^{n} \mathrm{a_k}\,(\mathrm{t})\mathrm{e}^{\mathrm{j}2\pi\int \mathrm{f}_{\mathrm{k}}^{\mathrm{i}}(\mathrm{t})\mathrm{dt}}, \tag{7.5}$$

in which a_k and *Re* stand for amplitude function in the HT and real part, respectively. The marginal spectrum can be obtained by Equation (7.6),

$$h(f^i) = \int_{-\infty}^{+\infty}(\,\mathrm{Re}\sum_{k=1}^{n} \mathrm{a_k}\,(\mathrm{t})\mathrm{e}^{\mathrm{j}2\pi\int \mathrm{f}_{\mathrm{k}}^{\mathrm{i}}(\mathrm{t})\mathrm{dt}})\mathrm{dt} = \sum_{k=1}^{n}\int_{-\infty}^{+\infty}(\mathrm{Re}\,\mathrm{a_k}(\mathrm{t})\mathrm{e}^{\mathrm{j}2\pi\int \mathrm{f}_{\mathrm{k}}^{\mathrm{i}}(\mathrm{t})\mathrm{dt}})\mathrm{dt} = \sum_{k=1}^{n} \mathrm{h_k}(\mathrm{f^i}), \tag{7.6}$$

while

$$\mathrm{h_k}(f^{\mathrm{i}}) = \int_{-\infty}^{+\infty}(\mathrm{Re}\,\mathrm{a_k}(\mathrm{t})\mathrm{e}^{\mathrm{j}2\pi\int \mathrm{f}_{\mathrm{k}}^{\mathrm{i}}(\mathrm{t})\mathrm{dt}})\mathrm{dt}. \tag{7.7}$$

From above equation, the amplitude of the marginal spectrum, which is the sum of amplitudes of corresponding frequencies along the whole time axis, indicates whether a frequency exists in the signal or not.

7.3 PCA

PCA is a mathematical procedure that uses an orthogonal transformation to convert a set of observations of possibly correlated variables into a set of values of uncorrelated variables called principal components. Although the concept of PCA has been proposed for almost 100 years, it was not widely used until personal computers were developed. PCA is used for analyzing one data set (one matrix). The number of principal components is less than or equal to the number of original variables, and the first principal component requires the highest variance. Considering the nonlinear relationship between signal characteristics, and to avoid the notorious differentiation of fatigue-caused frequency data from GW signals due to wave dispersion and multiple-mode coexistence, PCA reduces the dimension of a data matrix while still retaining its characteristic information, and then classifies the data into different sets, which can describe the evolution of structural integrity conditions. The sum of the variances of the first few principal components generally exceeds 80% of the total variance of original data, showing that the first few principal components are sufficient to characterize the information in the original data matrix and the remaining components are redundant with negligible contributions [130]. The basic principle in PCA is described by

$$\mathrm{X} = \mathrm{TL}' + \mathrm{E}. \tag{7.8}$$

In matrix *X*, the samples to be analyzed are held in different rows and columns. *T* is called the score matrix and *L* the loading matrix in a least squares sense. *E* is other residuals. Each principal component consists of one score and one loading vector. Component one has highest possible variance. Component two is orthogonal (in scores and loadings) and has the next highest possible variance, etc.

In this chapter, representative statistical parameters in the frequency domain were chosen as damage indices from signals obtained from individual sensors. The parameters were extracted at different steps during fatigue testing for a notched steel angle structure. Then PCA was applied to those original parameters to generate useful principal components in order to monitor the propagation of the fatigue crack.

7.4 Experimental Setup

A steel angle structure was welded with two identical orthogonal steel plates 600 mm×200 mm×5 mm in size to serve as an experimental sample (mechanical properties: Young’s modulus 210 GPa, Density 7850 kg/m3, Poisson’s ratio 0.28), shown in Figure

7.1 (a). An artificial notch 14 mm×4 mm in size was introduced into the middle of the welded zone causing a stress concentration occur so that a fatigue crack would quickly initiate from the notch. Before the fatigue test shown in Figure 7.1 (b), 12 circular PZT transducers 10 mm in diameter and 1 mm in thickness were freely surface-mounted on both upper sides of the structure, six on each plate, detailed in Figure 7.2. When one PZT transducer was identified as actuator the others served as sensors for monitoring GW propagation in the structure. The fatigue tests were carried out at the pressure of 15 kN-45 kN based on resonance between the steel sample and the PLG-200C high-frequency fatigue machine with vibration frequency about 110 Hz. The signals acquired from all sensing paths were extracted in unloading conditions when the fatigue crack grew to 15 mm, 21 mm, 28 mm and 38 mm. The fatigue crack is represented inside the structure as a surface-fatigue crack, shown in Figure 7.3.

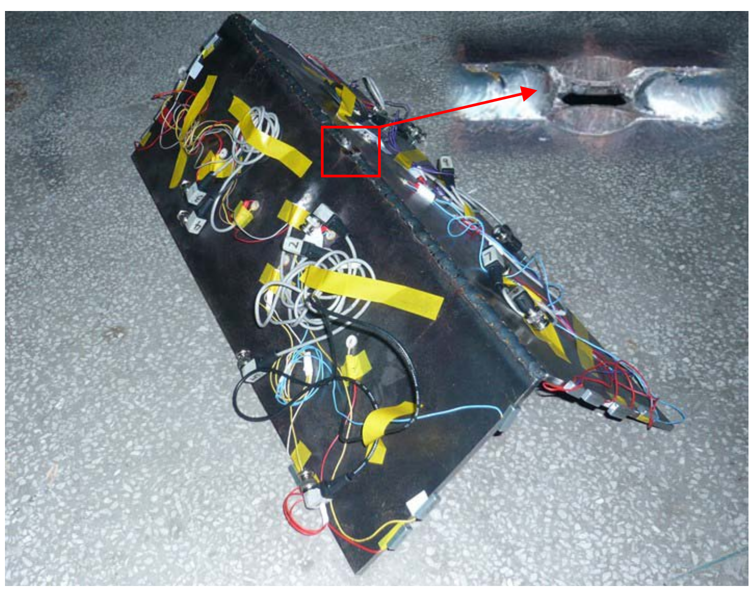

(a)

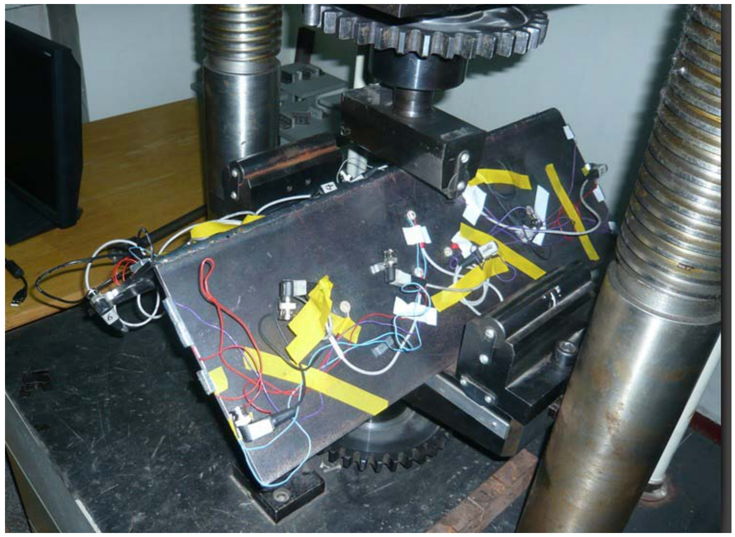

(b)

Figure 7.1 (a) Experimental sample for fatigue test (b) setup of fatigue test by three-point bending tests

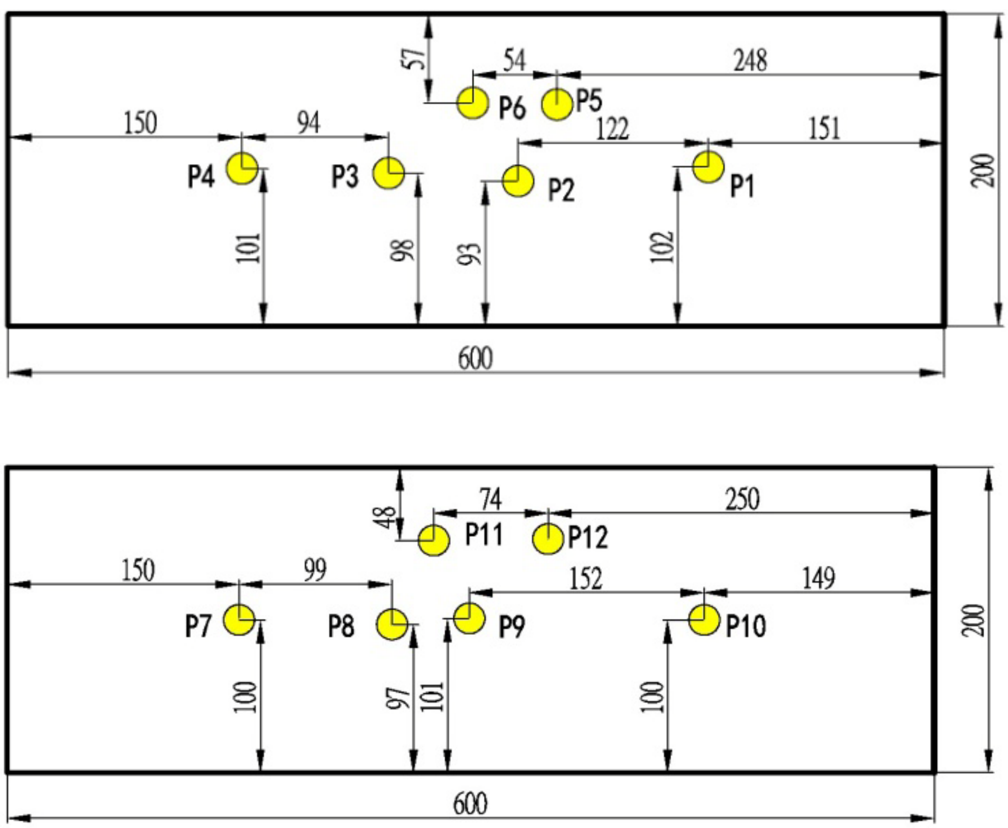

Figure 7.2 Schematic diagram of specimen and PZT positions (mm)

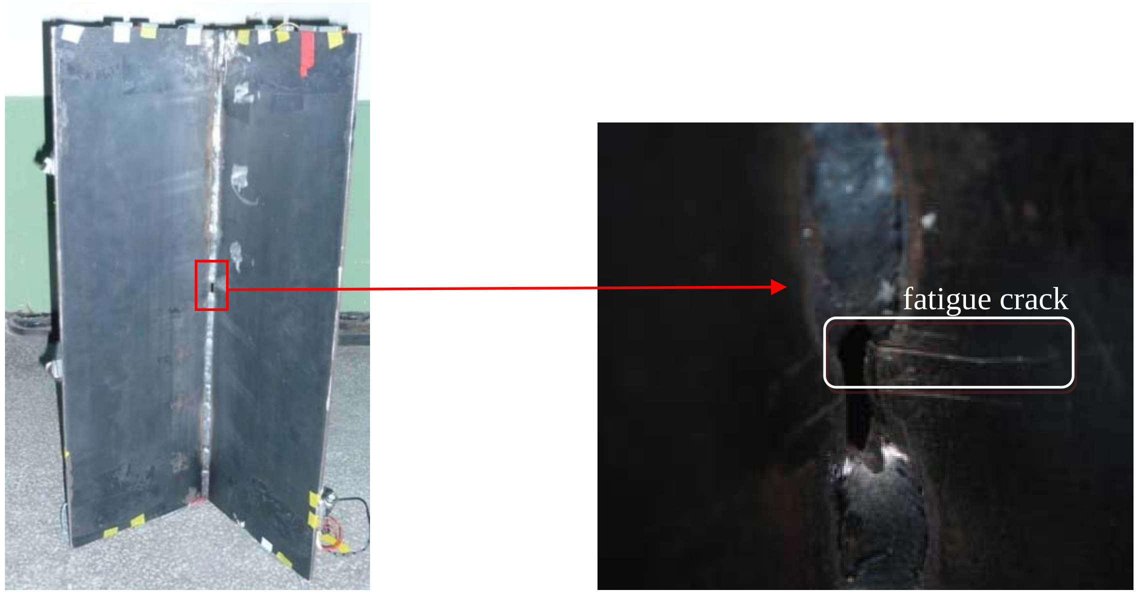

Figure 7.3 Fatigue crack inside the structure

The PZT transducers were excited as actuators in turn at 300 kHz by a 5-cycle Hanning-windowed toneburst by an Agilent® E1441 arbitrary waveform generator in order to generate GWs. An electric field was applied on the PZT actuators with a peak-to-peak voltage of 60 V after amplification by a Piezo system amplifier (PiezoSys® EPA-104). Dual-channel synchronous signal acquisition was performed on individual PZT sensors by a digitizer (Agilent® E1437A) through the IEEE-488 bus. As it was clear that multiple wave modes could not be avoided in the captured signals, the excitation frequency was strictly restricted to 300 kHz due to the multiple boundaries of the structure. Moreover, the wave packages scattered by the surface-fatigue crack were likely to overlap with those reflected from the notch because the fatigue crack was located particularly close to the physical edges of the notch. Because of these complexities, PCA was employed for identification of the integrity status of the structures.

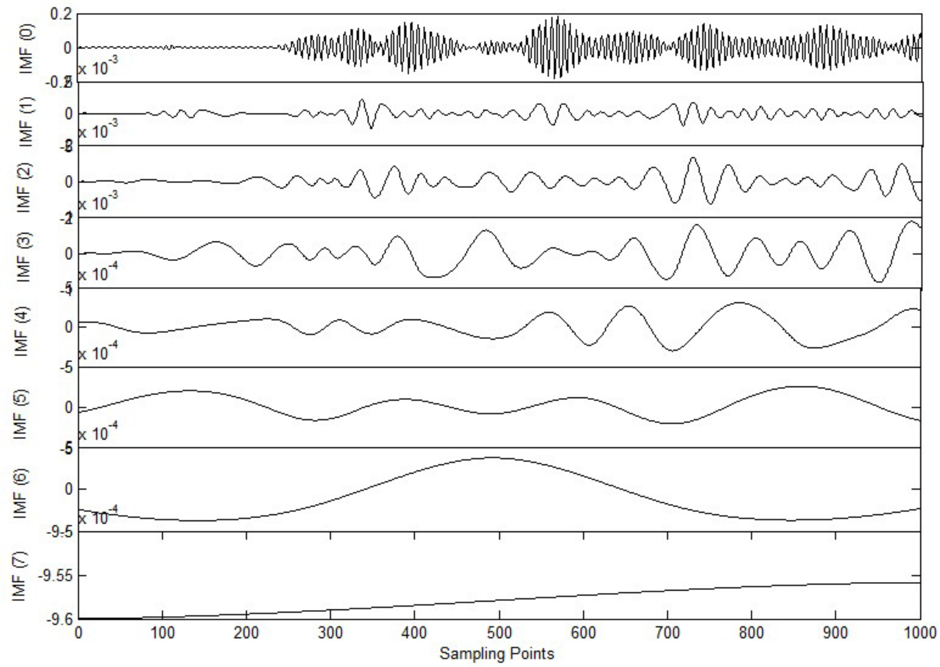

Figure7.4 EMD of the wave signal captured from $P_{1,4}$ for non-fatigue sample

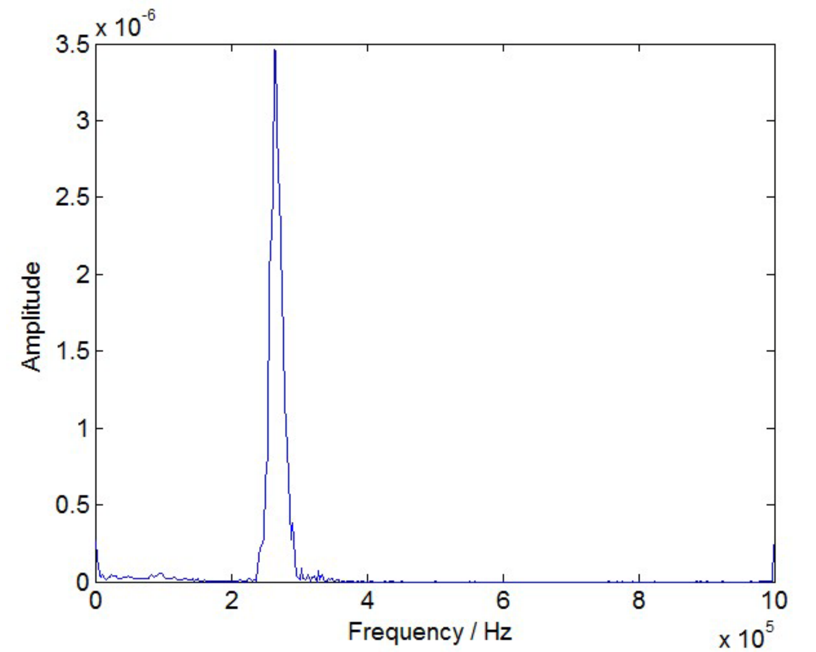

(a)

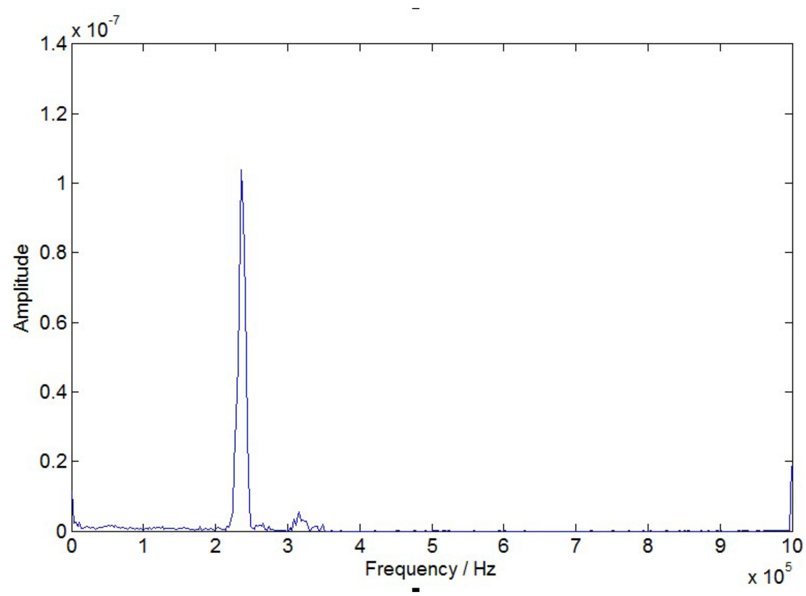

x 10^-7
1.4
1.2
1
0.8
0.6
0.4
0.2
0
Amplitude
0
1
2
3
4
5
6
7
8
9
10
Frequency / Hz
x 10^5

(b)

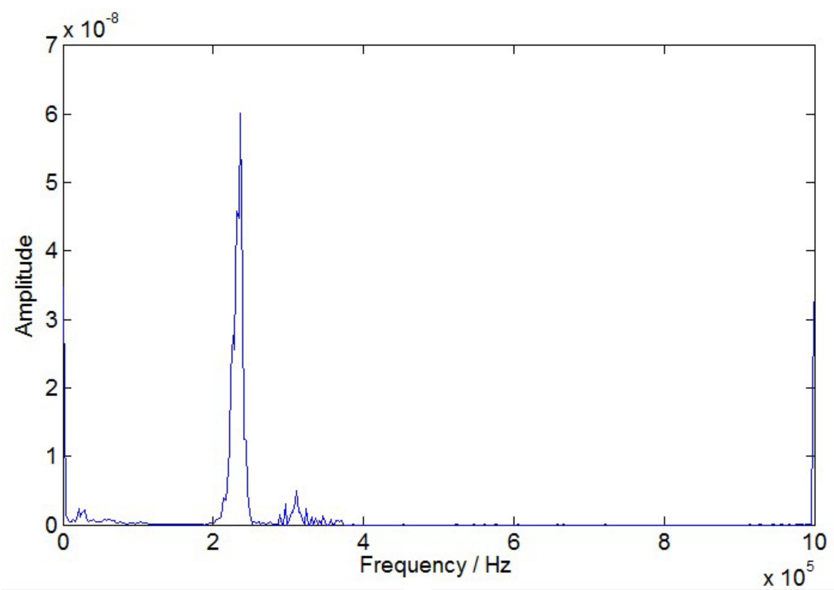

x 10^-8
7
6
5
4
3
2
1
0
Amplitude
0
2
4
6
8
10
Frequency / Hz
x 10^5

(c)

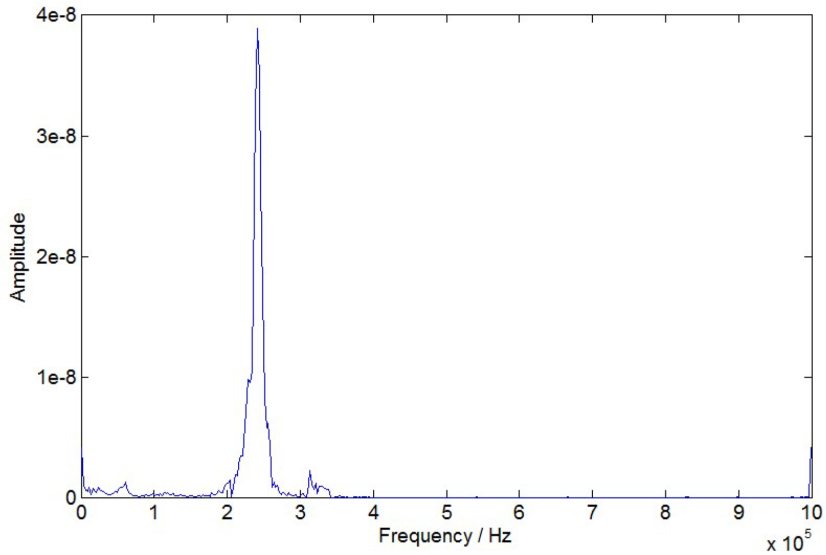

(d)

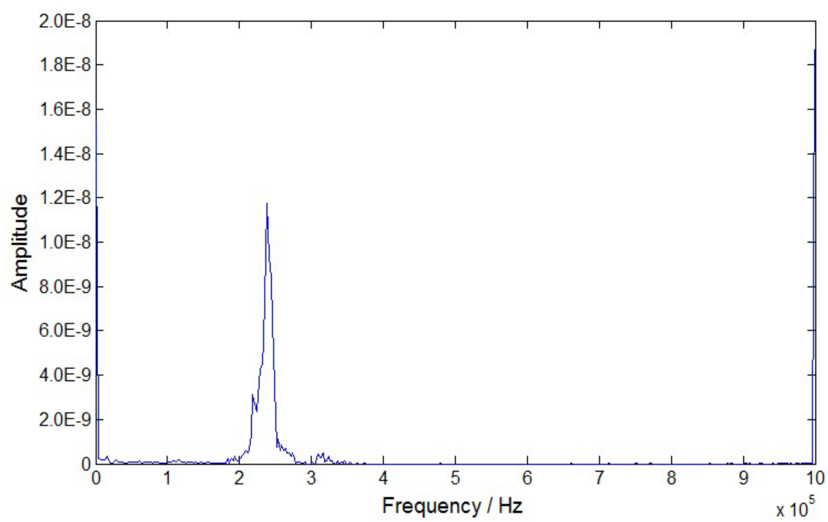

(e)

Figure 7.5 Marginal spectrum of (a) baseline data (b) 15 mm fatigue case (c) 21 mm fatigue case (d) 28 mm fatigue case (e) 38 mm fatigue case

7.5 Monitoring of Fatigue Crack Propagation by PCA

It was difficult to differentiate every waveform in the acquired signals even though the signals were purified. Statistical parameters from the frequency domain were calculated through the marginal spectrum in HHT. Figure 7.4 shows the IMF by HHT when the fatigue crack was 0 mm and Figure 7.5 shows five typical marginal spectra from signals of sensing path $P_{1,4}$ (P1 as actuator and P4 as sensor) at five different stages of fatigue cracks from 0 mm, 15 mm, 21 mm, 28 mm to 38 mm. From Figure 7.5 four statistical parameters were extracted, standing for the frequencies and amplitudes of the major frequency band, in which the changes of frequency either in value or amplitude indicated the difference caused by the fatigue crack. After introducing all sensing paths of actuator P1, 11 sensing paths and 5 different specimen conditions (benchmark and 4 crack lengths), 12 matrices for 12 actuators with identical dimensions of 55×4 were developed. Then, PCA was applied to these matrices to compress the characteristics in other major factors of lower dimension. The results of PCA from actuator P1 show that the matrix can be substituted by the first few principal components according to the sum of the variances. Signal variances explained by the principal components are shown in Figure 7.6, indicating that it was sufficient to take the first two principal components for analysis. Figure 7.7 shows the PCA result from actuator P1 for principal component 2 against principal component 1.

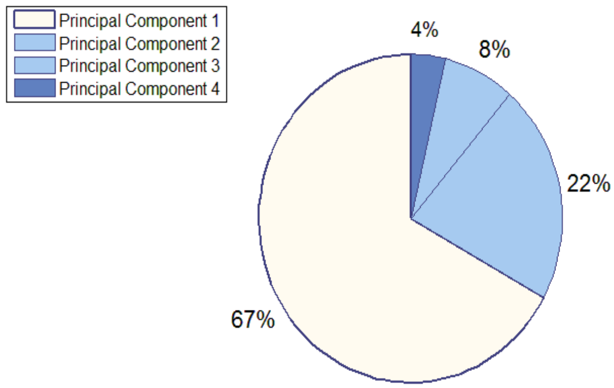

Figure 7.6 Signal variances explained by the principal components for actuator P1

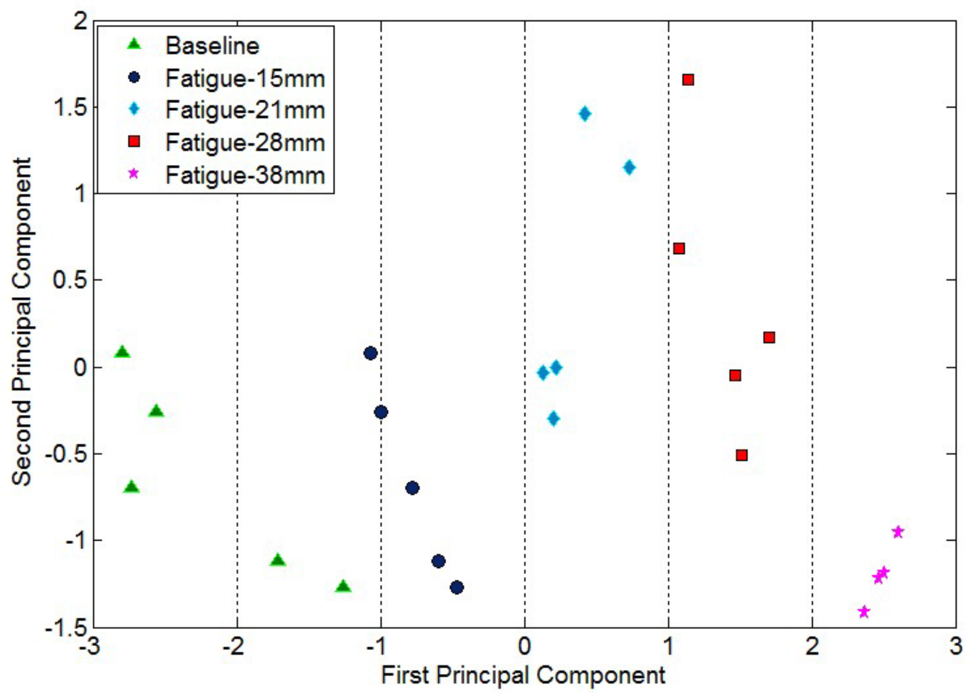

Figure 7.7 Distribution of the first two principal components of actuator P1 in all conditions

It is clearly shown that the principal components obtained by PCA can be classified into different groups for which non-fatigue data are located far from those of fatigue. The difference between the non-fatigue case and the 15 mm fatigue crack can be highlighted by different quadrants. However, differences between the cases of the 21 mm to 38 mm fatigue cracks are not identified by this result. Moreover, when actuator P7 was applied instead of actuator P1, the first two components were introduced into the analysis and the result is shown in Figure 7.8. From this figure, the tendency of fatigue crack propagation from 0 mm to 38 mm can be observed. If take P7 as the actuator and P8-P12 as sensors, we obtain a similar phenomenon that, with the increase in length of the fatigue crack, the ratio between principal component 2 and principal component 1 changes, locating information from different lengths of fatigue crack in different groups. The results in Figure 7.8 indicate that whether the actuator chosen for identifying principal components is located in the fatigued plate or not does not affect the evaluation result.

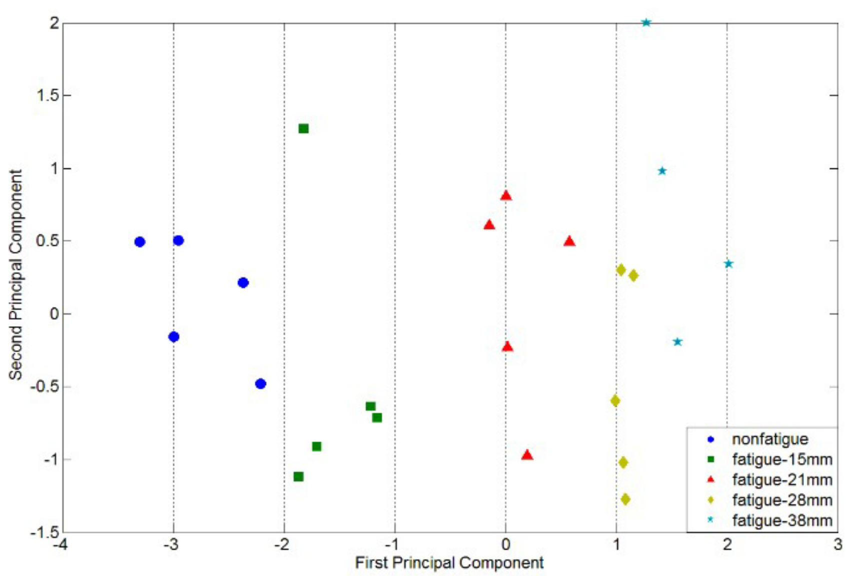

Figure 7.8 Distribution of the first two principal components of actuator P7 in three fatigue conditions

7.6 Concluding Remarks

In this chapter, a freely located PZT sensor network including 12 transducers surface-mounted on a WSAS was applied to generate and collect GW signals in order to monitor the propagation of a surface-fatigue crack. Signals corresponding to different fatigue crack lengths were acquired during a fatigue test to obtain statistical characteristics in the frequency domain by marginal spectrum in HHT as damage indices. PCA was then employed to the matrix of damage indices and was successful in classifying the data into different groups, indicating that the method could be used to identify a fatigue crack and monitor its propagation in complex steel structures.

CHAPTER 8 Conclusions and Future Directions

8.1 Conclusions

Welded structures with fatigue cracks exist widely in real engineering situations and usually play vital roles in the whole framework. Identification of a crack in such structures in operation is a highly challenging topic which deserves in-depth investigation. The GW-SHM technique, which can be regarded as the integration of actuators and sensors into structural components combined with automated advanced signal processing procedure for implementing a damage identification strategy, makes this challenging demand realizable. The subject of this thesis was detection of non-fatigue damage and fatigue damage based on GW-SHM technologies in plate-like structures and complex structures. Damage identification strategies were demonstrated in simple to complex structures, from artificial damage to fatigue crack, using either pulse-echo or pitch-catch configuration by PZT pairs.

The GW S_0 at the central frequency of 150 kHz was initially explored for the detection of a weld in a 10 mm thick steel plate from a PZT pair in pitch-catch configuration. Through comparison of the HT coefficients from an intact plate and from a plate with weld, by experiments and FEM, the weld effect was calibrated. Then the GW mode A_0, larger in amplitude than S_0 for the pulse-echo configuration, was applied for identification of an artificial notch within the welded zone of a steel plate. Subsequently, several kinds of materials were filled within the notch as impurities to investigate the detection effects of impurities in damage on the characteristics of GW propagation. The identification technique using GWs was shown to be suitable for the detection of weld and damage in welded structures.

It is evident that the above technologies and up-to-the-minute health surveillance can be extended to a WTSS to prevent the WTSS from being involved in catastrophic failure caused by cumulative defects and fatigue loads during operation, avoiding any possible loss of life and property. In this section, the propagation of GWs in a WTSS is investigated using experimental analysis and FEM for identification of single and dual welding damage. A PZT sensor network was organized and surface-mounted on the WTSS to excite and acquire GWs. According to the characteristics of GWs, different excitation frequencies were explored in both the experiments and simulations. A concept DPP, based on a signal feature termed ToMD, which is extracted from captured GW signals, was used in data analysis. With ToMD and DPP, a probability-based damage imaging approach and a two-level image fusion scheme were adopted to enhance the robustness of the approach in the presence of measurement noise and uncertainties. The results demonstrate the effectiveness of the developed approach for identifying multiple instances of damage in a WTSS.

To establish the proposed method of fatigue crack identification, a fatigue crack was introduced into a 10 mm thick steel plate with multiple boundaries due to notches for initiating fatigue cracks and holes for supporting the fatigue sample during fatigue testing. The capability of the probability-based damage imaging approach in terms of a signal feature ToF was evaluated experimentally and numerically for estimation of the presence and location of a 15 mm fatigue crack in a metallic structure based on GWs generated by an active PZT network. The characteristics of captured signals were extracted from the purified signals based on the wave energy distribution with the aid of a correlation function, DWT and CWT. This procedure ensured that the wave signal and its corresponding energy distribution in the time domain were concentrated in a narrower band of the excited frequency after the WT analysis, to enhance the wave scattering by the presence of a defect. Then a series of tests, including tensile and compressive tests, was undertaken to investigate loading effect on the wave signals. The simulation and experimental results agreed well, indicating that a fatigue crack could reflect and transmit GWs by reason of the discontinuous contact of crack surfaces, which demonstrated the effectiveness of the proposed method for real-time monitoring of fatigue cracks in metallic structures.

Apart from damage detection, it is obviously important to develop appropriate methods to monitor and evaluate fatigue crack propagation and the integrity of such structures. Thus, two damage identification strategies based on GWs for monitoring fatigue cracks in metallic structures were demonstrated, in which two sensor networks, with eight and six PZT transducers respectively, were employed. With application of a cyclic fatigue load, a fatigue crack grew from 7 mm to 37 mm. It was inevitable, however, that after a succession of fatigue tests of great intensity, the PZT transducers indicated a discrepancy in the properties of signal excitation and acquisition due to mechanical impact, in both PZTs and bonding layers. To decrease dependency on the baseline data, a damage detection technique, TRM, was adopted, which did not require direct comparison of the test signal with the baseline data. Based on the theory, the experimental results showed that the TRM combined with the DPP-based damage imaging approach was suitable for estimating the presence and propagation of fatigue crack in metallic structures. Moreover, the PCA-based damage classification method was capable of reducing the dimensions of a complex set of original data and classifying the different structural conditions due to crack growth. Further, PCA was still robust for classification of conditions in demanding circumstances, such as changes in environmental temperature, where some statistical parameters as damage indices were incapable of differentiating conditions with the existence of damage.

On the basis of previous sections, a GW-based fatigue crack monitoring technique for WSAS was developed based on features extracted in the frequency domain. Experimental results showed that the propagation of GWs in WSAS was highly complicated by wave dispersion, material attenuation, boundary reflection and structural complexity. In particular, there has been little study of skin-deep fatigue crack. To eliminate diverse interference and extract helpful signal characteristics, the PCA method based on marginal spectrum in HHT as damage indices was employed to obtain distinct structural states. The results indicate that the proposed methods can be used to identify fatigue crack and to monitor propagation of the fatigue crack in complex steel structures.

8.2 Future Directions

The effective technologies described in this thesis are basically in terms of linear ultrasonic waves which are incapable of detecting the microstate of fatigue cracks in their initial states. Applications of the technologies are currently limited to laboratory conditions. However, detection of fatigue cracks in their initial state is extremely important for our research work for engineering applications. In the future, nonlinear ultrasonic techniques which can quantitatively detect and characterize plastic deformation such as fatigue cracks, especially microcracks, will be demonstrated by numerical and experimental analysis.

Experimental studies

In this thesis, detection of fatigue damage and monitoring of its propagation in plate-like structures and complex structures were demonstrated in the time domain, frequency domain and time-frequency domain by pitch-catch and pulse-echo configurations based on baseline-free method and baseline-referee approaches. The smallest fatigue crack identified successfully was 7 mm in length, which was not enough for proving the proposed method in detection of the initiation of fatigue crack. In the near future, more plate-like or complex structures such as plate with girder geometry, even tubular structures, will be considered for locating fatigue damage in the initial state, to extend the present studies into more practical situations.

FEM studies

Clearly, the fatigue crack model established in this thesis is different to some degree from detection of real fatigue cracks, for which reason the FEM results were not identical to the experimental results. It is acknowledged that a correct model is important for FEM studies. A model that can replicate applications in the real world and produce accurate FEM results can save much manpower and time. Thus, in future, we will work on development of a model for simulating fatigue crack which can be used for comparing and forecasting situations in experiments and real-world applications.

Advanced signal processing process

Apart from experimental study and numerical analysis, signal processing methods for feature extraction and damage diagnosis are also of great importance in GW-SHM. In real-world applications, GWs in engineering structures are considerably complicated due to wave dispersion, material attenuation, boundary reflection and structural complexity. Under these circumstances, the wave components containing damage information can easily be overlapped by background noise. Great need exists, therefore, for further development of signal processing and data fusion to enhance the stability of damage detection technology.

REFERENCES

1. Giurgiutiu, V., 2008, Structural health monitoring with piezoelectric wafer active sensors., *Academic Pr.*
2. http://en.wikipendia.org/wiki/NDE
3. Su, Z. Q. and Ye L., 2009, Identification of damage using guided waves: from fundamentals to applications, *Lecture Notes in Applied and Computational Mechanics,* 48, London, UK: Springer-Verlag GmbH & Co.
4. Worden, K., Farrar, C. R., Manson, G., and Park, G., 2007, The fundamental axioms of structural health monitoring, *Proceedings of the Royal Society A: Mathematical, physical and Engineering Sciences*, 463(2082):1639-1664.
5. Boller, C., and Buderath, M., 2007, Fatigue in aerostructures - where structural health monitoring can contribute to a complex subject, *Philosophical Transactions of the Royal Society A: Mathematical, Physical and Engineering Sciences,* 365(1851): 561-587.
6. Worden, K., and Dulieu-Barton, J. M., 2004, An overview of intelligent fault detection in systems and structures, *Structural Health Monitoring*, 3(1): 85-98.
7. Farrar, C. R., Doeblíng, S. W., and Nix, D. A., 2001, Vibration-based structural damage identification, *Philosophical Transactions of the Royal Society A: Mathematical, Physical and Engineering Sciences,* 359(1778): 131-149.
8. Banerjee, S., Ricci, F., Monaco, E., Lecce, L., and Mal, A., 2007, Autonomous impact damage monitoring in a stiffened composite panel, *Journal of Intelligent Material Systems and Structures,* 18(6): 623-633.
9. Huguet, S., Godin, N., Gaertner, R., Salmon, L., and Villard, D., 2002, Use of acoustic emission to identiff damage modes in glass fibre reinforced polyester, *Composite Science and Technology*, 62(10-11): 1433-1444.
10. Hu, N., Cai, Y. D., Zhu, G. J., Tsuji, C., Liu, Y. L., Alamusi, and Cao, Y. P., 2012, Characterization of damage size in metallic plates using guided waves, *Structural Health Monitoring: An International Journal,* 11:125-137.
11. Su, Z. Q., Ye, L., and Lu, Y., 2006, Guided waves for identification of damage in composite structures: A review, *Joumal of Sound and Vibration*, 295(3-5): 753-780.
12. Schubert, L., Kuttner, M., Frankenstein, B., and Hentschel, D., 2007, Structural Health Monitoring of a rotor blade during statical load test, *18th International Workshop on Database and Expert Systems Applications,* (DEXA '07).
13. Hu, N., Shimomukai, T., Fukunaga, H., and Su, Z. Q., 2008, Damage identification of metallic structures using A0 mode of guided waves, *Structural Health Monitoring,* 7: 271-285.
14. Cawley, P., and Alleyne, D., 1996, The use of guided waves for the long range inspection of large structures, *Journal of Ultrasonics,* 34: 287-290.

15. Giurgiutiu, V., 2005, Tuned guided wave excitation and detection with piezoelectric wafer active sensors for structural health monitoring, *Intelligent Material Systems and structures*, 16: 291-305.

16. Lu, Y., Ye, L., and Su, Z. Q., 2006, Crack identification in aluminum plates using guided wave signals of a PZT sensor network, *Smart Mater. Struct.*,15: 839-849.

17. Su, Z. Q., and Ye L., 2004, Fundamental lamb mode-based delamination detection for CF/EP composite laminates using distributed piezoelectrics, *Structural Health Monitoring*, 3: 43-67.

18. Su, Z. Q., and Ye L., 2005, Guided wave propagation-based damage identification for quasi-isotropic cf/ep composite laminates using artificial neural algorithm: part i – methodology and database development, *Intelligent Material Systems and Structures*, 16: 97-111.

19. Guo, N. Q., and Cawley, P., 1994, Guided wave reflection for the quick nondestructive evaluation of large composite laminates, *Materials Evaluation*, 404-411.

20. Zheng, P., Greve, D. W., and Oppenheim, I. J., 2008, Crack detection with wireless inductively-coupled transducers, *Sensors and smart structures technologies for civil, mechanical, and aerospace systems 2008* : (10-13 March 2008, San Diego, California, USA), vol. 6932 (2), 69321H.1-69321H.10.

21. Wang, X. J., Tse, P. W., Mechefske, C. K., and Hua, M., 2010, Experimental investigation of reflection in guided wave-based inspection for the characterization of pipeline defects, *NDT&E International* 43: 365-374.

22. Tse, P. W., 2006, The use of cylindrical guided waves for inspecting defects in surface/buried pipelines, *Journal of Hong Kong Engineer*, 34(12): 17.

23. Park, S. C, Yun, B., Roh, Y., and Lee, J. J., 2006, PZT-based active damage detection techniques for steel bridge components, *Smart Mater. Struct.*, 15: 957-966.

24. Juluri, N., Lowe, M., and Cawley, P., 2007, The guiding of ultrasound by a welded joint in a plate, *American Institute of Physics*, 26: 1079-1086.

25. Croxford, A. J., Wilcox, P. D., Drinkwater, B. W., and Konstantinidis, G., 2007, Strategies for guided-wave structural health monitoring, *Proceedings of the Royal Society A: Mathematical, Physical and Engineering Sciences*, 463(2087): 2961-2981.

26. Wang, D., 2010, Damage diagnostic imaging technique for structural health monitoring, Doctor of Philosophy, Sydney, Australia: The University of Sydney.

27. Parker, R. P., 1984, Medical applications of X-ray and gamma-ray imaging methods, *Nuclear Instruments & Methods in Physics Research Section a-Accelerators Spectrometers Detectors and Associated Equipment*, 221: 221-225.

28. Park, G., and Inman, D. J., 2007, Structural health monitoring using piezoelectric impedance measurements, *Philosophical Transactions of the Royal Society A: Mathematical, Physical and Engineering Sciences*, 365(1851): 373-392.

29. http://64.105.143.179/Sensors.asp

30. Hill, K. O., Fujii, Y., Johnson, D. C. and Kawasaki, B. S., 1978, Photosensitivity in optical fiber waveguides: application to reflection fiber fabrication, *Appl. Phys. Lett.*, 32(10): 647.

31. Othonos, A., and Kalli, K., 1999, Fiber Bragg gratins: fundamentals and applications in telecommunications and sensing, *Boston, Artech House.*

32. National_Aeronautics_and_Space_Administration_(NASA), 2007, *Derailed System failure case studies*, 1(5): 1-4.

33. MTR. CIRCULAR FOR RAIL MERGER (1) CONNECTED TRANSACTIONS (2) VERY SUBSTANTIAL ACQUISITION. 2007; Available from: http://www.mtr.com.hk/eng/investrelation/circulars2007/ew%200066cir%2020070903.pdf.

34. Achenbach, J. D., 2000, Quantitative nondestructive evaluation, *International Journal of Solids and Structures*, 37(1-2): 13-27.

35. Gray, J., and Tillack, G. R., 2011, X-ray imaging methods over the last 25 years - new advances and capabilityes, in Review of Progress in Quantitative Nondestructive Evaluation, D.O. Thompson and D.E. Chimenti, Editors, *American Institute of Physics*: New York.

36. Balageas, D. L., 2002, Structural health monitoring R&D at the "European Research Establishments in Aeronautics" (EREA), *Aerospace Science and Technology,* 6(3): 159-170.

37. Sohn, H., Farrar, C. R., Hemez, F. M., Shunk, D. D., Stinemates, D. W., and Nadler, B. R., 2003, Review of Structural Health Monitoring Literature: 1996-2001, *Los Alamos National Laboratory Report*, LA-13976-MS.

38. Boller, C., 2001, Ways and options for aircraft structural health management, *Smart Materials & Structures*, 10(3): 432-440.

39. Alleyne, D. N., and Cawley. P., 1992, The Interaction of guided waves with Defects, *Ieee Transactions on Ultrasonics Ferroelectrics and Frequency Control*, 39(3): 381-397.

40. Kessler, S. S., Spearing, S. M., and Soutis, C., 2002, Damage detection in composite materials using guided wave methods, *Smart Materials & Structures,* 11(2): 269-278.

41. Staszewski, W. J., Boller, C., and Tomlinson, G. R., 2004, Health Monitoring of Aerospace Structures: Smart Sensor Technologies and Signal Processing, New York, USA: John Wiley & Sons, Inc.

42. Giurgiutiu, V., and Bao. J., 2004, Embedded-ultrasonics structural radar for in situ structural health monitoring of thin-wall structures, *Structural Health Monitoring-an International Journal*, 3(2): 121-140.

43. Moyo, P., and Brownjohn, J. M. W., 2002, Detection of anomalous structural behaviour using wavelet analysis, *Mechanical Systems and Signal Processing,* 16 (2-3): 429-445.

44. Chang, F. K., 2002, Introduction to health monitoring: context, problems, solutions,

Presentation at the 1st European Pre-workshop on Structural Health Monitoring, Paris, France, July, 9, 2002.

45. Anton, S. R., Inman, D. J., and Park, G., 2009, Reference-free damage detection using instantaneous baseline measurements, *Aiaa Journal*, 47(8): 1952-1964.
46. Badcock, R. A., and Birt, E. A., 2000, The use of 0-3 piezocomposite embedded guided wave sensors for detection of damage in advanced fibre composites, *Smart Materials & Structures*, 9(3): 291-297.
47. Kundu, T., Das, S., and Jata, K. V., 2009, Health monitoring of a thermal protection system using guided waves, *Structural Health Monitoring-an International Journal*, 8 (1): 29-45.
48. Lin, X., and Yuan, F. G., 2005, Experimental study applying a migration technique in structural health monitoring, *Structural Health Monitoring-an International Journal*, 4 (4): 341-353.
49. Ostachowicz, W., Kudela, P., Malinowski, P., and Wandowski, T., 2009, Damage localisation in plate-like structures based on PZT sensors, *Mechanical Systems and Signal Processing*, 23 (6): 1805-1829.
50. Park, H. W., Sohn, H., Law, K. H., and Farrar, C. R., 2007, Time reversal active sensing for health monitoring of a composite plate, *Journal of Sound and Vibration*, 302(1-2): 50-66.
51. Ihn, J. B., and Chang, F. K., 2004, Detection and monitoring of hidden fatigue crack growth using a built-in piezoelectric sensor/actuator network: I. Diagnostics, *Smart Materials & Structures*,13(3): 609-620.
52. Zhao, X. L., Gao, H. D., Zhang, G. F., Ayhan, B., Yan, F., Kwan, C., and Rose, J. L., 2007, Active health monitoring of an aircraft wing with embedded piezoelectric sensor/actuator network: I. Defect detection, localization and growth monitoring, *Smart Materials & Structures*, 16(4): 1208-1217.
53. Barke, D., and Chiu, W. K., 2005, Structural health monitoring in the railway industry: A review, *Structural Health Monitoring-an International Journal*, 4(1): 81-93.
54. Rose, J. L., Avioli, M. J., and Song, W.J., 2002, Application and potential of guided wave rail inspection, *Insight*, 44: 353-358.
55. Wilcox, P., Evans, M., Pavlakovic, B., Alleyne, D. N., Vine, K., Cawley, P., and Lowe, M., 2003, guided wave testing of rail, *Insight*, 45: 413-420.
56. Rose, J. L., 1995, Recent advances in guided wave NDE, *in Proceedings of the IEEE Ultrasonics Symposium*, Nov., Seattle, USA, 761-770.
57. Demma, A., Cawley, P., Lowe, M., and Roosenbrand, A. G., 2003, The reflection of the fundamental torsional mode from cracks and notches in pipes, *The journal of the Acoustical Society of America*, 114(2): 611-625.
58. Alleyne, D. N., Pavlakovic, B., Lowe, M. J. S., and Cawley, P., 2001, Rapid long-range inspection of chemical plant pipework using guided waves, *Review of Progress in Quantitative Nondestructive Evaluation*, 20:181-187.

59. Rose, J. L., 2002, A baseline and vision of ultrasonic guided wave inspection potential, *Journal of Pressure Vessel Technology*, 124(3): 273-282.

60. Juluri, N., Lowe, M., and Cawley, P., 2007, The guiding of ultrasound by a welded joint in a plate, *Journal of American Institute of Physics*, 26: 1079-1086.

61. Alleyne, D. N., Pavlakovic, B., Lowe, M. J. S., and Cawley, P., 2001, Long-range propagation of guided waves in chemical plant pipework, *Materials Evaluation*, 55(4): 504-508.

62. Lowe, M. J. S., Alleyne, D. N., and Cawley, P., 1998, Defect detection in pipes using guided waves, *Ultrasonics*, 36(1-5): 147-154.

63. Liu, Z. H., He, C. F., Wu, B.,Wang, X. Y., and Yang, S. M., 2006, Circumferential and longitudinal defect detection using T(0,1) mode excited by thickness shear mode piezoelectric elements, *Ultrasonics*, 44(s1): E1135-E1138.

64. Pruell, C., Kim, J. Y., Qu, J. M., and Jacobs, L. J., 2009, Evaluation of fatigue damage using nonlinear guided waves, *Smart Mater. Struct., 18:* 035003:1-7.

65. Su, Z. Q., Ye, L., and Lu, Y., 2006, Guided waves for identification of damage in composite structures: A review, *Journal of Sound and Vibration*, 295**:** 753-780.

66. Staszewski, W. J., Lee, B. C., Mallet, L., and Scarpa, F., 2004, Structural health monitoring using scanning laser vibrometry: Part I. guided wave sensing, *Smart Mater. Struct.,* 13: 251-260.

67. Mallet, L., Lee, B. C., Staszewski, W. J., and Scarpa, F., 2004, Structural health monitoring using scanning laser vibrometry: Part II. guided waves for damage detection, *Smart Mater. Struct*., 13: 261-269.

68. Lu, Y., Ye, L., Su, Z. Q., and Yang, C. H., 2008, Quantitative assessment of through-thickness crack size based on guided wave scattering in aluminum plates, *NDT & E International*,41(1): 59-68.

69. Kercel, S. W., Kisner, R. A., Klein, M. B., Bacher, G. D., and Pouet, B., 1999, In-process detection of weld defects using laser-based ultrasound, *Proc. SPIE,* 3852, 81-92.

70. Schumacher, N. A., Duffer, C., and Burger, C. P., 1991, Non-contact non-destructive evaluation of composite panel with plate waves, *Compos. Mater. Technol.*, 37: 219-223.

71. Mizutani, Y., Yamada, H., Nishino, H., Takemoto, M., and Ono, K., 2001, Non-contact detection of delaminations in impacted cross-ply CFRO using laser generated guided waves, *Proc. SPIE,* 4335: 330-341.

72. Qing, X., Kumar, A., Zhang, C., Gonzalez, I. F., Guo, G., and Chang, F. K., 2005, A hybrid piezoelectric/fiber optic diagnostic system for structural health monitoring, Smart Materials and Structures, 14(3): S98-S103.

73. Hayashi, Y., Ogawa, S. H., Cho, H., and Takemoto, M., 1999, Non-contact estimation of thickness and elastic properties of metallic foils by the wavelet transform of laser-generated guided waves, *NDT & E International*, 32**:** 21-27.

74. Lu, M. Y., Lu, X., Zhou, L. M., Su, Z. Q., and Ye, L., 2009, Guided-wave-based detections of weld and crack in steel plates, *Proc. SPIE, 7493,* 74932S.

75. Lu, X., Lu, M. Y., Zhou, L. M., Su, Z. Q., Cheng, L., Ye, L., and Meng, G., 2011, Evaluation of welding damage in welded tubular steel structures using guided waves and probability-based imaging approach, *Smart Mater. Struct.*, 20, 015018.

76. Su, Z. Q., Ye, L., and Bu, X., 2002, A damage identification technique for CF/EP composite laminates using distributed piezoelectric transducers, *Compos. Struct.*, 57: 465-471.

77. Diamanti, K., Hodgkinson, J. M., and Soutis. C., Damage detection of composite laminates using PZT generated guided waves, 2002, *Proceedings of the First European Workshop on Structural Health Monitoring*, 10–12, Paris, France, 398-405.

78. Fernandes, B., Gaydeck, P., and Burdekin, F. M., 2006, An intelligent sensor system for monitoring fatigue damage in welded steel components, *Nondestructive Testing and Evaluation,* 21: 13-25.

79. Wang, C. S., and Chang, F. K., 2000, Diagnosis of impact damage in composite structures with built-in piezoelectrics network, *Proc. SPIE, 3990,* 13-19.

80. Leong, W. H., Staszewski, W. J., Lee, B. C., and Scarpa, F., 2005, Structural health monitoring using scanning laser vibrometry: III. guided waves for fatigue crack detection, *Smart Mater. Struct.,*14: 1387-1395.

81. Teramoto, K., and Uekihara, A., 2008, Time-reversal imaging for subsurface defect detection over the lamb-wave field, *Proceedings of* S*ICE Annual Conference,* The University Electro-Communications, Japan, 514-519.

82. Grave, D. W., Tyson N. L., and Oppenheim, I. J., 2006, guided waves in plate girder geometries, *Proceedings of Conference & Exposition on Structural Dynamics.*

83. Ihn, J. B., and Chang, F. K., 2004, Detection and monitoring of hidden fatigue crack growth using a built-in piezoelectric sensor/actuator network: II. Validation using riveted joints and repair patches. *Smart Materials and Structures,* 13(3): 621-630.

84. Grondel, S. C., Delebarre, J., Assaad, J., Pierre, D., and Reithler, L., 2002, Fatigue crack monitoring of riveted aluminum strap joints by guided wave analysis and acoustic emission measurement techniques, *NDT&E International*, 35:137-146.

85. Moyo, P., and Brownjohn, J. M. W., 2002, Detection of anomalous structural behaviour using wavelet analysis, *Mechanical Systems and Signal Processing,* 16(2-3): 429-445.

86. Rokhlin, S. I., and Kim, J. Y., 2003, In situ ultrasonic monitoring of surface fatigue crack initiation and growth from surface cavity, *International Journal of Fatigue*, 25: 41-49.

87. Staszewski, W. J., Lee, B. C., and Traynor, R., 2007, Fatigue crack detection in metallic structures with guided waves and 3D laser vibrometry, *Meas. Sci. Technol.*, 18: 727-739.

88. Na, J. K., and Blackshire, J. L., 2010, Interaction of Rayleigh surface waves with a tightly closed fatigue crack, *NDT&E International*, 43: 432-439.

89. Dawson, B., 1976, Vibration condition monitoring techniques for rotating machinery, *The Shock and Vibration Digest (London: SpingerLink)*, 8(12): 3.

90. Lu, X., Zhou, L. M., Su, Z. Q., Ye, L., and Li, F. C., 2011, Fatigue crack detection using guided waves and probability-based imaging approach, *Proc. of The 8th International Workshop on Structural Health Monitoring*, Stanford (IWSHM8), USA, Sep. 2011.

91. Lu, M. Y., Wang, D., Zhou, L. M., Su, Z. Q., Cheng, L., and Ye, L., 2011, Monitoring of fatigue crack propagation of engineering structures using time reversal method, *Proc. of 18th International Conference on Composite Materials (ICCM 18)*, Jeju, Korea, Aug. 2011.

92. Lu, Y., Lu, M. Y., Ye, L., Wang, D., Zhou, L. M., and Su, Z. Q., 2011, Monitoring of fatigue crack growth using principal component analysis on guided wave signals, submitted to *Smart Materials and Structures*.

93. Vanlanduit, S., Guillaume, P., and Linden, G.V.D., 2003, On-line monitoring of fatigue cracks using ultrasonic surface waves. *NDT & E International*, 36: 601-607.

94. Gupta, S., Singh, D. S., and Ray, A., 2008, Statistical pattern analysis of ultrasonic signals for fatigue damage detection in mechanical structures, *NDT & E International*, 41: 491-500.

95. Doebling, S.W., et al., 1996, Damage identification and health monitoring of structural and mechanical systems from changes in their vibration characteristics: a literature review, Los Alamos Laboratory Report, LA-13070-MS.

96. Kim, B. H., Park, T., and Voyiadjis, G. Z., 2006, Damage estimation on beam-like structures using the multi-resolution analysis, *International Journal of Solids and Structures*, 43(14-15): 4238-4257.

97. Konstantinidis, G., Drinkwater, B., Drinkwater, W., and Wilcox, P. D., 2006, The temperature stability of guided wave structural health monitoring systems. *Smart Materials and Structure*, 15: 967-976.

98. Blaise, E., and Chang, F. K., 2001, Built-in diagnostics for debonding in sandwich structures under extreme temperatures, *Proceedings of the 3rd International Workshop on Structural Health Monitoring: the Demands and Challenges*, edited by Chang, F. K., CRC Press, Boca Raton, 154-163.

99. Kim, S. B., and Sohn, H., 2008, Continuous fatigue crack monitoring without baseline data, *Fatigue & Fracture of Engineering Materials & Structures*, 31: 644-659.

100. Rokhlin, S. I., et al., 2007, Nondestructive sizing and localization of internal microcracks in fatigue samples, *NDT & E International*, 40: 462-470.

101. Kim, J. Y., and Rokhlin, S. I., 2002, Surface acoustic wave measurements of small fatigue cracks initiated from a surface cavity, *International Journal of Solids and Structures*, 39: 1487-1504.

102. Lu, Y., et al., 2009, Artificial neural network (ANN)-based crack identification in aluminum plates with guided wave signals, *Journal of Intelligent Material Systems and Structures*, 20: 39-49.

103. Lu, Y., et al., 2007, Quantitative evaluation of crack orientation in aluminum plates based on guided waves. *Smart Materials and Structure*, 16: 1907-1914.

104. Chetwynd, D., et al., 2008, Damage detection in an aluminum plate using outlier analysis, *Fatigue & Fracture of Engineering Materials & Structures*, 31: 629-643.

105. Mujica, L. E., et al., 2010, Q-statistic and T2-statistic PCA-based measures for damage assessment in structures, *Structural Health Monitoring,* in press: DOI: 10.1177/1475921710388972.

106. Diligent, O., and Lowe, M. J. S., 2005, Reflection of the S0 lamb mode from a flat bottom circular hole, *Acoustical Society of America,* 118(5): 2869-2879.

107. Yu, D. J., Cheng, J. S. and Yang, Y., 2006, Hilbert-Huang transform method for mechanical damage detection.

108. Su, Z., and Ye, L., 2004, Selective generation of guided wave modes and their propagation characteristics in defective composite laminates, *Proceedings of the Institution of Mechanical Engineers Part L-Journal of Materials-Design and Applications*, 218 (L2): 95-110.

109. Rose, J. L., 1999, Ultrasonic Waves in Solids, New York: Cambridge University Press.

110. Walpole, R. E., Myers, R. H., and Myers, S. L., 1998, Probability and statistics for engineers and scientists, *Upper Saddle River, NJ: Prentice Hall Inc*., 51-61, 143-157.

111. Ihn, J. B., and Chang, F. K., 2008, Pitch-catch active sensing methods in structural health monitoring for aircraft structures, *Structural Health Monitoring-an International Journal*, **7** (1): 5-19.

112. Wang, C. H., Rose, J. T., and Chang, F. K., 2004, A synthetic time-reversal imaging method for structural health monitoring, *Smart Materials & Structures,* 13(2): 415-423.

113. Michaels, J. E., and Michaels, T. E., 2007, Guided wave signal processing and image fusion for in situ damage localization in plates, *Wave Motion* 44(6): 482-492.

114. Konstantinidis, G., Wilcox, P. D., and Drinkwater, B. W., 2007, An investigation into the temperature stability of a guided wave structural health monitoring system using permanently attached sensors, *Ieee Sensors Journal,* **7** (5-6): 905-912.

115. Su, Z. Q., Wang, X. M., Cheng, L., Yu, L., and Chen, Z. P., 2009, On selection of data fusion schemes for structural damage evaluation, *Structural Health Monitoring-an International Journal,* 8 (3): 223-241.

116. Lemistre, M., and Balageas, D., 2001, Structural health monitoring system based on diffracted guided wave analysis by multiresolution processing, *Smart Mater. Struct.*, 10: 504-511.

117. Ding, Y., Reuben, R. L., and Steel, J. A., 2004, A new method for waveform analysis for estimating AE wave arrival times using wavelet decomposition, *NDT & E Int.*, 37: 279-290.
118. Bloch, I., 1996, Information combination operators for data fusion: A comparative review with classification, *IEEE Trans. Syst. Man Cybern. Paart A-Syst. Hum.*, 26(1): 52-67.
119. Wang, D., Ye, L., and Lu, Y., 2009, A Probabilistic Diagnostic Algorithm for Identification of Multiple Notches Using Digital Damage Fingerprints (DDFs), *Journal of Intelligent Material Systems and Structures*, 20: 1439-1450.
120. Cohen, J., Cohen, P., West, S. G., and Aiken, L. S., 2003, Applied Multiple Regression/Correlation Analysis for the Behavioral Sciences, *Lawrence Erlbaum Associates,* Mahwah, NJ.
121. Pavlakovic, B. N., and Lowe, M. J. S., 2001, *Disperse User's Manual: version 2.0.11*, University of London.
122. Li, F. C., et al., 2009, Multiple damage assessment in composite laminates using a Doppler-effect-based fiber-optic sensor, *Measurement Science and Technology,* 20: 115109.
123. Lu, Y., et al., 2010, Piezo-activated guided wave propagation and interaction with damage in tubular structures. *Smart Structures and Systems,* 6(7): 835-849.
124. Wang, D., et al., 2010, Probabilistic damage identification based on correlation analysis using guided wave signals in aluminum plates, *Structural Health Monitoring,* 9(2): 133-144.
125. Lu, Y., et al., 2009, Time-domain analyses and correlations of guided wave signals for damage detection in a composite panel of multiple stiffeners, *Journal of Composite Materials*, 43(26): 3211-3230.
126. Harria, K., Guillaume, P., 2008, and Vanlanduit, S., On-line damage detection on a wing panel using transmission of multisine ultrasonic waves, *NDT & E International*, 41: 312-317.
127. Wang, D., et al., 2010, A damage diagnostic imaging algorithm based on the quantitative comparison of guided wave signals, *Smart Materials and Structure*, 19: 065008.
128. Huang, N. E., 1998, The empirical mode decomposition and the Hilbert spectrum for nonlinear and non-stationary time series analysis, *J.Proc.R. Soc. Lond. A,* 454: 903-995.
129. Zhong, Y. M., Qin, S. R. and Tang, B. P., 2004, Study on the marginal spectrum in Hilbert-Huang transform, *Systems Engineering and Electronics,* 26(9).

130. Cammarata, M., et al., 2010, Application of principal component analysis and wavelet transform to fatigue crack detection in waveguides, *Smart structures and systems*, 6(4): 349-362.

131. Koehler, B., Hentges, G., and Mueller, W., 1997, A novel technique for advanced ultrasonic testing of concrete by using signal conditioning methods and a scanning laser vibrometer, *Proceedings of the NDT in Civil Engineering*, 123-134.